

<b>REPORT DOCUMENTATION PAGE</b>			Form Approved OMB No. 0704-0188	
Public reporting burden for this collection of information is estimated to average 1 hour per response, including the time for reviewing instructions, searching existing data sources, gathering and maintaining the data needed, and completing and reviewing the collection of information. Send comments regarding this burden estimate or any other aspect of this collection of information, including suggestions for reducing this burden, to Washington Headquarters Services, Directorate for Information Operations and Reports, 1215 Jefferson Davis Highway, Suite 1204, Arlington, VA 22202-4302, and to the Office of Management and Budget, Paperwork Reduction Project (0704-0188), Washington, DC 20503.				
1. AGENCY USE ONLY (Leave blank)		2. REPORT DATE August 22, 2001	3. REPORT TYPE AND DATES COVERED Technical 02/01/99 to 08/22/01	
4. TITLE AND SUBTITLE Near-wall Investigation of Three-dimensional Turbulent Boundary Layers			5. FUNDING NUMBERS N00014-99-1-0302	
6. AUTHORS David D. Kuhl and Roger L. Simpson				
7. PERFORMING ORGANIZATION NAME(S) AND ADDRESS(ES) Department of Aerospace and Ocean Engineering Virginia Polytechnic Institute and State University Blacksburg, Virginia 24061-0203			8. PERFORMING ORGANIZATION REPORT NUMBER VPI-AOE-273	
9. SPONSORING/MONITORING AGENCY NAME(S) AND ADDRESS(ES) Office of Naval Research 800 N. Quincy Street Arlington, Virginia 22217			10. SPONSORING/MONITORING AGENCY REPORT NUMBER	
11. SUPPLEMENTARY NOTES				
12a. DISTRIBUTION/AVAILABILITY STATEMENT Unlimited <b>DISTRIBUTION STATEMENT A</b> Approved for Public Release Distribution Unlimited			12b. DISTRIBUTION CODE	
13. ABSTRACT (Maximum 200 words) This report documents the experimental study for four different three-dimensional turbulent flows. The investigation focuses on near wall measurements in these flows. Several experimental techniques are used in the studies; however, the bulk of the investigation focuses on a three-orthogonal-velocity-component fiber-optic laser Doppler anemometer (3D-LDA) system. The control volume of the 3D-LDA is on the order of 50 micro-meter in size, or a y+ distance of around 2.3 units. An auxiliary small boundary layer wind tunnel (auxiliary tunnel) and a low speed linear compressor cascade wind tunnel (cascade tunnel) are utilized in this study. One of four flow experiments is done in the auxiliary tunnel the other three are in the cascade tunnel. The first three-dimensional turbulent flow is a vortical flow created by two half-delta wing vortex generators. Near wall secondary flow features are found. The second flow is an investigation of the first quarter chord tip gap flow in the cascade tunnel. Strong three-dimensional phenomena are found. The third flow investigated is the inflow to the compressor cascade with the moving wall. The experiment records shear layer interaction between the upstream flow and moving wall. Finally the fourth flow investigated is the inflow to the compressor cascade with the moving wall with half-delta wing vortex generators attached. Phase-averaged data reveal asymmetrical vortex structures just downstream of the vortex generators. This is the first time near wall turbulence data have been taken on these types of flows.				
14. SUBJECT TERMS Three-dimensional Flow, Turbulent Boundary Layers, compressor flows, tip gap flows, vortex generators			15. NUMBER OF PAGES 211	
			16. PRICE CODE	
17. SECURITY CLASSIFICATION OF REPORT UNCLASSIFIED	18. SECURITY CLASSIFICATION OF THIS PAGE UNCLASSIFIED	19. SECURITY CLASSIFICATION OF ABSTRACT UNCLASSIFIED	20. LIMITATION OF ABSTRACT UNLIMITED	

# Contents

Acknowledgements	i
Table of Contents	ii
List of Figures	vii
List of Tables	xiv
Nomenclature	xv
<b>1 Introduction</b>	<b>1</b>
1.1 Motivation . . . . .	1
1.2 Objective . . . . .	1
1.3 Thesis Layout . . . . .	3
<b>2 The Auxiliary Small Boundary Layer Wind Tunnel</b>	<b>4</b>
2.1 Introduction . . . . .	5
2.2 Apparatus and Test Flow . . . . .	6
2.2.1 Auxiliary Tunnel . . . . .	6
2.2.2 Trips . . . . .	6
2.2.3 Upstream Flow Quality . . . . .	7

2.2.4	Vortex Generators . . . . .	7
2.2.5	Measurement Section Flow Quality . . . . .	8
2.2.6	LDA System . . . . .	8
2.3	Post Processing . . . . .	9
2.4	Experimental Data . . . . .	12
2.5	Conclusions . . . . .	15
<b>3</b>	<b>Low-speed Linear Compressor Cascade Wind Tunnel</b>	<b>30</b>
3.1	Previous Set-up of the Cascade Tunnel . . . . .	31
3.2	Cascade Tunnel Modification . . . . .	32
3.2.1	Environmental containment tent . . . . .	32
3.2.2	Cooling system . . . . .	32
3.2.3	Particle injection system . . . . .	33
3.2.4	Plywood Bed . . . . .	33
3.2.5	Plexiglass and Optical glass inserts . . . . .	33
3.2.6	Teflon sheet . . . . .	34
3.2.7	Belt Control System . . . . .	35
3.2.8	Active Suction . . . . .	35
3.2.9	Belt Leading Edge Cover . . . . .	36
3.2.10	Anti-static brushes . . . . .	36
3.2.11	Micro-lift (tape) system for Mylar . . . . .	36
3.2.12	LDA head and BELT-HITE sensor traverse . . . . .	37
3.2.13	Vortex Generator Sensor Mount . . . . .	38
3.3	LDA Optical System Modifications . . . . .	38
3.4	Data Acquisition (DAQ) System . . . . .	38

3.4.1	Input Signals . . . . .	39
3.4.2	DAQ Hardware . . . . .	42
3.4.3	DAQ Software . . . . .	43
3.5	Data Post-Processing . . . . .	43
3.5.1	Hardware . . . . .	43
3.5.2	Software . . . . .	44
3.6	Issues with the Cascade Tunnel . . . . .	46
3.6.1	Issues with the LDA System . . . . .	46
3.6.2	Issues with the DAQ System . . . . .	47
3.6.3	Issues with the Mylar Belts and Teflon Bed . . . . .	47
3.7	Corrections for the Unresolved Issues . . . . .	49
3.8	Conclusions . . . . .	51
<b>4</b>	<b>Cascade Tunnel Results and Discussion</b>	<b>67</b>
4.1	Introduction . . . . .	68
4.2	Stationary End-Wall . . . . .	69
4.2.1	Flow and Data Quality . . . . .	69
4.2.2	Characterizing Flow Under Blade . . . . .	76
4.3	Moving End-wall and Vortex Generators . . . . .	80
4.3.1	Flow and Data Quality . . . . .	81
4.3.2	Characterizing Flow . . . . .	82
4.4	Conclusions . . . . .	85
4.4.1	Stationary End-Wall . . . . .	85
4.4.2	Moving End-Wall . . . . .	87
4.4.3	Moving End-Wall with Vortex Generators . . . . .	87



<b>5</b>	<b>Conclusions</b>	<b>135</b>
5.1	Auxiliary Tunnel . . . . .	135
5.2	Cascade Tunnel Apparatus . . . . .	135
5.3	Cascade Tunnel Results . . . . .	136
5.3.1	Stationary End-Wall . . . . .	136
5.3.2	Moving End-Wall . . . . .	137
5.3.3	Moving End-Wall with Vortex Generators . . . . .	137
5.4	Final Thoughts . . . . .	138
<b>A</b>	<b>Trips</b>	<b>140</b>
A.1	Introduction . . . . .	140
A.2	Configurations . . . . .	141
<b>B</b>	<b>Uncertainty Analysis</b>	<b>157</b>
B.1	Small Boundary Layer Tunnel Data . . . . .	157
B.1.1	Velocities . . . . .	157
B.1.2	Y position . . . . .	157
B.2	Linear Cascade Tunnel Data . . . . .	158
B.2.1	Stationary Wall Velocities . . . . .	158
B.2.2	Y position Uncertainty . . . . .	158
B.2.3	Flow Angle Uncertainty . . . . .	159
B.2.4	Moving Wall . . . . .	159
B.2.5	Moving Wall With Vortex Generators . . . . .	160
<b>C</b>	<b>Auxiliary Tunnel Data</b>	<b>164</b>

D Cascade Tunnel Triple Product Data	182
E Turbulence Grid Flow	191
Vita	195

# List of Figures

2.1	Experimental test section set-up, Auxiliary Small Boundary Layer Tunnel	19
2.2	Secondary Flow Vectors, Auxiliary Tunnel . . . . .	19
2.3	Picture of LDA Head . . . . .	19
2.4	Schematic of LDA Head . . . . .	20
2.5	Picture of aerosol generator . . . . .	20
2.6	Auxiliary Tunnel and Test Section, Picture of Auxiliary Tunnel . . . . .	21
2.7	Trip test surface and Suction Slot Incline, auxiliary tunnel . . . . .	21
2.8	Stream-wise Free-stream velocity, auxiliary tunnel . . . . .	21
2.9	2D Flow, 7 cm, auxiliary tunnel . . . . .	22
2.10	2D Flow, 22 cm, auxiliary tunnel . . . . .	22
2.11	Oil Flow Visualization, auxiliary tunnel . . . . .	23
2.12	Tunnel Symmetry, auxiliary tunnel . . . . .	23
2.13	Correlation Coefficient, auxiliary tunnel . . . . .	24
2.14	Velocity bias, auxiliary tunnel . . . . .	24
2.15	Wall shear Stress, auxiliary tunnel . . . . .	24
2.16	Data Comparison Plots, auxiliary tunnel . . . . .	25
2.17	Components of the Secondary Flow Vectors and $-\overline{v'w'}$ Reynolds Shear Stress, auxiliary tunnel . . . . .	25

2.18 Streamlines 10.5 cm d/s of v.g., auxiliary tunnel . . . . .	26
2.19 Streamlines 44.4 cm d/s of v.g., auxiliary tunnel . . . . .	26
2.20 Streamwise Vorticity 10.5 cm d/s of v.g., auxiliary tunnel . . . . .	27
2.21 Streamwise Vorticity 44.4 cm d/s of v.g., auxiliary tunnel . . . . .	27
2.22 TKE contours 10.5 cm d/s of v.g., auxiliary tunnel . . . . .	28
2.23 TKE contours 44.4 cm d/s of v.g., auxiliary tunnel . . . . .	28
2.24 TKE Transport Vectors 10.5 cm downstream of v.g, auxiliary tunnel . . .	29
2.25 TKE Transport Vectors 44.4 cm downstream of v.g, auxiliary tunnel . . .	29
3.1 Top View of Experimental test set-up, Low-speed Linear Compressor Cascade Wind Tunnel . . . . .	54
3.2 Side View of Experimental test set-up, Low-speed Linear Compressor Cascade Wind Tunnel . . . . .	55
3.3 Picture of Environmental containment tent, cascade tunnel . . . . .	56
3.4 Picture of Window in tent, cascade tunnel . . . . .	56
3.5 Picture of seeder system, cascade tunnel . . . . .	57
3.6 Picture of seeding pipe in contraction, cascade tunnel . . . . .	57
3.7 Picture of upstream end of bed, cascade tunnel . . . . .	58
3.8 Picture of active suction slot pipes, cascade tunnel . . . . .	58
3.9 Picture of LDV head and traverse, cascade tunnel . . . . .	59
3.10 Picture of LDV head and traverse system in tunnel, cascade tunnel . . .	59
3.11 Picture of anti-static brushes mounted next to Mylar sheet, cascade tunnel	60
3.12 Picture of vortex generators and marks, cascade tunnel . . . . .	60
3.13 Picture of micro-lift tape, vortex generator signal, vortex generators and beams in tunnel, cascade tunnel . . . . .	61
3.14 Schematic of LDA Signal Conditioning for auxiliary and cascade tunnels	62

3.15	Picture of setup for calibration of BELT HITE sensor, cascade tunnel . . .	62
3.16	Calibration curve for BELT HITE sensor, cascade tunnel . . . . .	63
3.17	Typical plot of output from BELT HITE sensor, cascade tunnel . . . . .	63
3.18	Picture of Vortex Generator Processing Equipment, cascade tunnel . . .	64
3.19	Typical plot of output from photodiode sensor processor, cascade tunnel	64
3.20	Typical plot of output from triangular pulse processor, cascade tunnel . .	65
3.21	Vortex Generator Processing Conceptual drawing, cascade tunnel . . . .	66
4.1	Angles in the Low-speed Linear Compressor Cascade Wind Tunnel . . . .	90
4.2	Test Matrix in the Low-speed Linear Compressor Cascade Wind Tunnel .	91
4.3	Tunnel Calibration, cascade tunnel . . . . .	92
4.4	Blade loading, Pressure Coefficient, cascade tunnel . . . . .	92
4.5	Comparison with DNS data, cascade tunnel . . . . .	93
4.6	Turning angles in the freestream, cascade tunnel . . . . .	94
4.7	Profile 1F Compared with Hot Wire Data Free-stream Coordinate System, cascade tunnel . . . . .	95
4.8	Profile 2B Compared with Hot Wire Data, cascade tunnel . . . . .	96
4.9	Profile 3F Compared with Hot Wire Data, cascade tunnel . . . . .	97
4.10	Profile 4F Compared with Hot Wire Data, cascade tunnel . . . . .	98
4.11	Profile 5F Compared with Hot Wire Data, cascade tunnel . . . . .	99
4.12	Profile 6F Compared with Hot Wire Data, cascade tunnel . . . . .	100
4.13	Blade loading, Difference in Pressure Coefficient across Blade, cascade tunnel	101
4.14	Schematic of Blade with $U_\tau$ and $\Delta C_p$ , cascade tunnel . . . . .	102
4.15	Tip Gap Velocity Magnitudes, cascade tunnel . . . . .	103
4.16	Turning angles in the Tip Gap, cascade tunnel . . . . .	104

4.17 $\overline{U}$ and $\overline{W}$ Vectors with Tip Gap and Hot-wire data, cascade tunnel . . .	105
4.18 $\overline{V}$ $\overline{W}$ Chord Coordinate System Tip Gap Plot, cascade tunnel . . . . .	106
4.19 $Q^+$ under the Blade, cascade tunnel . . . . .	107
4.20 $u^+$ under the Blade, cascade tunnel . . . . .	108
4.21 $v^+$ under the Blade, cascade tunnel . . . . .	109
4.22 $w^+$ under the Blade, cascade tunnel . . . . .	110
4.23 $\overline{u^2}/U_\tau^2$ under the Blade, cascade tunnel . . . . .	111
4.24 $\overline{v^2}/U_\tau^2$ under the Blade, cascade tunnel . . . . .	112
4.25 $\overline{w^2}/U_\tau^2$ under the Blade, cascade tunnel . . . . .	113
4.26 $-\overline{uw}/U_\tau^2$ under the Blade, cascade tunnel . . . . .	114
4.27 $-\overline{vw}/U_\tau^2$ under the Blade, cascade tunnel . . . . .	115
4.28 $-\overline{wv}/U_\tau^2$ under the Blade, cascade tunnel . . . . .	116
4.29 Turning Angle, Shear Stress Angle and Flow Gradient Angle under the Blade, cascade tunnel . . . . .	117
4.30 Anisotropy Factor N, cascade tunnel . . . . .	118
4.31 A1, Shear Stress:TKE Ratio, cascade tunnel . . . . .	119
4.32 1/S, Shear Stress:Fluctuating $\overline{V}$ Velocity Ratio, cascade tunnel . . . . .	120
4.33 B2, V Transport:Y Direction Stresses, cascade tunnel . . . . .	121
4.34 B, V Transport:TKE Ratio, cascade tunnel . . . . .	122
4.35 Moving Wall Flow Angle Plot with Stationary Wall, cascade tunnel . . .	123
4.36 Vortex Generator Data Unshifted Unmatched, cascade tunnel . . . . .	124
4.37 Vortex Generator Data Shifted Matched, cascade tunnel . . . . .	125
4.38 Moving Wall $\overline{U}$ $\overline{W}$ Vector Plots, cascade tunnel . . . . .	126
4.39 Vortex Generator Bin Size Comparison Mean Velocities, cascade tunnel .	127

4.40 Vortex Generator Bin Size Comparison Reynolds Normal Stresses, cascade tunnel . . . . .	128
4.41 Vortex Generator Bin Size Comparison Reynolds Shear Stresses, cascade tunnel . . . . .	129
4.42 Moving Wall Flow Mean Velocities, cascade tunnel . . . . .	130
4.43 Vortex Generator Flow Mean Velocities, cascade tunnel . . . . .	131
4.44 Vortex Generator Flow Reynolds Normal Stress Velocities, cascade tunnel	132
4.45 Vortex Generator Flow Reynolds Shear Stress Velocities, cascade tunnel .	133
4.46 Vortex Generator Flow Mean Velocities Normalized on $U_{eb}$ , cascade tunnel	134
A.1 Simple schematics of Trips on Test Surface, auxiliary tunnel . . . . .	145
A.2 Profile 2C1 Mean Velocities and Reynolds Stresses, auxiliary tunnel . . .	146
A.3 Profile 2C2 Mean Velocities and Reynolds Stresses, auxiliary tunnel . . .	147
A.4 Profile 2C3 Mean Velocities and Reynolds Stresses, auxiliary tunnel . . .	148
A.5 Profile 3C Mean Velocities and Reynolds Stresses, auxiliary tunnel . . .	149
A.6 Profile 4C Mean Velocities and Reynolds Stresses, auxiliary tunnel . . .	150
A.7 Profile 5C Mean Velocities and Reynolds Stresses, auxiliary tunnel . . .	151
A.8 Profile 6C Mean Velocities and Reynolds Stresses, auxiliary tunnel . . .	152
A.9 Profile 7C Mean Velocities and Reynolds Stresses, auxiliary tunnel . . .	153
A.10 Profile 8C1 Mean Velocities and Reynolds Stresses, auxiliary tunnel . . .	154
A.11 Profile 8C2 Mean Velocities and Reynolds Stresses, auxiliary tunnel . . .	155
A.12 Profile 8C3 Mean Velocities and Reynolds Stresses, auxiliary tunnel . . .	156
B.1 Law of the Wall Fit to Moving Wall Data in the Low-speed Linear Compressor Cascade Wind Tunnel . . . . .	163

C.1 Profiles 0F, 1F and 2F Mean Velocities and Reynolds Stresses, auxiliary tunnel . . . . .	166
C.2 Profiles 0F, 1F and 2F Triple Products, auxiliary tunnel . . . . .	167
C.3 Profiles 3F, 4F and 5F Mean Velocities and Reynolds Stresses, auxiliary tunnel . . . . .	168
C.4 Profiles 3F, 4F and 5F Triple Products, auxiliary tunnel . . . . .	169
C.5 Profiles 6F, 7F and 8F Mean Velocities and Reynolds Stresses, auxiliary tunnel . . . . .	170
C.6 Profiles 6F, 7F and 8F Triple Products, auxiliary tunnel . . . . .	171
C.7 Profiles 9F, 10F and 11F Mean Velocities and Reynolds Stresses, auxiliary tunnel . . . . .	172
C.8 Profiles 9F, 10F and 11F Triple Products, auxiliary tunnel . . . . .	173
C.9 Profiles 0S, 1S and 2S Mean Velocities and Reynolds Stresses, auxiliary tunnel . . . . .	174
C.10 Profiles 0S, 1S and 2S Triple Products, auxiliary tunnel . . . . .	175
C.11 Profiles 3S, 4S and 5S Mean Velocities and Reynolds Stresses, auxiliary tunnel . . . . .	176
C.12 Profiles 3S, 4S and 5S Triple Products, auxiliary tunnel . . . . .	177
C.13 Profiles 6S, 7S and 8S Mean Velocities and Reynolds Stresses, auxiliary tunnel . . . . .	178
C.14 Profiles 6S, 7S and 8S Triple Products, auxiliary tunnel . . . . .	179
C.15 Profiles 9S, 10S and 11S Mean Velocities and Reynolds Stresses, auxiliary tunnel . . . . .	180
C.16 Profiles 9S, 10S and 11S Triple Products, auxiliary tunnel . . . . .	181
D.1 Profiles 1F1 and 1F2 Triple Products in Freestream Coordinates, cascade tunnel . . . . .	183



D.2	Profiles 3F and 4F Triple Products in Freestream Coordinates, cascade tunnel . . . . .	184
D.3	Profiles 5F and 6F Triple Products in Freestream Coordinates, cascade tunnel . . . . .	185
D.4	Profiles 1B Triple Products in Freestream Coordinates, cascade tunnel . .	186
D.5	Profiles 3S, 3C and 3P Triple Products in Chord Coordinates, cascade tunnel	187
D.6	Profiles 4S, 4C and 4P Triple Products in Chord Coordinates, cascade tunnel	188
D.7	Profiles 5S, 5C and 5P Triple Products in Chord Coordinates, cascade tunnel	189
D.8	Profiles 6S, 6C and 6P Triple Products in Chord Coordinates, cascade tunnel	190
E.1	With and Without Turbulence Grid Point 6C Mean Velocities and Reynolds Stresses in the cascade tunnel . . . . .	193
E.2	With and Without Turbulence Grid Point 6C Triple Products in the cascade tunnel . . . . .	194

# List of Tables

1	Nomenclature . . . . .	xvi
4.1	Cascade Tunnel Test Matrix . . . . .	70
4.2	Cascade Tunnel Skin Friction Values . . . . .	74
4.3	Cascade Tunnel Shear Stress Magnitudes . . . . .	78
4.4	Cascade and Auxiliary Tunnel Vortex Magnitude Results . . . . .	86
A.1	Trip Test Results in the Auxiliary Tunnel . . . . .	141
B.1	Uncertainties for the Auxiliary Small Boundary Layer Wind Tunnel . . .	158
B.2	Uncertainties for the Stationary Wall Data in the Cascade Wind Tunnel .	159
C.1	Auxiliary Tunnel Test Matrix . . . . .	165
E.1	Values used in Hancock Relationship for With and Without Turbulence Grid . . . . .	192

# Nomenclature

Table 1: Nomenclature

B	Points found just upstream of the Blade
c	Chord length: 25.4 cm
C	Points found on the camberline of the Blade
$c_a$	Axial Chord length: 13.868 cm
CC	Correlation coefficient
$C_{fo}$	Skin friction without a grid
$C_p$	Coefficient of pressure
$D_{vor}$	Diameter of vortex
F	Points found in the free-stream Flow
FA	Flow angle: $\arctan(\frac{\overline{W}}{\overline{U}})$
FGA	Flow gradient angle: $\arctan \frac{d\overline{W}/dy}{d\overline{U}/dy}$
h	Height of Vortex Generator (1 cm)
H	Shape Factor $\delta^*/\theta$
$L_u^e$	turbulence length scale
n	Number of points in ensemble
N	Anisotropy Factor
P	Points found on the pressure side of the Blade
Q	Coordinate system independent velocity: $\sqrt{U^2 + W^2}$
$r_i$	Data rate: $1/(t_i - t_{i-1})$
R	Statistical mean data rate from the selected ensemble: $\sum_{i=1}^n  r_i /n$
$Re_\theta$	Momentum thickness Reynolds number: $U_\infty \theta / \nu$
$Re_x$	Reynolds number: $U_\infty x / \nu$
S	Points found on the suction side of the Blade
SSA	Shear stress angle: $\arctan(\frac{-\overline{vw}}{\overline{uw}})$
$t_i$	Absolute time of the $i^{th}$ velocity measured in the selected ensemble
$T_{input}$	Slope of the triangular pulse from the triangular pulse processor
TKE	Turbulent Kinetic Energy: $(\overline{u^2} + \overline{w^2} + \overline{v^2})/2$
$Trans_{TKE_y}$	TKE transport vector in the y direction: $(\overline{u^2 v} + \overline{v^3} + \overline{vw^2})/TKE$
$Trans_{TKE_z}$	TKE transport vector in the z direction: $(\overline{u^2 w} + \overline{v^2 w} + \overline{w^3})/TKE$

$\bar{u}, \bar{v}, \bar{w}$ $\bar{U}, \bar{V}, \bar{W}$ $u_i, v_i, w_i$	or	Statistical mean velocity from the selected ensemble in tunnel co-ordinates
$\overline{u^2}, \overline{v^2}, \overline{w^2}$		The $i^{th}$ velocity measured in the selected ensemble in tunnel co-ordinates
$u^+, v^+, w^+$ $-\overline{uv}, -\overline{uw}, -\overline{vw}$		Statistical mean velocity squared quantities from the selected ensemble in tunnel co-ordinates
$\overline{u^2v}, \overline{vw^2}, \overline{v^3}$		$\bar{u}/U_\tau, \bar{v}/U_\tau, \bar{w}/U_\tau$
$U_{ap}$ $U_e$ $U_{eb}$		Statistical mean shear stress quantities from the selected ensemble in tunnel co-ordinates
$U_{mode}$ $U_\tau$ $ V $		Statistical mean triple product quantities from the selected ensemble in tunnel co-ordinates
$V_{belt}$ $V_{def}$ $ v_i $		X component of the Free-stream Velocity at a specific profile
$x, y, z$		Free-stream Velocity, always in the upstream direction
$X_{vg}$		Free-stream Velocity component in the bed coordinate system (see Figure 4.2)
$y^+$ $y_t$		The mode value of the velocity in the U direction
		Skin Friction velocity: $\sqrt{\tau/\rho}$
		Statistical mean velocity magnitude from the selected ensemble: $\sum_{i=1}^n  \nu_i /n$
		Velocity of the Belt
		Velocity deficit, normalized on the free-stream velocity
		The $i^{th}$ measured velocity magnitude from the selected ensemble: $\sqrt{u_i^2 + v_i^2 + w_i^2}$
		Tunnel co-ordinate system (see Figure 2.1 for auxiliary tunnel see Figure 4.2 for cascade tunnel).
		distance to vortex generator (in the bed coordinate system in the Cascade tunnel see Figure 4.2)
		$yU_\tau/\nu$
		tunnel height

---

$Z_{vg}$	Spacing between the vortex generators
$Z_{sen-mv}$	Z distance between the vg sensor and the measurement volume
$Z_{vg-bm}$	Z distance between the vortex generator and the belt marks
$Z_{vg_mv}$	Z distance between the vortex generator and the measurement volumen
$z_b$	Blade spacing, 23.6 cm
$\delta$	boundary layer thickness when $\delta = y$ when $\frac{U}{U_e} = 0.99$
$\delta_h$	height length scale
$\Delta C_f$	Change in Skin friction
$\Delta C_p$	Difference in pressure, at same chord location, across blade
$\Gamma_c$	Circulation (in the z-y plane)
$\sum_{i=1}^n$	Summation from i=1 to n
$\sigma_r$	Standard deviation data rate: $(\sum_{i=1}^n  r_i ^2 / (n-1))^{1/2}$
$\sigma_v$	Standard deviation of velocity magnitude: $(\sum_{i=1}^n  v_i ^2 / (n-1))^{1/2}$
$\rho$	Mass density of flow
$\nu$	Kinematic viscosity
$\tau_{vg}$	Time it takes the vortex to travel a particular distance
$\tau_w$	Wall shear stress
$\Omega_x$	Vorticity curl V: $(\partial v / \partial z - \partial w / \partial y)$
$\omega_x$	$(\Omega_x * h) / U_e$

---

# Chapter 1

## Introduction

### 1.1 Motivation

The larger goal of the study is to gain greater insight into complex flow through turbomachinery. An idealized wind tunnel model is utilized to investigate the basic components of the compressor flow. The results obtained from this study will be used directly to understand this particular flow and indirectly to calibrate computational models of the flow, specifically Large Eddy Simulations (LES) which can be programmed with design geometries. Specifically, what is being investigated is the flow through the tip gap between the turbomachinery blades and the wall. This tip gap flow causes losses in the efficiency of the turbomachinery and possibly is the source of unwanted effects such as cavitation in hydro-turbomachinery. By gaining a better understanding of this idealized flow, designers may be able to increase the efficiencies and decrease noise and wear caused by the fluid dynamics.

### 1.2 Objective

There are four three-dimensional turbulent flows studied in this investigation. One of the four turbulent flow experiments is carried out in an auxiliary small boundary layer wind tunnel (auxiliary tunnel) the remaining three are carried out in a low-speed linear compressor cascade wind tunnel (cascade tunnel). Each of the flows is idealization of

another flow. The first flow is the idealization of the wake from stator blades using two half-delta wing vortex generators. The second flow is the idealization of flow through a stationary set of linear cascade compressor blades. The third flow is the idealization of flow through a moving set of linear cascade compressor blades. The fourth flow is the same as the third flow with added idealized wakes from upstream stator blades.

The first three-dimensional turbulent flow is created by two half-delta wing vortex generators, at  $\pm 18^\circ$  angle of attack, resulting in two counter rotating vortices in the auxiliary tunnel. The second flow is an investigation of the first quarter chord tip gap flow in the cascade tunnel. This experiment does *not* incorporate the moving end-wall facility. The third flow investigated is the inflow to the compressor cascade incorporating the moving end-wall. Finally, the fourth flow investigated incorporates the moving end-wall and vortex generators and the inflow to the compressor cascade is studied. Normally the blades of the compressor move past a stationary end-wall which houses them. In this idealization the blades are kept stationary and the wall is moved past them. The vortex generators are intended to model wakes created by stator blades. Therefore, the vortex generators are mounted to the moving end-wall upstream of the compressor blades.

This study may be thought of as three independent investigations with three goals in mind. The first investigation is carried out in order to better understand the near wall nature of the counter rotating vortices. The vortices are placed in a two-dimensional flow so that the changes to the flow structure may be easily studied. These vortex generators are used then in the fourth investigation in a highly three-dimensional flow. The second investigation into the tip gap region of the compressor blades, without a moving end-wall, provides important information about the tip gap flow. Near the quarter chord of the blade, in the tip gap region, it has been theorized the tip leakage vortex is created. This stationary end-wall flow is important to understanding the origins of the tip leakage vortex. The third investigation gives parameters of the inflow to the cascade of rotor blades with the moving end-wall. This investigation also gives insights into the interactions between the viscous boundary layer starting at the suction slot and the viscous boundary layer created by the moving end-wall. Understanding the complex viscous interaction is important to understanding the inflow conditions. The last flow, which has a moving end-wall with vortex generators, is the main flow of interest of the entire study. How the vortex generators modify the inflow to the blades is critical to understanding the fluid dynamics of the tunnel. Before the tip leakage flow in can be understood properly



the conditions upstream must be completely documented in a complex flow such as this. All four investigations come together, piece by piece, attempting to fully document and understand this highly idealized but extremely complex flow.

## 1.3 Thesis Layout

The thesis is arranged into three large stand-alone chapters; Chapter 2, Chapter 3 and Chapter 4. Each chapter includes a stand alone introduction and conclusion. Figures and references may be found at the end of each chapter.

Chapter 2 investigates the simple flow in the auxiliary tunnel with the vortex generators. Chapter 3 discusses the experimental setup of the cascade wind tunnel. Chapter 4 investigates the three flows in the cascade tunnel; stationary end-wall, moving end-wall inflow and moving end-wall with vortex generator inflow. A final chapter, Chapter 5, summarizes the results of the previous three chapters and concludes the thesis. Five appendices are also included to provide supplemental information to the main discussion. The appendices are referenced throughout the thesis.

## Chapter 2

# The Auxiliary Small Boundary Layer Wind Tunnel

This chapter describes the investigation of the flow in the auxiliary small boundary layer wind tunnel (auxiliary tunnel) at Virginia Tech. The purpose of this investigation is to study a simplified simulation of the flow found in the low-speed linear compressor cascade wind tunnel (cascade tunnel). The laser-Doppler anemometer (LDA) measurement system is also a simplified version of the one used in the cascade tunnel, therefore much of the discussion of the test setup is extended to both tunnel's sets of data.

A turbulent boundary layer downstream of a pair of half-delta wing vortex generators is investigated. Coincident instantaneous  $U$ ,  $V$ ,  $W$  components of velocity are measured with a simultaneous three-orthogonal component LDA system. The LDA system has a measurement volume on the order of  $50\text{ }\mu\text{m}$  in size. Measurements below  $y^+ = 5$  were collected to deduce the wall skin friction.

Careful considerations are given to the evaluation of bias and broadening effects on the data. Data for a 2-D turbulent boundary layer closely agree with direct numerical simulation (DNS) results. All turbulence data satisfy the realizability conditions. This is the first time that detailed near-wall 3-velocity-component measurements have been made in this type of flow. While large streamwise vorticity is generated away from the wall, significant opposite sign vorticity is generated by the viscous interaction of the vortex and the wall.

## 2.1 Introduction

The present work is a study of large-scale streamwise vortices in a turbulent boundary layer. Detailed measurements are collected near the wall to capture the structure of the flow downstream of a half-delta wing vortex generator pair. Previous experimental studies of this nature (Pauley and Eaton, 1989) have used hot-wire anemometry to measure the flow velocities. However, hot-wire anemometry is of limited use in detecting all three velocity components within the boundary layer near-wall region.

Figure 2.1 shows the approximate shape of the test section and the location of the vortex generator pair. Vortex generators with a chord length of 2.5 cm and height of 1 cm are attached 9 cm downstream of a suction slot. This configuration is designed to produce the common flow directed downward to the wall, otherwise known as "common flow down" shown in Figure 2.2.

This particular geometry is a simplified version of the cascade tunnel to be discussed in Chapters 3 and 4. The suction slot shape is the same in both tunnels as is the geometry of the vortex generators and the position of the vortex generators relative to the suction slot. Aside from the cascade of blades downstream of the vortex generators, the main differences between the two tunnels are the direction of and velocity of the incoming flow. The upstream flow is perpendicular to the suction slot in the auxiliary tunnel whereas it is skewed to the suction slot in the cascade tunnel (Figure 3.1).

The present study utilizes a miniature fiber-optic 3-orthogonal-velocity-component LDA probe as described by Chesnakas and Simpson (1994) and shown in Figure 2.3 and Figure 2.4. Experimental data are collected at three streamwise positions in the tunnel. The first streamwise position is 7 cm downstream of the suction slot. The second and third streamwise positions are 10.5 cm and 44.4 cm, respectively, downstream of the vortex generator pair. The first test position, 7 cm downstream of the suction slot, simply served as a point to measure the quality of the flow and provide flow information upstream of the vortex generators. The 10.5 cm and 44.4 cm streamwise positions are the two main experimental cross-sections at which the vortex turbulence structure is examined.

## 2.2 Apparatus and Test Flow

### 2.2.1 Auxiliary Tunnel

The measurements were made in the Virginia Polytechnic Institute and State University Auxiliary Small Boundary Layer Wind Tunnel (Smith et al., 1990). This tunnel was recently modified into a continuous closed return tunnel to accommodate particle seeding in the flow.

The test section is approximately 1.25 m (50 inches) in length, 24 cm (9.5 inches) in width and 10 cm (4 inches) in height. A picture of the auxiliary tunnel and test section along with the laser table is shown in Figure 2.6. A schematic of the tunnel test section is shown in Figure 2.1. The nominal free-stream velocity of the tunnel was 13 m/s for all runs performed in the tunnel. This velocity is approximately the same as the velocity component perpendicular to the suction slot of the cascade tunnel.

The stream-wise velocity profile along the length of the test section is shown in Figure 2.8. A suction slot (Figure 2.7) is located 9 cm upstream of the vortex generators and serves to remove the upstream boundary layer from the flow. The leading edge slightly inclines to the level tunnel test section floor (see Figure 2.7).

### 2.2.2 Trips

A single square bar, 2.4 mm in height, 0.6 cm (0.25 inches) downstream of the suction slot trips the flow. This same trip is used in the cascade tunnel. Different types of trips were studied before a final trip design was chosen (see Appendix A). One design incorporated several lines of staggered vertical posts with diameters of the order of 0.75 mm and 1.5 mm. Another design investigated was wires of the same diameter glued to the floor span-wise. Finally a span-wise bar was selected as the appropriate trip. The posts created highly 3-dimensional flow in the boundary layer near the vortex generators. The wires were not large enough to create the desired boundary layer momentum thickness. Finally the bar created a nicely 2-dimensional boundary layer (Figure 2.9) as well as the desired boundary layer momentum thickness. The  $Re_\theta$  measured from the bar averaged to be approximately 700 at a location 7 cm downstream of the suction slot.

### 2.2.3 Upstream Flow Quality

Three profiles 7 cm downstream of the suction slot were collected, these are all in the upstream measurement plane shown in Figure 2.1. The first was located at the center of the tunnel and the second and third were located 2.54 cm from the center on either side. Figure 2.9 shows the close two-dimensionality of this flow. In these figures the data are compared with the 2-D channel flow DNS results of Kim et al. (1987). The plots include  $u^+$ ,  $\overline{u^2}/U_\tau^2$ ,  $\overline{v^2}/U_\tau^2$ ,  $\overline{w^2}/U_\tau^2$  and  $\overline{uv}/U_\tau^2$ . It appears as though the structure of the flow has not completely relaxed. This is most likely caused by the step created by the trip upstream, however, there is also the edge of the optical glass. This accounts for the disagreement with Kim's DNS results shown in Figure 2.9c and to a lesser extent in Figure 2.9b. Another explanation is that the disagreement is caused by the differences in  $Re_\theta$  as discussed in AGARD (1996). However this could only account for part of the difference.

This trip, however, showed the least distortion of the boundary layer of any trips tested which produced the required  $Re_\theta$  values (see Appendix A). Without vortex generators the profiles match-up almost perfectly with Kim's DNS results 21.8 cm downstream of the suction slot (or at the 10.5 cm measurement cross section), where  $Re_\theta = 1100$  (see Figure 2.10). It is more likely that the differences seen between Kim's DNS results and the data at these downstream locations are from Reynolds number effects.

### 2.2.4 Vortex Generators

The vortex generators have a chord length of 2.5 cm and are 1 cm in height, the same aspect ratio studied by Pauley and Eaton (1989). The spacing between the generators – measured between the midway point of the delta wing chord – was 0.8 times the chord length. The angle of attack measured between each vortex generators and the tunnel centerline, was 18 degrees, also as studied by Pauley and Eaton. The trailing edge of the vortex generators is 11.3 cm downstream of the suction slot. These vortex generators and their configuration are also used in the cascade tunnel.

### 2.2.5 Measurement Section Flow Quality

Figure 2.11 shows a surface oil flow on the tunnel floor. From the oil flow you can see that the streaklines in the dark higher shear stress region downstream and between the vortex generators run parallel to the white low wall shear stress streaklines. This line separates a region of high wall shear stress from that of lower wall shear stress. At the first test profile section (10.5 cm downstream of the vortex generators) the line is 1.82 cm from the centerline of the tunnel. At the second profile section (44.4 cm downstream of the vortex generators) the line is 2.81 cm from the centerline of the tunnel (Both the cross sections are shown in Figure 2.1).

When collecting the first cross section, shown in Figure 2.12, the measurement volume was positioned 10.5 cm downstream of the vortex generators and raised to a height of 0.75 cm above the wall. It then traversed from -2.54 cm to +2.54 cm across the centerline of the tunnel. The plotted quantities are  $\bar{u}/U_e$ ,  $\bar{v}$ ,  $\bar{w}$ ,  $\overline{u^2}$ ,  $\overline{v^2}$ ,  $\overline{w^2}$ ,  $\overline{uv}$ ,  $\overline{uw}$  and  $\overline{vw}$ . As can be seen from these plots, the vortices are nearly perfectly symmetrical; therefore, it was only necessary to collect data on one half of the tunnel. Data were collected for the half in the negative z direction.

### 2.2.6 LDA System

Chesnakas and Simpson (1994) describe the laser head, a two-color, three-orthogonal-velocity-component, fiber-optic design used in the current study, which is shown in Figure 2.3. The fiber-optics transmit 3 green (514.5 nm) and 2 blue (488 nm) argon-ion laser beams and receive the off-axis backscatter signal through an optical glass window. In this manner the flow is undisturbed by the presence of the probe under the tunnel. The probe was mounted to a system of two traverses in the y and z directions, both of which had a travel of +/- 2.54 cm. This same laser head is used in the cascade tunnel.

The optical glass window rests in a hole, flush to the floor of the tunnel. The optical glass is 8 inches in diameter and 6 mm thick. The optical glass is coated with an anti-reflective coating to improve LDA measurements close to the floor.

The fringe spacing for each pair of laser beams was calculated to be approximately 5  $\mu\text{m}$  using equations found in Durst et al. (1981). The crossing of these beams created

a nearly spherical control volume of around  $50\mu m$  diameter, which was calculated using formula found in Durst et. al. (1995). The uncertainties of all the calculated velocities are shown in Table B.1 in Appendix B.

The Doppler frequency of the LDA signals were analyzed using three Macrodyne model FDP3100 frequency domain signal processors operating in coincidence mode. An IBM PC along with a Dostek (1400A Laser Velocimeter Interface with TCEM daughterboard option) was used to collect and store the data from the Macrodynes.

An aerosol generator designed by Echols and Young (1963) was used to seed the flow (Figure 2.5). The fluid in the generator is dioctyl phthalate with a mean particle size slightly less than  $1\mu m$ . The smoke was injected into the plenum chamber of the auxiliary tunnel. The same processors and aerosol generator are used in the cascade tunnel as in the auxiliary tunnel.

## 2.3 Post Processing

There are two major steps for the post-processing of the data, the first being preparation of the acquired data and the second being calculation of the desired quantities. The preparation of the data was conducted with the three problem areas in LDA data in mind: noise, signal biasing and broadening effects, and co-ordinate and wall location adjustments. Mean velocities, turbulent stresses and the triple products were calculated. These quantities were then used to calculate vorticity ( $\Omega_x$ ), circulation ( $\Gamma_c$ ), an octant analysis of fluctuations and turbulent diffusion.

With LDA systems, like any electronic measurement system, there is always a certain amount of extraneous noise present during data collection. The method used to remove noise from the data was that used by Olcmen and Simpson (1995). A parabola was fit to each side of the logarithm of the velocity component histogram ordinate in the range between 1 % to 80 % of the peak histogram value. The data lying outside of the intersection of the parabolas with the ordinate value were discarded; if one of the velocity components was deemed unusable, all three were discarded. The clean velocity information for all three velocity components was transformed into tunnel co-ordinates and saved. Once more a parabola was fit to each side of the logarithm of the histogram, this time to the transformed data, and the noise was removed. The number of samples

taken at each point ranged from 15,000 to 30,000.

First, the velocity bias was investigated. To assess whether or not there were velocity bias effects in our data, a method similar to that of Meyers et al. (1992) was used. A standard correlation coefficient (CC) between velocity magnitude fluctuation and data rate fluctuation was calculated for each location in our two test cases (3-D and 2-D). The correlation coefficient was calculated as follows (Equation 2.1).

$$CC = \frac{(\sum_{i=1}^n (|V_i| - |v_i|)(R - r_i)/n}{\sigma_v \sigma_r} \quad (2.1)$$

The measured correlation coefficient for both of our flows is shown in Figure 2.13. The 2-dimensional test case is taken at the 10.5 cm cross section, at  $z=0$ , without vortex generators. The 3-dimensional case is taken also at 10.5 cm cross section cutting through the vortex center. As all the correlation coefficients are on the order of  $10^{-2}$ , there is no correlation between the velocity magnitude fluctuation and data rate fluctuation for either case, and thus no velocity bias.

Figure 2.14 is a plot of this set of data processed with and without the velocity bias correction of Fuchs et al. (1992). The chosen data set was taken at the first experimental test section (10.5 cm downstream of the vortex generators) and in the center of the tunnel. There were no vortex generators in the tunnel and thus the mean flow was 2-dimensional. Upon examining Figure 2.14 it is clear to see that the velocity bias correction factor had very little effect on the data. It is also important to note how favorably these data compare with the Kim et al. (1987) DNS channel results. Any deviations between the DNS results and the experimental data can be explained by the difference in Reynolds numbers. The Reynolds number for the DNS results was  $Re_\theta = 700$ . The Reynolds number for the experimental data was  $Re_\theta = 1100$ . The difference between these values increased the deviation between the DNS and experimental values away from the wall and near the freestream (AGARD, 1996). It should be noted that all of the 2-D data were also compared with the famous DNS simulation from Spalart (1988) ( $Re_\theta = 1410$ ).

Chen et al. (1996) proposed that for 3-component LDA systems, the change in projected area of the coincident measurement volume for different flow directions will introduce an 'angular' bias in naturally sampled data. For the LDA optics used here, there is only a small variation in the measurement-volume-projected cross-sectional area for the various



flow directions. Thus, negligible angular bias is present in the current correlation measurements. The fringe bias effects described by Whiffen et al. (1979) is not present since only particles passing through the coincident measurement volumes are validated. The geometric bias proposed by Brown (1989) is practically removed since the measurement volume is nearly spherical.

There are three types of broadening effects that need to be addressed: velocity gradient broadening, finite transient time broadening, and instrument broadening effects. Velocity gradient broadening occurs because the LDA system receives signals over the measurement volume in a flow with velocity gradients. However, with a small enough measurement volume this effect can be greatly reduced. Using equations suggested by Durst et al. (1992), the effect of gradient broadening could be calculated. The effect of gradient broadening was found to be orders of magnitude less than the uncertainty in the data.

To measure the effect of transient time broadening, the data were compared with the Ma et al. (2000) data. Ma measured the same outer region flow at the same cross-sections, except using hot-wire anemometry. When the two data sets were compared it was found that there were negligible differences in the measured velocities. Therefore, it was concluded that the effect of transient time broadening on the data was insignificant. Olcmen et al. (1998) studied the instrument broadening effects for this system and found that the bandwidth broadening of the Macrodyne signal processors contribute a negligible amount of broadening to the signal.

When the measurement volume is focused just onto the surface, a strong signal results that determines an approximate reference location for the LDA head traversing system. This is a good method to determine the location of the wall however because of accuracy of the movements of the traverse, and the size of the control volume, the uncertainty in the wall position is  $\pm 50\mu\text{m}$ . A more refined determination of the measurement volume location relative to the wall can be determined by a least squares curve fit of the sublayer mean velocity profile in Equation 2.2:

$$Q = C_1 * y + C_2 * y^4 \quad (2.2)$$

with  $Q = (\bar{u}^2 + \bar{w}^2)^{1/2}$ , and  $C_1$  and  $C_2$  as coefficients. The curve is fit through  $Q = 0$  at  $y = 0$ . Using only the data for  $y^+ < 10$ , an iterative process was developed to maximize

the curve fit correlation coefficient by adjusting the  $y$  values. This was performed at each of the profiles using at least 5 points. Most of the  $y$  shifts were on the order of  $50\mu m$ , the size of the measurement volume. This is the uncertainty of finding the wall (see Appendix B).

By using the curve fit above  $\tau_w = \mu \frac{\partial u}{\partial y}|_{wall}$  can be determined with a similar method to that of Durst et al. (1996). The first coefficient in the above equation relates to  $U_\tau$  by:  $C_1 = U_\tau^2/n$ . This is the method used to calculate  $U_\tau$ . Upon examination of Figure 2.15 a sharp change in  $U_\tau$  at  $z = -1.8$  cm is noticed in the first cross section, 10.6 cm downstream of the vortex generator. Then for the 44.4 cm cross section the sharp change in  $U_\tau$  comes at  $z = -2.8$  cm. Both of these values correspond to the sharp contrast of light and dark found on the oil flow in Figure 2.11.

In setting up the LDA head there is no way to avoid slight misalignment of the coordinate system for the LDA head relative to the tunnel coordinate system. A procedure was developed to determine the transformation. Each time the probe head was moved to another  $x$  plane a two-dimensional flow case was measured, i.e. the vortex generators were removed and a velocity profile was taken. An iterative process was developed to rotate the coordinate system pitch angle for these data until the values reached a minimum value within a tolerance. Next, the coordinate system yaw angle was adjusted until the combination of  $\overline{w}$  and  $\overline{uw}$  had reached a minimum value within a tolerance. Finally, the coordinate system roll angle was adjusted until  $\overline{vw}$  had reached a minimum value within a given tolerance. Once the LDA head to tunnel coordinate system transformation was determined, it was applied to all of the three-dimensional data sets until the head was moved to another  $x$  location. At this point a new coordinate transformation was determined. The angle adjustments were usually on the order of  $1^\circ$ .

Confidence in the post-processing schemes may be found in the plots in Figure 2.14 and Figure 2.16. There is close agreement between the experimental and DNS results near the wall. These plots confirm the low uncertainties in all the calculated quantities as given in Table B.1 of Appendix B.

## 2.4 Experimental Data

All turbulent results satisfy the realizability conditions of Schumann (1977). Figures 2.16 and 2.17 show the results from comparisons between a two-dimensional case and a purely 3-dimensional case. Appendix C presents the complete set of three-dimensional data.

The two-dimensional case data were collected without vortex generators at 10.5 cm downstream of the vortex generator location in the center of the tunnel. The 3-dimensional case data were collected at 10.5 cm downstream of the vortex generators and 1.8 cm left of center (or -1.8 cm in the  $z$  tunnel co-ordinates). The 3-dimensional profile position was located almost exactly in the center of the vortex, 1.77 cm from the centerline. The boundary layer thickness for the two-dimensional data is roughly 1.34 cm thick. The boundary layer thickness was found by first by averaging  $Q$  of 8 points taken across the cross section in the freestream, without vortex generators. Then 99% of this free-stream value is taken and the  $y$  position is interpolated from the profile taken at the center of the tunnel without vortex generators.

There is much to be noted in Figure 2.16. The figure shows the plot of the  $u^+$ . As noted above the 2-dimensional flow plot closely follows the DNS results (Kim 1987) near the wall but increases as it approaches the outer portion of the boundary layer. Again, this can be explained as a difference of Reynolds numbers,  $Re_\theta = 700$  for the DNS versus the experimental  $Re_\theta = 1100$ . The dip in the velocity for the 3-D case in this plot indicates the decrease in the streamwise velocity through the core of the vortex, a velocity deficit. The peak velocity deficit is 0.75 normalized on the free-stream velocity. This is nicely contrasted with the log region of the 2-D profile.

Upon examination of Figure 2.16b a peak may be noted in  $\overline{v^2}/U_\tau^2$  around  $y^+ = 295$ . As was determined above from Figure 2.16a, this is near the center of the vortex. It should be noted how well the DNS results follow the experimental 2-D data near the wall ( $y^+ < 30$ ) in Figure 2.16c. The value of the peak for the  $-\overline{uv}$  is less than the value of the peak  $\overline{v^2}$  that is near  $y^+ = 80$ .

Figures 2.16d-f show close agreement for the 2-D flows between all profiles near the wall. As the 3-dimensionality of the vortex becomes dominant, there are large differences with a 2-D flow. Figure 2.16f shows a large amount of transport of the turbulent kinetic energy towards the freestream. For all these plots it should be noted that small variations are for

the most part real phenomena and not random jitter of the data (Olcmen and Simpson, 1995)

Circulation was calculated in both planes of data using a numerical integration around the outer edge of the flow field (Equation 2.3).

$$\Gamma_c = \oint V ds \quad (2.3)$$

Since the vortices were roughly perpendicular to the measurement planes, the circulation was calculated in the z-y plane. The circulation was normalized on the average free-stream velocity over all of the profiles and with the height of the vortex generators ( $h=1\text{cm}$ ). The circulation decreased from  $\Gamma_c = -0.18$  at the first cross section to  $\Gamma_c = -0.12$  at the second cross section.

Figure 2.17 shows plots of the components of the secondary flow vectors as well as the  $-\overline{vw}$  Reynolds shear stress. The first plot demonstrates how closely the 2-D data are to zero and that the 3-D  $v^+$  component is quite negligible when compared to  $w^+$ , as would be expected in the plane intersecting the center of the vortex. We can determine the center of the vortex from Figure 2.17. The profile is for the z position that passes directly through the center of the vortex, so that the  $w = 0$  location is at the center of the vortex. As stated above it was interpolated that the center of the vortex is at  $y^+ = 295.4$ . This value of  $y^+$  corresponds to  $y = 7.25$  mm in tunnel coordinates. This is half the boundary layer thickness.

Figure 2.17b shows some interesting behavior near the wall for the spanwise shearing stress  $-\overline{vw}$ , where major terms of the  $-\overline{vw}$  transport equation are production and diffusion:  $\overline{v^2} \frac{\partial w}{\partial y} = \frac{\partial}{\partial y}(-\overline{v^2 w})$ , respectively. From this it is apparent that there is a slight rise around  $y^+ < 11$  due to production of  $-\overline{vw}$  and a reduction at higher  $y^+$  due to the vortex production and diffusion.

The last sets of figures show the results from the data collected at the two streamwise positions, 10.5 cm and 44.4 cm downstream of the vortex generators. Figure 2.18 and 2.19 show the  $\overline{v-w}$  mean secondary flow streamlines at the two cross sections. The spanwise or z locations where  $U_\tau$  in Figure 2.15 changes abruptly is close to the position at which secondary flow velocities near the wall change significantly. As can be seen from these plots the center of the vortex moves up and away from the wall as it moves downstream.

Figure 2.20 and 2.21 show the non-dimensional streamwise vorticity contours of  $\Omega * h / U_e$  for the two streamwise positions. The peak non-dimensional vorticity decreases as the flow moves downstream. The peak vorticity at the 10.5 cm cross section is estimated to be 0.746. The peak vorticity at the 44.4 cm cross-section is estimated to be 0.284. As reported by Pauley and Eaton (1989), there is significant opposite sign or "induced" streamwise vorticity generated by the viscous interaction of the vortex and the wall. The vortices are not circular but rather elliptical.

Figure 2.22 and 2.23 show the TKE contours for the two streamwise positions. The TKE normalized on the free-stream velocity is  $TKE / U_e^2 = (\overline{u^2} + \overline{w^2} + \overline{v^2}) / (2 * U_e^2)$ . The peak TKE sits between the primary and secondary vortices in both cross-sections. The peak TKE moves away from the center of the tunnel with the two vortices.

A spectral analysis was done on the mean velocities of the 3-D and 2-D test case data. The 2-dimensional test case is taken at the 10.5 cm cross section, at  $z=0$ , without vortex generators. The 3-dimensional case is taken also at 10.5 cm cross section cutting through the vortex center. The scatter in the data did not reveal any trends. The spectral analysis was done to see if there were any low frequency oscillations in the positions of the vortices.

An octant analysis, which separates the measurements into octants of velocity space, is being done on the data set. This technique separates the flow events in to ejections, sweeps and interactions depending upon the signs of the velocities in that particular octant. The results of the octant analysis will be available in Long (2001).

The TKE transport vectors are shown in Figures 2.24 and Figure 2.25. The equation of the TKE transport vectors is shown in Equation 2.4).

$$\begin{aligned} (Trans_{TKE_z} / U_e) \vec{j} + (Trans_{TKE_y} / U_e) \vec{k} = \\ ((\overline{u^2 w} + \overline{v^2 w} + \overline{w^3}) / (TKE * U_e)) \vec{j} + ((\overline{u^2 v} + \overline{v^3} + \overline{vw^2}) / (TKE * U_e)) \vec{k} \end{aligned} \quad (2.4)$$

These vectors show the amount of jitter, or small quick jumpy movements, in the position of the vortex. Another way of looking at the Trans variable is that this is the direction of infrequent large-scale motions since the triple products are skewed in that direction. The larger the vectors the higher the jitter. The vectors also show the direction of jitter. Here, just outside of the centers of the vortex on the top and inside edges of the flow, the

most jitter is occurring. The jitter shows movement out and away on top with a fairly strong jitter back down and in on the inside edge.

## 2.5 Conclusions

The velocity structure of a boundary layer with a streamwise vortex pair has been measured using a 3-orthogonal-velocity-component fiber-optic LDA system with a  $50\mu\text{m}$  measurement volume. There is no significant correlation between data rate fluctuations and velocity magnitude fluctuations. Results for a 2-D turbulent boundary layer agree closely with those from a DNS near the wall, which confirms that velocity bias and signal broadening effects are negligible. While large streamwise vorticity is generated away from the wall, significant opposite sign vorticity is generated by the viscous interaction of the vortex and the wall. It was found that an abrupt step change in the wall shear stress magnitude occurs just outside of the vortex center.

## References

- AGARD, Advisory Group for Aerospace Research and Development 1996 *"Turbulent Boundary Layers in Subsonic and Supersonic Flow,"* AGARD-AG-335, North Atlantic Treaty Organization, pp. 25-28.
- Brown, J.L. 1989, *"Geometric bias and time coincidence in 3-dimensional laser Doppler velocimeter system,"* Experimental Fluids Vol. 7, pp. 25-32.
- Chen, C.-Y., Kim, P.J., and Walker, D.T. 1996 *"Angular Bias Errors in Three-Component Laser Velocimeter Measurements,"* J. Fluids engineering, Vol. 118, pp.555-561.
- Chesnakas, C.J., and Simpson, R.L. 1994 *"Full three-dimensional measurements of the cross-flow separation region of a 6 : 1 prolate spheroid,"* Experiments in Fluids, Vol. 17, pp. 68-74.
- Durst, F., Jovanovic, J., and Sender, J. 1995 *"LDA measurements in the near-wall region of a turbulent pipe flow,"* Journal of Fluid Mechanics Vol. 295, pp. 305-335.
- Durst, F. Kikura, H., Lekakis, I., Jovanovic, J., and Ye, Q. 1996 *"Wall shear stress determination from near-wall mean velocity data in turbulent pipe and channel flows,"* Experiments in Fluids, 20, pp. 417-428.

- Durst, F., Martinuzzi, R., Sender, J., and Thevenin, D. 1992 *"LDA-Measurements of Mean Velocity, RMS-Values and Higher Order Moments of Turbulence Intensity Fluctuations in Flow Fields with Strong Velocity Gradients,"* Proceedings of the 6th International Symposium on Applications of Laser Techniques to Fluid Mechanics, Lisbon, Portugal, paper 5.1.1.
- Durst, F., Melling, A., and Whitelaw, J.H., 1981 Principles and Practice of Laser-Doppler Anemometry, Second ed., Acad. Press, pp. 32.
- Echols, W.H., and Young, J.A., 1963 Studies of portable air-operated aerosol generator, *NRL Report*, 5929.
- Fuchs, W., Albrecht, H., Nobach, H., Tropea, C. and Graham, L.J.W. 1992 *"Simulation and experimental verification of statistical bias in laser Doppler anemometry including non-homogenous particle density,"* Proceedings of the 6th International Symposium on Applications of Laser Techniques to Fluid Mechanics, Lisbon, Portugal, paper 8.2.1.
- Kim, J., Moin, P. and Moser, R. 1987 *"Turbulence statistics in fully developed channel flow at low Reynolds number,"* Journal of Fluid Mechanics Vol. 177, pp. 133.
- Long, H., 2001, M.S. Thesis, Virginia Tech, Blacksburg VA (in progress).
- Ma, R., Saha, N., Devenport, W.J., and Wang, Y. 2000 *"Unsteady Behavior of a Tip Leakage Vortex Produced by Simulated Stator/Rotor Interaction,"* AIAA paper 2000-2217, Fluids 2000, Denver, CO, June 19-22.
- Meyers, J.F., Kjelgaard, S.O., and Hepner, T.E. 1992 *"Investigation of Particle sampling Bias in the Shear Flow Field Downstream of a Backward Facing Step"* Proceedings of the 6th International Symposium on Applications of Laser Techniques to Fluid Mechanics, Lisbon, Portugal, paper 29.1.
- Olcmen, S.M., and Simpson, R.L. 1995 *"A five-velocity -component laser-Doppler velocimeter for measurements of a three-dimensional turbulent boundary layer,"* Measurement Science and Technology, Vol. 6, pp. 702-716.
- Olcmen, S.M., Simpson, R.L., and Goody, M. 1998 *"An Experimental Investigation of Two-Point Correlations in Two- and Three Dimensional Turbulent Boundary Layers,"* AIAA paper 98-0427, 36th Aerospace Sciences Meeting and Exhibit, Reno, NV, January 12-15.
- Pauley, W.R., and Eaton, J.K. 1989 *"Boundary Layer Turbulence Structure in the Presence of Embedded Streamwise Vortex Pairs,"* Seventh Symposium on Turbulent Shear Flows, Stanford University, August 21-23.

- Schumann, U. 1977 *"Realizability of Reynolds-stress turbulence models,"* The Physics of Fluids, Vol 20, No. 5, May 1977 pp. 721-725.
- Smith, E.J., Rife, M.C., and Devenport, W.J. 1990 *"Investigation of the Small Boundary Layer Tunnel,"* Aerospace and Ocean Engineering Department, Virginia Polytechnic Institute and State University Report VPI-AOE-175, July 17.
- Spalart, P.R. 1988 *"Direct simulation of a turbulent boundary layer up to  $R=1410$ ."* Journal of Fluid Mechanics, Vol.187, pp. 61.
- Whiffen, M.C., Lau, J.C., and Smith, D.M. 1979 *"Design of LV Experiments for Turbulence Measurements,"* Laser Velocimetry and Particle Sizing, Thompson, H.D. and Stevenson, W.H., eds. Hemisphere, pp. 197-207.



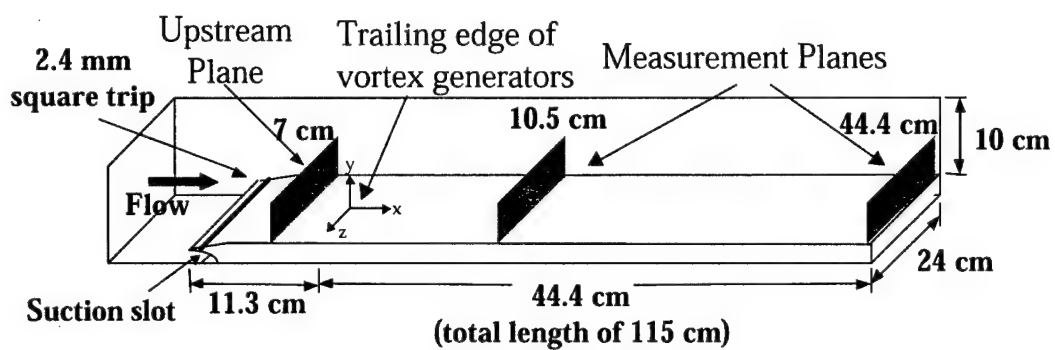


Figure 2.1: Experimental test section set-up showing suction slot, boundary layer trip and vortex generator pair position

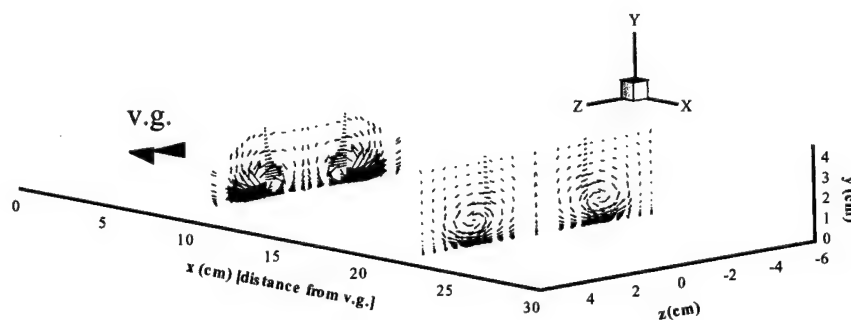


Figure 2.2: VW mean secondary flow vectors in 2 measurement planes



Figure 2.3: 3-orthogonal-velocity-component fiber-optic LDA head

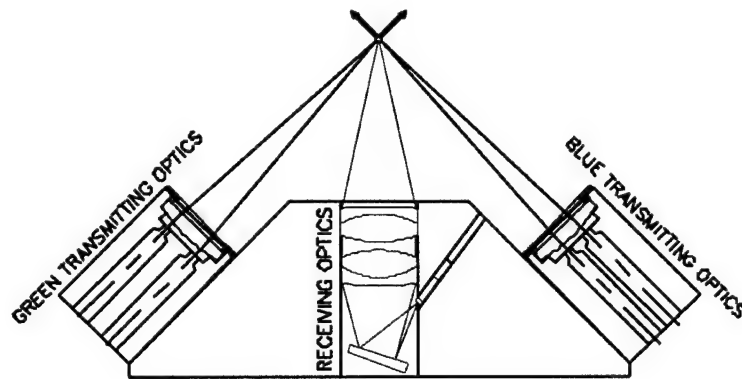


Figure 2.4: Schematic of 3-orthogonal-velocity-component fiber-optic LDA head

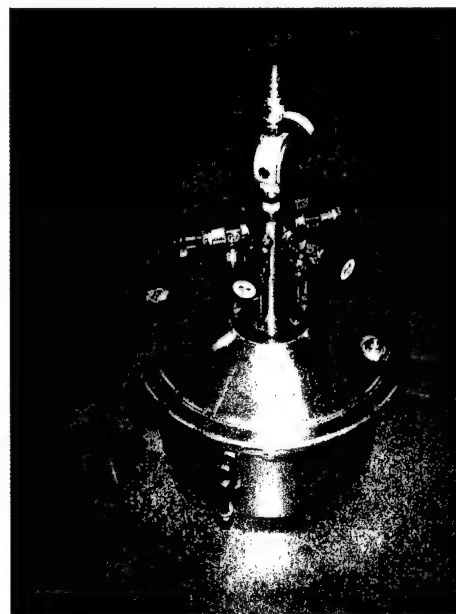


Figure 2.5: Aerosol generator (used both in auxiliary and cascade tunnels)

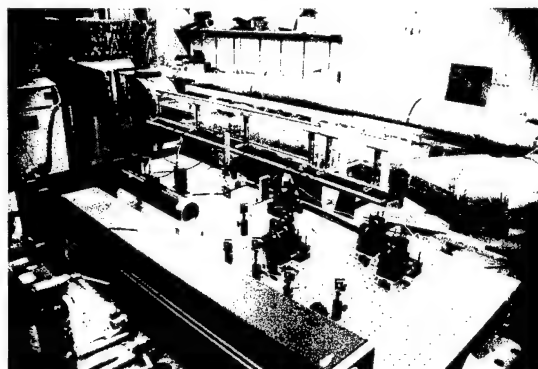


Figure 2.6: Auxiliary tunnel and test section

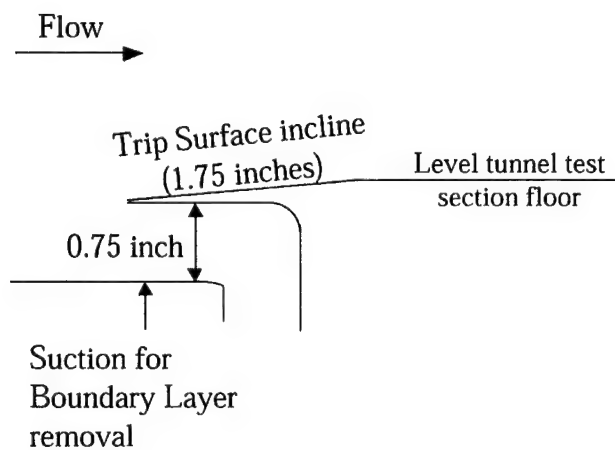


Figure 2.7: Trip test surface and suction slot incline

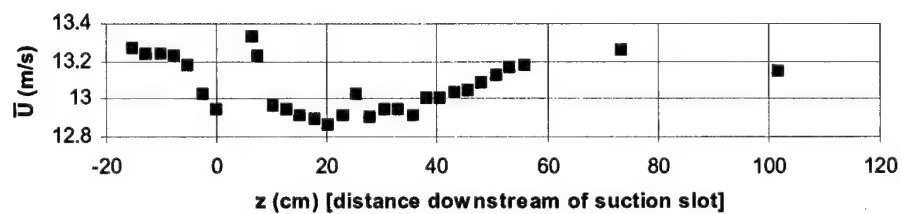


Figure 2.8: Stream-wise free-stream velocity profile approx. 3 cm above floor of tunnel, taken along the tunnel centerline

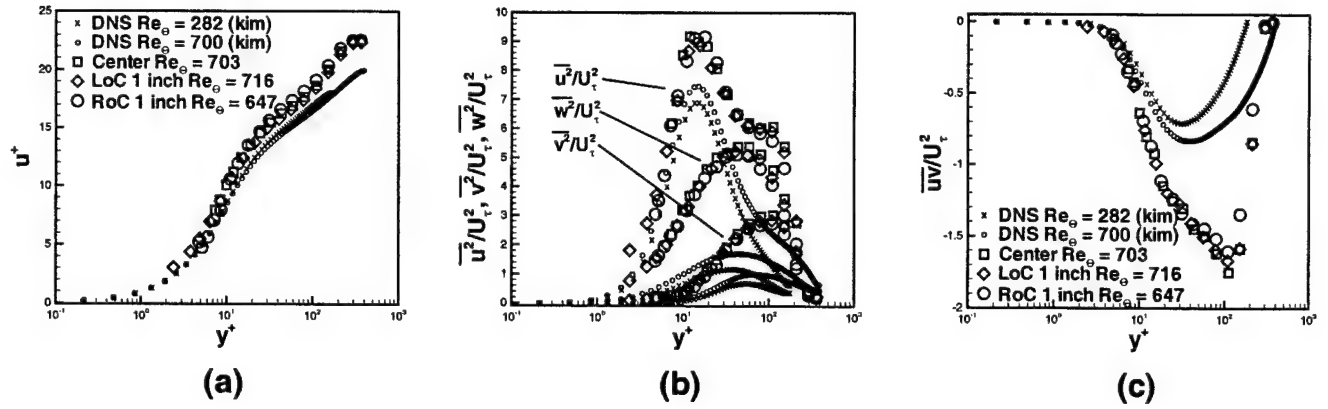


Figure 2.9: 7 cm downstream of suction slot, no vortex generators

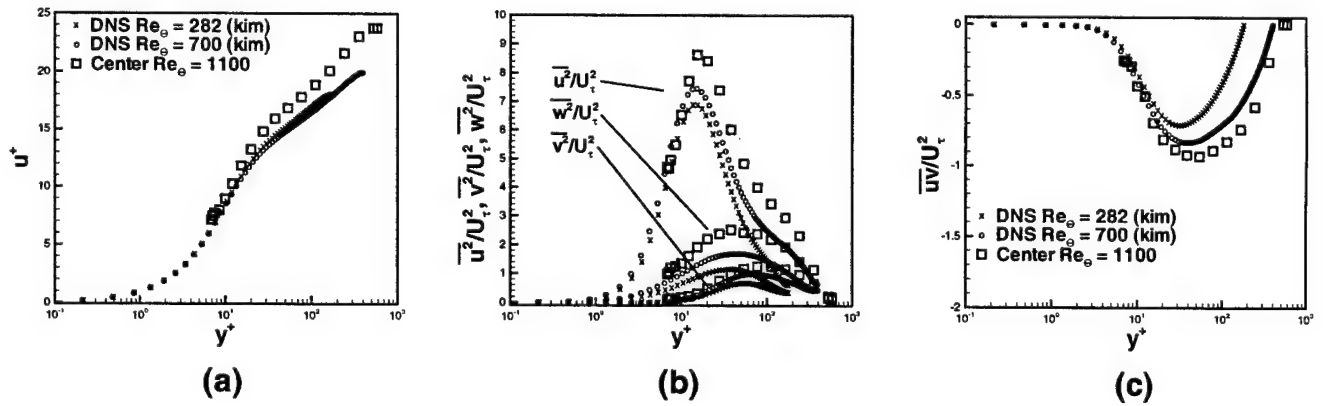


Figure 2.10: 21.8 cm downstream of suction slot (10.5 cm downstream of where vortex generators would be, no vortex generators)

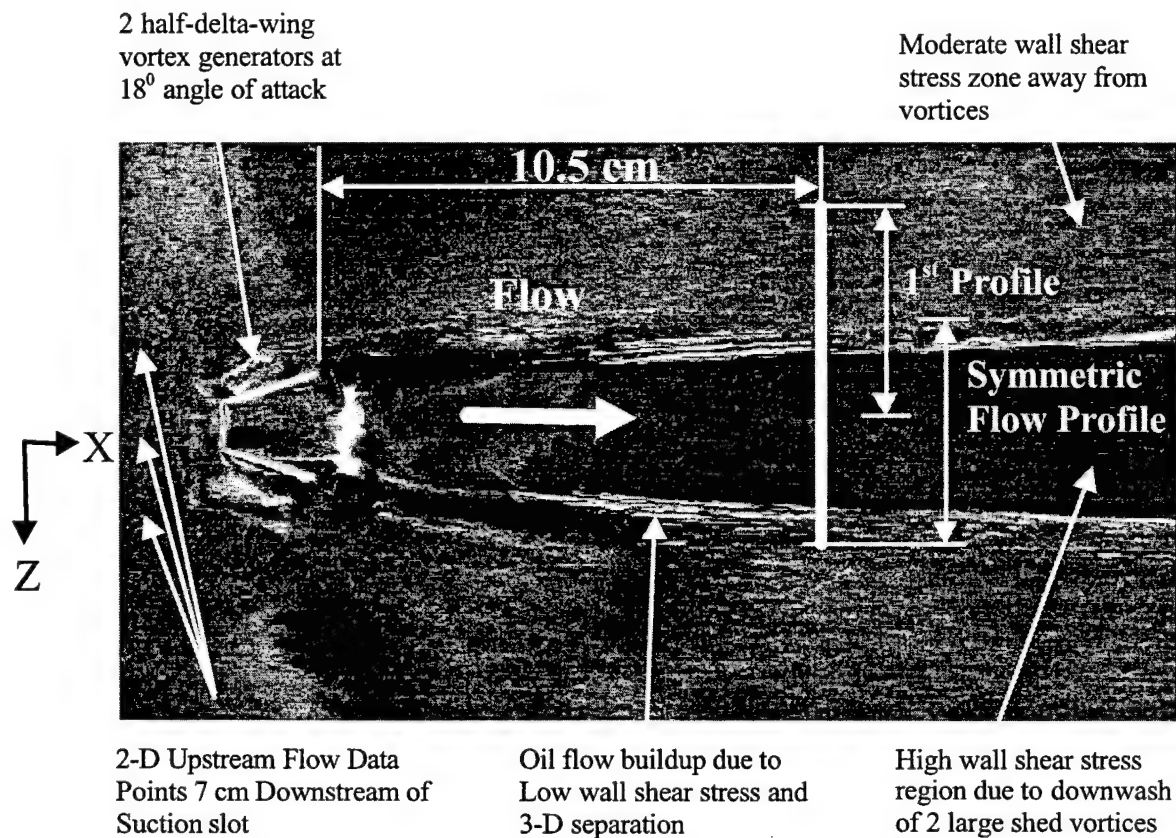


Figure 2.11: Oil flow visualization

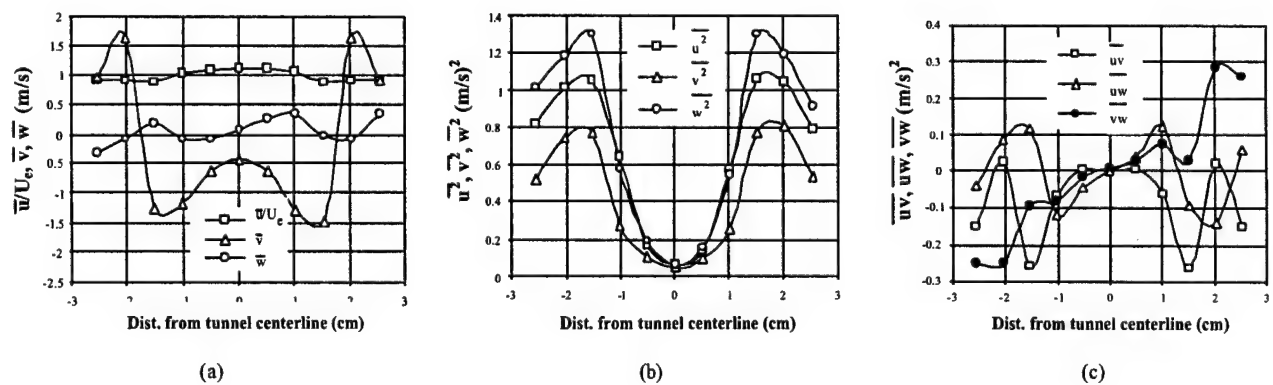


Figure 2.12: Tunnel symmetry 10.5 cm downstream of v.g., 0.75 cm off of wall

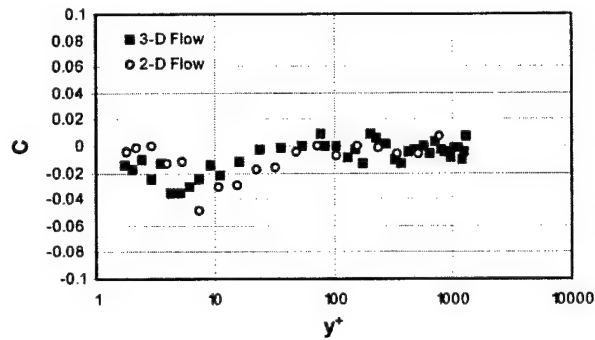


Figure 2.13: Correlation coefficient between velocity magnitude fluctuation and data rate fluctuation

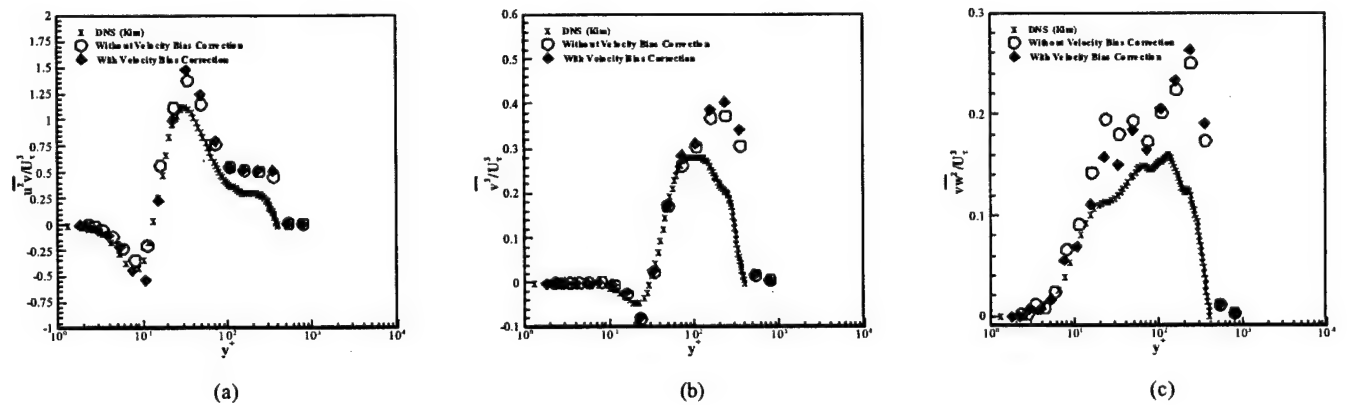


Figure 2.14: Velocity bias correction comparison for 2-D flow data,  $Re_\theta = 1100$

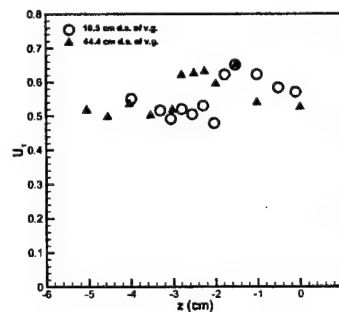


Figure 2.15: Wall shear stress across tunnel

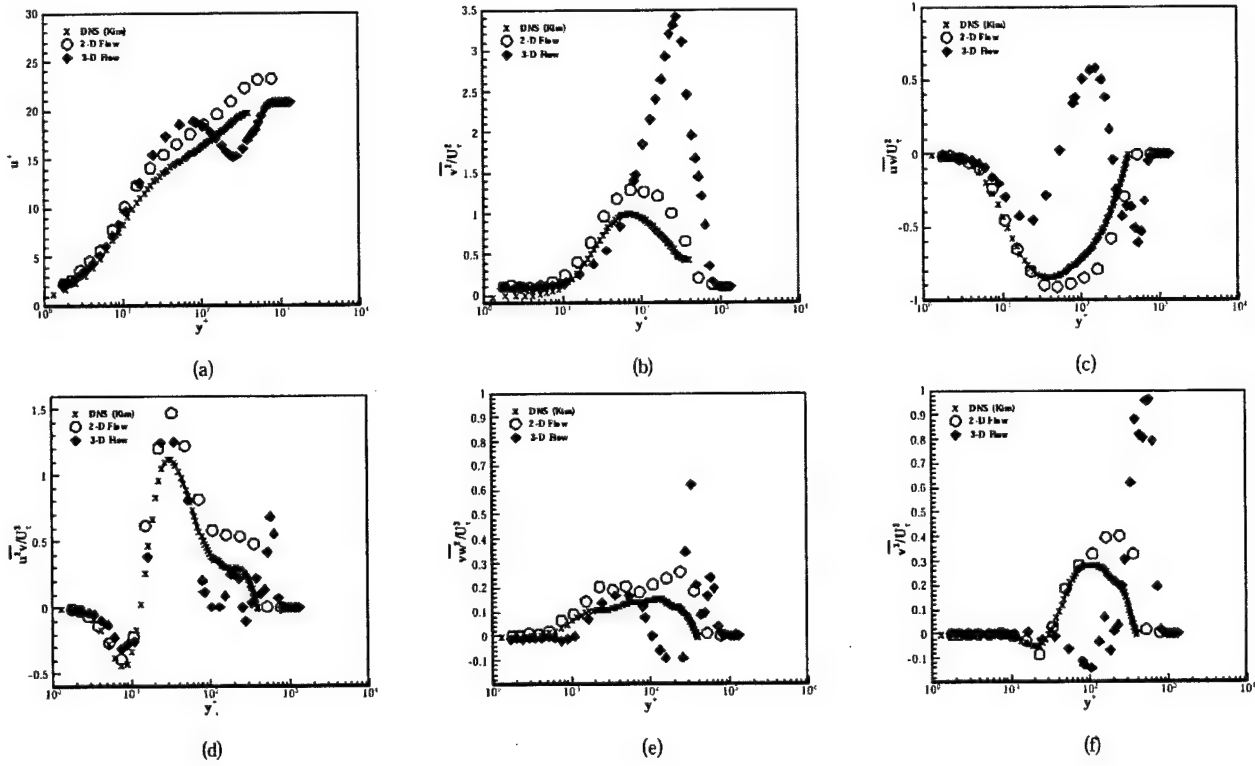


Figure 2.16: Comparison of 2-D ( $Re_\theta = 1100$ ) ( $x = 10.5$  cm) , DNS results ( $Re_\theta = 700$ ) and 3-D results through vortex core ( $x = 10.5$  cm)

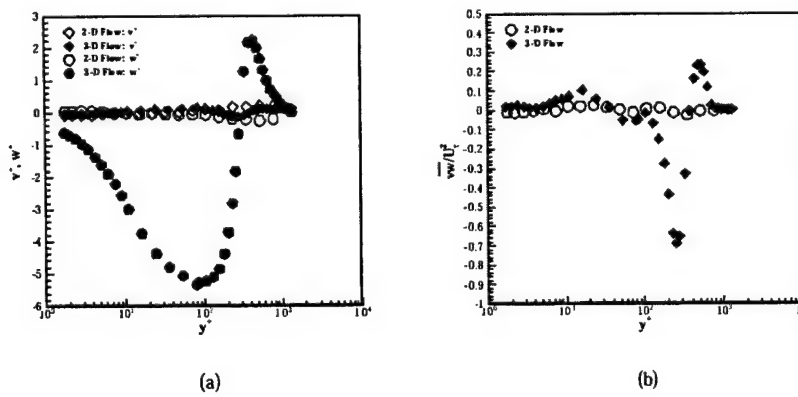


Figure 2.17: Plots of the components of the secondary flow vectors and  $-\overline{vw}$  Reynolds shear stress (2-D center of the tunnel ( $x = 10.5$  cm) and 3-D at results through vortex core at ( $x = 10.5$  cm)

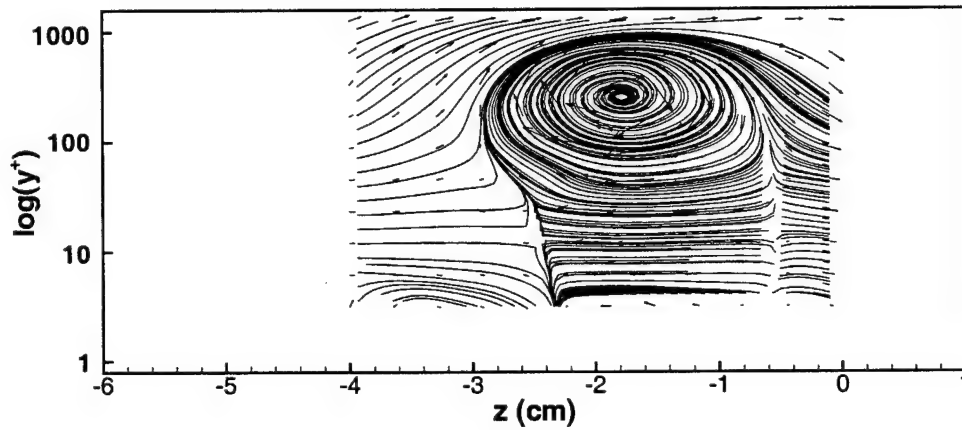


Figure 2.18: Log  $y^+$  secondary flow ( $\bar{v}\bar{W}$ ) streamlines 10.5 cm downstream of v.g (in vortex axis coordinates, normalized on  $U/\tau_w$ , 0 on the  $z$  (cm) axis is the tunnel centerline)

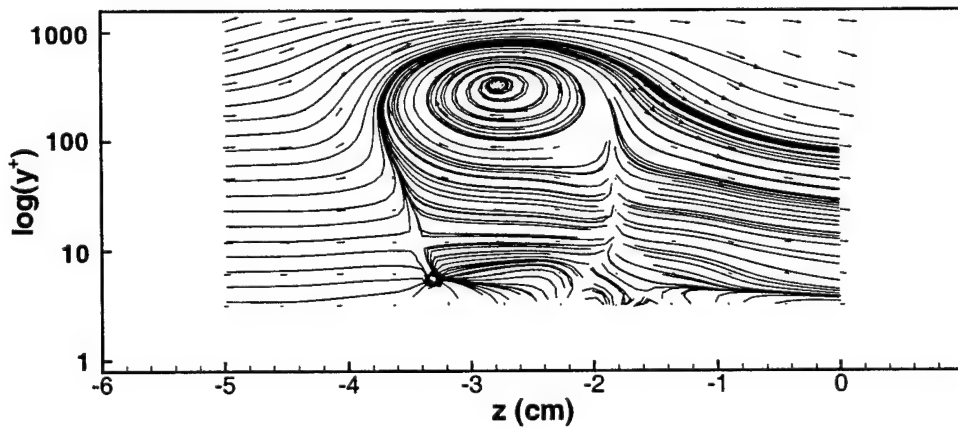


Figure 2.19: Log  $y^+$  secondary flow ( $\bar{v}\bar{W}$ ) streamlines 44.4 cm downstream of v.g (in vortex axis coordinates, normalized on  $U/\tau_w$ , 0 on the  $z$  (cm) axis is the tunnel centerline)



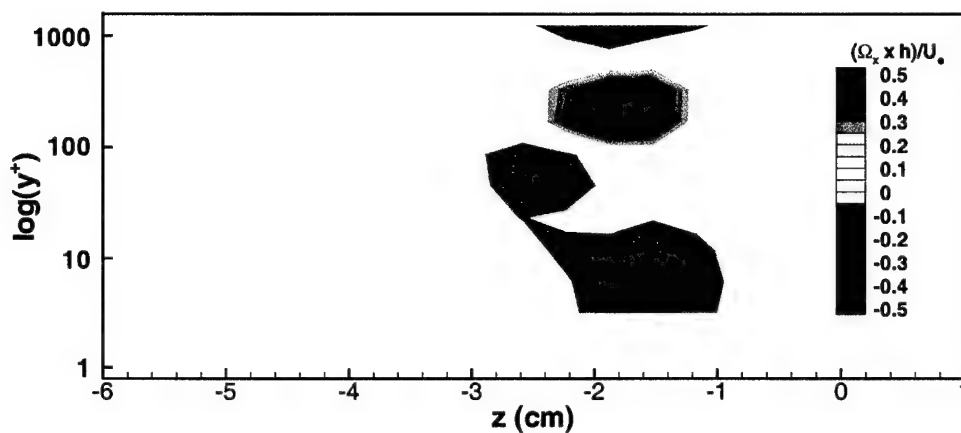


Figure 2.20: Log  $y^+$  streamwise vorticity  $\omega_x$  10.5 cm downstream of v.g (in vortex axis coordinates, normalized on  $U_e$ , 0 on the  $z$  (cm) axis is the tunnel centerline)

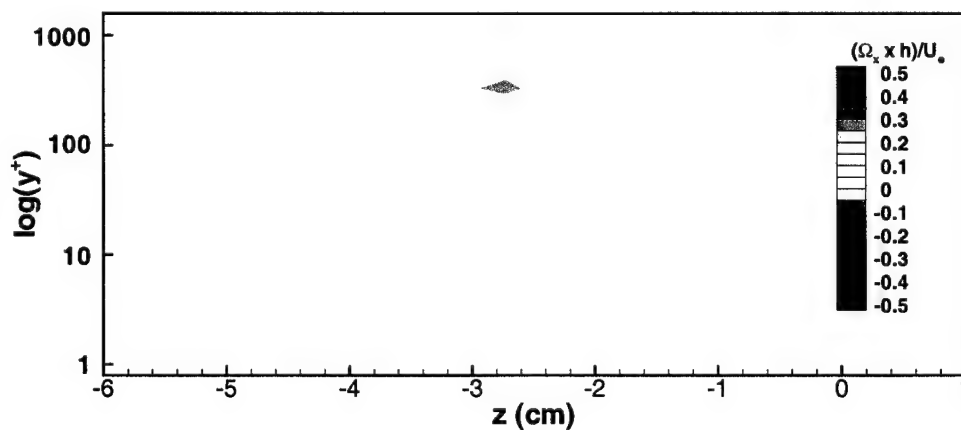


Figure 2.21: Log  $y^+$  streamwise vorticity  $\omega_x$  44.4 cm downstream of v.g (in vortex axis coordinates, normalized on  $U_e$ , 0 on the  $z$  (cm) axis is the tunnel centerline)

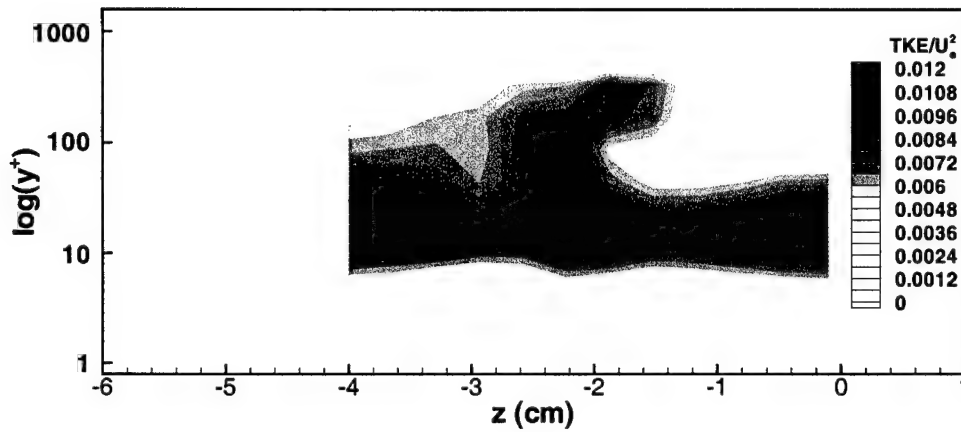


Figure 2.22: Log  $y^+$  TKE contours at 10.5 cm downstream of v.g (in vortex axis coordinates, normalized on  $U_e^2$ , 0 on the  $z$  (cm) axis is the tunnel centerline)

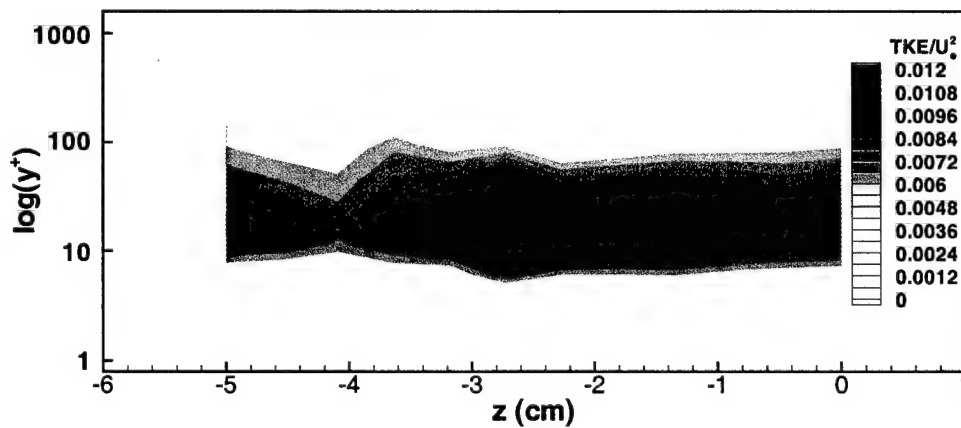


Figure 2.23: Log  $y^+$  TKE contours 44.4 cm downstream of v.g (in vortex axis coordinates, normalized on  $U_e^2$ , 0 on the  $z$  (cm) axis is the tunnel centerline)

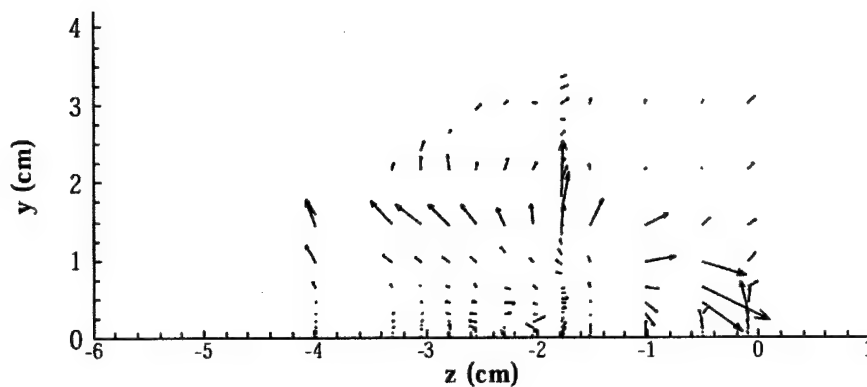


Figure 2.24: TKE Transport Vectors,  $Trans_{TKE_y}$   $Trans_{TKE_z}$ , 10.5 cm downstream of v.g (in vortex axis coordinates, normalized on  $U_e$ , 0 on the  $z$  (cm) axis is the tunnel centerline)

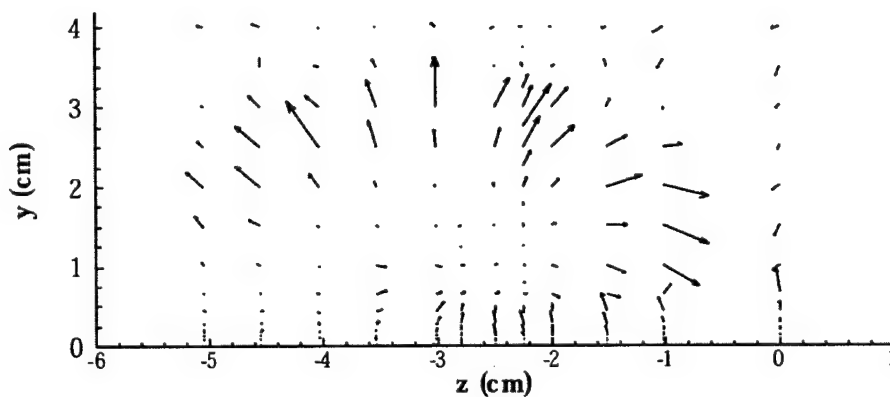


Figure 2.25: TKE Transport Vectors,  $Trans_{TKE_y}$   $Trans_{TKE_z}$ , 44.4 cm downstream of v.g (in vortex axis coordinates, normalized on  $U_e$ , 0 on the  $z$  (cm) axis is the tunnel centerline)

## Chapter 3

# Low-speed Linear Compressor Cascade Wind Tunnel

This chapter describes the modifications to the low-speed linear compressor cascade wind tunnel (cascade tunnel) at Virginia Tech. The purpose of the modifications is to measure the flow through the tip gap with a simultaneous three-orthogonal-velocity-component fiber-optic laser-Doppler anemometer (LDA). With each LDA measurement two analog signals are taken simultaneously to measure positions of a moving belt and vortex generators relative to the measurement location. Previous to this study only hot-wire measurements were performed in this tunnel. This is the experimental setup for the data collected and discussed in Chapter 4.

The tunnel has three major running configurations; 1) a stationary end-wall, 2) a moving end-wall and 3) a moving end-wall with vortex generators. In the stationary end-wall configuration the flow is a model of a cascade of rotor blades with a turning angle of  $11.8^\circ$ . The moving end-wall configuration models the movement of the compressor casing past the blades. The moving end-wall with vortex generators models the upstream stator wakes interacting with the flow through the cascade of rotor blades.

Figure 3.1 is a schematic of the tunnel. The blades in figure hang down from the ceiling with a tip gap between the lower surface of the blade and the floor (see Figure 3.2). The tip gap region of blade 5 is the region of investigation as noted by the LDA head and optical glass insert mounted underneath the tunnel Figure 3.1. The moving end-wall travels on the Teflon bed in the direction  $V_{belt}$  specified in figure.

The modifications to the tunnel are limited to incorporating a LDA measurement system under

the Blade 5. The rest of the tunnel is kept in the same configuration as Ma et al. (2000), who utilized hot-wire anemometry to measure the wake of the Blades 4 and 5 with moving end-wall and vortex generators. The first section describes the previous set-up of the tunnel. The main section of the chapter details the tunnel modifications as well as the modifications to the LDA measurement system used in Chapter 2. The chapter ends with a discussion of the continuing issues with the set-up and possible recommendations for solutions.

### 3.1 Previous Set-up of the Cascade Tunnel

The initial configuration of the low-speed linear compressor cascade wind tunnel at Virginia Tech with a moving end-wall is fully described by Wang et al. (1999). The flow is contracted at a 3.88:1 ratio before entering the 30"x12" rectangular section which guides the flow onto the cascade. The cascade consists of 8 cantilevered GE rotor B section blades mounted with a tip gap of 3.3% chord. The blades have a chord of 10" and an effective span of just under 10". The cascade configuration has a rectangular cross section of 65"x10". The blade spacing is 9.29". The stagger angle of the cascade is 56.93°. The inlet angle of the cascade is 65.1°. The approach free-stream velocity is approximately 25 m/s. At 18.8 cm upstream of the leading edge of the cascade are two, three-quarter inch high, suction slots on the upper and lower end-walls removing the boundary layers from the inlet (see Figure 3.2). The flow is tripped by a square bar mounted on the lower suction slot also shown in Figure 3.2. The trip is the same as the square bar used in the auxiliary tunnel (see Section 2.2.2).

The moving end-wall system is described in Wang et al. (1999). The moving belt extends more than two-chord lengths axial downstream of the trailing edge plane of the blades as well as a short distance upstream. The belt is 27" wide. The belt is run at around 23 m/s which approximately matches the tangential velocity of the freestream ( $25\text{m/s} \cos(24.9) = 23\text{m/s}$ ). The belt material is 0.01" thick Dupont Mylar D film. The belt is joined into a continuous loop by spot-melting a Mylar belt joint using a soldering iron at several hundred points at a 45° angle (see Figure 3.1). The joint region is approximately 1.5" wide and takes up around 0.5% of the whole belt length. The belt is driven by a 15HP AC synchronous motor. The Mylar belt rolls over a Teflon coated bed.

The same vortex generators described in Section 2.2.4 are used in the cascade tunnel. The vortex generators are glued to the belt 3.35 cm from the leading edge of the Teflon bed. The vortex generators are aligned relative to the Teflon bed as apposed to the Mylar edge. Once the micro-lift tape is placed on the belt relative to the LDA beams (see Section 3.2.11) the position

of the belt and vortex generators is set to take data only at one position (see Appendix B for uncertainty of positioning). The pairs of vortex generators are spaced at 236 mm apart, or one blade space (see Appendix B). This creates a periodic unsteady boundary condition. A laser pointer and a photodiode are utilized to detect the position of the vortex generators. The V.G. marks painted on the surface of the belt relative to the vortex generators block the laser pointer beam from the photodiode (see Figure 3.2). The belt joint is also painted on the surface to block the laser pointer beam from the photodiode. A similar setup is found in Ma et al. (2000).

## 3.2 Cascade Tunnel Modification

### 3.2.1 Environmental containment tent

LDA measurements require particles (seed) in the flow as described in Section 2.2.6. Since the cascade tunnel is a open ended wind tunnel, the whole room would quickly fill with smoke creating an unacceptable working environment. To contain the smoke a plastic tent was erected over the entire tunnel containing the fan and the test section. A steel frame constructed out of electrical conduit supports the tent. The tent material is Dura-Therm Clear HVA Greenhouse Film manufactured by AT Plastics Inc. The plastic is relatively clear, stretchable and 8 mils thick. Weights are placed on the bottom edge of the tent to seal it to the concrete floor. Figure 3.3 shows the tent looking at the upstream test section. The tunnel contraction and plenum are shown in the figure as well, with the tent and frame incasing the entire tunnel.

Careful consideration was taken to make sure the tent was not interfering with the flow. Measurements in the tunnel show that with and without the tent down no discernable difference is seen in the mean free-stream velocity. A 2ft x 5ft thin Mylar window is on the side of the tent to clearly view the test section from outside of the tent (see Figure 3.4). Heat shrink tape adheres the Mylar to the tent plastic.

### 3.2.2 Cooling system

Near the inlet to the tunnel's fan is a 29000 Btu/hr air conditioner. Because the tent completely contains the tunnel, over time the temperature of the air in the tent rises. The purpose of the air conditioner is to keep the air in the tent at a constant temperature. The air conditioner blows cool air into the tent and exhausts warm air into the surrounding room. As long as the temperature in the room is around 20°C the air conditioner keeps the tent temperature around

25°C. However if the room temperature is over 25°C then over time the temperature in the tent can raise to as much as 30°C. For the LDA measurements the temperature of the air in tunnel should be 25°C.

### 3.2.3 Particle injection system

The particle seeding system is described in Section 2.2.6. The same aerosol generator used in the auxiliary tunnel is used in the cascade tunnel (Echols and Young, 1963). The seeding apparatus used in the cascade tunnel is shown in Figure 3.5. The right hand side of the figure shows the seed piped into the inlet of the tunnel contraction through a 0.5 inch pipe. The pipe is shown in upstream of the tunnel contraction, in the tunnel, in Figure 3.6. The last plenum screen is shown just upstream of the pipe. The pipe nozzle is rotate left and right as well moved up and down until the smoke is injected into the LDA probe volume. Several traverses with the pitot probe approximately 100 cm upstream of the suction slot show no measurable influence or effect of the pipe on the downstream flow. The maximum mean velocity difference was within 0.2% with and without the pipe.

### 3.2.4 Plywood Bed

The cascade tunnel has a plywood bed mounted underneath the cascade of compressor blades. The bed dimensions are 0.8 m x 3.2 m x 1.9 cm. The bed starts 5.2 cm beyond the leading edge of the lower suction slot. The bed forms the floor beneath the cascade of rotor blades over which the Mylar belt runs. The bed is shown in Figure 3.1.

The Mylar does not scrape on the ends of the bed because they are curved (see Figure 3.7). The curved ends are constructed out of 12 inch diameter PVC pipe. The pipe overlaps the bed where it is screwed together.

### 3.2.5 Plexiglass and Optical glass inserts

The Plywood bed has a Plexiglass insert mounted beneath blades 4, 5 and 6. The Plexiglass insert is approximately 16 inches wide and 20 inches long (on a side) and the edges make a 45° angle with the suction slot (see Figure 3.1). The Plexiglass insert has an optical glass insert mounted beneath blade 5. The optical glass insert is 8 inches in diameter.

The purpose of the plexiglass insert is to allow for multiple positions of the optical glass so

that many different regions of the flow can be probed. Only one optical glass position was used in this study. The center of the optical glass is  $z = -0.65$  inches and  $x = 0.75$  inches from the leading edge of blade 5 (using the coordinate system labelled in Figure 3.1). In the future there are multiple positions under the blades which can be investigated with the LDA, pressure taps or any other measurement system by simply constructing the new appropriate insert.

The optical glass mounted in the Plexiglass insert is described in Section 2.2.6. Four adjustable feet attached to the Plexiglass hold the optical glass from underneath. High temperature tape (3M 5413 Polyimide Film Tape) is applied around the glass insert, attaching it to the plexiglass from the top side. The tape is 2.7 mils thick and the adhesive resists melting up to  $260^{\circ}\text{C}$ . The tape keeps the glass from spinning when the belt is running.

There is an 8 inch x 0.5 inch hole cut parallel to the suction slot 0.65 inches downstream of the optical glass insert. Through this hole the BELT-HITE sensor is traversed to measure the displacement of the belt in the  $y$  direction when the belt is running (see Figure 3.1).

### 3.2.6 Teflon sheet

The Mylar belt does not slide across the bare plywood and Plexiglass, this would create too much friction and melt the belt. Both the Mylar and Plexiglass are coated with a sheet of 1/16 inch thick Teflon. The Teflon is specially coated on one side so that slow curing epoxy fuses the Teflon and the plywood (or plexiglass) together. Much care was taken to make sure there are no air bubbles formed between the Teflon and the respective material. Invariably some bubbles form and once the epoxy has cured a syringe is used to inject more epoxy under the Teflon. Once all of the air bubbles are taken care of a reciprocating 12"x3" sander with a fine grit sand paper is used across the entire Teflon surface to sand it as level as possible. Any bump causes more friction between the Mylar and the Teflon and a potential melting point for the Mylar.

The joints between the different sections (the plexiglass and the plywood and the optical glass and the plexiglass) of the floor form the most hazardous area for melting of the Mylar. Changes in humidity cause the joints between the plexiglass insert and the plywood (as well as the glass insert and the plexiglass) to expand and contract. This movement can alter the setup and form small steps in the floor. Much care is taken to make sure that the Mylar belt does not encounter such steps when it is running. To be sure of this the trailing material edge is aligned slightly above the leading material edge or perfectly level. This difference is never more than 1/16 inch, however it is quite necessary. Any detectable edge by hand will cause the belt to melt.

To compensate for changes in humidity, several precautions are taken to prevent Mylar belt



melting. Each time the belt is replaced all the interfaces are carefully checked by hand. Once the new belt is installed, it is ramped up to 4 m/s and run for 10 minutes, with the tunnel and active suction on and then stopped. The belt is then carefully checked and then run up to 8 m/s for 10 minutes and then stopped. Each time it is checked if any melting, or excess scratching is seen at any position; the section joints are checked and adjusted. This process is repeated in 4 m/s increments until the full speed (23 m/s) is reached.

### 3.2.7 Belt Control System

The Mylar belt is looped around two parallel 20 cm diameter cylindrical rollers approximately 4.2 m apart and set at either end of the plywood bed. Recall that the plywood bed is 3.2 m in length and thus the rollers are mounted approximately 0.5 m from the bed edge on either end. Figure 3.1 shows the relative position of the drive and free rollers relative to the tunnel. The speed of the drive roller is adjusted with a variable speed controller while the free roller spins freely.

The Mylar belt loops around both rollers and is fused together at the belt joint as shown in Figure 3.1. The drive roller controls the velocity of the belt,  $V_{belt}$ . The uncertainty in the belt speed while running was 0.24% r.m.s. or  $V_{belt} \pm 0.03 \text{ m/s}$  (Ma et al., 2000). The standard deviation of the belt velocity between runs was 1.52%, this was calculated from the moving end-wall data taken before each run. The free roller controls the axial position of the belt. The free roller is controlled with screws mounted on either end of the drum. These screws twist the free roller axis relative to the drive roller axis creating a difference in tension axially across the belt. The differential in tension drives the belt back and forth across the rollers.

While starting and stopping the belt, much adjustment is required to prevent it from slipping axially along the roller. If care is not taken, the belt either slides off of the bed or into the suction slot. As the belt speeds up the adjustments become more fine to control the belt position. The tolerance of controlling the axial position of the belt at full speed is approximately  $\pm 0.25$  inch. The level of control is dependent upon the particular belt and may vary depending upon the quality of the belt.

### 3.2.8 Active Suction

When the belt is moving across the floor it is not necessarily going to lay flat on the bed, therefore active suction must be used to keep it flat. The belt is sucked to the floor through

small holes in the bed with a vacuum cleaner all outside of the tunnel test section. The position of the holes are shown in Figure 3.1. A 6.25 hp vacuum cleaner is hooked up to 26 holes in the bed the bed from underneath through a series of PVC pipes. The pipes are shown in Figure 3.8. Two rows of 1/16th inch holes are cut into the bed spanning the entire cross-section of bed.

### 3.2.9 Belt Leading Edge Cover

A belt leading edge cover prevents the tunnel air from getting under the belt and lifting it up. The belt leading edge cover is taped to the suction slot and overlaps the moving Mylar by 1/2 inch. The belt leading edge cover Mylar is the same material that the belt is made out of (0.01 inch thick Dupont Mylar D). The belt leading edge cover is pointed out in Figure 3.1. When the tunnel air flow is running the belt leading edge cover lays flat against the moving belt, there is no gap between the cover and the moving belt.

### 3.2.10 Anti-static brushes

When the Mylar belt is moving around the two rollers the system acts just like a Van de Graaff generator. After running the belt for only 5 minutes at a slow speed, the belt collects enough charge to make a spark jump over 25 cm. The spark is caused from the differential in charge from one side to the other of the Mylar. To neutralize this charge two anti-static brushes are wired together and mounted one on top and the other underneath the belt. The anti-static brushes are Meech Passive Induction Bars Model 974, one 28 inches long the other 45 inches long. The anti-static brushes consist of an aluminum rod with thousands of tiny carbon fibers coming out of it around 1.6 cm in length. The rods sit just above and below the belt so as to not touch or hit the vortex generators as they go by. Figure 3.11 shows a picture of the two brushes which are mounted next to the downstream roller (see Figure 3.1).

### 3.2.11 Micro-lift (tape) system for Mylar

There is very little friction between the moving Mylar and the stationary Teflon; however, there is still enough to scratch the Mylar. The scratches form on the Mylar in the direction of movement of the belt,  $V_{belt}$ . When the scratches form directly over the LDA beams, the beams become blocked and no data can be taken. To prevent scratches from forming in this area, a piece of tape is attached longitudinally to the underside of the belt next to the measurement volume. The tape extends the entire length of the belt and lifts the area next to it just enough

to lift it off the floor and prevent scratches from forming (see Figure 3.1). The tape is 8.3 mils thick 3M 5453 PTFE Glass Cloth tape. The tape is high temperature tape that resists melting caused from the friction between the tape and the Teflon. The adhesive on the tape resists melting up to 204° C. The width of the optically clear region kept clean by the tape, at operating velocity, is roughly 0.35 inches wide.

For a time two pieces of tape were positioned on either side of the measurement volume spaced at 0.5 inch. Instead of keeping the area clean the two tapes trapped Teflon particles between them and scratched the surface even more.

### 3.2.12 LDA head and BELT-HITE sensor traverse

Mounted underneath Blade 5, the Mylar belt and the optical glass is the LDA head shooting laser beams into the tunnel and collecting the scatter of light off of the particles in the flow. The LDA head is mounted to a traverse which is screwed into a steel table attached to the underside of the tunnel. Also mounted to this traverse is the BELT-HITE position sensor which sticks up through the hole next to the optical glass. Figure 3.9 shows the traverse for the LDA head and BELT-HITE position sensor outside of the tunnel. Figure 3.10 shows the head, sensor and traverse mounted to the table under the tunnel.

The two probes are mounted so that they move back and forth on the 9.5 inch traverse together (using the knob at the end of the traverse). The LDA head moves up and down on an independent y traverse as described in Section 2.2.6. The LDA head z traverse is used to line up the measurement volume with the BELT-HITE sensor. The BELT-HITE sensor perpendicular to the head on the aluminum support is shown in Figure 3.9. The sensor is lined up sensor hole next to the optical glass. The BELT-HITE sensor then is traversed up into the hole on a 2 inch traverse in the y direction. The tip of the BELT-HITE sensor sits 0.5 mm away from the moving Mylar belt. The BELT-HITE sensor is shown in the hole in Figure 3.10.

The table underneath the tunnel, on which the traverse system rests, is a 1/4 inch thick sheet of steel mounted screwed into the bed frame. The table is shown in Figure 3.2 and Figure 3.10. The return section of the belt passes by 2 inches ( $\pm 1$  inch) below the steel table. The table is slightly larger than the Plexiglass insert to allow for different measurement apparatus to be mounted to it. Using a system of clamps the table can be easily raised and lowered from the tunnel without disrupting the head alignment.

### 3.2.13 Vortex Generator Sensor Mount

The vortex generator sensor (a photodiode) is screwed into the Plexiglass insert in at the position shown in Figure 3.1. The sensor goes up into the floor as shown in Figure 3.2. A laser pointer is mounted to the top of the tunnel and shoots a beam into the photodiode. The painted marks shown in Figure 3.12 and Figure 3.1 block the sensor as they go by.

There were two different configurations of the marks on the belt. The first system is shown in Figure 3.12 and the marks are positioned right between the vortex generator pairs themselves. In the second system, shown in Figure 3.1, the marks are set halfway between each pairs of vortex generators. In both configurations the distance between any two marks is the same as the distance between any two vortex generators (one blade passage). The reason for the two different configurations is discussed in Section 4.3.

An area 2.5 blade spaces is blocked out over the Mylar belt joint. The Mylar belt joint mark is shown in Figure 3.1. The Mylar belt joint is not flat since the belt is overlapped at this point, and melted and taped. With a total thickness of around 0.04 inches (1.2% tip gap) this potentially disrupts the flow in the tip gap. Therefore the region before and after the joint is blocked out so that the data can be removed from the data set.

The final working configuration of the tunnel is shown in Figure 3.13. In this figure the relative positions of the Micro-lift tape, the vortex generators, the vortex generator marks, the beams, the blades and the optical glass can be seen. The beams are shown in the 1F profile position (position described in Section 4.1).

## 3.3 LDA Optical System Modifications

The LDA optical equipment used in the cascade tunnel are identical to the ones used in the auxiliary tunnel. Only the photo-multiplier (PM) tubes were changed between the two systems. The photo-multiplier tubes were updated to new tubes from Electron Tubes Limited models 9125B and 9124B. These tubes are optimized for green and blue light, respectively.

## 3.4 Data Acquisition (DAQ) System

Each of the configurations of the tunnel has a different DAQ setup. The stationary end-wall does not use any of the analog signals in the DAQ. At each point of the stationary end-wall

30,000 samples of data are collected. The moving end-wall uses both of the analog signals of the DAQ and at each point 30,000 samples of data are collected. The moving end-wall with vortex generator also uses both of the analog signals of the DAQ and at each point 150,000 samples of data are taken. The vortex generator data require so much more data because it is phase-averaged over each position of the vortex generators. In each bin there must be enough samples for a velocity reading of acceptable uncertainty (Appendix B).

### 3.4.1 Input Signals

There are five signals recorded by the data acquisition system. Three of these signals are the simultaneous digital output of the velocity components from the LDA system. These digital signals contain the frequencies created by the particles passing through the measurement volume. The two other signals are analog signals. The two analog signals are taken simultaneously with the digital signal so that they are all synchronized. Any two of three analog inputs can be synchronized with the LDA signals. The first analog input is the BELT-HITE belt position measurement sensor signal. This measures the belt displacement in the y direction. The second analog input is the pulse from the vortex generator signal processor. This signal contains a negative pulse whenever a mark is blocking the sensor. The third available input is the triangular pulse processor. This processor transforms the pulses from the vortex generator signal processor into a triangular wave which starts at 0 and ramps up until the next pulse occurs.

#### Three Digital Inputs: LDA signals

The LDA input signals are the digital signals coming from the three Macrodyne model FDP3100 frequency domain signal processors. The Macrodynes process is condition analog input signals the from the two photomultiplier tubes. The photomultiplier tubes receive the signals through a fiber-optic cable from the LDA head. Data were only acquired when the LDA incident beams passed clearly through the optical glass and Mylar belt, reflected off of the flow seeding particles and received back into a lens which focused on a fiber mounted between the beams (See Figure 2.4). The receiving fiber is shown as a black dot in Figure 3.1.

An optimal data rate occurred when all the LDA beams shot through the optically clear region right next to the Micro-lift tape (see Section 3.2.11). As discussed in Section 3.2.7, the tolerance of controlling the axial position of the belt along the rollers at full speed is approximately  $\pm 0.25$  inch. The optically clear region is only 0.35 inch wide. Given these conditions, and the fact that the beams can take up as much as 0.2 inches of the clear area, a meaningful data rate

occurred sporadically over the data collection time period. Only during roughly 15% of the data collection time period could the peak data rate be obtained with the moving end-wall, the highest peak was around 400 samples/second. Only during roughly 30% of the data collection time period could one get one quarter of the peak (100 samples/second). The rest of the 55% of the time no data would be collected. This effectively reduces a peak data rate of 400 samples/second to less than 100 samples/second. It takes around a half hour to collect data at one point with a moving end-wall and vortex generators (150,000 samples). This is only true if the belts work properly for the complete half hour.

The signal conditioning for the cascade tunnel is identical to the one in the auxiliary tunnel. Figure 3.14 shows a schematic of the conditioning system. The left hand side of the figure shows the beam coming in from the LDA head. The beam is split with a dichroic mirror into a blue and a green beam. These beams are amplified and converted into an electrical signal in the PM tubes. Coaxial cable connects the rest of the components together. Three variable RF generators are used to down-shift mix the LDA signals into a frequency range from 0-5 MHz. All of the signals are amplified and then mixed with their respective RF generated signal. This amplified electrical analog signal is fed into the FDP3100 Macrodynes. The 27MHz and 50MHz signals are separated in the Macrodyne units which only process a bandwidth of 0-5 MHz.

The Macrodyne units basically perform three functions: check if the signal is valid, check that all three signals are coincident within 10  $\mu$ s and perform a FFT on each burst signal. The frequency is digitized and sent to the computer over 3, 25-pin cables. A more in-depth description of the Macrodyne units is found in the Macrodyne Manual (1992).

### First Analog Input: BELT-HITE Position

The BELT-HITE sensor is a Philtec, Inc Fiber Optic Displacement Sensor. The model used with this study is the RC24-BR probe with a measurement area of  $1\text{mm}^2$ . The RC sensors have two parallel rectangular fiber bundles each of which partially send and receive laser light. As the target surface (Mylar) gets closer to the tip of the probe the more light is reflected back through the bundle. To compensate for the differences in reflectance of the surface, the probe processor forms the ratio of the two fiber bundles output signals. The analog input into the DAQ system is this ratio as a voltage from 0 to 10 Volts.

The BELT-HITE sensors were calibrated using a 1/10000 inch resolution micrometer and a piece of Mylar. The calibration set-up is shown in Figure 3.15. The probe requires a DC voltage between 9 and 30 volts to operate, provided by the DC power supply (top center). The

probe signal processor is shown top left. The probe is taped to a small optical table adjusted by a micrometer shown lower center. The output is sent to the multimeter, top right.

The data from the calibration is shown in Figure 3.16. The stand-off distance of the sensor is between 0.5 and 1 mm. The slope of the curve fit is approximately 0.011 Volts/ $\mu\text{m}$ . The vertical displacement resolution of the probe is  $\pm 0.021259 \mu\text{m}$  and has a max sample rate of 100 kHz. At this frequency 0.23 mm resolution of longitudinal displacement of the belt is possible.

When the belt is moving at full speed the plot of the sensor output is seen in Figure 3.17. This represents approximately one full rotation of the belt. The large jump in signal is when the belt joint passes over the probe. The standard deviation of the signal (not including the belt joint jump) is  $6.58 \mu\text{m}$ . When the belt joint passes over the sensor, the signal jumps. The jump displacement is measured to be greater than  $100 \mu\text{m}$ . The signal shown in Figure 3.17 was taken at 30 kHz (a resolution of 0.8 mm longitudinal movement of the belt).

### Second Analog Input: Vortex Generator Pulse

As discussed earlier in Section 3.2.13, black marks are painted on the belt to trigger a signal from a photodiode mounted directly beneath the belt (see Figure 3.2). There are two types of marks; vortex generator marks and belt joint marks. The vortex generator marks are 0.25 inches wide and approximately 1 inch long (see Figure 3.12). The belt joint marks are 2.5 blade widths wide and one inch long (see Figure 3.1). The total length of the belt joint mark is approximately 25 inches or 8% of the belt length.

The signal from the photodiode is processed with the V.G. position photodiode processor. The processor was designed and built by Nilanjan Saha. Figure 3.18 shows V.G. position photodiode processor on the right. The photodiode processor has an off and on switch and an adjustable knob. The knob adjusts the mean voltage out of the photodiode processor. For this experiment the mean voltage is set between 6.5 and 7.5 Volts. Figure 3.19 is the typical output of the photodiode processor when the belt is running at full speed. The data were taken at 30 kHz and two belt jumps are shown. By removing all data when the photodiode sensor processor output is less than 5.8 Volts, the data obtained in the presence of belt joints can be removed from the data set. At full speed the frequency of the pulses is approximately 100 Hz.

### Third Analog Input: Vortex Generator Triangular Pulse

The triangular pulse signal is created by the triangular pulse processor. This processor was also designed and built by Nilanjan Saha. Figure 3.18 shows the triangular pulse processor on the left.

The triangular pulse processor simply has input for the signal from the photodiode processor and an output for the computer. When the pulse drops below 5.5 Volts, the output from the processor is 0 Volts. When the pulse rises above 6.0 Volts a triangular pulse with a slope of 351 Volts/second starts. Figure 3.20 is the typical output of the triangular pulse processor.

The position of the vortex generators is recorded by the computer with the Voltage from this signal ( $T_{input}$ ). The distance between the black mark and the vortex generator is known ( $Z_{vg-bm}$ ). The slope of the pulse is known ( $M_{tria}$ , Volts/second). The speed of the belt is known ( $V_{belt}$ ). The distance between the sensor and the measurement volume is known ( $Z_{sen-mv}$ ). With all this information the distance between the vortex generator and the measurement volume ( $Z_{vg-mv}$ ) can be found using Equation 3.1.

$$Z_{vg-mv} = Z_{sen-mv} - (Z_{vg-bm} + (T_{input}/M_{tria}) * V_{belt}) \quad (3.1)$$

Figure 3.21 is a conceptual drawing of the signal from the photodiode, the processed signal from the photodiode processor and the triangular signal from the triangular pulse processor.

### 3.4.2 DAQ Hardware

The DAQ hardware/software used in the cascade tunnel is completely different to the DAQ hardware/software used in the auxiliary tunnel. With the addition of synchronizing two additional analog signals with the coincident LDA signals, the old system was of no use. Incorporating the signals into the LDA data required modification to a data acquisition system originally designed by Kevin Shinpaugh (hardware) and Christopher Chesnakas (software). Their systems was set-up to synchronize one analog signal with each LDA signal output by the processors.

Since time variation is such an important consideration in LDA experiments, as well as moving end-wall experiments, much care was taken to synchronize the three LDA signals with the two analog signals. A full description of the Shinpaugh's and Chesnakas's DAQ set-up is found in Chesnakas (1995). A second A/D board and copies of the analog cable wiring were made as well as a two-input terminal box.



The computer used to collect the data and run the DAQ software is a 166MHz IBM 350 P90 (6586-47H) with a 8 GB hard drive (4 partitions) and 64 MB of RAM. DOS 6.2 operating system is installed on the computer. The computer uses a Iomega 100 zip drive to transport the raw data to the processing computer.

### 3.4.3 DAQ Software

Minor modifications were done to Chesnakas's software. Basically the code was duplicated from a one analog signal input to a two signal input. The code was changed from a 4 digital signal output to a 5 digital signal output.

However, there was one major modification required of the DAQ software. The DAQ data rate was more than 3 times slower (and sometimes much worse than that) than the Macrodyne data rate out. The code was re-calculating coincidence between the three LDA signals in an "If" statement while it was taking the data. The Macrodynes were already set in coincidence mode and therefore there was no need to repeat the process. Precious acquisition time was being lost to this redundant task. Once the "If" comparison was modified, the DAQ data rate shot up to around 80% of the Macrodyne data rate or about 700 samples/second at peak data rate (900 samples/second). This is an acceptable and reasonable rate. It is to be expected that some data will be lost due to processing time adding on the additional two analog signals. Minor modifications to the code included adding beam angle distances to the output file as well as other starting parameters specific to the cascade tunnel.

## 3.5 Data Post-Processing

### 3.5.1 Hardware

The computer used to post-process the data is a PII 300 MHz computer with a 9.1 GB hard drive (3 partitions) and 64 MB of RAM. The computer runs off of Windows NT 4.0 with service pack 6a. Along with an Iomega 100 zip drive the computer also has a Writable CD-ROM (8x4x32) to burn the raw and processed data to compact disks. The computer has all SCSI components to increase file transfer speed between large storage devices. The computer is hooked up to the Network for file sharing capabilities.

### 3.5.2 Software

The data are split into three different categories for post-processing: stationary end-wall data, moving end-wall data and moving end-wall with vortex generators data. With the stationary end-wall the Mylar belt is not used and therefore the two extra analog signals are not used. With the moving end-wall data the analog signals are used only to remove the belt joint data. The moving end-wall with vortex generators data uses both analog signals, one to remove the belt joint data and the other to sort the data into bins corresponding to vortex generator position relative to the measurement volume.

#### Stationary End-Wall Data Post-Processing

The stationary end-wall data processing is nearly identical to the processing described in Section 2.3. Specifically the same noise removal scheme was used on the data. The post-processing code was basically modified in two ways. The data file input was modified to accept the new DAQ format. The data file output was changed for an analog output to a digital output. The output of the initial post-processing procedures was the time averaged mean velocities, Reynolds and Shear Stresses and Triple products.

#### Moving End-Wall Data Post-Processing

With each new belt put on the bed and before taking each profile of moving end-wall LDV data, a pre-run file is recorded by the computer. The pre-run file is a 16,000 samples, 30 kHz, data file recording the output from the two analog signals. This pre-run file is used as a benchmark for the operation of the belt. The pre-run file data are not simultaneous data, the two analog signals are taken sequentially.

When a new belt is put on the bed, and after it has been ramped up to full speed (discussed in Section 3.2.6) two pre-run tests are done with the moving end-wall to check the belt. The first pre-run test is with the BELT-HITE position and vortex generator pulse analog inputs hooked into the computer. The belt is run up to full speed and a pre-run file is collected; then the belt is then stopped. The second pre-run test the vortex generator pulse and vortex generator triangular pulse analog inputs are hooked into the computer. The belt is run up to full speed, a second pre-run file is collected, and a profile of the LDA data is then collected.

The first pre-run test checks the longitudinal displacement and speed of the belt. By looking at the displacement signal of the belt, problems such as air-bubbles under the belt can be detected.

The velocity of the belt can also be checked for possible excessive slipping on the rollers. The second pre-run test calibrates the velocity of the belt which is used in the processing of the data. This velocity is cross-checked with the velocity measured with the LDA in the moving end-wall. The second pre-run test also calibrates the upper voltage of the signal when the Mylar joint mark is passing over the sensor.

The first step in processing the moving end-wall LDA data is the removal of the data taken when the belt joint was near the measurement volume. The second pre-run determines the maximum voltage of the vortex generator pulse at the passage of the belt joint. This signal is used to remove the LDA data when the belt joint passes. As is stated above, with each coincident LDA signal there are two analog signals; when the vortex generator pulse signal is below the calibration voltage the data point is removed from the set. The vortex generator pulse voltages have a tendency to drift from day to day making the re-calibration necessary. The vortex generator pulse normally dips below around 6 Volts when the belt joint mark is covering up the photodiode. Since the black mark takes up approximately 8% of the belt, this is approximately the amount of data which should be removed from the data set. Once the belt joint data are removed from the data set the post-processing is the same as for the stationary end-wall data.

### Moving End-Wall with Vortex Generators Data Post-Processing

Just like the moving end-wall data, before a profile is taken with the moving end-wall and vortex generators, two pre-run files are taken. The pre-run files have exactly the same input as for the moving end-wall data. The only difference is that the second pre-run file is also used to check the quality of the triangular pulses.

The quality of the triangular pulses is assessed by how well the signal returns to zero when each v.g. marker blocks the photodiode. If the system is not set correctly the triangular pulse may only drop half the distance from the peak; for example in Figure 3.20 the triangles would drop only to 2 Volts before ramping. Because of the drift of the vortex generator pulse mean and maximum voltages, the triangular pulse can become distorted when those voltages fall outside a predetermined range set in the processor. Adjustments to the mean voltage knob of the vortex generator pulse processor can reset the mean and maximum voltages in to the prescribed range. The triangular pulses are continuously monitored on an oscilloscope by the belt driver to make sure no gross changes in the signal occur.

Again the belt joint data are removed from the data set using the calibrated vortex generator

pulse signal. The same procedure as described in Section 3.5.2 is used.

Equation 3.1 is used with the triangular pulse data and the information is taken from the second pre-run file to determine the relative position between the vortex generators and the measurement volume. For each data point that this is calculated, the data are then sorted into bins based on this position. The number of bins can be adjusted and 32, 64 and 128 were used. The data are then output to a file for each of the bins.

The noise removal scheme described in the auxiliary tunnel and used with the stationary and moving end-wall data are not used with the moving end-wall vortex generator data. The reason for this is that there is just too little data to fit the curves properly. Therefore the velocities are directly calculated from the files without removal of any extraneous noise which might be included in them. Another reason not to remove the noise is that with 128 files and no way to automate the process this becomes an unbelievably tedious task.

## 3.6 Issues with the Cascade Tunnel

### 3.6.1 Issues with the LDA System

Many issues were dealt with involving each of the major parts of the LDA system; the laser, the fibers, the LDA head, the photo-multiplier (PM tubes) and the Macrodyne Processors.

Initially a single 2.5 Watt argon-ion laser, taken from the auxiliary tunnel, formed the 5 LDA beams (see Section 2.2.6). After 3 months of work it was determined that the 2.5 Watt laser was not powerful enough to be used in the cascade tunnel. A new Coherent 5 Watt laser is now used in the tunnel.

In the process of moving the LDA head from the auxiliary tunnel to the cascade tunnel the beams became misaligned. Because the beam traverses on the LDA head would not allow for enough travel to cross the beam properly, metal shims were used to force the beams into alignment. These shims relax over time and are very sensitive to movement. It took several months to realign the beams on the LDA head with new shims. Once the beams were aligned the processors showed a very good 900 samples/second coincident signal through the optical glass. The head is now being redesigned and rebuilt with enough travel on the traverses.

The polarization of the beams rotated when the tunnel was running. The vibrations in the cascade tunnel are much higher than those in the auxiliary tunnel. The LDA head rested on the floor in the auxiliary tunnel whereas in the cascade tunnel the LDA head rests on a table

connected to the tunnel itself. The vibrations of the tunnel stressed the fibers enough to cause the polarization to rotate. The beams had to be properly launched into the fibers (in order to optimize their polarization preserving capabilities) and the rotation stopped. The beams must be launched into the fibers with a  $3^\circ$  accuracy to work properly. When the beams are not launched properly they become even more sensitive to vibrations and stresses.

Before the laser power problem was solved two new PM tubes were purchased to amplify the LDA signal. Each of the PM tubes is specially tuned for a specific wavelength. One is specially tuned at green (514.5 nm) and the other blue (488 nm). The new PM tubes also have reduced the noise. The new tubes improved the data rate at the Macrodynes.

Several months of setup time were taken trouble shooting problems with newly purchased Macrodynes. The Macrodynes are now in complete working order. The traverse used in the auxiliary tunnel was used in the cascade tunnel because of problems with the computer controlled traverse.

### 3.6.2 Issues with the DAQ System

The chips on the digital I/O boards had a tendency to burn out. This occurred when the computers were being moved around and the boards were being taken in and out of the slots quite frequently. As long as the boards are not moved around and the cables are not pulled in and out this problem will not occur.

### 3.6.3 Issues with the Mylar Belts and Teflon Bed

Several issues were found with the Mylar. The issues break down into four parts; optical issues, friction issues, melting issues and control issues.

When the Mylar was stationary no data could be taken below  $100\ \mu\text{m}$  due to the scatter of the beams on the Mylar. When the belt is moving the value rises to  $500\ \mu\text{m}$ . Because of this phenomenon it was impossible to collect viscous sublayer data with a moving end-wall.

When the Mylar is run at full speed, the friction between the Mylar and the Teflon increases to the point that particles of Teflon are "sanded" off. The quantity of particles is enough to coat the BELT-HITE sensor as discussed in Section 3.6.2. These particles also smear across the optical glass and block the beams. The particles also coat the optically clear portion of the Mylar belt. Every 30 minutes the belt must be stopped to remove the excessive amounts of

Teflon particles from the optical glass and the Mylar optical region. The continuous starting and stopping made it difficult to acquire a complete profile in one run of the belt. At lower speeds the wear of the Teflon is much less.

Another result from the friction between the Mylar and the Teflon is that the BELT-HITE position sensor is quickly covered with Teflon particles when the belt is running at full speed. By cleaning off the bed and belt thoroughly, as well as the sensor itself, the BELT-HITE sensor will stay operational for approximately 10 minutes (enough time to take the pre-run file for each new belt). Because the standard deviation of the belt vertical displacement ( $6.58 \mu\text{m}$ ) is so small while running and the optical qualities of the belt prevented extremely near wall measurements it was never required to take the real time belt vertical displacements simultaneously with the LDA data signal.

The increased friction between the Mylar and the Teflon at full speed cause melting of the belt and increases the susceptibility to scratching of the belt. As discussed in Section 3.2.6 even small bumps on the floor can cause the Mylar to melt. Operating closely to the melting temperature the Mylar scratches much more easily. For this reason the optically clear region of the belt reduces to approximately 0.25 inches. At lower speeds the size of the optically clear region is much wider.

The increase to the friction between the Mylar and the Teflon cause the belt to be much more unstable at full speed. There are two types of belt control adjustments, fine and gross. With the fine adjustments the socket wrenches are only rotated approximately  $1/4$  of a turn. With the gross adjustments the wrenches maybe rotated as much as three times around as fast as the belt controller can spin them. The control area is the axial distance the belt can be controlled within. At full speeds the fine adjustment control area increases to over  $\pm 0.25$  inches (see Section 3.2.7). Also at full speeds the occasional jumps of the belt become more violent and more frequent, requiring gross adjustment control. These jumps greatly increases the wear on the belt and further decrease the optically clear area making the fine adjustments even harder. At lower speeds the fine adjustment control is much tighter and the gross adjustment control more infrequent.

All of these control problems stack up to reduce a 400 samples/second peak data rate to less than 100 samples/second with the moving end-wall. At this data rate, and 16 points in a profile, it would take 8 hours to take a profile of vortex generator moving end-wall data. This would be true if the belt wouldn't have to be stopped every 30 minutes for a complete cleaning, which takes roughly 30 minutes to do. Thus, to take one profile of vortex generator moving end-wall data would take 16 hours to complete; however the belts have never lasted over 5

hours. Therefore, only two points of moving end-wall data with vortex generators were taken and only one profile of moving end-wall (30,000 samples) was taken.

## 3.7 Corrections for the Unresolved Issues

The cascade tunnel system as described above was adequate to collect the data reported in Chapter 4. This does not mean the system cannot, or should not, be improved. As discussed in Section 3.6 there are still some issues which have not been resolved.

The issues with the LDA System for the most part were all addressed and in the end the system was working great. Data rates of over 900 samples/sec clearly show a good working LDA system for the stationary end-wall. For the moving end-wall data rates of over 400 samples/sec were seen. This was higher than any data rate obtained in the auxiliary tunnel. As is stated in Section 3.6, however, the LDA head beam traverse system needs to be improved. With extended traverse range it should be relatively simple to realign the beams. This modification will make the whole system more stable for transport.

The issues with the DAQ System for the most part have been corrected; however, there are still improvements that can be made. It would be of great value to design a system which would allow the BELT-HITE sensor to be used while taking moving end-wall data. This issue is obviously related to issues of the Teflon bed and Mylar. However, no solution will completely stop the Teflon from flaking, and there will always be some particles which will coat the sensor. Possibly some sort of simple system to automatically clean the sensor may be designed. Such systems could focus on removing the Teflon particles from the moving belt. Possibly by introducing a suction or brush system just ahead of the sensor, in the belt direction, to clean off the belt could resolve the issue. There is already a hole in which to place such a device.

Several issues with the DAQ system need consideration before large amounts of data are taken. The first involves the triangular pulse processor. The processor appears to be working; however, it is not completely consistent with changing voltages out of the vortex generator pulse processor. This should be able to be corrected with some minor adjustment to the circuitry. The length of the belt joint mark should to be investigated to optimize the length so that the smallest amount of data is discarded. The width of the vortex generator marks possibly could be made narrower, also reducing the amount of lost data and decreasing the uncertainties in the vortex generator data.

Clearly most of the unresolved issues are with the Mylar belt and Teflon bed. These issues must

be addressed before a large data set of moving end-wall vortex generator data can be taken. There are two sets of solutions presented here; the first set are relatively inexpensive, partially addressing one local problem, the second are costly, and address the global issues. The first set of inexpensive solutions address three issues; 1) particles, 2) melting and 3) signal filtering. The second set of costly solutions fall into three categories; 1) changing the materials, 2) changing the set-up or 3) changing the flow.

The first inexpensive solution addresses the Teflon particles on the Mylar belt which get onto the optical glass and block the beams. By designing a vacuum or brush type system just ahead of the optical glass, in the direction of the belt movement, possibly enough particles could be removed to keep the optical glass clear a little bit longer.

The second inexpensive solution addresses the Mylar melting. By designing some sort of cooling system the Mylar may be able to be kept from melting a little bit longer. The cooling system could either consist of air blowing over the belt or possibly cooling the bed itself. However, one reason air may not be too effective is because of the localized nature of the melting seen on the belt. Because of the very low thermal conductivity of Teflon, a bed cooling system may be very hard to implement.

The third inexpensive solution addresses the optical quality of the Mylar belt. A notch filtering system could be designed in the signal conditioning system which effectively only removes the frequencies associated with the moving belt. Once this information is filtered out, what is left should be the flow information. A careful study of the belt signal needs to be made to guarantee that only the moving belt data are being removed. This solution seems somewhat plausible because a small secondary peak is seen in some of the histograms near the wall with the moving belt.

The first costly solution involves changing the materials. There are two materials which could be changed the Mylar and/or the Teflon. One solution is to find a better belt material than Mylar. The new material must be as strong as Mylar, have a higher melting temperature, have better optical qualities, have a harder surface finish and be as light weight as Mylar. If the new material is not as light as Mylar the current roller system may need to be redesigned. Another option is to replace the Teflon. The new material must not flake when worn by the belt. The material must lay flat to the floor and should have a melting point at least as high as the Mylar. Due to the amount of research which has already been conducted to investigate these materials, an easy and inexpensive solution is not likely. The second solution is to find a better bed material. Teflon flakes easily but has a low coefficient of friction. From information from the manufacturing facilities there is a possibility that a chromed steel floor may work. The



steel is easier to cool and won't flake like the Teflon. Tests with Mylar mounted on a sander need to be performed first to test system.

Modifying the set-up could certainly reduce wear and possibly make the current system usable. Improving the control system of the belt certainly would also reduce wear and possibly make the current system usable. By reducing the axial movement of the belt, the risk of melting and scratching the Mylar is reduced as well as the wearing of Teflon. Holding the belt within the 0.25 inch axial window will certainly allow for much more data to be acquired in a shorter period of time. This increase in control could possibly be achieved with extra control rollers, a tension monitoring device or possibly an active electronic control mechanism. By adding extra control rollers to the system, the degree of control will certainly increase. Certainly by regulating the tension in the belt, especially under the tunnel in the return section, could help the control of the belt. The belt fluctuates by over an inch underneath the tunnel. By controlling this movement and possibly regulating this tension, the belt life would certainly increase and possibly increase the overall control as well. Finally adding on a computerized controller may also be able to increase control of the belt. However, this would also require redesigning the entire belt controller system. Also with a computerized controller a major issue is the gross movements at top speed when the belt dangerously slides quickly to one side. There may be simpler and more practical solutions that could be discovered upon further investigation.

Changing the belt speed may possibly be the quickest and easiest solution. The idea is to run the belt at a slower speed, which would require little change to the current system. It will however require a complete re-calibration of the tunnel. The tunnel speed would need to be reduced proportionally with the belt speed. This obviously changes the flow in the tunnel and possibly make comparisons with the old/current data impossible. Also, re-calibration is quite time consuming. As is stated above in Section 3.6 slowing down the belt will decrease the wear on the Teflon, stop the melting of the Mylar and increase the control of the belt. It is proposed that the new speed be around 16 m/s to have all these advantages.

## 3.8 Conclusions

The low-speed linear compressor cascade wind tunnel at Virginia Tech was modified to allow for LDA measurements upstream of the blades and in the tip gap of blade 5. Three basic areas were modified; 1) the tunnel itself, 2) the data acquisition system and 3) the post-processing programs.

Data rates of over 900 samples/sec show a good working LDA system for the stationary end-wall

data. An adequate moving end-wall data rate of over 400 samples/sec was setup. Modifications to the LDA head beam traverse system would allow for more stable and easier alignment of the beams.

Throughout the work many problems were encountered, some of which remain to be addressed. A new design needs to be developed which will allow the BELT-HITE sensor to be used while taking moving end-wall data. The triangular pulse processor is working well enough for small sets of data. However the processor should be made less sensitive to changing voltages out of the vortex generator pulse processor. One or all of the three following suggestions needs to be followed to increase the data rate with a moving end-wall to an adequate level. First, a better belt material may be found to replace the Mylar belt. Second, the control system may be made more accurate for running the belt. Finally, the belt speed may be slowed down to decrease wear on the belt and increase control.

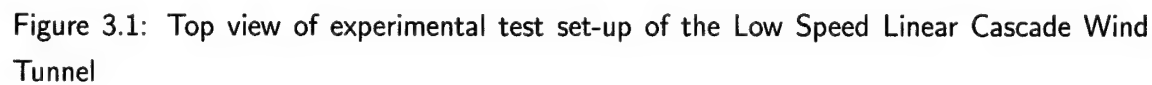
The tunnel system and test apparatus were all extensively modified to collect the data set presented in Chapter 4.

## References

- Brown, J.L. 1989 "Geometric bias and time coincidence in 3-dimensional laser Doppler velocimeter system," Experiments in Fluids Vol. 7, pp. 25-32.
- Chesnakas, C.J. 1995 "The Miniature, 3-D, Fiber-Optic, Laser Doppler Velocimeter," Aerospace and Ocean Engineering Department, Virginia Polytechnic Institute and State University Report, November.
- Echols, W.H., and Young, J.A. 1963 Studies of portable air-operated aerosol generator, *NRL Report*, 5929.
- Ma, R., Saha, N., Devenport, W.J., and Wang, Y. 2000 "Unsteady Behavior of a Tip Leakage Vortex Produced by Simulated Stator/Rotor interaction," AIAA paper 2000-2217, Fluids 2000, Denver, CO, June 19-20.
- Macrodyne 1992 "Laser Doppler Velocimetry (LDV) Electronics Frequency Domain Processor Model 3100 Users Manual," Rev. 060192A, Macrodyne Inc., 4 Chelsea Place, PO box 376, Clifton Park, NY 12065.
- Madden, M.M., and Simpson, R.L. 1997 "Octant Analysis of the Reynolds Stresses in the

*Three-Dimensional Turbulent Boundary Layer of a Prolate Spheroid,"* Report Number VPI-AOE-252, Aerospace and Ocean Engineering Dept, VPI&SU.

Wang, Y., Muthanna, C., and Devenport, W. J. 1999 *"The Design and Operation of a Moving End-Wall System for a Compressor Cascade Wind Tunnel,"* AIAA paper 99-0741, 37th Aerospace Sciences Meeting and Exhibit, Reno, NV, January 11-14.



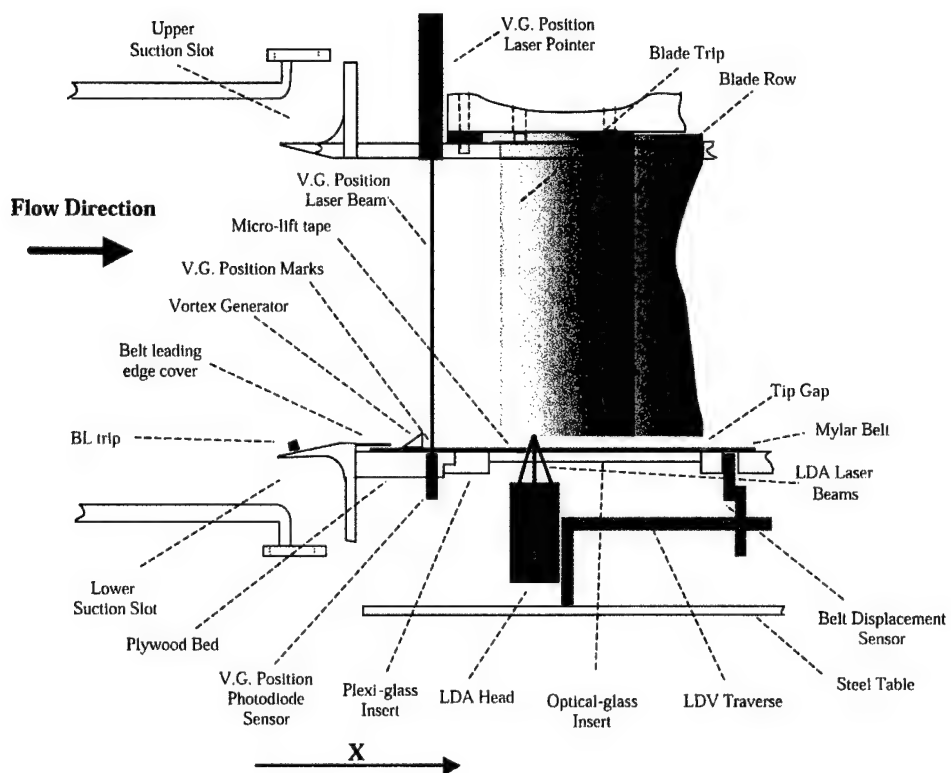


Figure 3.2: Side view of experimental test set-up of the Low Speed Linear Cascade Wind Tunnel



Figure 3.3: Environmental containment tent encasing the tunnel as seen from inside looking at the upstream test section tunnel contraction and plenum

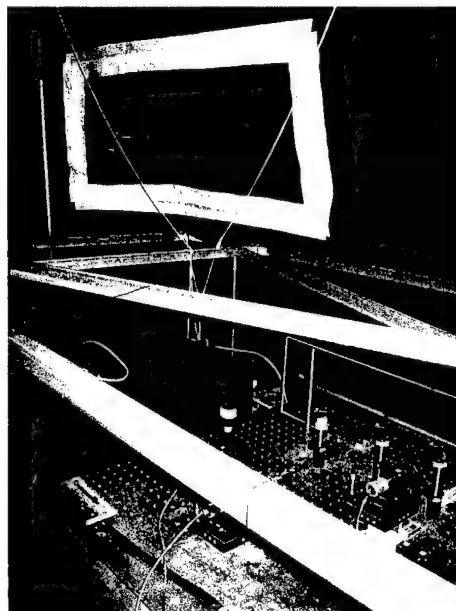


Figure 3.4: Window in tent used to view test section from the optical table



Figure 3.5: Aerosol generator with impactor can under contraction of cascade tunnel

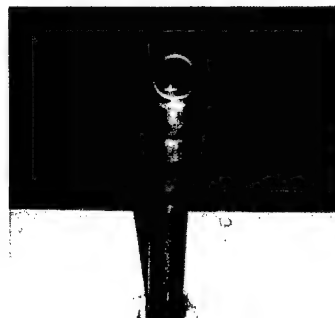


Figure 3.6: Seeding pipe in contraction with plenum screens in background

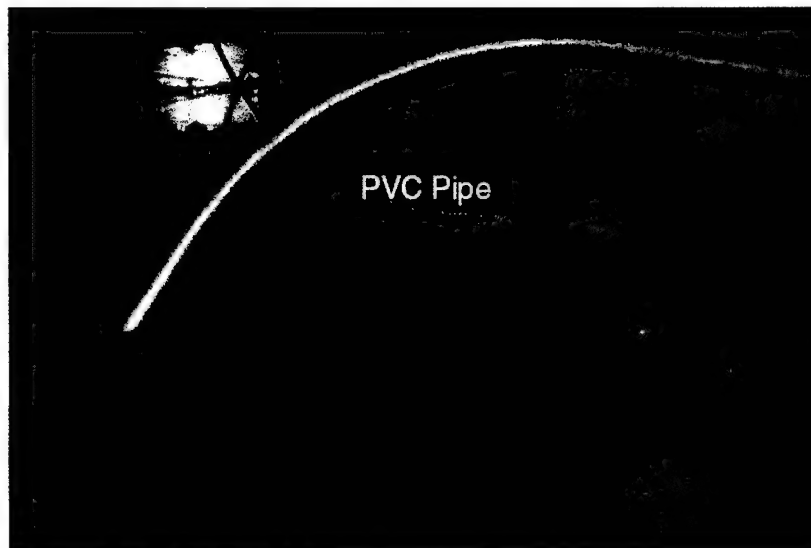


Figure 3.7: Upstream end of bed with 12" PVC pipe attached

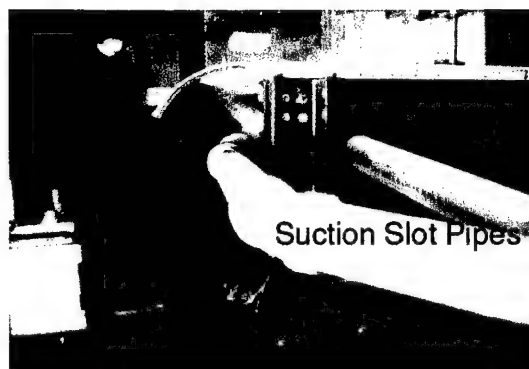


Figure 3.8: Suction slot pipes



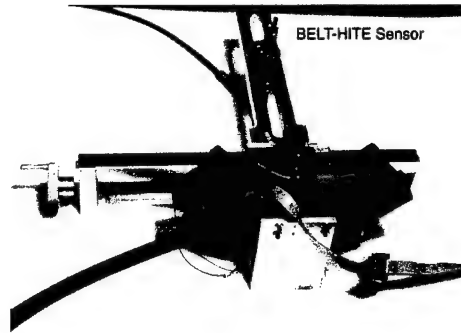


Figure 3.9: LDV head and traverse along with BELT-HITE belt vertical position measurement probe

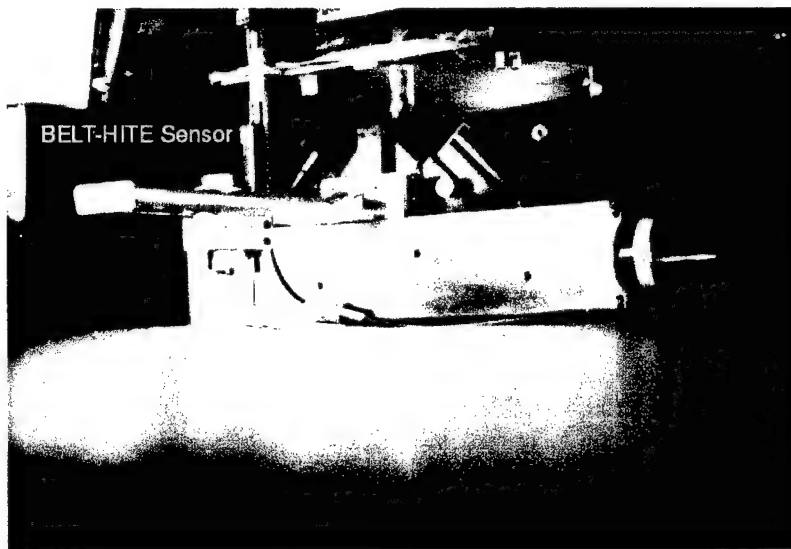


Figure 3.10: LDV head mounted to traverse in the tunnel with the BELT-HITE vertical position sensor

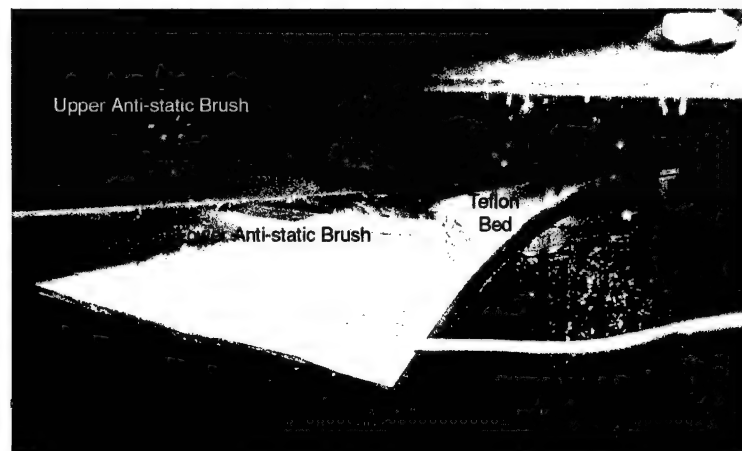


Figure 3.11: Anti-static brushes mounted next to Mylar sheet



Figure 3.12: Vortex generator marks are shown in black in picture

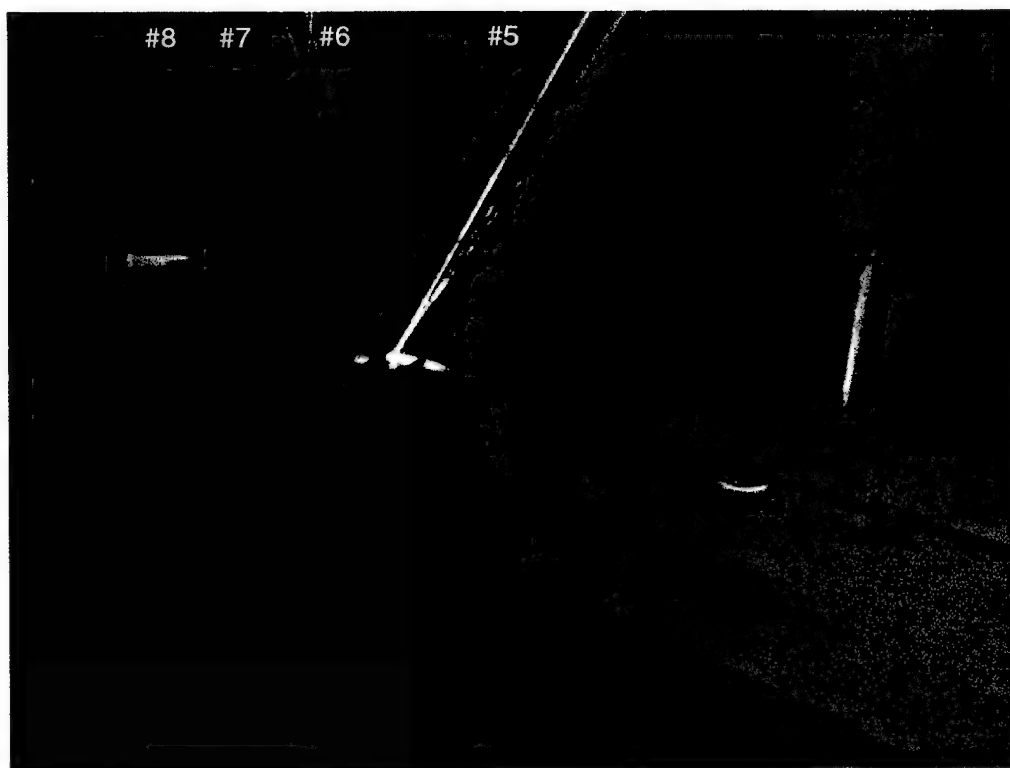


Figure 3.13: The working tunnel with beams as 1F profile position (Vortex generator sensor is just beneath the red dot in the picture)

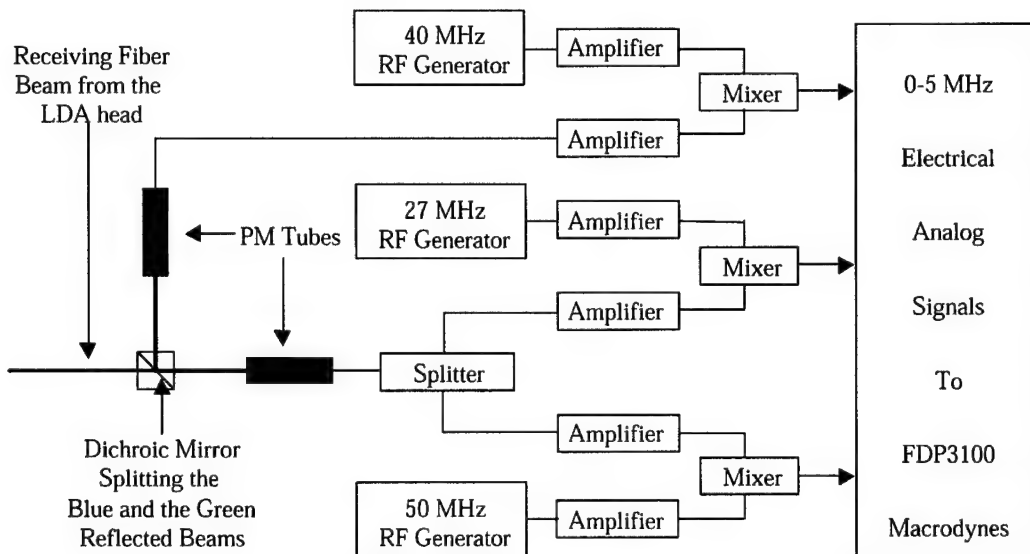


Figure 3.14: Schematic of LDA signal conditioning for auxiliary and cascade tunnels

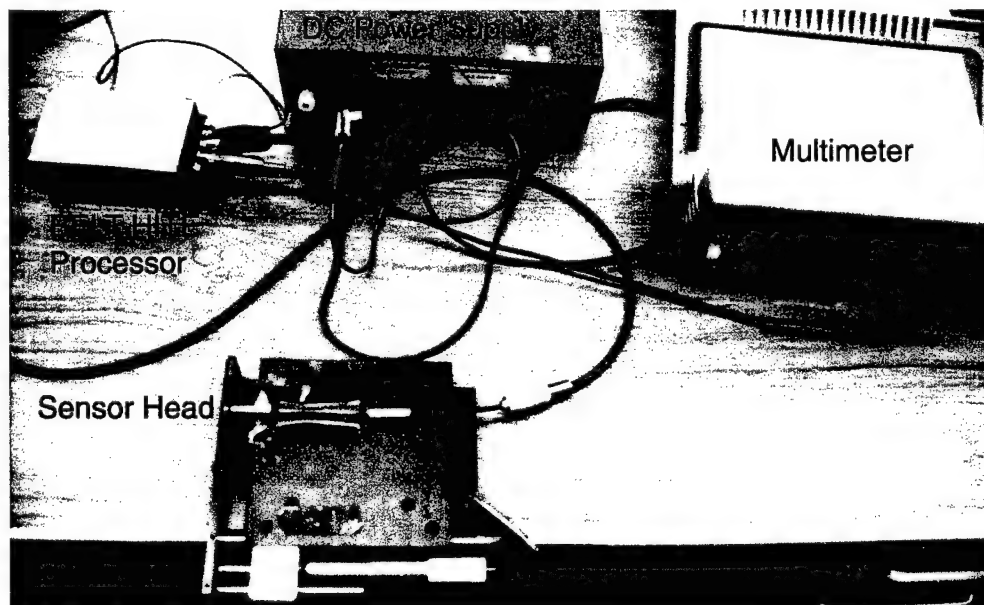


Figure 3.15: Calibration set-up of BELT HITE sensor

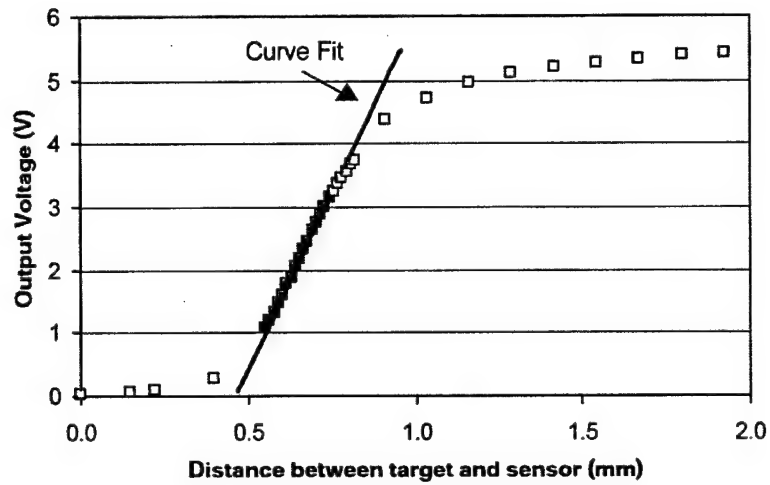


Figure 3.16: Calibration curve for BELT HITE sensor

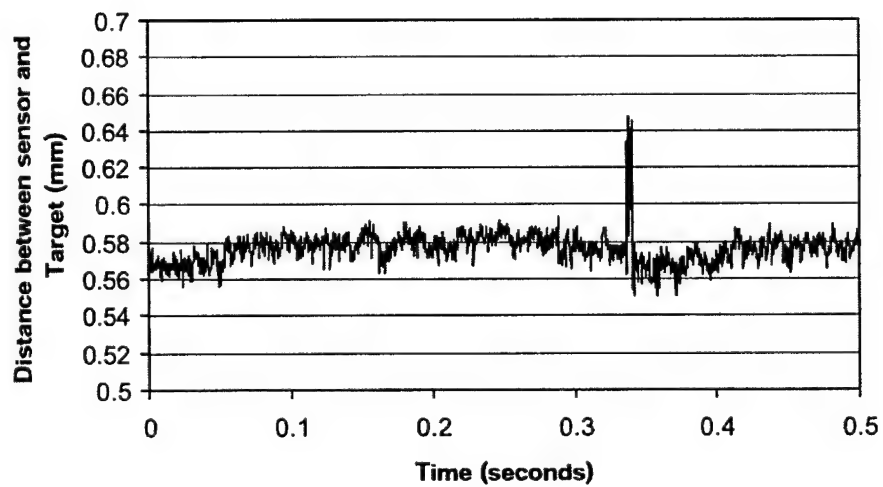


Figure 3.17: Typical plot of output from BELT HITE sensor with belt running at full speed

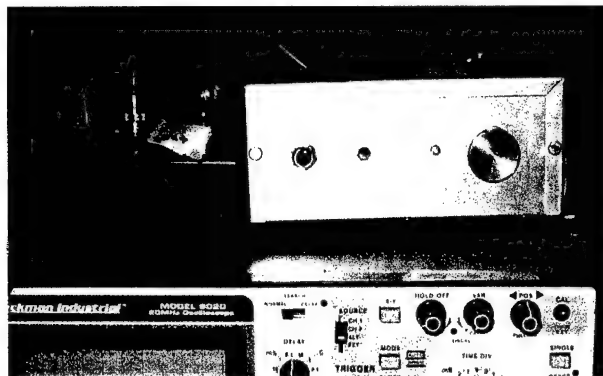


Figure 3.18: Vortex generator processing equipment (photodiode processor is on the right; triangular pulse processor is on the left)

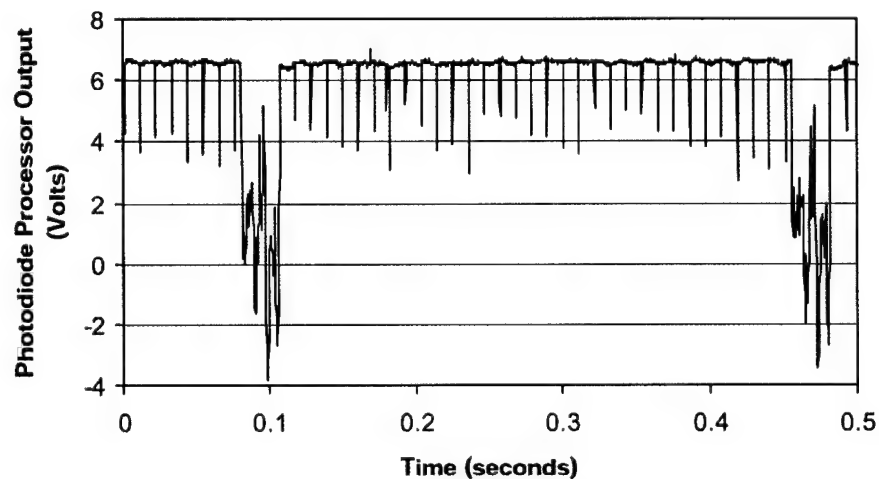


Figure 3.19: Typical plot of output from photodiode sensor processor with belt running at full speed. (Small Pulses are vortex generator position marks; large pulses Mylar belt joint mark)

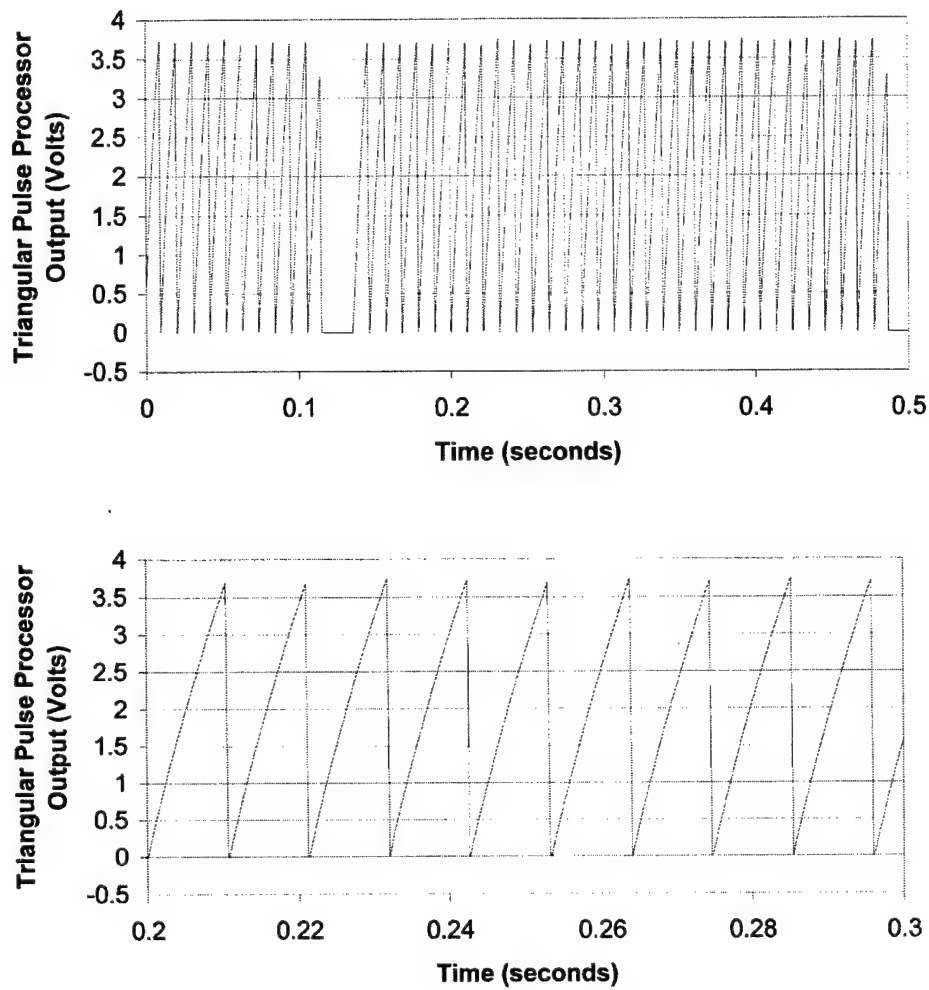


Figure 3.20: Typical plot of output from triangular pulse processor with belt running at full speed

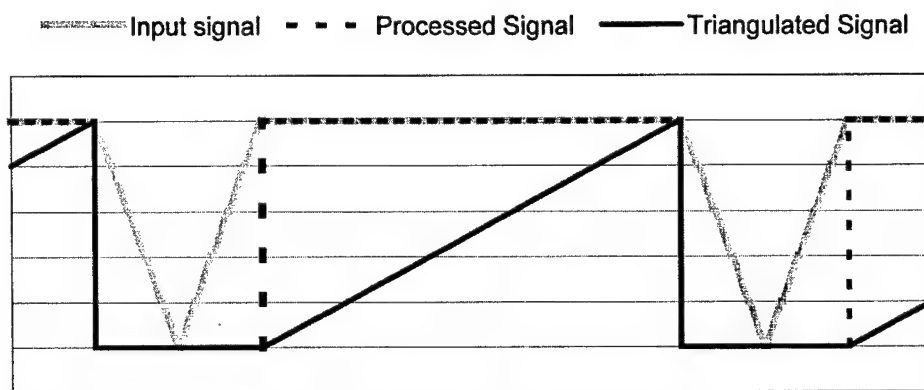


Figure 3.21: Vortex Generator Processing Conceptual drawing



## Chapter 4

# Cascade Tunnel Results and Discussion

This chapter describes the investigation of the flow in the low-speed linear compressor cascade wind tunnel (cascade tunnel) at Virginia Tech. The purpose of this investigation is to study complex flow behavior through the tip gap of a compressor cascade. The tip gap is the region between the floor of the tunnel and the lower surface of the compressor blades.

The tip gap flow creates losses of efficiency in turbo-machinery. It has been estimated that the entire end-wall flow consists of  $1/3$  to  $1/2$  of the total aerodynamic losses in turbo-machinery (Murthy, 1985). The loss in efficiency comes from four sources. First, energy is lost from the tip leakage vortex interacting destructively with other "working" vortices in the flow. Second, work is lost in the energy of pushing fluid from one side of the blade to the other. Third, the fluid worked in one passage is lost when it migrates to the next blade passage. Fourth, in the blade tip passage there is no blade fluid interaction to transfer work to the fluid.

For the previous reasons understanding the tip gap flow is important to increasing the efficiency in turbo-machinery. The first part of this chapter attempts to provide a description of the flow through the first quarter chord of the tip gap region of flow. It has been found in this facility, and others like it, that the tip leakage vortex originates around the quarter chord (Muthanna, 1998). Therefore; to understand this phenomenon the flow which leads up to this point is studied. These studies are all done without the moving end-wall apparatus.

A data set taken with a hot-wire probe in the wake of the blades with the moving end-wall and with vortex generators was done by Ma et al. (2000). To fully understand the flow passing out

of the blades the flow going into the blades should be known. One complete profile with the moving end-wall is taken upstream of the blades. Several points, at the same location, with the moving end-wall and the vortex generators upstream of the blades were taken. For the reasons discussed in Section 3.6.3 and time constraints, the investigation was halted at this point.

## 4.1 Introduction

The previous chapter described the low speed linear compressor cascade wind tunnel equipment and apparatus. The tunnel is an open-ended wind tunnel and contains 8, 10 inch chord, low aspect ratio, compressor blades. There is a tip gap between the floor and the blades of 3.3% chord. The compressor blade row is at an angle of  $24.9^\circ$  to the freestream. The blades sit at an angle of attack of  $8^\circ$  to the freestream. The blade spacing is 23.6 cm. The flow angle just downstream of the compressor blades is  $11.8^\circ$  to the freestream. See Figure 4.1 for a schematic of the set-up.

The tunnel has three operating configurations: stationary end-wall, moving end-wall and moving end-wall with vortex generators. A suction slot sits 18.8 cm in front of the leading edges of the blades. The suction slot is aligned with the blade row. In the stationary end-wall configuration the upstream free-stream flow is set at approximately 25 m/s. Aligned with the blade row, and under the blades, is a Teflon bed on which a Mylar belt is run. In the moving end-wall configuration, the Mylar belt is run at a speed which approximately removes the tangential component of the freestream, or approximately 23 m/s. Upstream of the blade row 7.8 cm is where the trailing edge of the vortex generators are attached to the Mylar belt. The vortex generators are in pairs and generate two counter-rotating down vortices (see Section 2.1). Each pair is one blade spacing away from the next. When the moving end-wall with vortex generators configuration is run, there are approximately 30 pairs of vortex generators attached to the Mylar belt.

The LDA probe is situated underneath blade 5, looking through a piece of optical glass inserted into the floor. The optical glass is 8 inches in diameter. The maximum traverse in the y direction into the tunnel, is approximately 4.5 cm. The traverses in the x and z direction are limited by the size of the optical glass.

Six x locations are chosen to traverse the head at which comprise the six cross sections labelled in Figure 4.2. Two of the x locations are upstream of the blade row (1 and 2), the other four are in the blade passage and under the blades (3-6). A plot of the points taken in the tunnel relative to the tunnel is also shown in this figure. The profiles found in free-stream areas

are identified by "F." Those profiles found on the pressure side of the blades are identified by "P." Those profiles found on the camberline of the blades are identified by "C." Those profiles found on the suction side of the blades are identified by "S." The profile which is found just upstream of the blade is identified by "B." When identifying profiles, the first character is the cross section number, the second character is the letter representing the position of the profile and, if there is a third character, it is to distinguish between multiple profiles taken at the same point; therefore 1F2 refers to cross section 1, freestream, second profile.

Table 4.1 shows all the profiles taken in the study. The table is broken up into the three configurations of the tunnel: stationary end-wall, moving end-wall and moving end-wall with vortex generators.

This chapter details the sets of data collected in the cascade tunnel. One profile of data was collected at position 6C. A turbulence grid was inserted into the flow upstream of the test section. The results from the test are not discussed in this chapter, they are discussed in Appendix E.

## 4.2 Stationary End-Wall

### 4.2.1 Flow and Data Quality

Before the tests can begin on the flow, the flow and data quality must be assessed. The flow quality is assessed through a calibration of the tunnel. The data quality is assessed by looking at the viability of the different postprocessing techniques and then plotting the data against a comparable flow such as 2-dimensional DNS results or overlapping hot-wire data. There are three post-processing techniques studied; 1) the bias and broadening effects to the flow, 2) the appropriate technique for finding  $U_\tau$  and 3) the determination of the coordinate transformations. The coordinate transformation rotates the measurement volume coordinate system to the tunnel coordinate system.

#### Tunnel Calibration

With all of the changes to the cascade tunnel there was quite a bit of concern about the flow through the tunnel. Since this study is a collaboration with Ma et al. (2000), it is important to match their conditions. Figure 4.3 shows the comparison between the current cascade tunnel calibration and that done by Ma et al. (2000). Upstream refers to the upstream cross section which is taken approximately 17 cm upstream of the leading edge of the blades. Downstream

Table 4.1: Cascade Tunnel Test Matrix

Stationary End-Wall					
<i>Profile</i>	<i>X (cm)</i>	<i>Z (cm)</i>	<i>Profile</i>	<i>X (cm)</i>	<i>Z (cm)</i>
1F1	-4.87	-12.46	4F	1.19	-8.09
1F2	-4.91	-12.51	5S	1.87	-17.13
2B	-0.21	-11.29	5C	1.94	-16.70
3S	0.73	-14.14	5P	1.86	-15.48
3C	0.69	-13.60	5F	1.74	-7.89
3P	0.68	-13.12	6S	2.71	-18.73
3F	0.64	-7.99	6C1	2.74	-17.97
4S	1.27	-15.41	6C2*	2.68	-17.92
4C	1.23	-14.98	6P	2.66	-16.91
4P	1.28	-14.34	6F	2.46	-8.35
* Profile taken with turbulence grid					
Moving End-Wall					
<i>Profile</i>	<i>X (cm)</i>	<i>Z (cm)</i>	<i>Profile</i>	<i>X (cm)</i>	<i>Z (cm)</i>
1F1	-4.86	-12.46	1F4	-4.91	-12.51
1F2	-4.86	-12.46	1F5	-4.91	-12.51
1F3	-4.91	-12.51			
moving end-wall with Vortex Generator					
<i>Profile</i>	<i>X (cm)</i>	<i>Z (cm)</i>	<i>Profile</i>	<i>X (cm)</i>	<i>Z (cm)</i>
1F1	-4.91	-12.51	1F2	-4.91	-12.51

refers to the downstream cross section which is taken approximately 27 cm downstream of trailing edge of blades. The free-stream velocity,  $U_e$ , is measured approximately 60 cm upstream of the leading edge of the blades at passage mid height and a quarter of the way across the tunnel cross section.

There is some deviation between the data of Ma and the present data shown in Figure 4.3; however, the area between blades 4 and 5,  $Z = 0$ , in the upstream cross section the match is quite good. The downstream cross section matches quite well with Ma's data. The calculated theoretical value for the downstream, using conservation of mass and simple flow turning, is 0.7242. This theoretical value is slightly low, but within the acceptable range (0.6906 to 0.7242) for this flow.

Another check of the tunnel flow is the blade loading. This was matched with Ma et al. (2000) as well. The loading is shown in Figure 4.4, this loading is matched with loadings found on similar rotor blades found in compressors.

### Bias and Broadening effects

Whenever LDA is used in a new flow, some study of the bias and broadening effects must be done. This is discussed in Section 2.3.

The first check is the velocity bias. The velocity bias check was the same as the one detailed in Section 2.3. Again the correlation coefficient, between velocity magnitude fluctuation and data rate fluctuation, was found to be less than 0.02, well within the acceptable range.

The second check is the comparison with DNS. Figure 4.5 shows the comparison between profiles 1F1, 1F2 and the DNS results of Spalart (Spalart, 1988) over a flat plate at three different  $Re_\theta$ 's. As is seen in Figure 2.9 the differences between the DNS and the experimental data, mostly seen in  $-\overline{uv}^+$  plot, is mostly due to unrelaxed flow structure. There is also some effect caused by the differences in  $Re_\theta$ . Both of these effects raise the peak values in all of the Reynolds stress terms. The trip data in the auxiliary tunnel also had a high  $-\overline{uv}^+$  profile similar to what was found in the cascade tunnel.

The unrelaxed flow structure is most probably due to upstream steps. In the auxiliary tunnel there were two step sources, optical glass tunnel floor interface and the square trip. The optical glass interfaces was very smooth with the tunnel floor in the auxiliary tunnel and basically had no effect. The trip effects are discussed Section 2.2.3 as well as in Appendix A. In the cascade tunnel there are three sources for upstream steps; the trip, the belt leading edge cover and the optical glass floor interface. The trip is a 2.4 mm square trip setting 13.3 cm upstream of

the 1F measurement volume. Measuring this in the upstream flow direction, the trip is 28.65 cm from the 1F measurement volume. The overlap Mylar edge is just 6.3 cm upstream of the 1F measurement volume, or 13.57 cm in the flow direction. The belt leading edge cover is taped down for these measurements but it has a thickness of 10 mils. Finally there is the edge of the optical glass that is 6.6 cm upstream of the 1F measurement volume, measured in the flow direction. The step at the optical glass was minimized, levelling it to the flow as best as possible, however the floor is not perfectly flat and it has a tendency to warp over time making the step change. The step was certainly never more than a millimeter high while taking the data.

The differences in  $Re_\theta$  can affect the plots in Figure 4.5. In AGARD (1996) it is stated that there is a dependence between the Reynolds number and the peak values of  $uu^+$ ,  $vv^+$  and  $ww^+$ . The reported peak value of  $uu^+$  ranges from 7.84 at  $Re_\theta = 1,000$  to 10.24 at  $Re_\theta = 10,000$ . Our data shows peak  $uu^+$  of 8.5 to 8.9 at  $Re_\theta = 2000$ . For a linear trend AGARD (1996) data suggests 8.1, so this seems to be slightly high for this trend.

There is one other source which could cause differences between the DNS data and the experimental data and that is uncertainties in  $U_\tau$ . Because of the different methods for calculating  $U_\tau$  it is hard to define an appropriate uncertainty. However, looking at the uncertainty values in Appendix B, it is clear that most of these differences are quite small but may still be significant. Whatever caused the deviations between the DNS and experiment, the effect quickly dissipate as you go downstream as seen from the auxiliary tunnel data (See Section 2.2.3).

### Finding $U_\tau$

The first attempt at calculating  $U_\tau$  was to use a least squares curve fit of the sublayer mean velocity profile data. This is the method referred to in Section 2.3. The mean velocity points below  $y^+ = 10$  are fit to Equation 2.2. The results from the fit were inconclusive in obtaining the  $U_\tau$  or y-shift value. This occurred because there were not enough data points taken in the viscous sublayer to do a proper fit to the equation, less than three points on the average.

The second attempt at calculating  $U_\tau$  involved using the Spalding equation fit to the near-wall data. However, in order to use the Spalding equation the flow must be closely collateral (Madden and Simpson, 1997), or close to the uncertainties of the flow angle,  $1^\circ$  (see Appendix B). Figure 4.6 shows the flow angles ( $FA = \arctan(\frac{\overline{W}}{\overline{U}})$ ) calculated for all of the freestream, "F," stationary end-wall data. Zero flow angle is in the free-stream direction (FA was calculated in the free-stream coordinate system). Positive angles follow the right hand rule and are a counter-

clockwise rotation when looking down. The near wall flow is collateral for the free-stream points within  $\pm 3^\circ$  of flow angle for most of the profiles.

With the free-stream data collateral, it was fit to the Spalding equation using a method described in Madden and Simpson (1997). The Spalding equation, adjusted from White (1974), who used  $U^+$  as opposed to  $Q^+$ , is shown in Equation 4.1:

$$y^+ = Q^+ e^{-\kappa\beta} (e^{\kappa Q^+} - 1 - \kappa Q^+ - \frac{(\kappa Q^+)^2}{2} - \frac{(\kappa Q^+)^3}{6}) \quad (4.1)$$

with  $Q^+ = (\bar{u}^2 + \bar{w}^2)^{1/2}/U_\tau$ ,  $\kappa = 0.41$  and  $\beta = 5.0$ .  $\kappa$  and  $\beta$  are constants calculated by Spalding. This curve was fit to the data below  $y^+ = 100$ . An iterative method was used to fit the curve using  $U_\tau$  and the y-shift as variables in the equation. It should be noted that  $U_\tau$  value was basically independent of the y-shift. The y-shift is necessary when the exact location of the wall is not known.

As discussed in Madden and Simpson (1997) the use of the Spalding equation in pressure driven 3-dimensional flows has been documented. Other people who used the Spalding equation in highly three-dimensional flows include Flack and Johnston (1998) in a  $30^\circ$  bend flow and Chesnakas and Simpson (1996) in flow over a 6:1 prolate spheroid. Both of these were pressure driven 3-dimensional flows and both showed that the Spalding equation fit the data. Like Chesnakas and Simpson (1996) we only use the points measured near the wall which are as close to collateral as possible. Therefore, Spalding's equation is used to calculate  $U_{\tau\alpha}$  for all of the profiles.

In order to confirm the  $U_\tau$  values the Ludwig-Tillmann shear stress correlation (Equation 4.2 modified from White (1974)) was used to calculate  $U_\tau$ .

$$U_\tau = \sqrt{\frac{U_e^2 * 0.246 * Re_\theta^{-0.268} * 10^{-0.678H}}{2}} \quad (4.2)$$

H is the shape factor characterized by the ratio of the displacement to momentum thickness of the flow. To use this equation requires a profile outside of the boundary layer to get the correct displacement and momentum thicknesses. For this reason the equation cannot be used under the blade, since there is no edge to boundary layer in the tip gap.

Table 4.2 shows the  $U_\tau$  calculated for each profile both with Spalding and with Ludwig-Tillmann "L-T". The Ludwig Tillman is generally 2 to 8% higher than the Spalding, however both methods show the same trends in  $U_\tau$ . For the rest of the data the  $U_\tau$  values used will be from the Spalding equation.

Table 4.2: Cascade Tunnel Skin Friction values

Stationary End-Wall					
<i>Profile</i>	<i>Spalding</i>	<i>L-T</i>	<i>Profile</i>	<i>Spalding</i>	<i>LT</i>
$U_\tau$		$U_\tau$	$U_\tau$		$U_\tau$
m/s		m/s	m/s		m/s
1F1	0.964	0.981	4F	0.822	0.886
1F2	0.940	0.984	5S	0.982	
2B	0.792	0.858	5C	0.961	
3S	0.896		5P	0.873	
3C	0.882		5F	0.810	0.861
3P	0.876		6S	1.063	
3F	0.809	0.873	6C1	1.057	
4S	0.966		6C2*	0.947	
4C	0.933		6P	0.937	
4P	0.866		6F	0.775	0.834
* Profile taken with turbulence grid					



### Coordinate Transformation

Once data are taken with the LDA probe the proper coordinate transformation becomes a question. What needs to be found is the rotations from the measurement volume coordinate system to the tunnel coordinate systems. The three tunnel coordinate systems are shown in Figure 4.2. The bed coordinate system ( $X_{bed}$   $Z_{bed}$ ) is aligned with the suction slot and the direction of travel of the belt. The upstream coordinate system ( $X_{upstream}$   $Z_{upstream}$ ) is aligned with the upstream walls of the tunnel. The chord coordinate system ( $X_{chord}$   $Z_{chord}$ ) is aligned with the chord of the blades. The Y axis for all of these coordinate systems is up out of the floor. The beams measure orthogonal off-axis velocity components so a transformation matrix needs to be found for each of the coordinate systems.

In the auxiliary tunnel the two-dimensional data were compared with the DNS results to find the proper coordinate transformation. Since there is no truly two-dimensional flow in the tunnel some other comparison must be made.

At the point where moving end-wall data were taken an easy and accurate method for finding co-ordinate transformation exists. When the wall is moving and the beams are less than 500  $\mu\text{m}$  from the wall the LDA measures the floor movement. The signal looks fairly close to a particle signal; however, as you traverse in the positive y direction the signal rate drop as opposed to increasing. Normally when the beams are near the wall, and you are traversing in the positive y direction the signal rate rapidly increases. The decrease in sample rate continues until a sharp drop and a jump in the measured velocities, this happens when the floor stops being measured and transferred to the flow. This is primarily caused by the optical quality of the Mylar scattering the beams signal across the floor. It is unlikely that this effect is due to the belt bouncing up into the control volume since the standard deviation of the belt movement was around 6.6  $\mu\text{m}$  (see Section 3.4.1).

Once the data were processed it was clear that the moving end-wall was being measured. Since we are certain about the direction and speed of the moving belt a clear coordinate rotation can be done. The mean velocity  $\bar{U}$  in the bed coordinate system is rotated to zero. It is assumed that the  $\bar{V}$  is averaged to be zero as well, so  $\bar{V}$  is rotated to zero. By checking the  $\bar{W}$  against the measured velocity of the belt the difference is within 1% of the velocity.

For the cross sections which had no moving end-wall data, another method was found for the coordinate rotation. The best method was to compare the data to a known set which was rotated correctly. Muthanna (1998) took hot wire data in blade passage with no moving end-wall. However, it should be noted that this was taken with a tip gap of 1.64% (not 3.3%).

Another problem with the comparison is that the data do not lay exactly on the same points. However, one point at each cross section, the points in the freestream "F" and at the tip of the blade "B," are close enough for comparison purposes. The comparison reveal whether or not there was any drastic misalignments of the LDA head. Figure 4.7 through 4.12 show the free-stream plots with the hot-wire data and the LDA data. As was said above, the match is not exact for the points, the bottom of each figure shows the difference in x and z positions between the profiles. Figure 4.7 the z position for the hot wire is shifted by one blade width to match with the LDA data. All the data are plotted in the upstream coordinate system. In the end all of the coordinate rotations turned out to be less than  $2.5^\circ$ .

### 4.2.2 Characterizing Flow Under Blade

#### Pressure Forcing the Flow

Pressure loading data were taken on the blades at mid-passage height on the suction side of blade 4 and on the pressure side of blade 5. On both blades there are 46 taps total. Figure 4.4 shows a plot of the  $C_p$  distributions. The jump seen on the plot near the leading edge of the blade is caused by the trips mounted on the blades. The trips are 0.25 inch wide strips of glass bead coated tape. The strips are mounted on both the sides of the blade, pressure and suction, 1 inch from the leading edge of the blade. The strip spans the entire height of the blades as seen in Figure 3.2.

The difference in  $C_p$  is found across the blade perpendicular to the chord,  $\Delta C_p$ . Figure 4.13 shows this drop in pressure across the blade. The open circles on the plot are the interpolated profile chord positions. This is not the pressure difference near the tip of the blade; however, since there are no data there, this will be used.

A positive pressure force across the blade is the driving force in the tip gap flow. This result was also found by Storer and Cumpsty (1991) who measured a similar tip gap flow through a linear compressor as well. Storer and Cumpsty (1991) took pressure measurements at the wall and measured the flow through the tip gap with a pressure probe. The pressure difference causes the crossflow, which increases the total flow which then increases the  $U_\tau$ . Looking at Figure 4.14 the  $U_\tau$  increases both in the downstream direction as well as from the pressure to the suction side of the blade. The free-stream profiles show a decrease in  $U_\tau$  in the downstream direction.

The pressure force on the flow increases the velocity magnitude slightly as you go downstream

as well. On the pressure side the maximum velocity magnitude increases from 20.0 to 21.8 m/s going from cross section 3 to 6. The range of the maximum velocities on the suction side range from 20.5 to 23.1 m/s. A plot of the velocity magnitudes in the tip gap is shown in Figure 4.15.

There is also slight increase in velocity magnitude is seen across the blade. As noted above, cross section 6 goes from 21.8 to 23.1 m/s across the blade. Using the  $\Delta C_p$  and the velocity magnitudes on the pressure side of the blade, the velocity on the suction side can be approximated with inviscid theory ( $C_p = 1 - U^2/U_e^2$ ). Using the velocity magnitudes stated above on the pressure side inviscid theory finds a range from 27.2 to 38.6 m/s. This is far from the measured velocities. There are major viscous effects slowing down the velocity magnitudes underneath the blade. Therefore the tip-gap flow is not entirely controlled by the pressure force on the blades, there are some viscous effects effecting the flow

### 3D Flow

The flow angle ( $FA = \arctan(\frac{\bar{W}}{\bar{U}})$ ) shows the degree of three dimensionality of the flow (Olcmen and Simpson, 1995). The profiles upstream and underneath the blade are more collateral than the profiles downstream. This is seen in Figure 4.16. The profiles downstream underneath the blade show three dimensionality. The flow angles were calculated in the chord coordinate system with positive rotation following the right hand rule.

Another plot which clearly illustrates the three dimensionality of the flow is Figure 4.17, the  $\bar{U}$  and  $\bar{W}$  vector plot. Four different  $y/c_a$  positions under the blade are plotted. Around the outside of the blade is plotted hot wire data taken at  $y/c_a = 0.064$  cm (Muthanna, 1998). The Muthanna (1998) data do not have the same tip gap (1.64% as opposed to 3.3%), therefore this is not a direct comparison, but only gives the idea of the flow direction. The vectors clearly show the flow being forced through the gap and turning as you go downstream. At the leading edge of the blade the influence of the pressure gradient across the blade is minimal. However downstream, at quarter chord, the flow under the blade is completely driven by the pressure gradient.

Another good plot to compare with the Muthanna (1998) data is the  $\bar{V}$  and  $\bar{W}$  vector plot shown in Figure 4.18. The coordinate system used in this plot is the Chord Coordinate system. X is in the direction of the chord and Z is normal to the chord. This gives the general sense of the flow through the tip gap. Note that the Muthanna (1998) data are neither for the same tip gap nor at the same plane of the flow, this comparison is just to get a general sense of the flow.

A good quantity to compare different profiles under the blade is the  $Q^+$  scalar ( $Q^+ = (\bar{u}^2 +$

Table 4.3: Cascade Tunnel Shear Stress Magnitudes

Maximum/Minimum Values of Shear Stresses							
Profile	$-\overline{uv}/U_\tau$	$-\overline{uw}/U_\tau$	$-\overline{vw}/U_\tau$	Profile	$-\overline{uv}/U_\tau$	$-\overline{uw}/U_\tau$	$-\overline{vw}/U_\tau$
3P	0.910	-2.664	-0.400	5P	1.207	-2.623	-0.426
3C	1.254	-2.802	-0.343	5C	1.006	-2.205	-0.388
3S	1.192	-3.013	-0.591	5S	1.0736	-2.269	-0.474
4P	1.241	-2.940	-0.400	6P	0.964	-2.042	-0.468
4C	1.087	-2.761	-0.271	6C	0.857	-1.288	-0.251
4S	0.997	-2.613	-0.284	6S	0.910	-1.551	-0.299

$\overline{w^2})^{1/2}/U_\tau$ , as shown in Figure 4.19. Figures 4.20 to 4.28 show  $u^+$ ,  $v^+$ ,  $w^+$ ,  $\overline{uv}/U_\tau$ ,  $\overline{uw}/U_\tau$  and  $\overline{vw}/U_\tau$  plots under the tip gap. The tip gap triple products are all shown in Appendix D. All of these are in Chord coordinates and normalized on  $U_\tau$ .

An important thing to note in the Figures 4.26 to 4.28 is the magnitudes of the maximum  $\overline{uv}$ ,  $\overline{uw}$  and  $\overline{vw}$ . These are shown in Table 4.3. Note that for almost all of the profiles the  $\overline{uw}$  is more than twice that of the  $\overline{uv}$ . The  $\overline{uw}$  is close to an order of magnitude greater than the  $\overline{vw}$ . It is interesting to note that terms like  $\overline{uw}$  are usually neglected as higher order terms in the Reynolds-averaged Navier-Stokes equations with the boundary-layer approximations (Olcmen and Simpson, 1995).

### Isotropic Flow and Eddy Viscosity Models

Figure 4.29 shows a comparison between the flow angle ( $FA = \arctan(\frac{\overline{W}}{U})$ ), the Shear Stress Angle ( $SSA = \arctan(\frac{-\overline{vw}}{-\overline{uv}})$ ) and the Flow Gradient Angle ( $FGA = \arctan(\frac{d\overline{W}/dy}{dU/dy})$ ) found in the tip gap. As discussed in Olcmen and Simpson (1995) the flow angle shows the degree of three dimensionality of the flow and the shear stress angle and the flow gradient angle give the comparative directions of the shear stress vector and the velocity gradient vector in the (x,z) plane.

If the effective eddy viscosity is isotropic then the shear stress vector and the velocity gradient vector are in the same direction. This is seen in the first cross section 3P, 3C and 3S of Figure 4.29(a), (b) and (c). From Figure 4.29(e) to (l) the data are clearly not parallel and the shear stress vector is not aligned with the velocity gradient vector. Therefore, for any cross

section beyond 3, the effective eddy viscosity not isotropic.

Looking at the plot of the Anisotropy Factor,  $N = \tan SSA / \tan FGA$  of Figure 4.30 the semi-log plot collapses well. However, in the log-log plot the figure basically looks like a shotgun blast.  $N$  also is the ratio of eddy viscosity in the  $z$ -direction over the eddy viscosity in the  $x$ -direction.

### Shear Stress Ratio Parameters

The  $A1$  and  $1/S$  are parameters which are independent of rotation about the  $y$  axis. The parameters are used to collapse three-dimensional sets of data. The  $A1$  is a ratio of the shear stress to twice the turbulent kinetic energy (TKE) (equation 4.3). is shown in Figure 4.31. The parameter seems to collapse quite well near the wall; however, away from the wall, especially for the free-stream profiles, the collapse breaks down.

$$A1 = [(-\overline{uv})^2 + (-\overline{vw})^2]^{1/2} / (\overline{u^2} + \overline{v^2} + \overline{w^2}) \quad (4.3)$$

The  $1/S$  is a ratio of the shear stress to the fluctuating  $v$  velocity (equation 4.4). The parameter is plotted in Figure 4.32. This parameter collapses much better out away from the wall ( $30 < y^+ < 350$ ); however, near the wall ( $y^+ < 30$ ) the  $1/S$  breaks down. This was also observed in Simpson and Olcmen (1998) where it is believed to be due to high measured values of  $v'$  as the wall is approached.

$$1/S = [(-\overline{uv})^2 + (-\overline{vw})^2]^{1/2} / \overline{v^2} \quad (4.4)$$

### Triple Product Parameters

Another set of parameters used to collapse three-dimensional data is the triple product parameters  $B2$  and  $B$  (Simpson and Olcmen, 1998). Both of these parameters are also invariant to rotation about the  $y$  axis.  $B2$  is shown in Figure 4.33. The Equation 4.5 shows the definition of this parameter. This parameter relates the turbulent transport of the instantaneous stresses  $v^2$ ,  $-\overline{uv}$  and  $-\overline{vw}$  in the  $y$  direction. This figure shows that only a small region of the log layer has a good collapse of the data for this parameter.

$$B2 = (\overline{v^3}) / [(\overline{uv^2})^2 + (\overline{v^2w})^2]^{1/2} \quad (4.5)$$

The last parameter is  $B$  and it is defined in equation 4.6. The parameter is plotted in Figure 4.34. The log region is the best collapse for this parameter. Near the wall and far away from the wall some deviation occurs. The  $B$  shows that turbulent transport of TKE is closely related to the  $v$  transport of  $v^2$ . This could simplify outer region modelling (Simpson and Olcmen, 1998). Ciochetto (1997) also showed that  $B2$  and  $B$  near the wall is scattered but collapses for some range away from the wall.

$$B = (\overline{v^3})/[\overline{u^2v} + \overline{v^3} + \overline{w^2v}] \quad (4.6)$$

### 4.3 Moving End-wall and Vortex Generators

Only one profile position was investigated with the belt moving, 1F. Taking one continuous profile with the moving end-wall setup was virtually impossible (see Section: 3.6.3). Therefore, several half profiles are collected with the moving end-wall configuration. Two points are collected with the moving end-wall and vortex generator configuration, each point separately was taken with one run of the belt.

The two best sets of data collected with the moving end-wall occurred over a two day period. The first of these runs, MW1, a four point logarithmic distribution over the boundary layer was collected. The second run (MW2) only half of the points were collected in the profile, but regularly distributed near the wall. The MW2 run contains two points in the wall, for the coordinate transform and contains six other points near the wall in the flow. The MW3 and MW4 and MW5 runs were collected almost two weeks after MV1 and MV2. The MW3 consists of only one point taken in the middle of the boundary layer. The MW4 run has four points in the moving end-wall. The MW5 run has two points, one close to the wall the other further out in the boundary layer. All of these are shown in the plot of the flow angle in Figure 4.35a. Note how the points in the wall all line up at  $24.9^\circ$ . The points in the wall are removed and the rest of the points are combined to form one profile, MW, for the rest of the figures.

The single point of vortex generator data was collected twice. The position of the point is at 1F and 1 cm above the floor. Position 1F is approximately 3.1 cm downstream from the vortex generators. An error was made and the vortex generators are located 0.5 inches upstream of the location used in Ma et al. (2000). Two different systems of marking the belt were used as described in Section 3.2.13. The first point collected, VG1, the vortex generator marks are positioned to be triggered when the vortex generators were in front of the measurement volume. This is the most uncertain point in the measurement scheme because it is at the beginning and

end of the triangular pulse. In matching up the two ends of the triangular pulse, there is a 1/4 inch gap caused by the width of the trigger mark. For the second point collected, VG2, the vortex generator marks triggered the signal right in between the sets of vortex generators.

The part of the curve of most interest is in the middle of the triangular pulse, and the most certain area. The two data sets sorted into 128 bins plotted in the upstream coordinate system are shown in Figure 4.36. The  $z$  axis is normalized on the blade spacing of 23.6 cm ( $z/z_b$ ). Roughly at  $z/z_b$  the middle of the vortex generator pair is aligned with the measurement volume. Note that the normalized velocities are different between the two sets. Note the difference in the curve of the VG1 data between the vortices. However, note the similarities between the magnitudes of the velocity deficits between the two sets. Both of these differences can be attributed to the possible differences in position of the vortex generator relative to the measurement volume. The uncertainty of the axial position of the vortex generators is around  $\pm 3.25$  mm (see Section B.2.5). With the vortex generators only 3.1 cm away this is 10% of that distance.

To match up the two data sets, the velocities are normalized on the mode  $\bar{U}$  velocity in the upstream coordinate system ( $\text{VG1:}\bar{U} = 23.3$  m/s,  $\text{VG2:}\bar{U} = 23.2$  m/s). The first point of data is split in half and then matched up with the second set of data. The matching is done with the peaks of the velocity deficit. Figure 4.37 is the plot of the shifted normalized data. For the rest of the section only the VG2 data will be plotted and discussed.

### 4.3.1 Flow and Data Quality

#### Finding $U_\tau$

For the moving end-wall profiles there was not enough data in the viscous sublayer to use equation 2.2. Therefore the Spalding equation (Equation 4.1) was investigated. Again, to use the Spalding equation the flow must be collateral. Figure 4.35 (a) shows the flow angle of the moving end-wall flow and compares it to the stationary end-wall flow. Figure 4.35 (b) compares the flow angle in a stationary end-wall coordinate system to the flow angle in a moving end-wall coordinate system. Figure 4.38 is the plot of the  $\bar{U}$   $\bar{W}$  vectors with the bed coordinate axis shown. Figure 4.38 (a) is in the stationary end-wall coordinate system. Figure 4.38 (b) is in the moving end-wall coordinate system. To transform into the moving end-wall coordinate system the moving end-wall velocity is subtracted from the  $W$  component, in the bed coordinate system. In plot (b) there is a region where the flow angle doesn't change more than 8 degrees close to the wall or approximately collateral. This includes 8 data points all at approximately

18° turning angle to the bed (see Figure 4.35 (b)). There is no better method for computing the  $U_\tau$ , so the Spalding fit is used on these 8 data points. The  $U_\tau$  is measured to be 0.46 m/s. This decrease in  $U_\tau$ , as compared to the stationary end-wall, is caused from the relative decrease in the velocity from adding the moving end-wall. With the stationary end-wall the free-stream flow above the wall was approximately 25 m/s. With the moving end-wall the free-stream flow above the wall, as seen by the wall, is approximately 10.5 m/s perpendicular to the moving end-wall direction.

### Vortex Generator Bin Size

Different bin sizes were analyzed to see what captured the data the best. Figures 4.39, 4.40 and 4.41 shows the VG2 data processed with three different sizes of bins in the upstream coordinate system. The three different sizes corresponded to dividing the data set into 32, 64 or 128 bins based on relative position of the vortex generators to the measurement volume. There is not very much dependence on the mean velocity or Reynolds normal stresses on the bin size ( Figure 4.39 and Figure 4.40. The Reynolds shear stresses are fairly scattered and it is hard to tell dependence from the bin size. The 128 bins seems to represent the flow the best, so that will be used for all following discussion.

## 4.3.2 Characterizing Flow

### Belt Driven Flow

The interaction of the shear layers causes the twisting of the moving end-wall data. There are two shear layers interacting, the suction slot shear layer and the moving end-wall shear layer. The suction slot shear layer flow starts at the stationary suction slot. The moving end-wall shear layer is moving with the belt, and starts just after the belt leading edge cover. The complex flow creates the complex nature seen in Figure 4.38.

Looking at Figure 4.38 (a), the belt viscous layer is attempting to turn the flow to the belt movement direction. The vectors at the wall, and zero slip, are exactly in the belt direction. The vectors in the outer boundary layer are twisted into the upstream flow direction (shown the approximately zero turning angle in Figure 4.35).

Figure 4.38 (b) shows the basically collateral flow in the vectors from near the wall to  $y = 0.29$  cm. These vectors are at approximately an 18° turning angle to the bed. This is interesting because that is the same as angle of attack measured between one of the vortex generators and



the tunnel centerline. The point of measurement is not at the location of the vortex generators, however it is approximately 3.1 cm down stream of where they are positioned. The first vortex generator to pass by the measurement volume (positive rotation, using right hand rule, to the flow in the bed coordinate system) when the belt is running is at a  $-18^\circ$  to the flow angle. The second vortex generator, in the pair (negative rotation to the flow in the bed coordinate system), to pass by the measurement volume is at a  $18^\circ$  flow angle. The vortex generators are 1 cm tall at the trailing edge. If the vortex generators were positioned at this point on the moving end-wall  $1/3$  of the height of the second half-delta vortex generator would be parallel to the flow. At the point upstream of this point the turning would be less, because the moving end-wall viscous layer would have a shorter distance to turn the flow, however the effect would still be there. The effect is the decrease in strength of the second, negative rotating, vortex.

Figure 4.42 shows the mean velocities in the bed coordinate system for the moving end-wall data. Looking at Figure 4.42 (a) there are not many data points to determine a good boundary layer thickness, however an approximation is 0.94 cm. The boundary layer thickness is defined as the  $y$  location where  $U/U_e = 0.99$ . The freestream was taken as the value of the velocity in direction perpendicular to the belt at the outer point. The data were interpolated between the second to last point and an average between the third and fourth to last points. Looking back to Figure 4.7,  $Q/U_e$  was calculated using both  $\bar{U}/U_e$  and  $\bar{W}/U_e$  to find the boundary layer thickness for the stationary end-wall at point 1F2. The last three points in the profile were averaged for a composite freestream. Then the 0.99 of this composite freestream was found and interpolated between the fourth and third to last points to get the boundary layer thickness. The boundary layer thickness was found to be 1.04 cm. The boundary layer thickness is approximately 9% larger for the moving end-wall data than for the stationary end-wall data.

The boundary layer thickness at point 1F in the cascade tunnel with moving end-wall roughly matches the boundary layer thickness at the first cross section of the auxiliary tunnel. Again the boundary layer thickness for the cascade tunnel with moving end-wall is roughly 0.94 cm. The boundary layer thickness in the auxiliary tunnel at the first cross section is roughly 1.34 cm (see Section 2.4).

The  $Re_\theta$  at point 1F in the cascade tunnel with moving end-wall roughly matches the  $Re_\theta$  at the first cross section of the auxiliary tunnel. The  $Re_\theta$  is calculated for the moving end-wall data integrating over Figure 4.42 (a).  $Re_{\theta_{eta}} = 1344$  for the flow. The  $Re_\theta$  at the first cross section in the auxiliary tunnel is 1100 (see Section 2.2.3).

### Vortex Generated Flow

Figures 4.43, 4.44 and 4.45 shows the mean, Reynolds normal stress and Reynolds shear stress velocities for the vortex generated flow. For the  $z/z_b$  locations away from the presence of the vortices, the  $\overline{W}$  is roughly twice the  $\overline{U}$ . With the presence of the vortices, the peak  $\overline{w^2}$  is roughly half of the peak  $\overline{u^2}$ . The peak  $-\overline{uw}$  is higher than any of the other shear stresses, showing the beginning of the three dimensionality of the flow.

The first cross section in the auxiliary tunnel is 10.5 cm downstream of the vortex generators. The second cross section is 44.4 cm downstream of the vortex generators. In the cascade tunnel, vortex generator data are taken approximately 3.1 cm downstream of the vortex generators. However, as is noted above in the previous section, the boundary layer thickness and the  $Re_\theta$  roughly match between the first cross section of the auxiliary tunnel and the profile position of the vortex generator data. Obviously the vortices have not had as much distance to develop.

An assumption is going to be made that centers of both vortices are at the same height. This is not a completely unfounded assumption because the measurement position is only 3.1 cm downstream of the vortex generators. However, the flow is highly three-dimensional and this assumption may not be valid.

Figure 4.46 is normalized, not on the free-stream velocity, but rather the component of the vector in the direction normal to the wall movement, i.e. positive  $U$  in the bed coordinate system. In Figure 4.46 the velocity at  $z/z_b = 0.05$  is roughly 0.5 and the velocity at  $z/z_b = -0.06$  is roughly 0.72 (from the negative rotating vortex). The mean flow is 0.84 at this particular point. Therefore the velocity deficit at  $z/z_b = 0.05$  is roughly 0.34 (from the positive rotating vortex) and the velocity deficit at  $z/z_b = -0.06$  is roughly 0.12 (from the negative rotating vortex). The positive rotating vortex deficit is almost three times the size of the negative rotating vortex deficit. This can be attributed to the near wall flow not hitting the positive rotating vortex generator parallel to 0 angle of attack.

The velocity deficits can be compared between the auxiliary tunnel and the cascade tunnel. Two points can be compared, the peak deficit and the deficit at the same  $y$  position (1 cm). The first cross section in the auxiliary tunnel (10.5 cm downstream of the vortex generators) is compared (see Section 2.4). The velocity at the center of the vortex is 0.72 of the freestream. This peak deficit is 0.28. The velocity at 1 cm height is 0.84 of the freestream. This deficit is 0.16. Both of deficits in the auxiliary tunnel, the peak and the matching  $y$ , fall between the values of the two vortices in the cascade tunnel.

As shown in Section 2.4 the velocity deficit decreases as you go downstream. Therefore, there

is a fairly good possibility that we are not at the center of the vortex in our cross section, being 4 times closer to the vortex generator in the cascade tunnel than in the auxiliary tunnel.

For comparison purposes two assumptions will be made. The first assumption is that the center of the vortex is cut at the cascade tunnel data point. The first assumption is discussed above. The second assumption is that the vortices are circular and not ellipsoidal. The vortices are ellipsoidal in the auxiliary tunnel flow (see Section 2.4). This is probably a bad assumption as well.

The diameters of the vortices are found from Figure 4.46. The diameter of the positive rotating vortex is 1 cm. The diameter of the negative rotating vortex is 0.7 cm. In the auxiliary tunnel, at the first cross section the diameter of the vortex is 1.3 cm. The two diameters of the cascade tunnel vortices fall around the auxiliary tunnel diameter at the first cross section. If we are not at the center of the vortex these values should increase as we get to the center of the vortex. However the values should decrease if the vortex is found to be not circular and skewed in the  $z$  direction like in the auxiliary tunnel.

After making the above two assumptions the circulation can be calculated using Equation 4.7.

$$\Gamma_c = 2\pi r \bar{V} \quad (4.7)$$

The circulation is calculated from Figure 4.46. The circulation of the positive rotating vortex is  $\Gamma_c = -0.32$ , normalized on the height of the vortex generator. The circulation of the negative rotating vortex is  $\Gamma_c = 0.14$ . The circulation is opposite the sign of the rotation of the vortex because this is the normal sign convention for circulation. In the auxiliary tunnel at the first cross section  $\Gamma_c = -0.18$  (see Section 2.4). The circulation found in the auxiliary tunnel was done using Equation 2.3 and a simple numerical integration. The circulation values calculated on the cascade tunnel vortices fall around the values calculated for auxiliary tunnel vortices at the first cross section. If the vortex center assumption is incorrect then the value of  $\Gamma_c$  will increase. If the circular assumption is incorrect then the value of  $\Gamma_c$  will decrease. When Equation 4.7 was used to calculate  $\Gamma_c$  in the auxiliary tunnel, the value was came out 4 times larger than using Equation 2.3.

Table 4.4 shows all the above results compiled into table format.

Table 4.4: Cascade and Auxiliary Tunnel Vortex Magnitude Results

<i>Tunnel</i>	<i>Vortex Rotation</i>	$X_{vg}$ (cm)	$\delta$ (cm)	$Re_\theta$	$V_{def}$ peak	$D_{vor}$ (cm)	$\Gamma_c$
Auxiliary	Both	10.5	1.34	1100	0.28	1.3	$\pm 0.18$
Cascade	Positive	3.1	0.94	1344	0.34	1	-0.32
Cascade	Negative	3.1	0.94	1344	0.12	0.7	0.14

## 4.4 Conclusions

### 4.4.1 Stationary End-Wall

Eighteen profiles of stationary end-wall data are taken in and around the tip gap region. The stationary end-wall flow in the tunnel matches the conditions when hot-wire data were taken by Ma et al. (2000). The flow at position 1F, the upstream most point in front of the blade, is compared with two dimensional DNS results.

The Spalding equation is fit to the data to determine the  $U_\tau$  value for each profile taken in the flow. The flow is shown to be almost collateral for the free-stream points, and moderately collateral for the points under the blade. Due to lack of better method to determine  $U_\tau$ , the Spalding fit is used on all profiles.

Data taken at the wall while the belt is moving is the best way to set coordinate rotations for the data. A secondary method of comparing with older hot-wire data is used when the moving end-wall data is not available. All the coordinate rotations are less than  $2.5^\circ$ .

The major driving force of the flow under the blade, in the tip gap, is the pressure difference across the blade, which was also found by Storer and Cumpsty (1991). This pressure force drives the flow from the pressure side to the suction side of the blades. The pressure force causes the  $U_\tau$  to increase both in the downstream direction along the blade as well as from the pressure to the suction side of the blade. This behavior is in contrast to the free-stream profiles which show a decrease in  $U_\tau$  in the downstream direction.

In the tip gap there are major viscous effects that slow down the velocity magnitudes. These viscous effects make the use of the Bernoulli equation not applicable.

The first several profiles in the tip gap basically show a collateral flow. Past these initial

several profiles, the flow begins to show some three-dimensional effects. At quarter chord the three-dimensional effects in the flow are quite evident looking at the flow angles.

Vector plots in the x-z chord coordinate plane clearly show the flow forced through the tip gap. The leading edge of the blade shows little influence, but by the quarter chord the flow quite a bit turned relative to the free-stream flow. Further evidence of the pressure driven nature of the flow.

Three-dimensionality is shown through looking at the Reynolds shear stress magnitudes. Nearly all the  $\overline{uw}$  shear stress peak values are more than twice that of  $\overline{uv}$ . The  $\overline{uw}$  is close to an order of magnitude greater than the  $\overline{vw}$ ;  $\overline{uw}$  can be looked at a indicator of three dimensionality. High values and increasing values show that three-dimensional effects are most likely influencing the flow.

For any cross section beyond plane 3 it is found that the effective eddy viscosity is not isotropic. This is determined from the plots of the shear stress angle and the flow gradient angles. It is also seen in the N, eddy viscosity, ratio plot.

#### 4.4.2 Moving End-Wall

One profile of moving end-wall data and one point of moving end-wall with vortex generator data were collected. The one profile of moving end-wall data is at position 1F in the flow. This one profile is a combination of five different sets of data on five different days. The one point of vortex generator data is at position 1F. The point is approximately 3.1 cm downstream of the vortex generators and at a height of 1 cm off the wall. The vortex generator height is 1 cm at the trailing edge.

A collateral region for the moving end-wall data is found by looking at the data in a moving end-wall coordinate system. The region contains eight points and the flow angle doesn't change more than 8 degrees. The Spalding fit is used on the eight points to determine the  $U_\tau$  value.

#### 4.4.3 Moving End-Wall with Vortex Generators

There is not very much dependence on the mean velocity or Reynolds normal stresses on the bin size for the vortex generator data. The Reynolds shear stresses are fairly scattered and it is hard to tell dependence from the bin size. The 128 bins is chosen to represent the flow the best.

The interaction of the shear layers with the moving end-wall rotates the near wall flow direction into the direction of the moving end-wall. This interaction seems to cause a 9% increase to the boundary layer thickness from the stationary end-wall profile. Figures show the belt viscous layer turning the flow to the belt movement direction near the wall. In the collateral region, of the moving end-wall coordinate system, the flow angle is found to be nearly the same as the angle of attack measured between the negative vortex generator and the tunnel centerline; this is merely a coincidence. However, this has the affect of decreasing the strength of the negative rotating vortex. Even though this effect will be less at the vortex generator, due to the shorter travel distance for the moving end-wall viscous layer, some turn would still be there. The velocity plots of the vortex generator data show that the positive rotating vortex deficit is almost three times the size of the negative rotating vortex deficit.

Many attributes of the flow match between the auxiliary tunnel's first cross section and the position of the data point with vortex generator data in the cascade tunnel. These similarities are shown in Figure 4.4. The boundary layer thickness at point 1F in the cascade tunnel with the moving end-wall roughly matches the boundary layer thickness at the first cross section of the auxiliary tunnel. The  $Re_\theta$  at point 1F in the cascade tunnel with the moving end-wall roughly matches the  $Re_\theta$  at the first cross section of the auxiliary tunnel. The peak velocity deficit in the auxiliary tunnel at the first cross section falls between the values of the two vortices in the cascade tunnel. The diameter of the vortex measured in the auxiliary tunnel at the first cross section fall between the two diameters measured for the cascade tunnel vortices. The circulation values calculated on the cascade tunnel vortices fall around the values calculated for auxiliary tunnel vortices at the first cross section.

It seems that there are similar vortices found in the cascade tunnel as there were in the auxiliary tunnel. Obviously much more data need to be taken to fully understand the flow, especially with the moving end-wall and vortex generators. However, some confirmations are made about the flow. The tip gap for a non-moving end-wall is generally driven by the pressure gradient. The moving end-wall viscous sublayer skews and increases the boundary layer. The skewed moving end-wall generates two asymmetrical vortices in the flow.

## References

AGARD, Advisory Group for Aerospace Research and Development 1996 *"Turbulent Boundary Layers in Subsonic and Supersonic Flow,"* AGARD-AG-335, North Atlantic Treaty Organization, pp. 25-28.

- Ciochetto, D.S. 1997 *"Analysis of Three-Dimensional Turbulent Shear-Flow Experiments with Respect to Algebraic Modeling Parameters,"* M.S. Thesis, Virginia Tech, Blacksburg VA.
- Chesnakas, C.J. and Simpson R.L. 1996 *"Measurements of the Turbulence Structure in the Vicinity of a 3-D Separation"* Transactions of the ASME Journal of Fluids Engineering, Vol. 118, June, pp. 268-275.
- Flack, K.A. and Johnston, J.P. 1998 *"Near-wall flow in a three-dimensional boundary layer on the endwall of a 30° bend,"* Experiments in Fluids, Vol. 24, pp. 175-184.
- Ma, R., Saha, N., Devenport, W.J., and Wang, Y. 2000 *"Unsteady Behavior of a Tip Leakage Vortex Produced by Simulated Stator/Rotor Interaction,"* AIAA paper 2000-2217, Fluids 2000, Denver, CO, June 19-22.
- Madden, M.M., and Simpson, R.L. 1997 *"Octant Analysis of the Reynolds Stresses in the Three-Dimensional Turbulent Boundary Layer of a Prolate Spheroid,"* Report Number VPI-AOE-252, Aerospace and Ocean Engineering Dept, VPI&SU.
- Murthy, K.N.S. 1985 *"An Experimental Investigation of End-wall Flowfield of a Compressor Rotor"* Ph.D. Thesis, Pennsylvania State University, State College PA.
- Muthanna, C., 1998 *"Flowfield downstream of a compressor Cascade with Tip Leakage,"* M.S. Thesis, Virginia Tech, Blacksburg VA.
- Olcmen, S.M., and Simpson, R.L. 1995 *"A five-velocity -component laser-Doppler velocimeter for measurements of a three-dimensional turbulent boundary layer,"* Measurement Science and Technology, Vol. 6, pp. 702-716.
- Simpson, R.L., and Olcmen, S.M. 1998 *"Some Structural Features of Pressure-driven Three-dimensional Turbulent Boundary Layers from experiments for  $500 \leq Re_\theta \leq 23000$ ."* 22nd ONR Symposium on Naval Hydrodynamics, Washington, D.C., August 9-14.
- Spalart, P.R. 1988 *"Direct simulation of a turbulent boundary layer up to  $R=1410$ ."* Journal of Fluid Mechanics, Vol.187, p. 61.
- Storer, J.A. and Cumpsty N.A. 1991 *"Tip Leakage Flow in Axial Compressors"* Transactions of the ASME Journal of Turbomachinery, Vol 113, April, pp. 252-259.
- Wetzel, T.G. 1996 *"Unsteady Flow Over a 6:1 Prolate Spheroid,"* Ph.D. Disertation, Virginia Tech, Blacksburg VA.
- White, F.M. 1974 *"Viscous Fluid Flow,"* McGraw-Hill pp. 475.

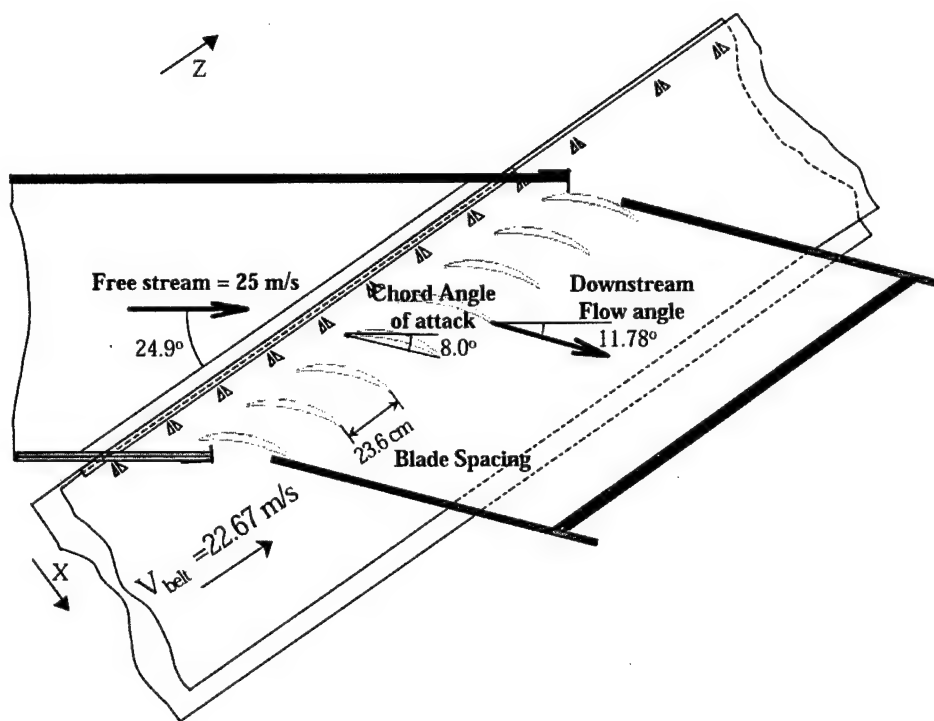


Figure 4.1: Angles in the Low Speed Linear Cascade Wind Tunnel



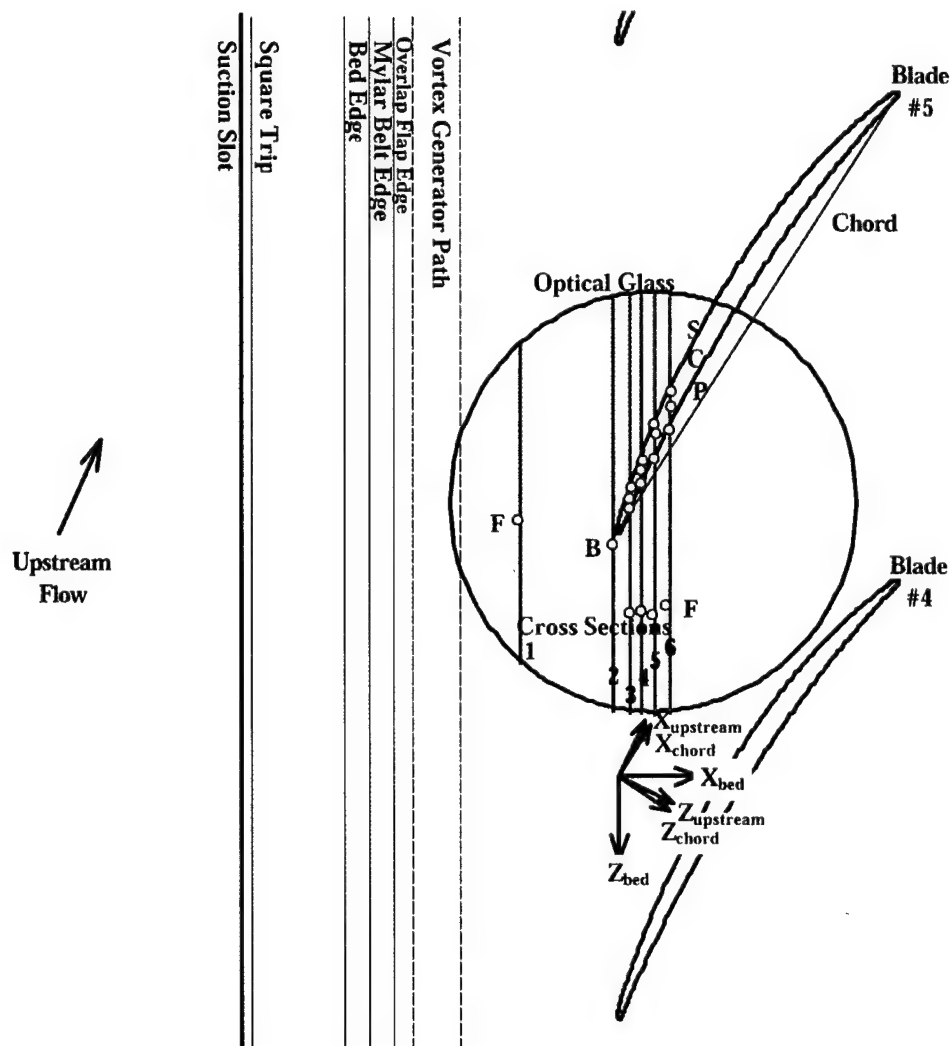


Figure 4.2: Test Matrix in the Low Speed Linear Cascade Wind Tunnel

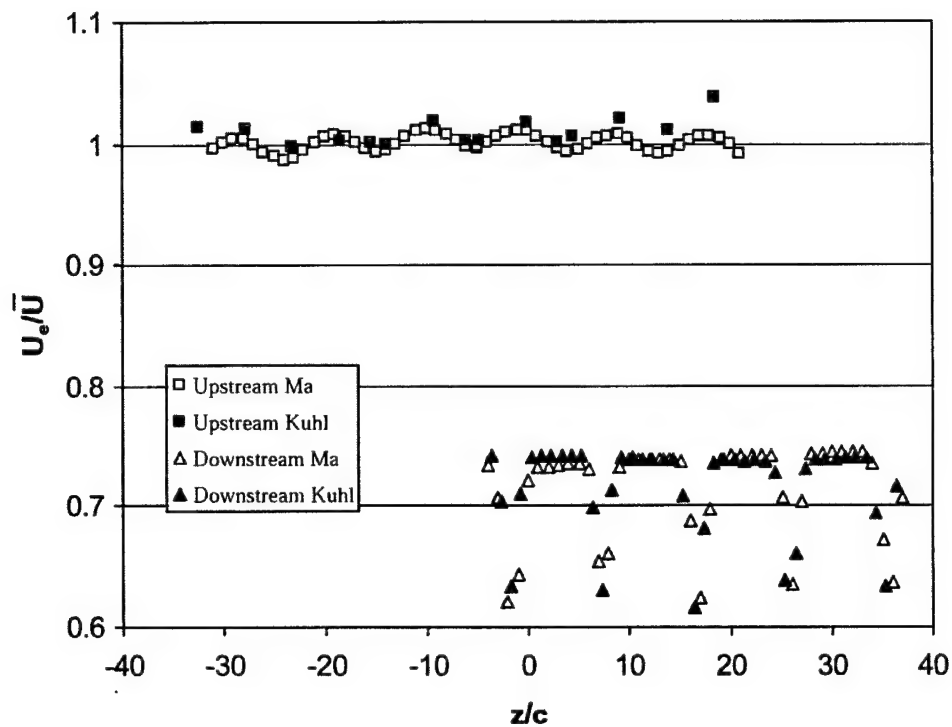


Figure 4.3: Tunnel calibration cascade tunnel comparison between pitot probe traverses of the tunnel before Ma's hot-wire data was taken and Kuhl's LDA was taken (same tip-gap)

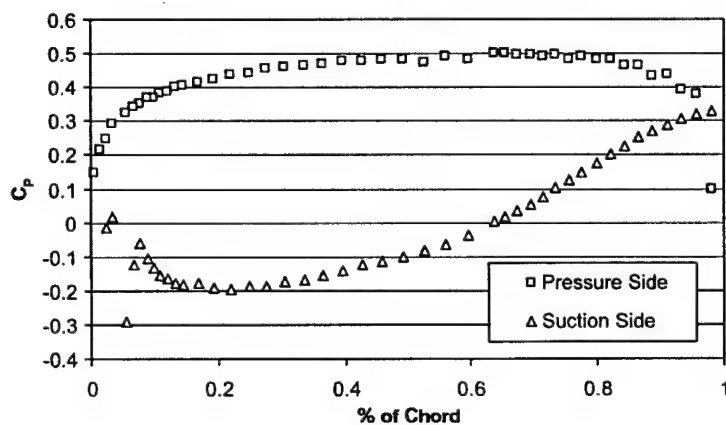


Figure 4.4: Blade loading, suction side of blade 4 pressure side of blade 5

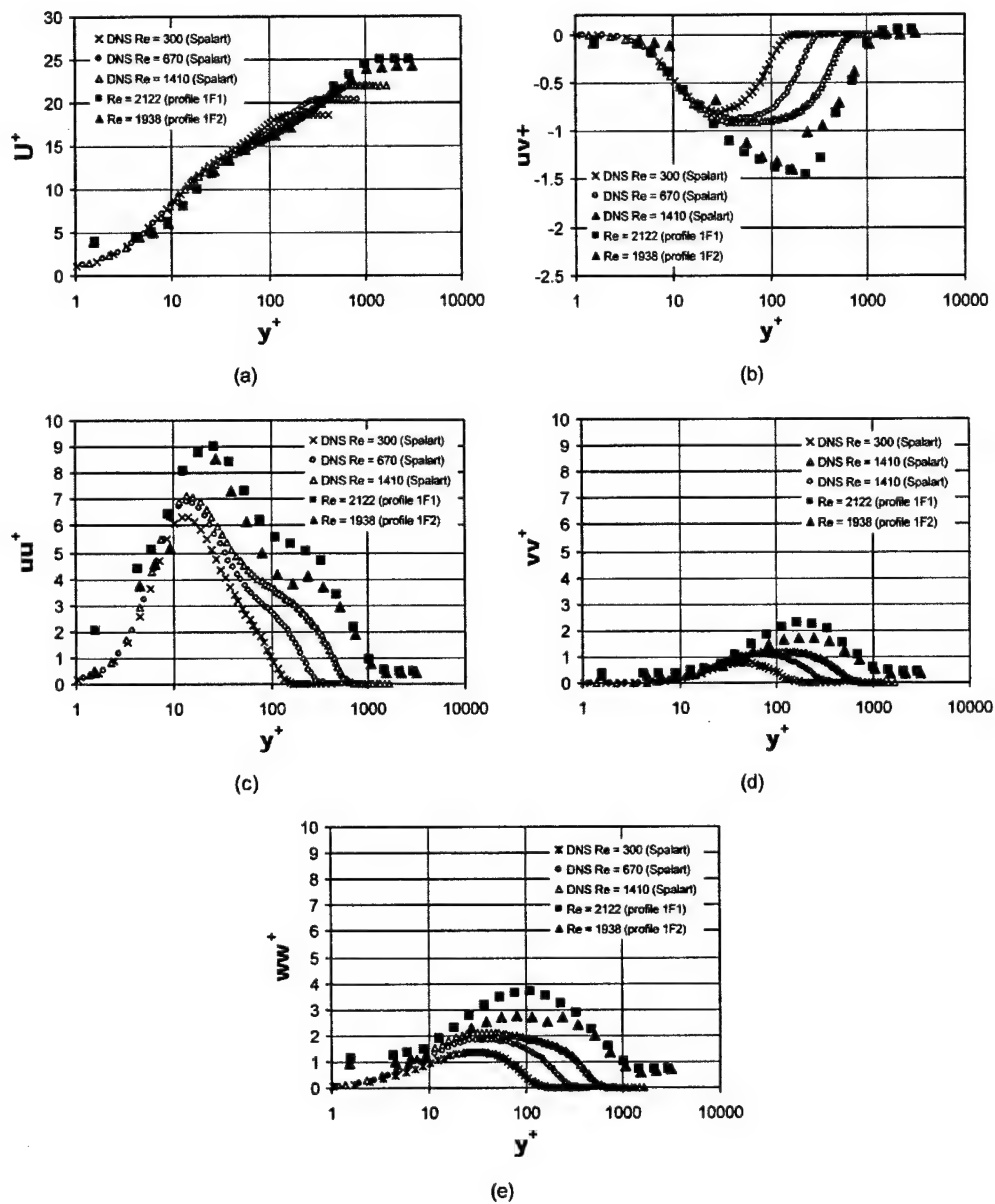


Figure 4.5: Comparison with DNS data and cascade tunnel data

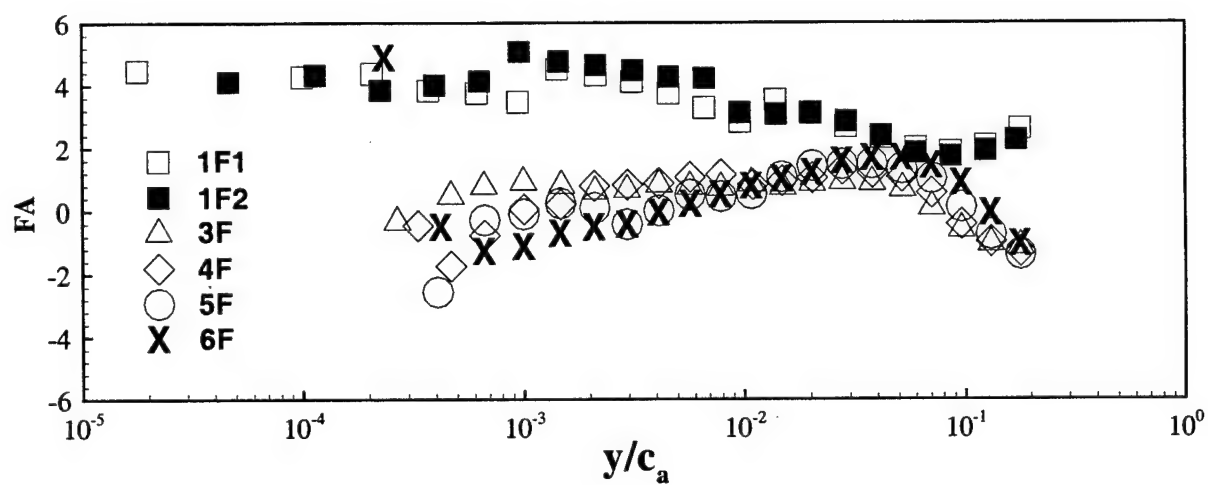


Figure 4.6: Turning angles in the freestream "F",  $y$  is normalized on axial chord, in free-stream coordinates (the first number refers to the profile location, the last number refers to the profile number at that profile location, see Figure 4.2)

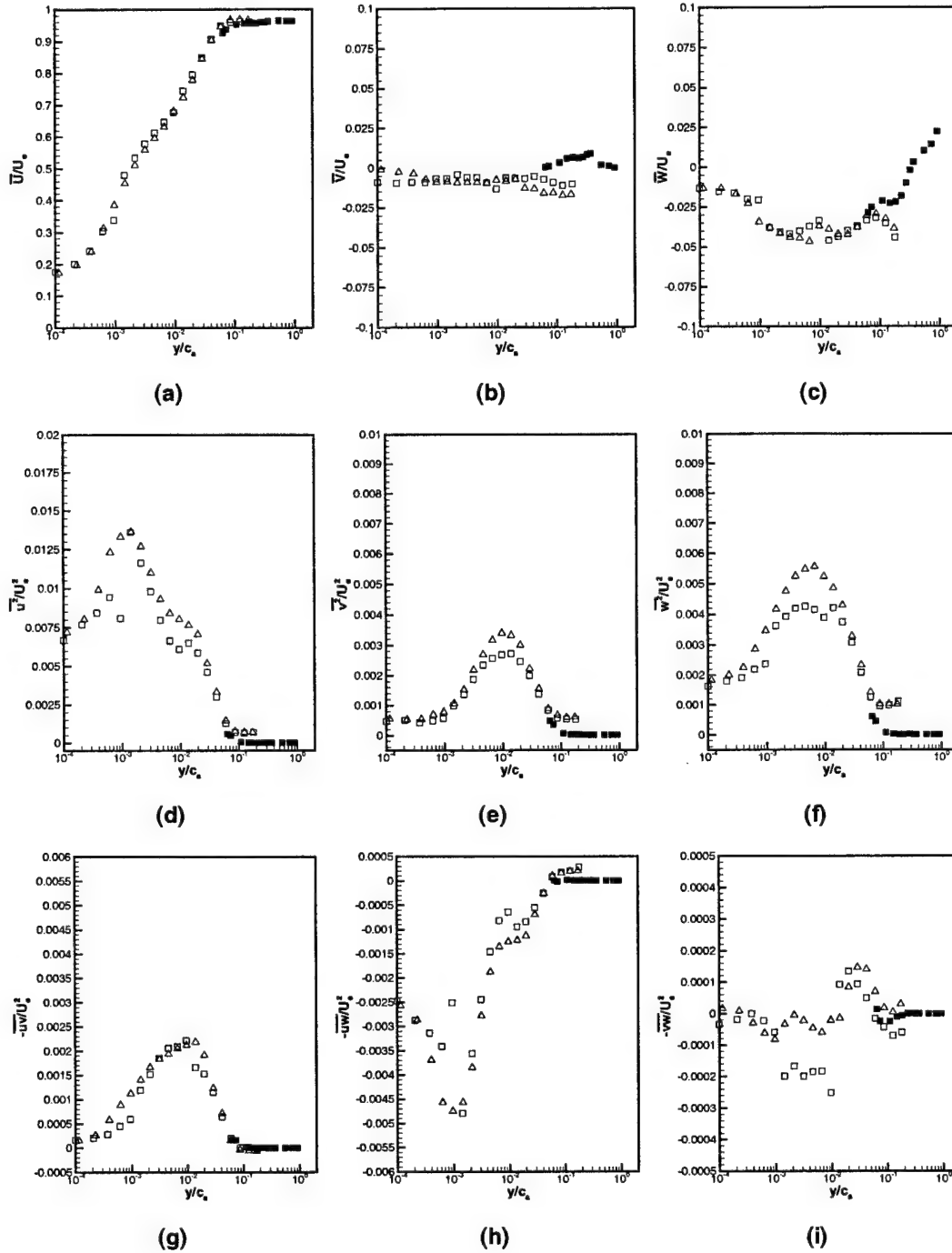


Figure 4.7: Profile 1F1 and 1F2 Compared with hot wire data ( $\square$  is 1F1,  $\triangle$  is 1F2 [ $x=-4.9\text{cm}$   $z=-12.5\text{cm}$ ],  $\blacksquare$  hot-wire [ $x=-3.2\text{cm}$   $z=16.7\text{cm}$ (shifted=-6.9cm)]) free-stream coordinate system

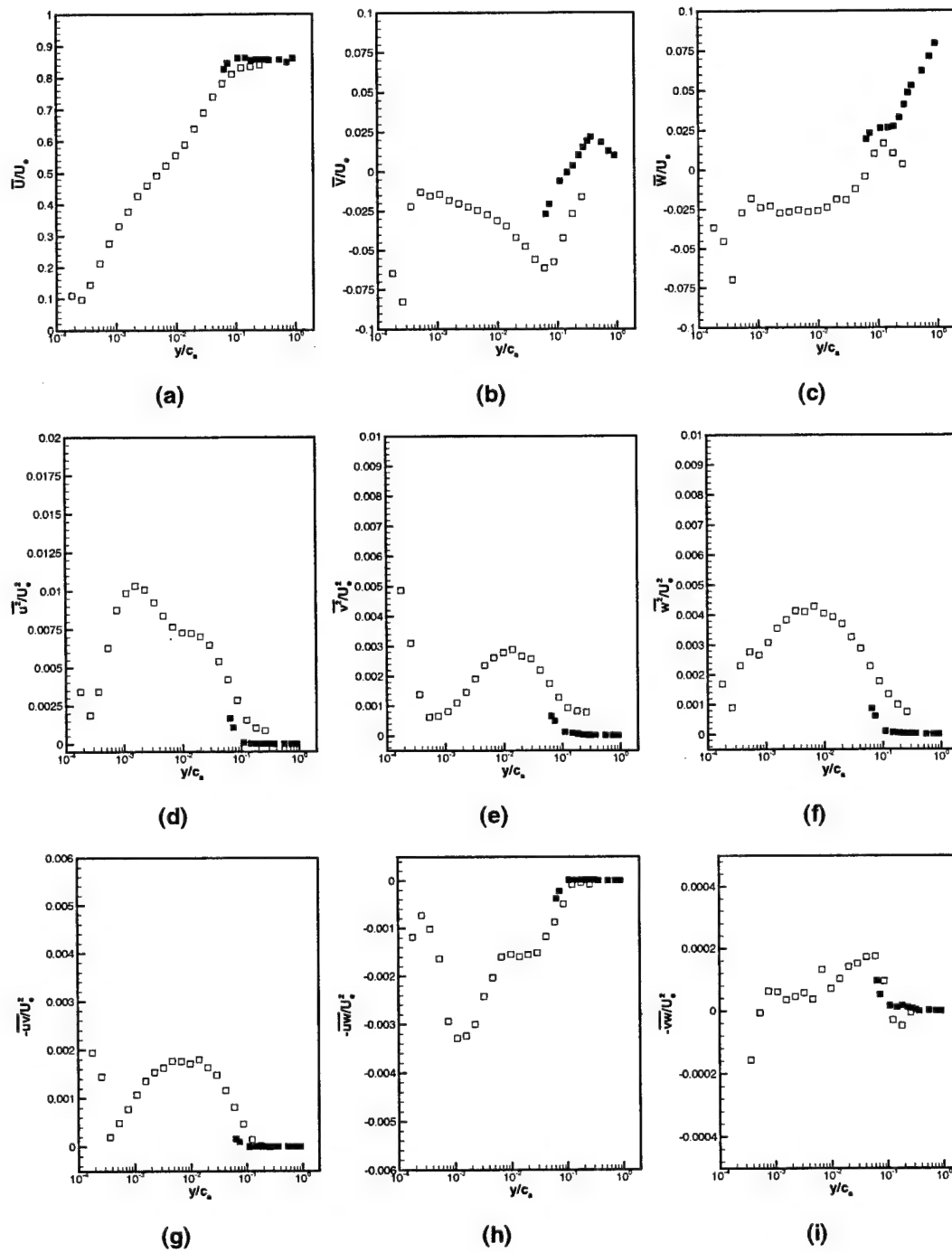


Figure 4.8: Profile 2B Compared with hot wire data ( $\square$  is 2B [ $x = -0.2 \text{ cm}$ ,  $z = -11.3 \text{ cm}$ ],  $\blacksquare$  hot-wire [ $x = 0 \text{ cm}$ ,  $z = -11.3 \text{ cm}$ ]) free-stream coordinate system

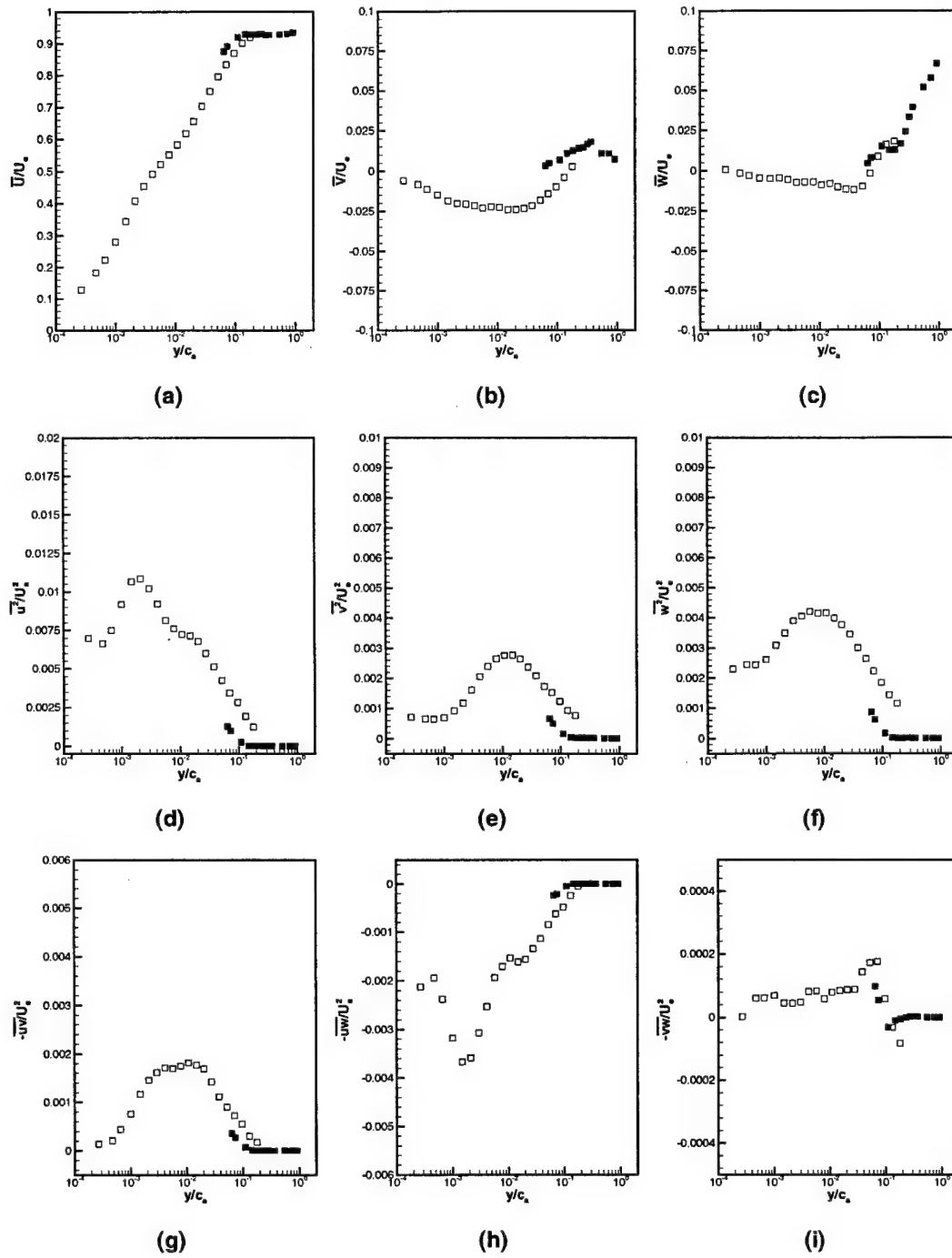


Figure 4.9: Profile 3F Compared with hot wire data ( $\square$  is 3F [ $x=0.6\text{cm}$   $z=-8.0\text{cm}$ ],  $\blacksquare$  hot-wire [ $x=0\text{cm}$   $z=-8.0\text{cm}$ ]) free-stream coordinate system

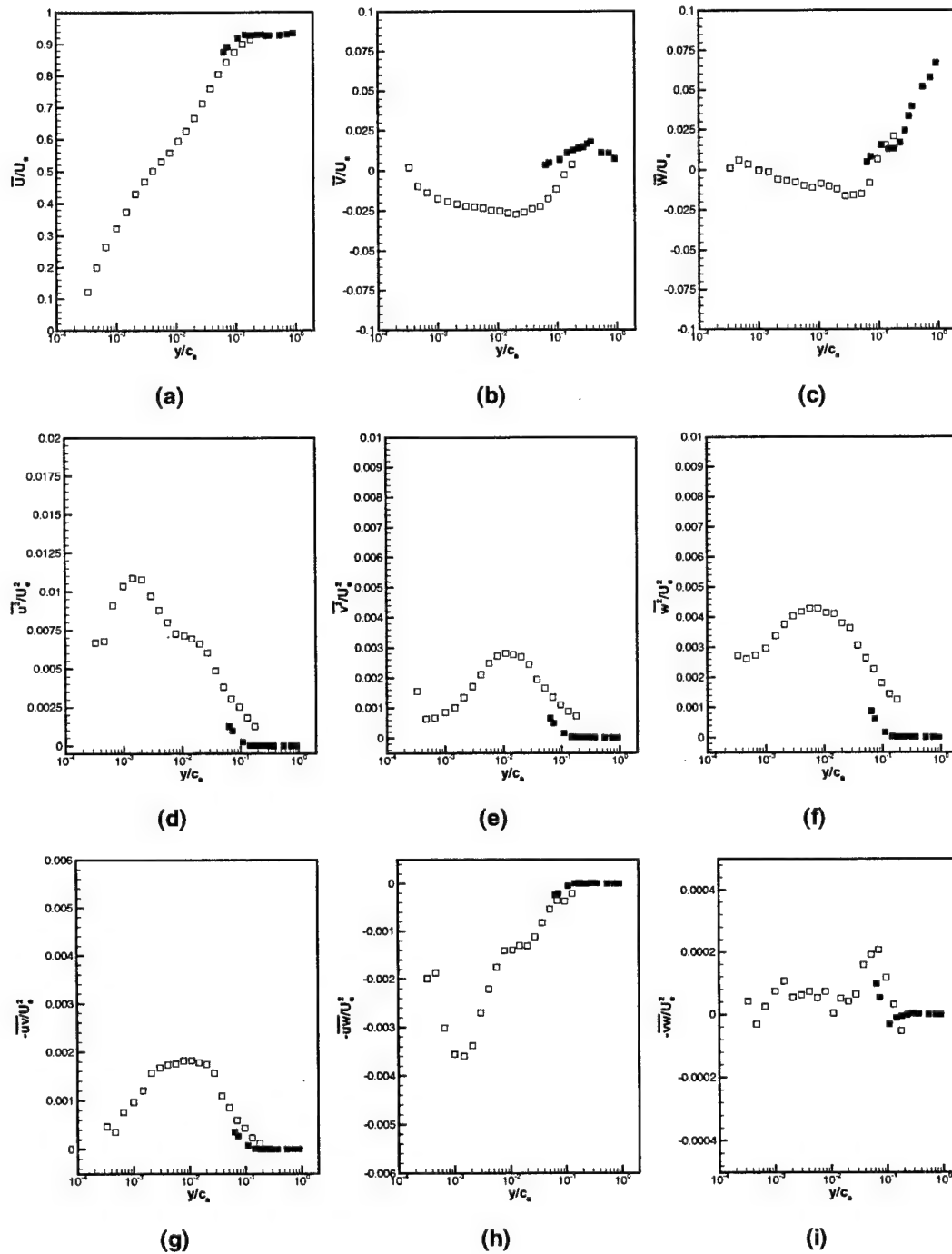


Figure 4.10: Profile 4F Compared with hot wire data ( $\square$  is 4F [ $x=1.2\text{cm}$   $z=-8.1\text{cm}$ ],  $\blacksquare$  hot-wire [ $x=0\text{cm}$   $z=-8.0\text{cm}$ ]) free-stream coordinate system



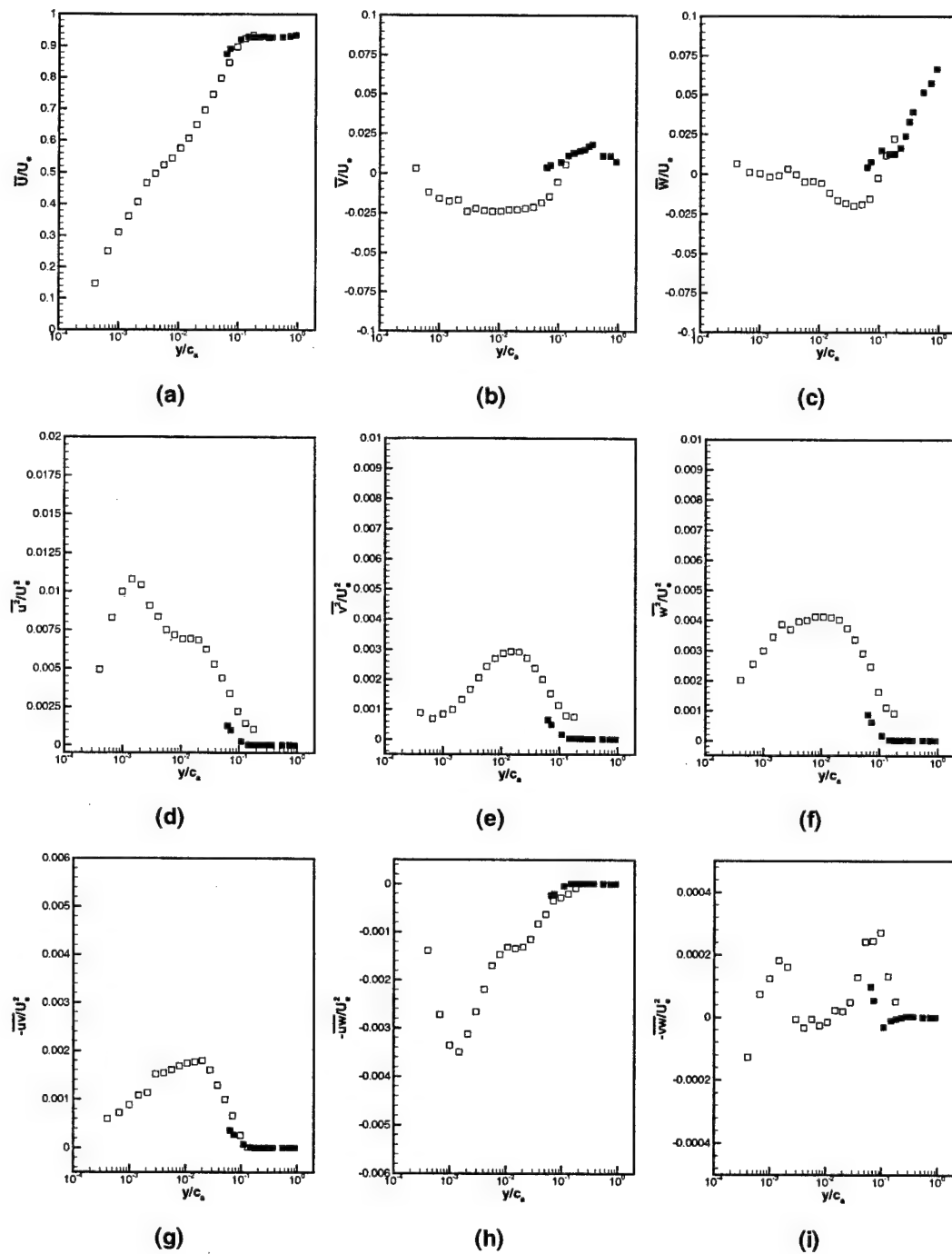


Figure 4.11: Profile 5F Compared with hot wire data ( $\square$  is 5F [ $x=1.7\text{cm}$   $z=-7.9\text{cm}$ ],  $\blacksquare$  hot-wire [ $x=0\text{cm}$   $z=-8.0\text{cm}$ ]) free-stream coordinate system

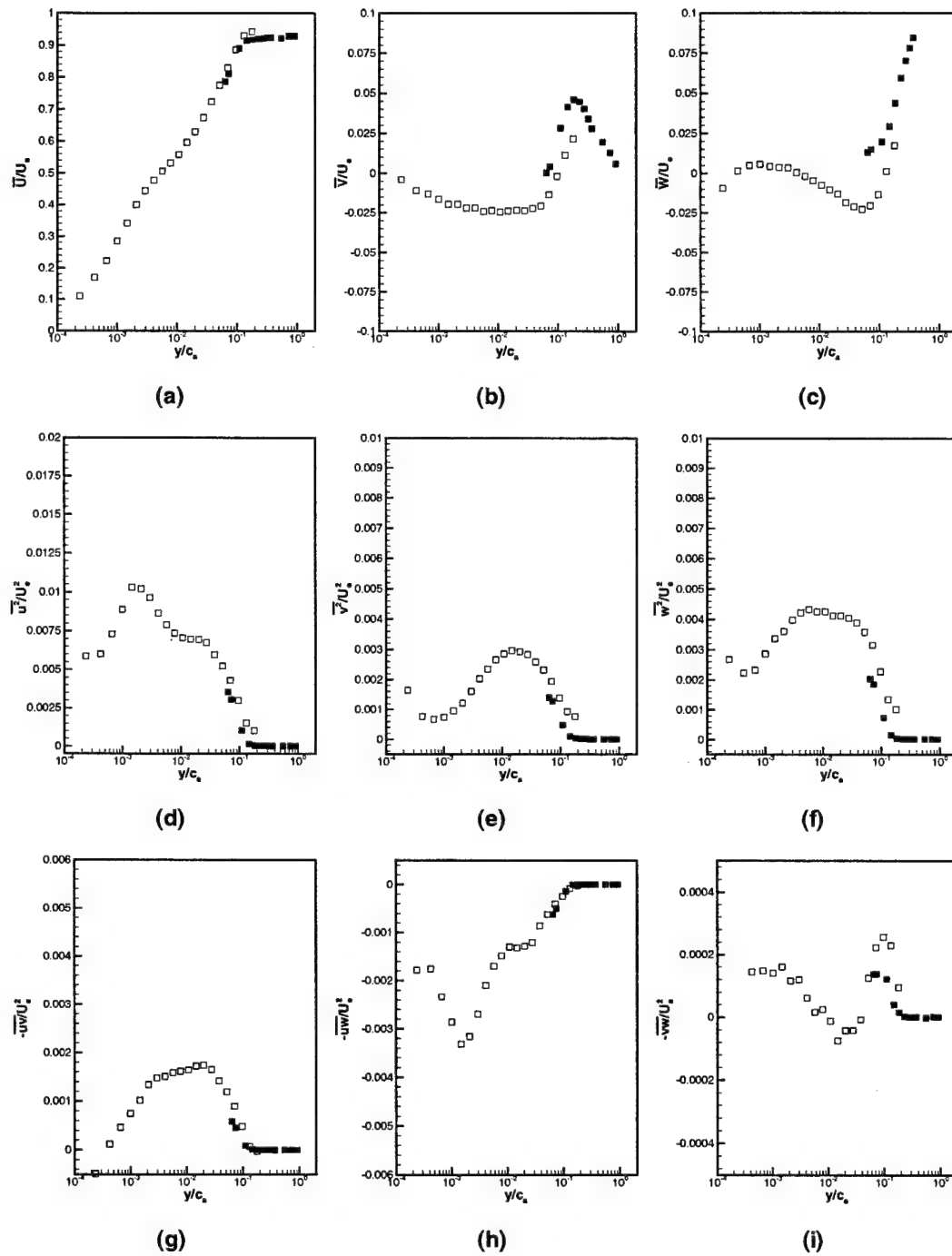


Figure 4.12: Profile 6F Compared with hot wire data ( $\square$  is 6F [ $x=2.5\text{cm}$   $z=-8.3\text{cm}$ ],  $\blacksquare$  hot-wire [ $x=3.7\text{cm}$   $z=-7.7\text{cm}$ ]) free-stream coordinate system

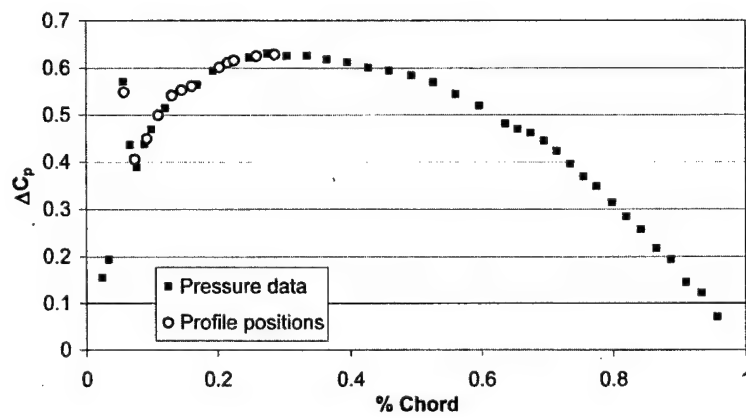


Figure 4.13: Blade loading, difference in pressure coefficient across blade (interpolated chord locations of experimental points)

Profile	$U_\tau$	$\Delta C_p$
3S	0.90	0.45
4S	0.97	0.55
5S	0.98	0.61
6S	1.06	0.63
3C	0.88	0.41
4C	0.93	0.54
5C	0.96	0.60
6C	1.06	0.63
3P	0.88	0.55
4P	0.87	0.50
5P	0.87	0.56
6P	0.94	0.62

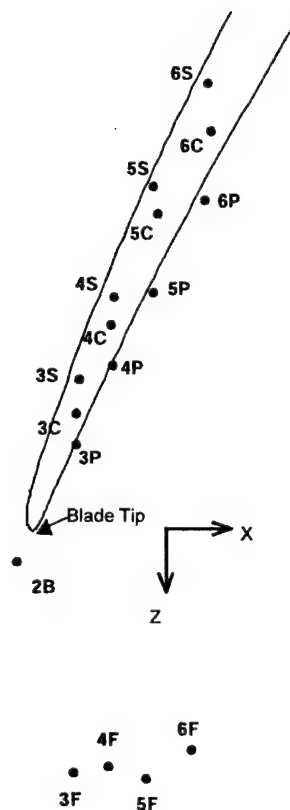
S = Suction side of blade  
C = Camberline of blade  
P = Pressure side of blade

• 1F1

Profile	$U_\tau$
1F1	0.96
3F	0.81
4F	0.82
5F	0.81
6F	0.78
2B	0.79

F = Freestream Flow  
B = Blade Tip

Freestream  
Direction

Figure 4.14: Schematic of Blade with  $U_\tau$  and  $\Delta C_p$

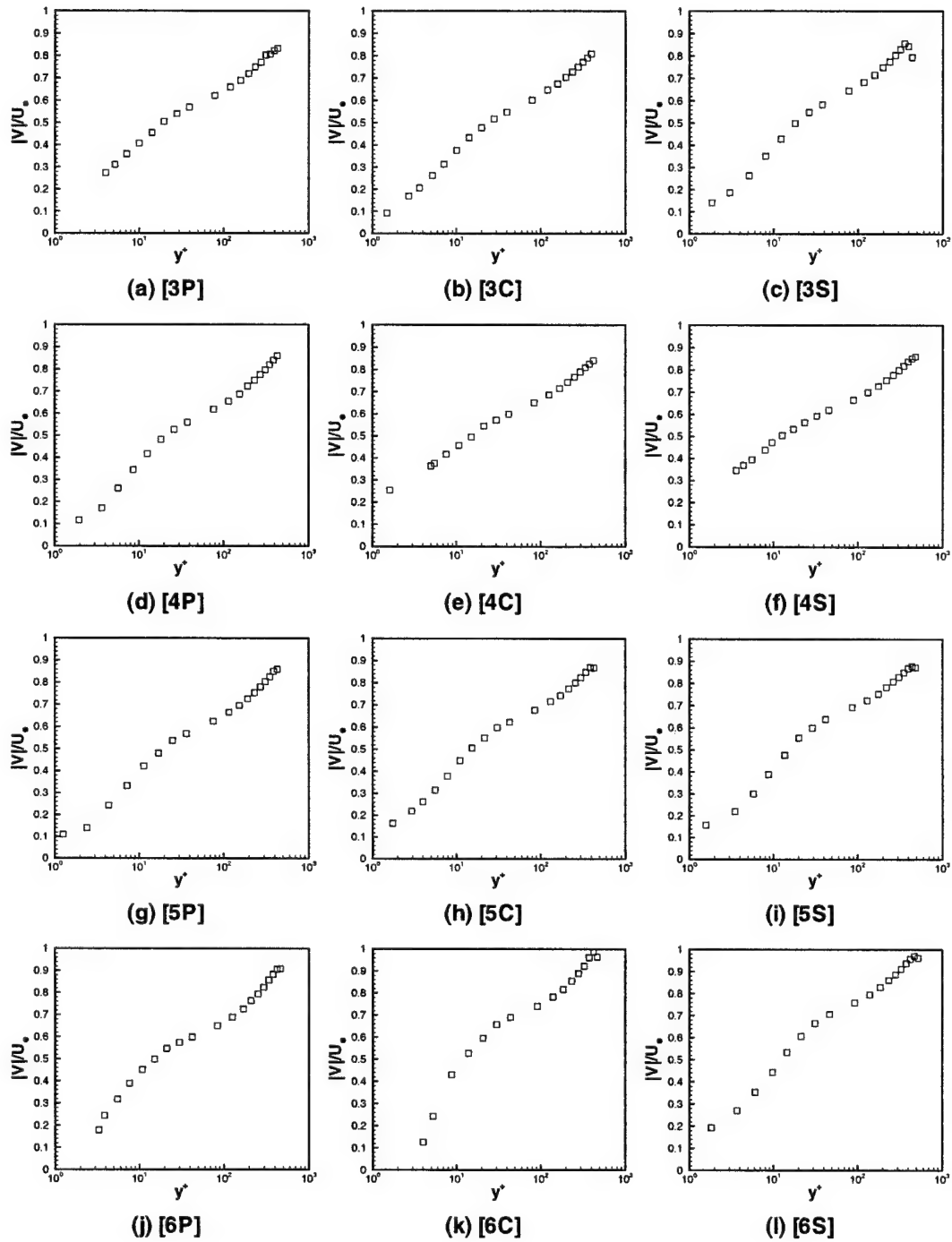
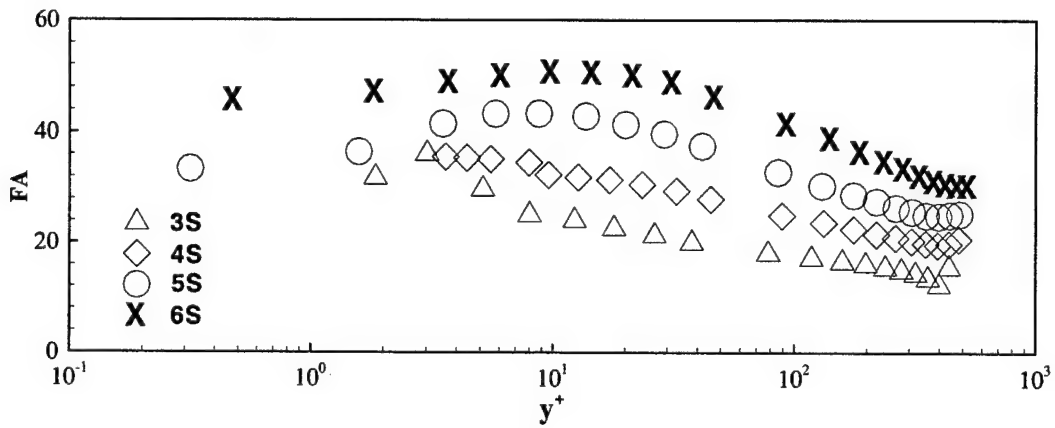
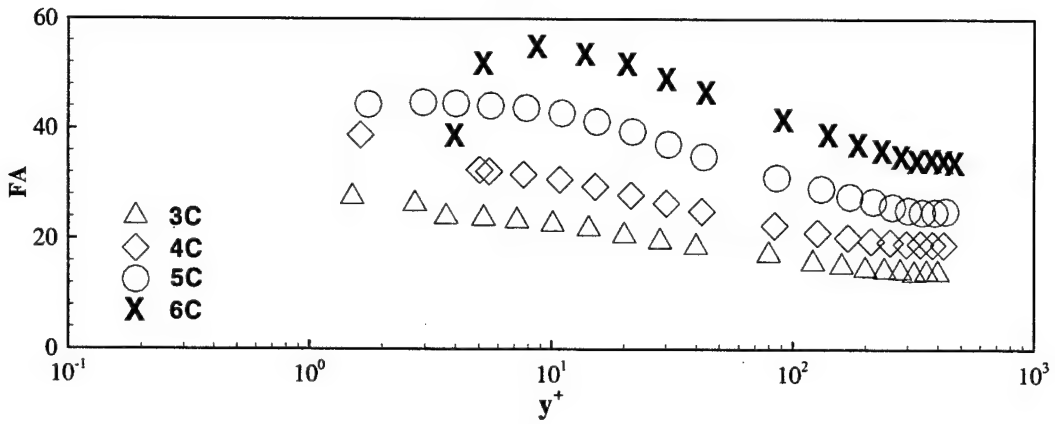


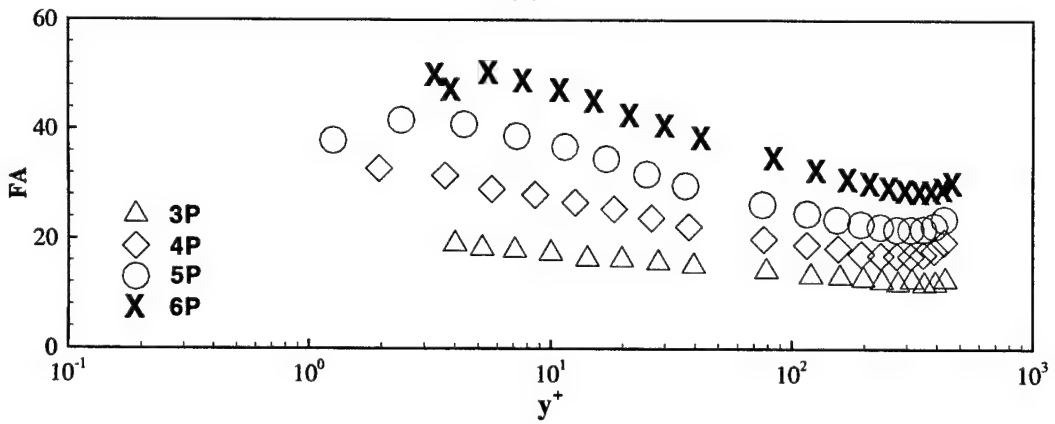
Figure 4.15: Tip gap velocity magnitudes normalized on free-stream velocity



(a)



(b)



(c)

Figure 4.16: Turning angles in the Tip gap vs.  $y^+$  (in chord coordinates)

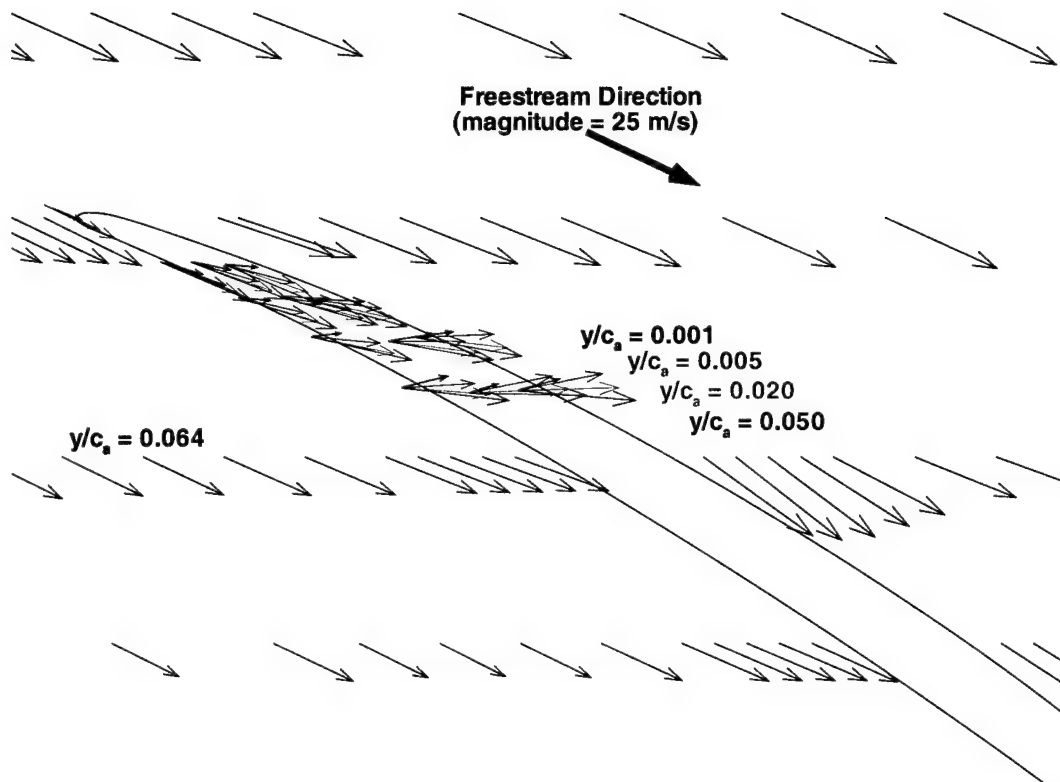


Figure 4.17:  $\bar{U}$  and  $\bar{W}$  Vectors with Tip Gap and Hot-wire data

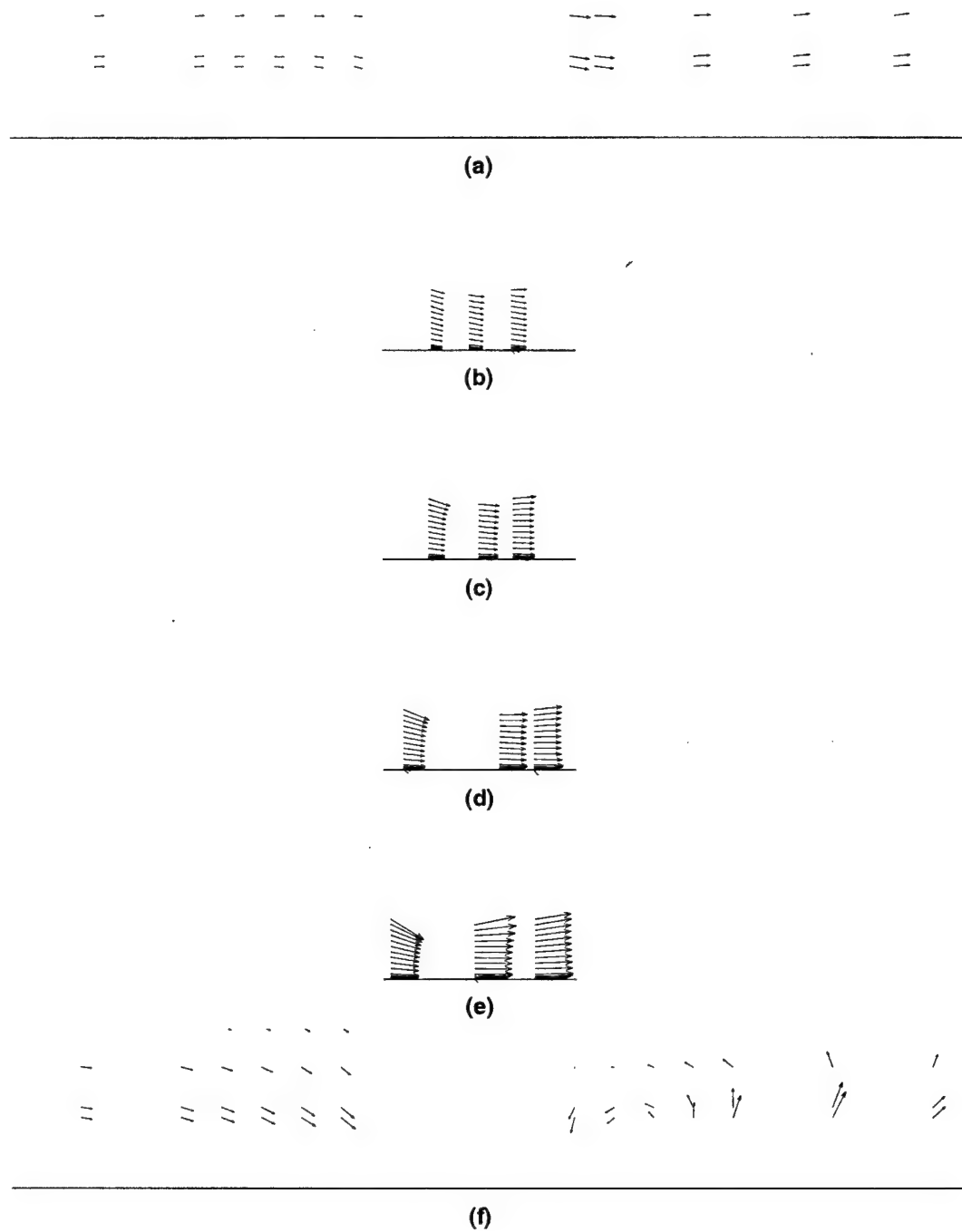
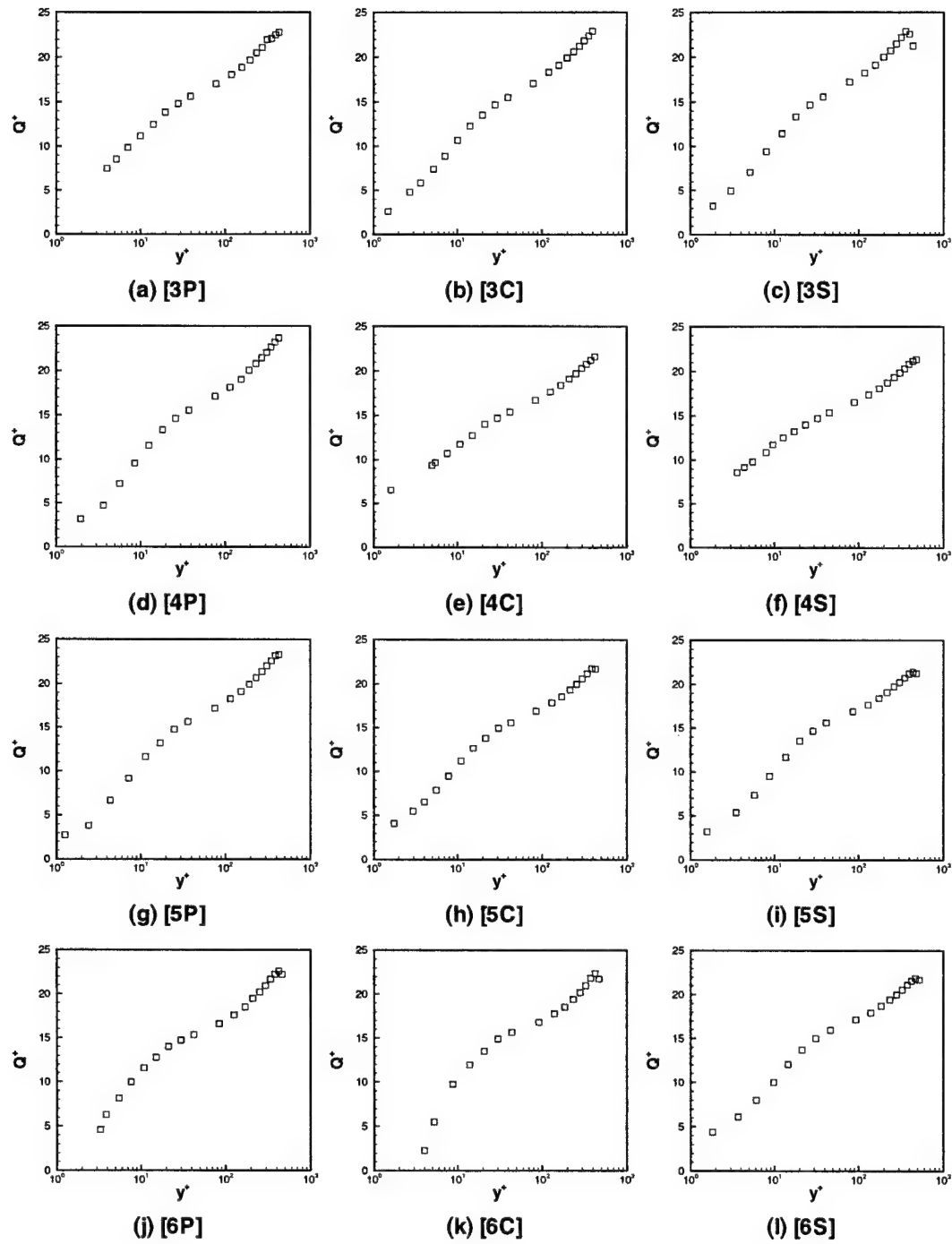
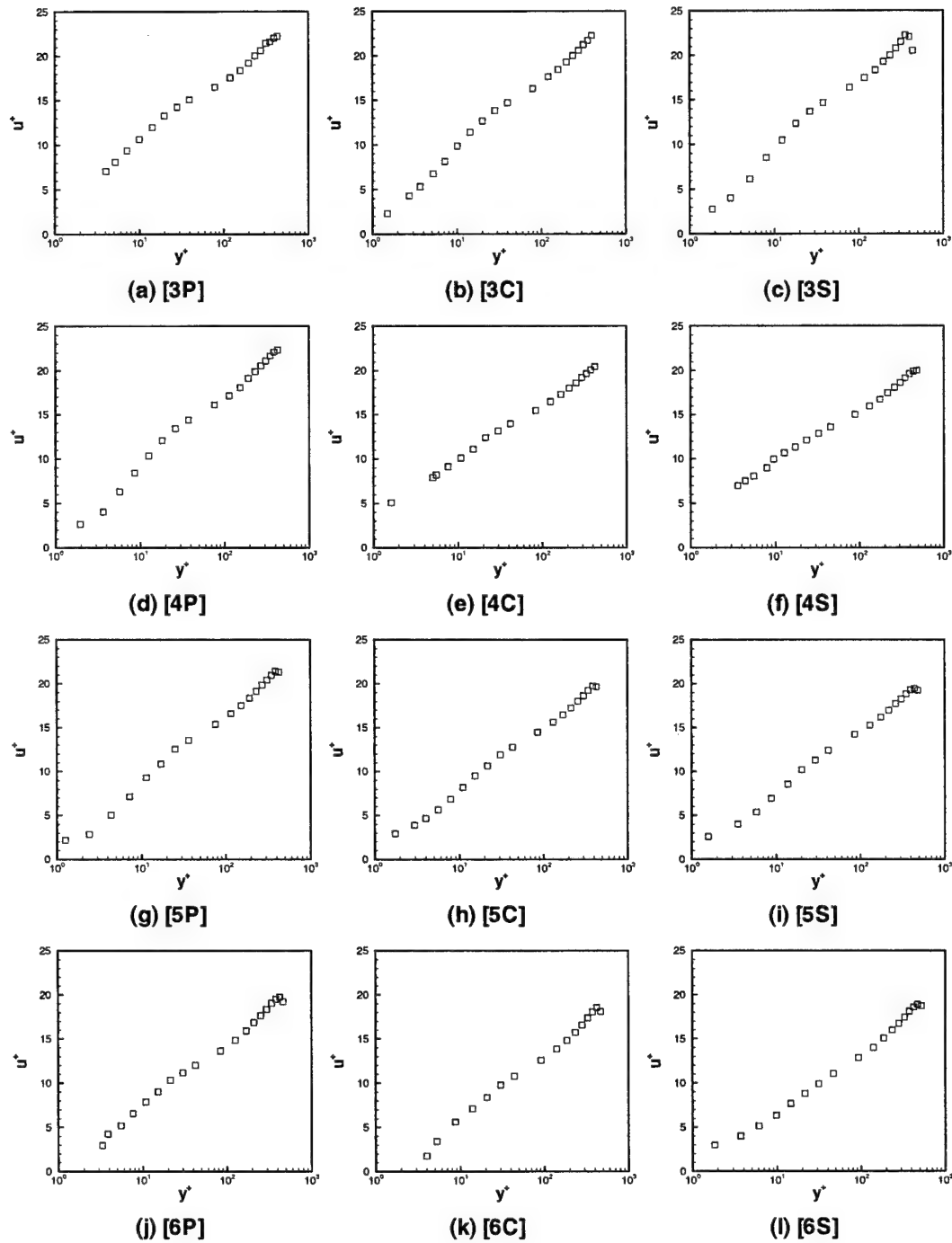
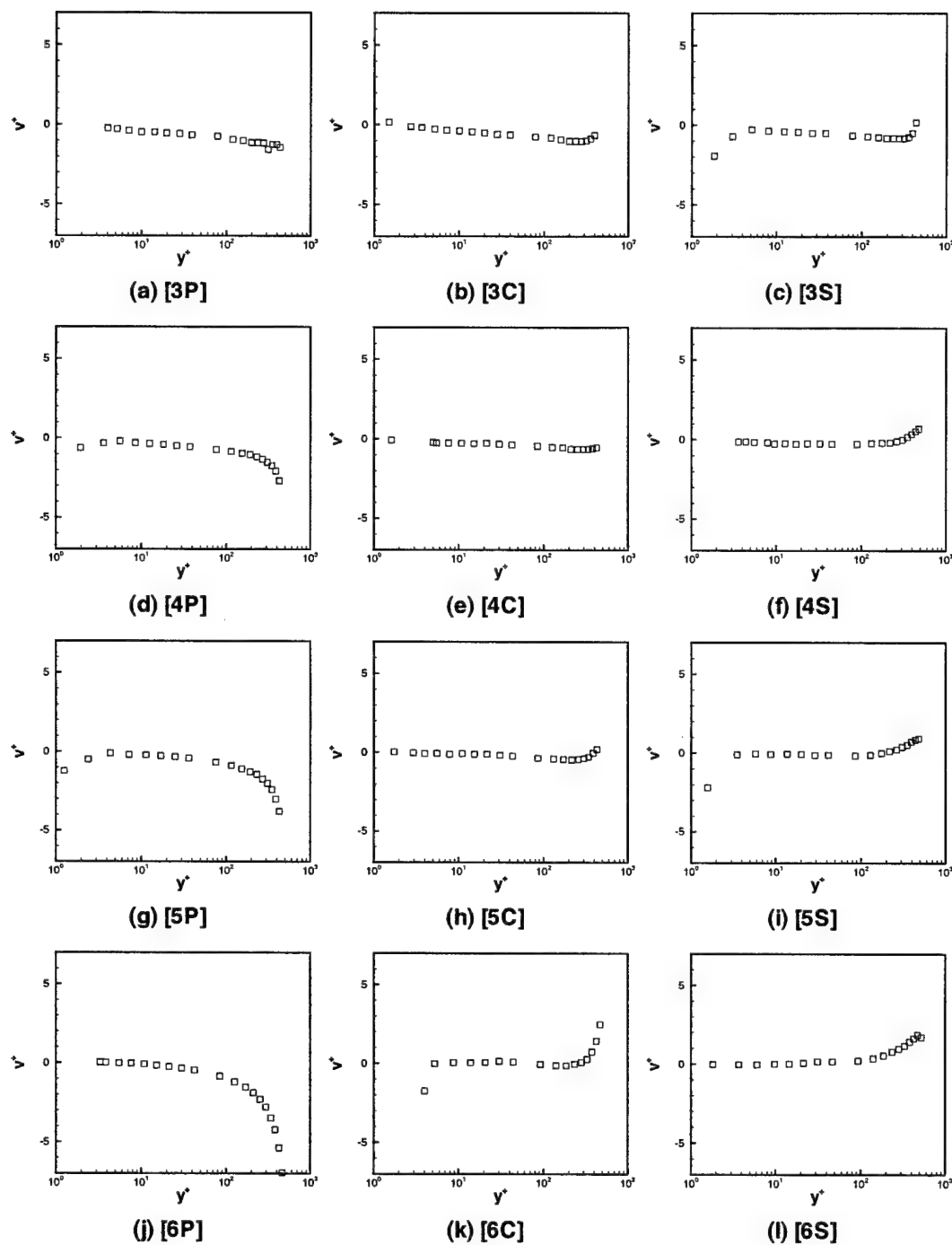


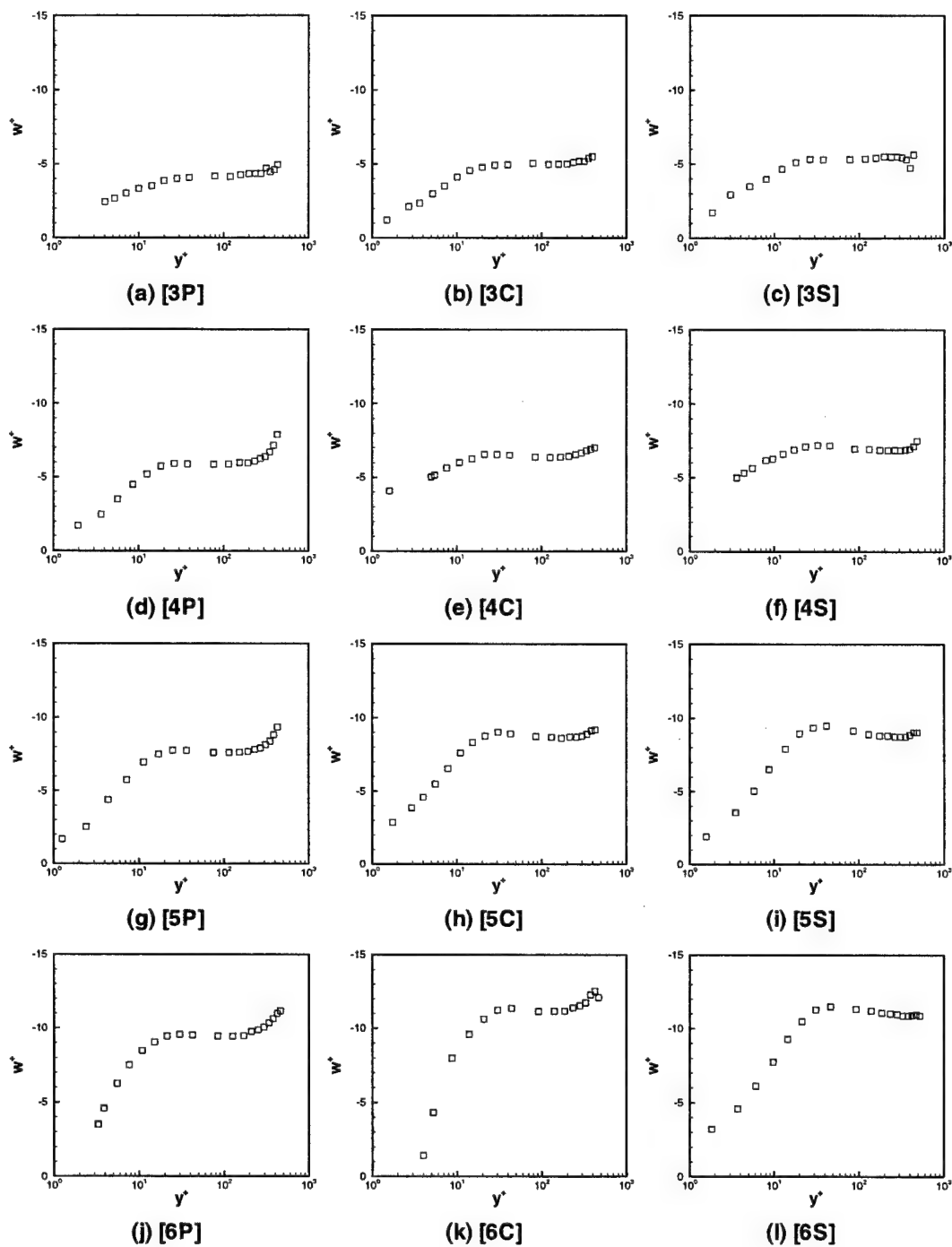
Figure 4.18:  $\bar{V}$   $\bar{W}$  chord coordinate system tip gap plot [(a): $x/c_a=0$  (hot-wire), (b): $x/c_a=0.05$ , (c): $x/c_a=0.09$ , (d): $x/c_a=0.14$ , (e): $x/c_a=0.19$ , (f): $x/c_a=0.27$  (hot-wire)]

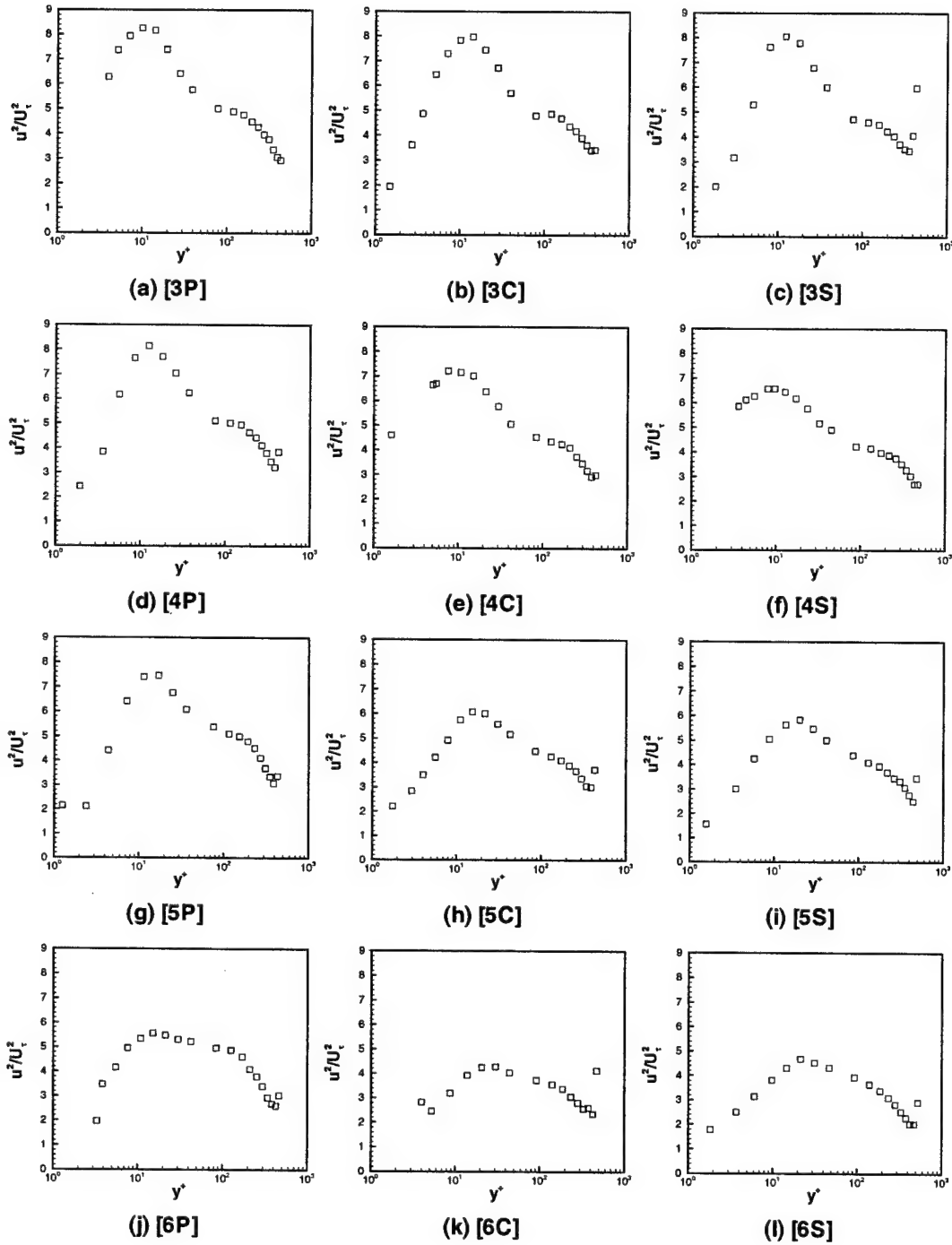


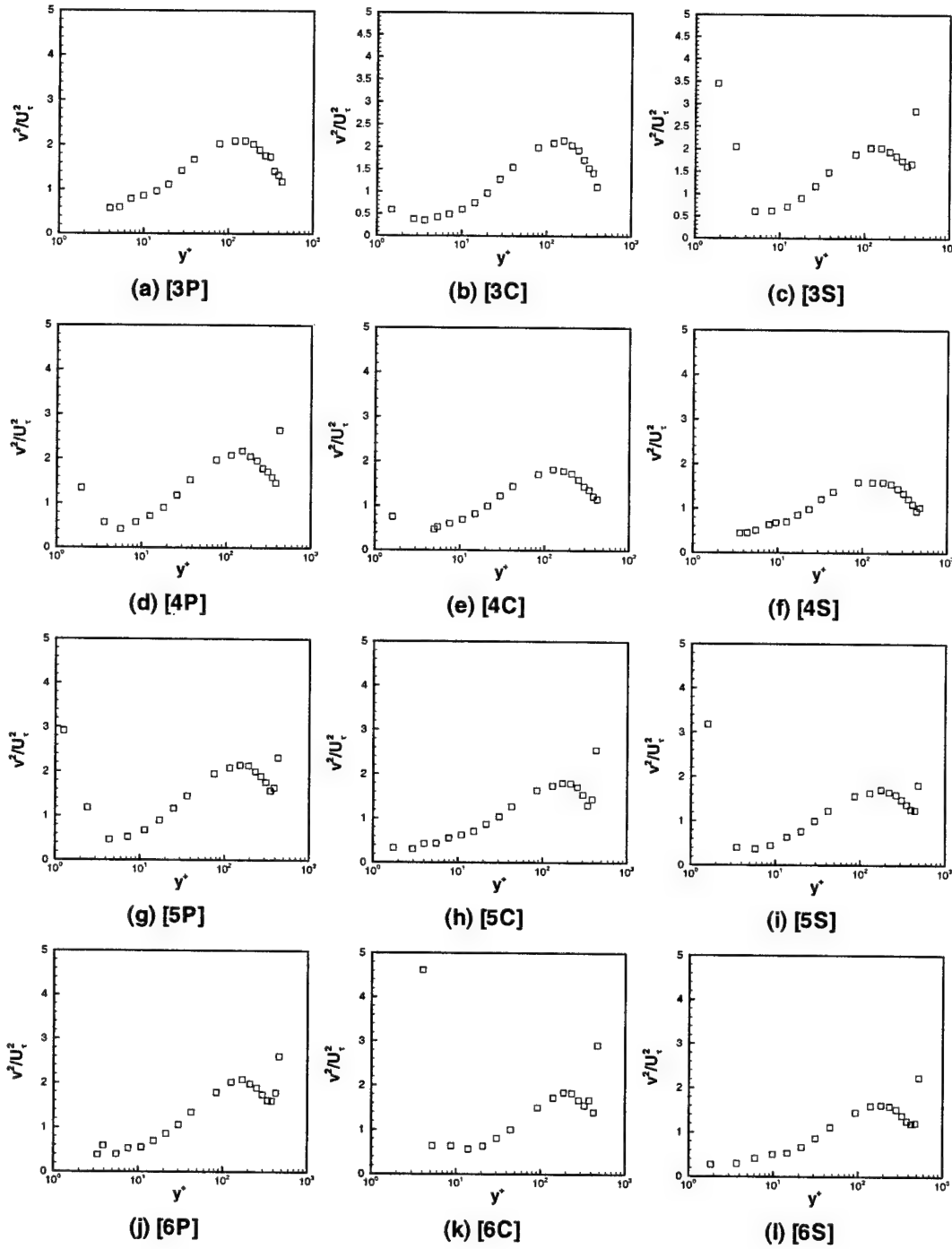
Figure 4.19:  $Q^+$  under the Blade vs  $y^+$

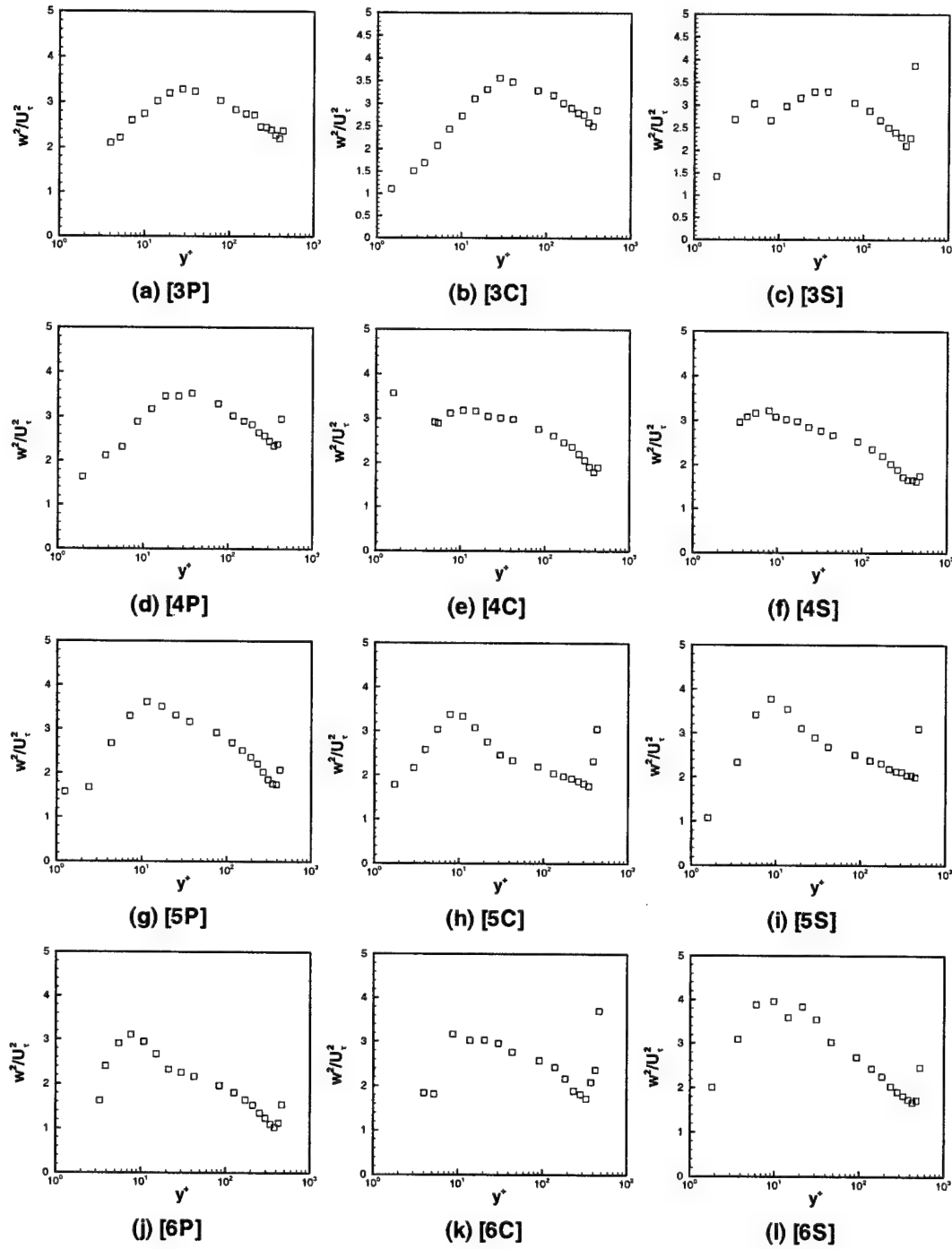
Figure 4.20:  $u^+$  under the Blade vs  $y^+$

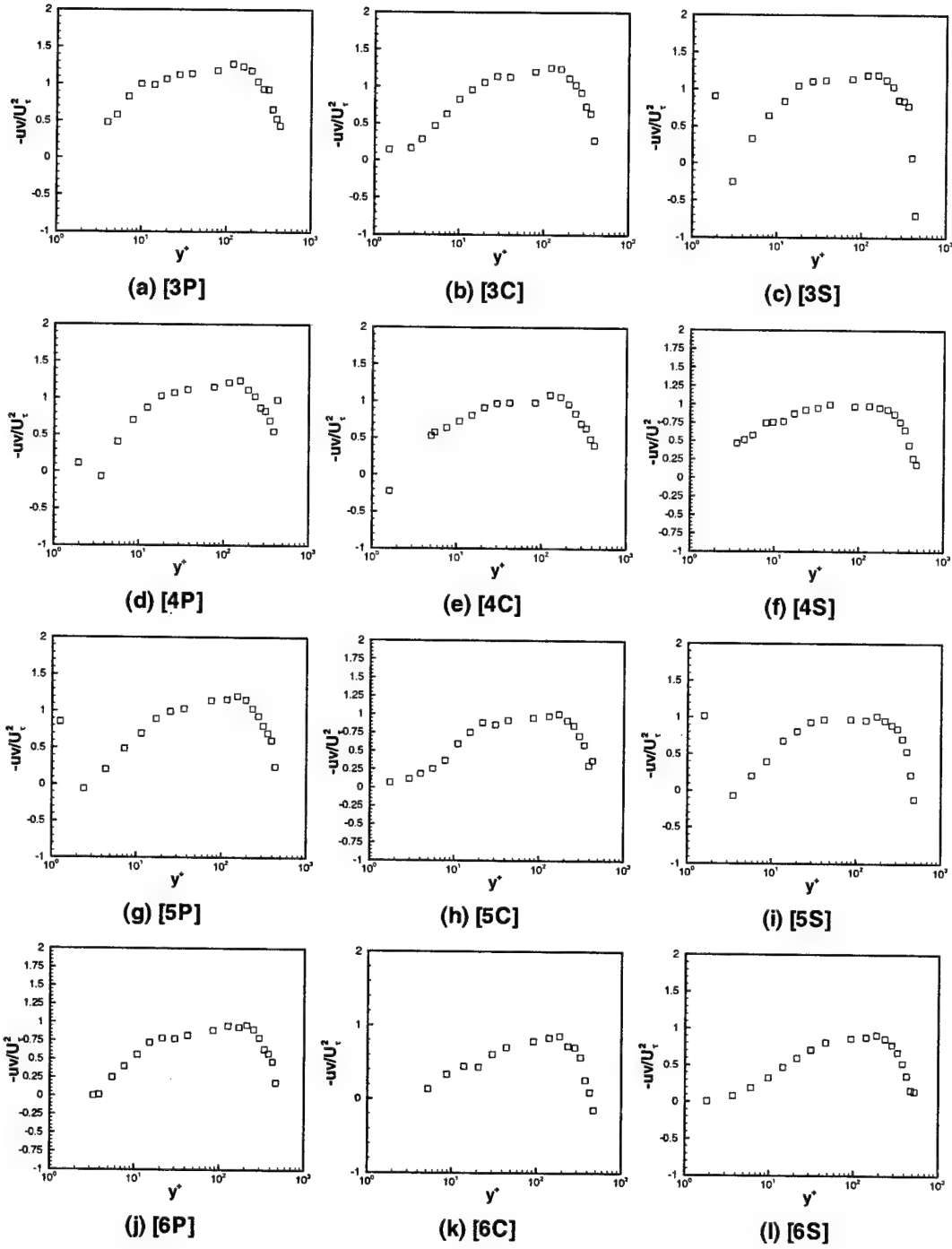
Figure 4.21:  $v^+$  under the Blade vs  $y^+$

Figure 4.22:  $w^+$  under the Blade vs  $y^+$

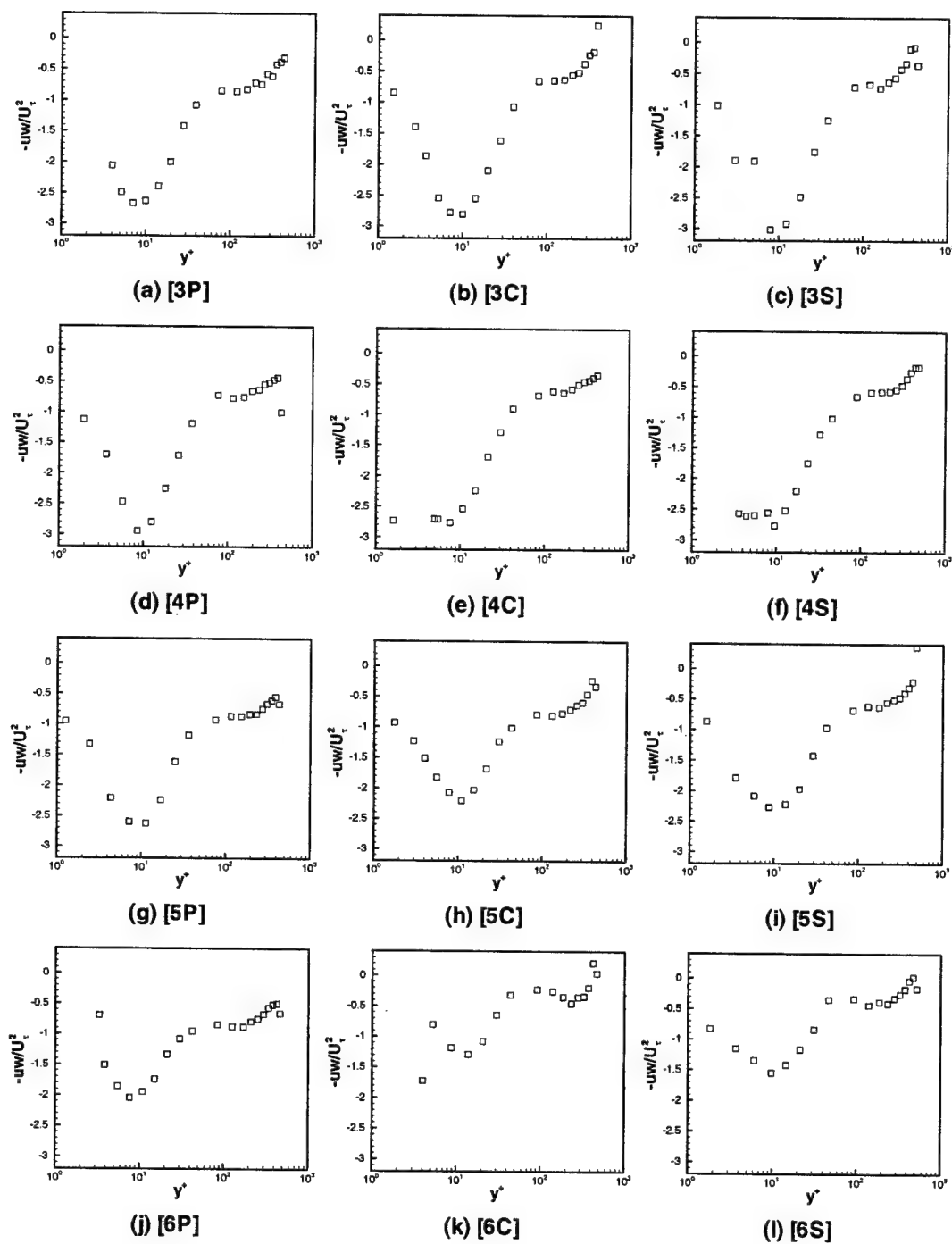
Figure 4.23:  $\overline{u'^2}/U_\tau^2$  under the Blade vs  $y^+$

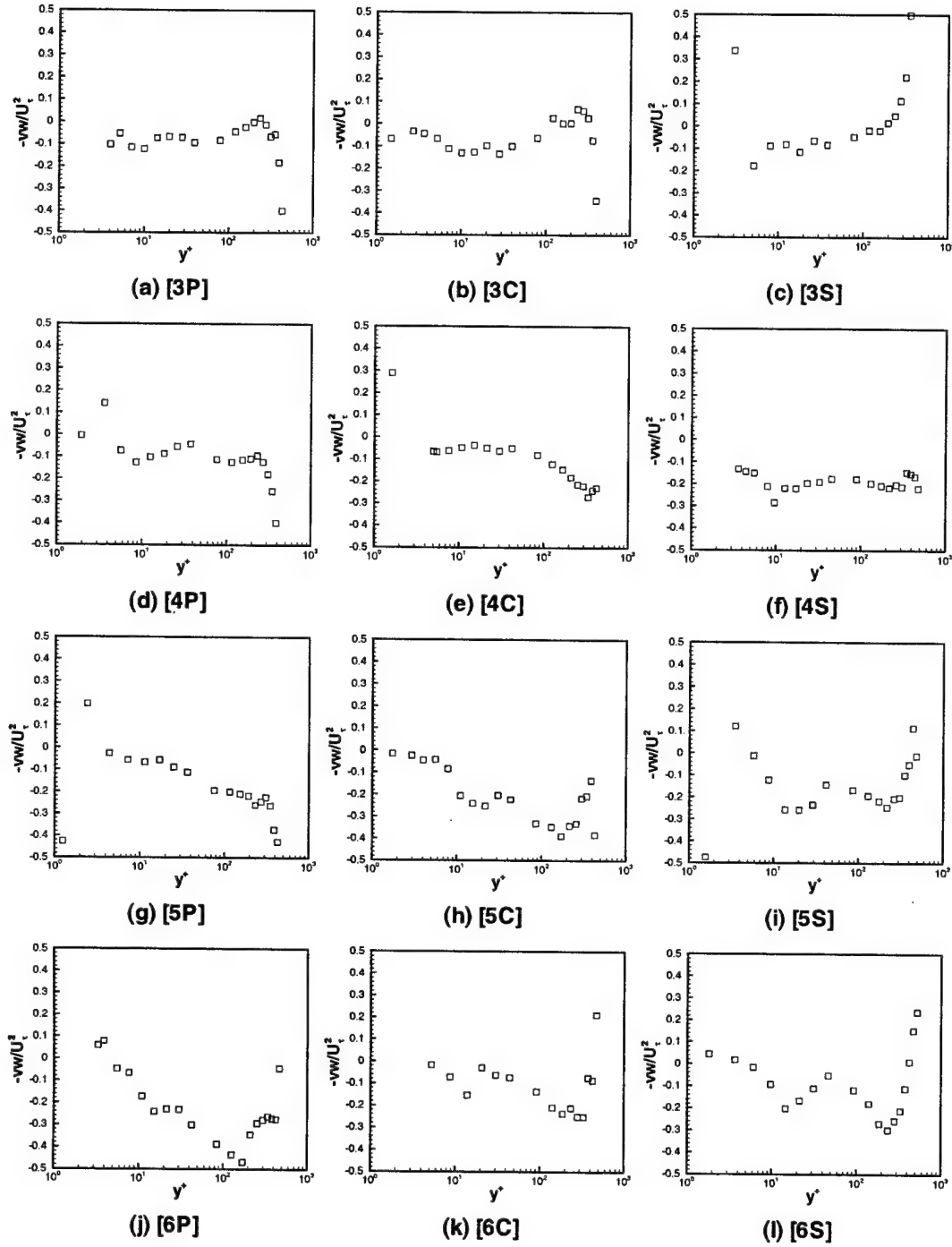
Figure 4.24:  $\overline{v^2}/U_\tau^2$  under the Blade vs  $y^+$

Figure 4.25:  $\overline{w^2}/U_\tau^2$  under the Blade vs  $y^+$

Figure 4.26:  $-\overline{uv}/U_\tau^2$  under the Blade vs  $y^+$



Figure 4.27:  $-\overline{uw}/U_\tau^2$  under the Blade vs  $y^+$

Figure 4.28:  $-\overline{vw}/U_\tau^2$  under the Blade vs  $y^+$

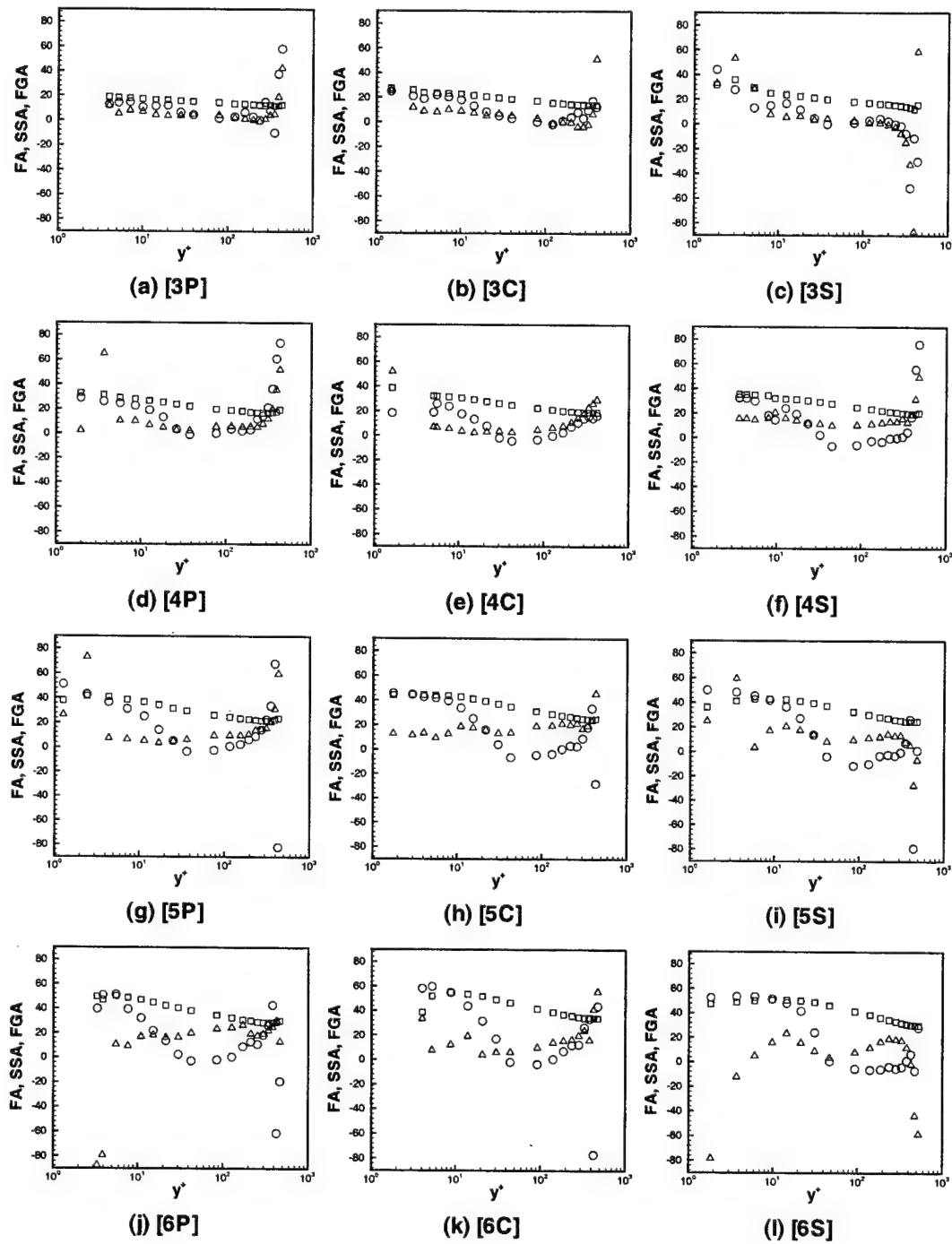


Figure 4.29: Turning Angle ( $\square$ ), Shear Stress Angle ( $\triangle$ ) and Flow Gradient Angle ( $\circ$ ) under the Blade vs  $y^+$

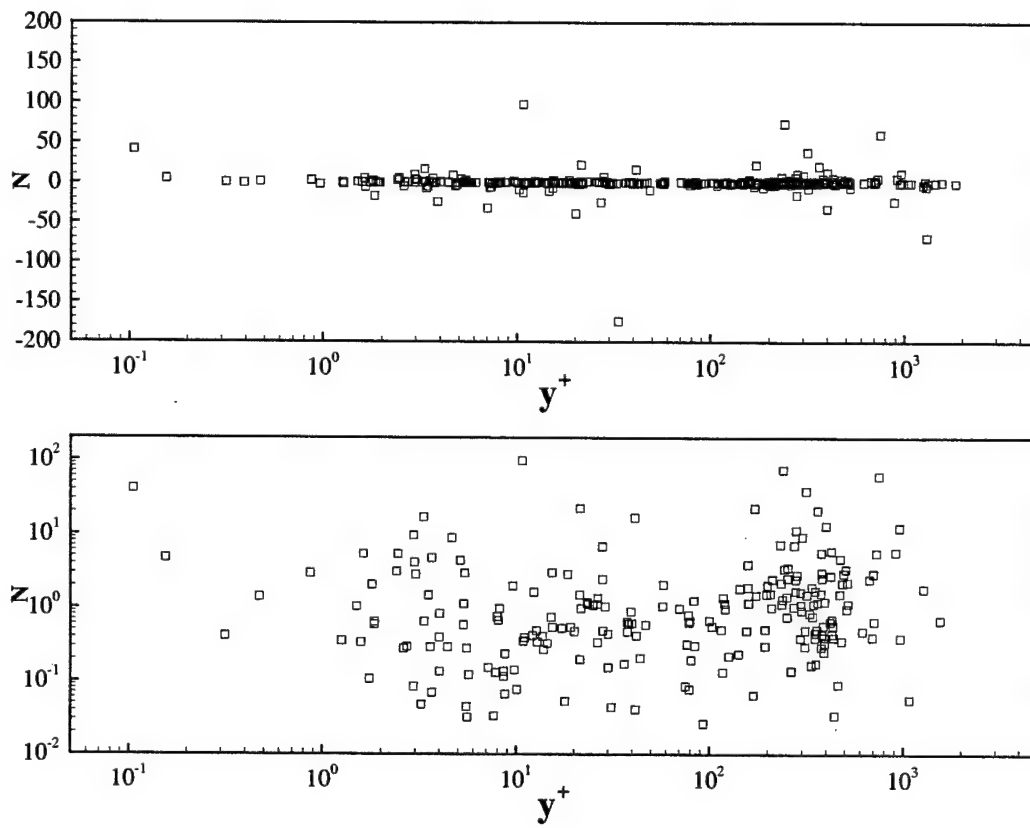
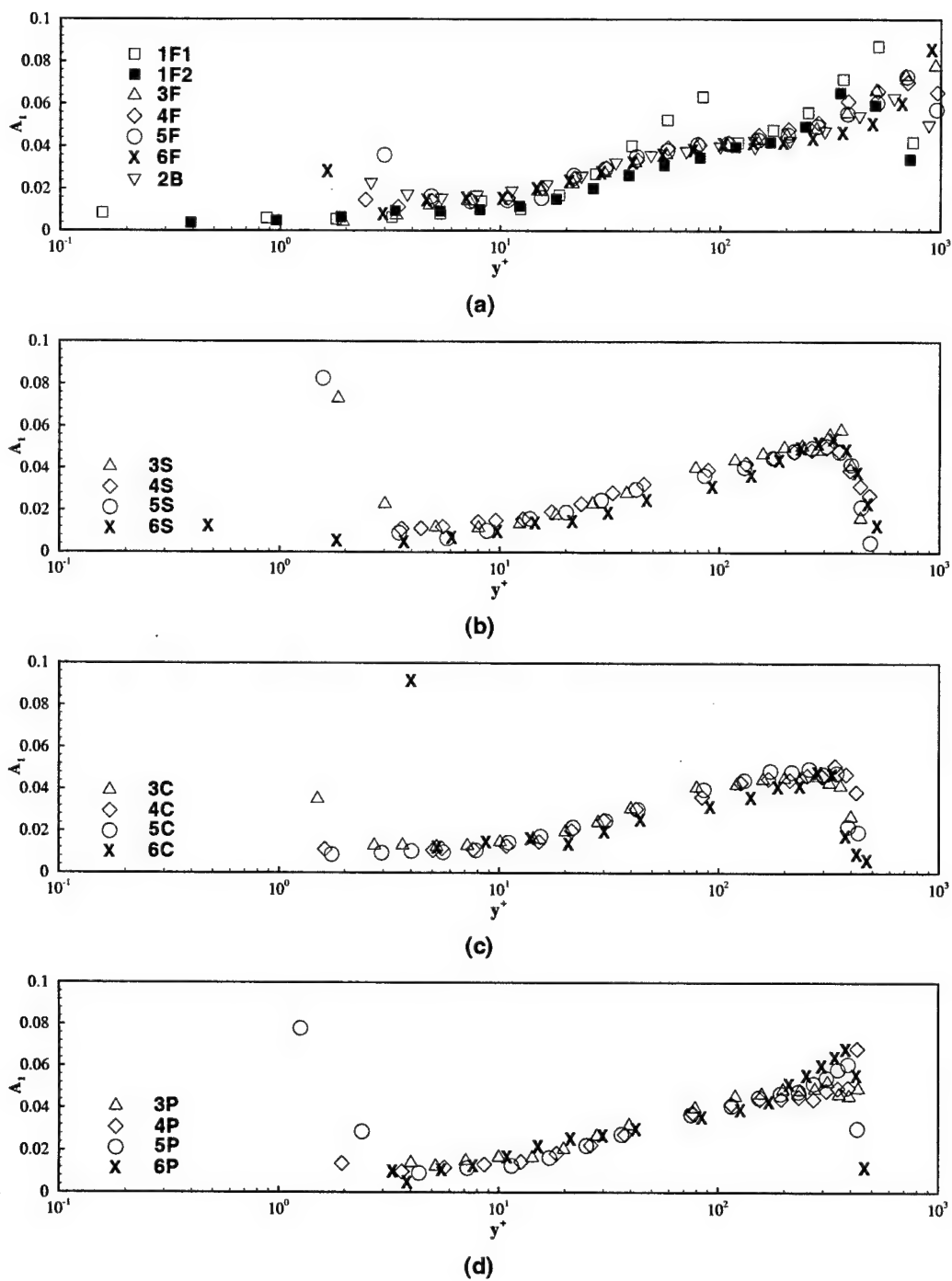
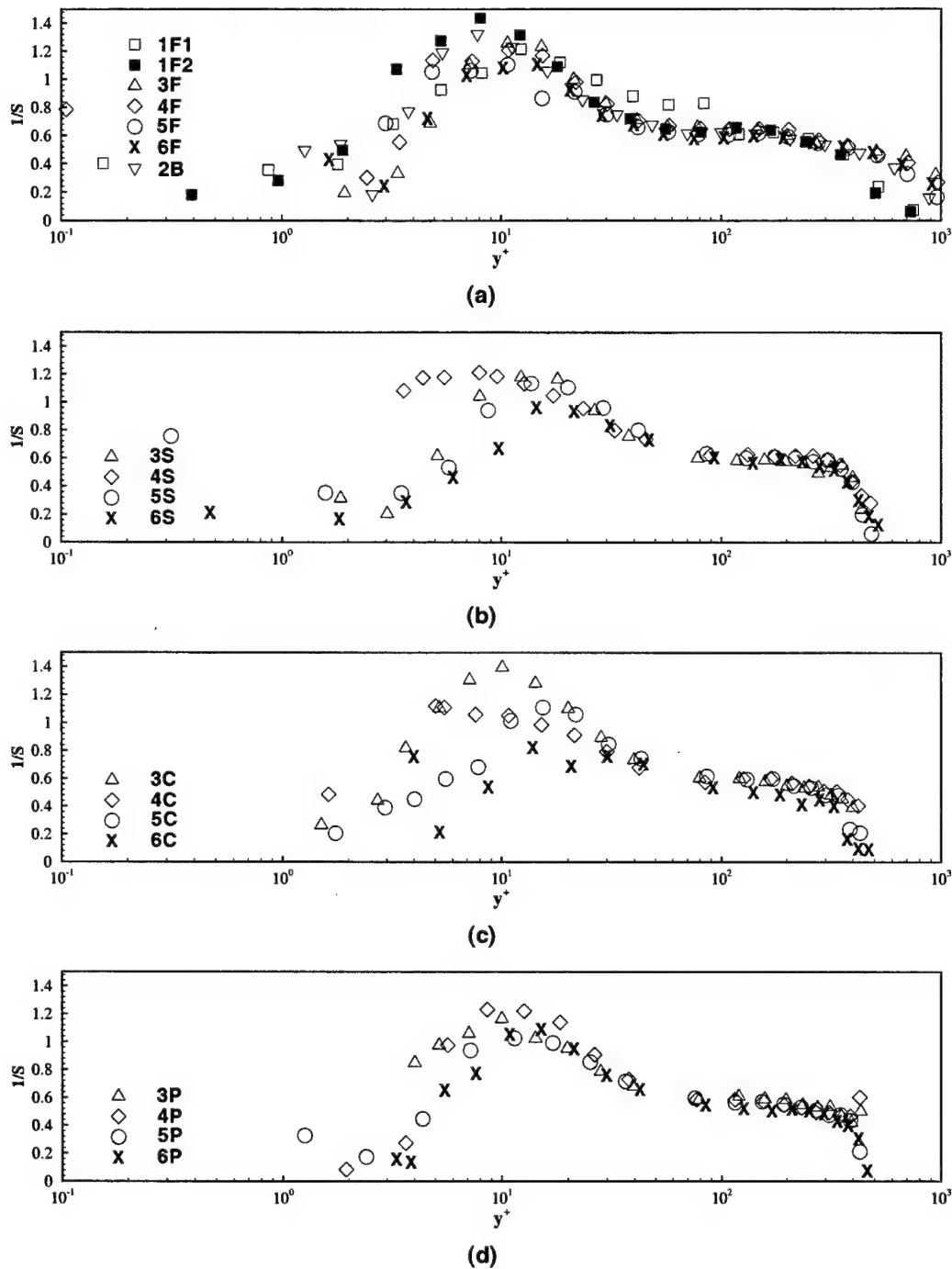


Figure 4.30: Anisotropy Factor

Figure 4.31:  $A_1$ , Shear Stress:TKE Ratio

Figure 4.32:  $1/S$ , Shear Stress:Fluctuating  $\bar{V}$  Velocity Ratio

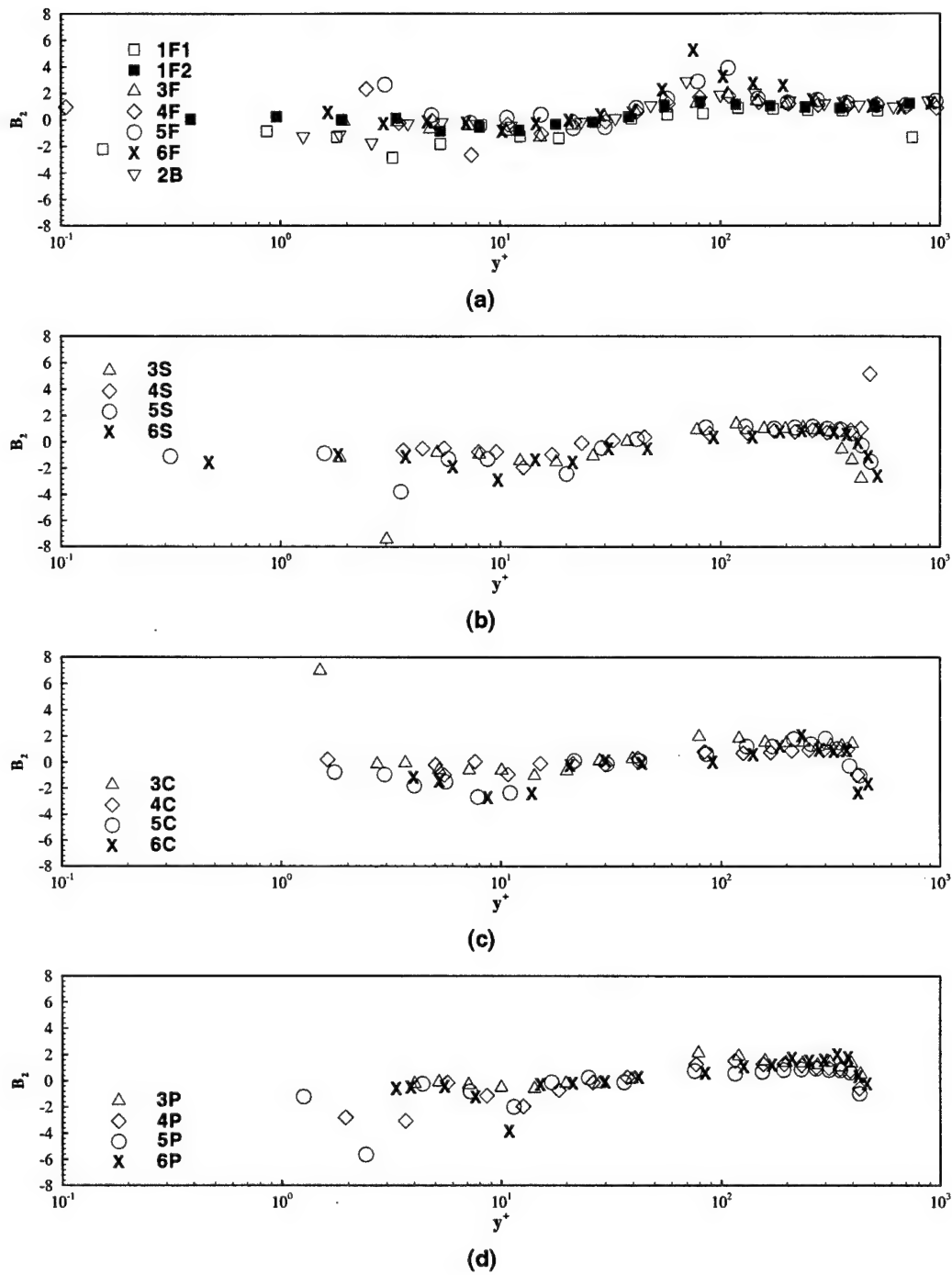


Figure 4.33: B2, V Transport:Y Direction Stresses

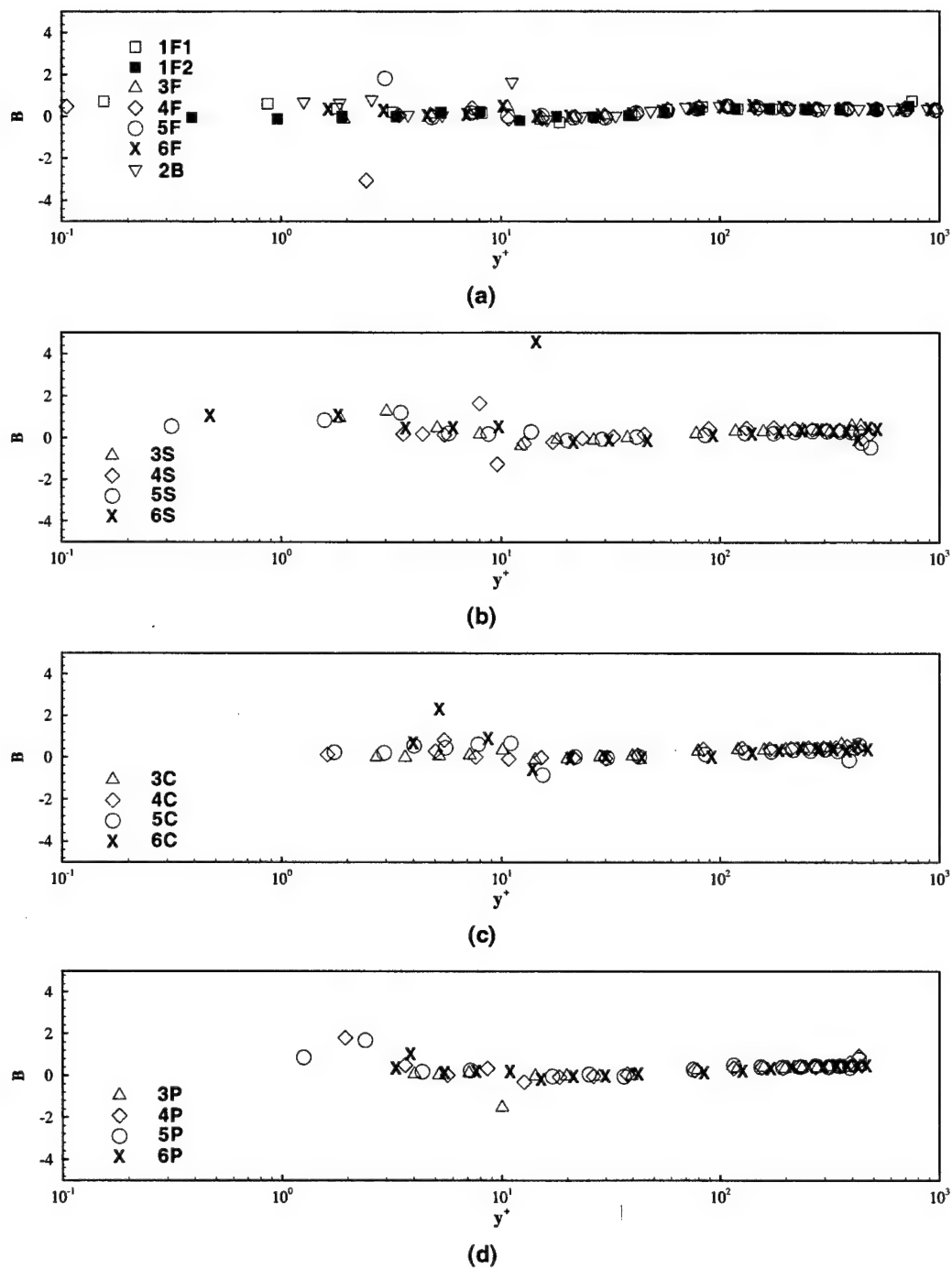


Figure 4.34: B, V Transport:TKE Ratio



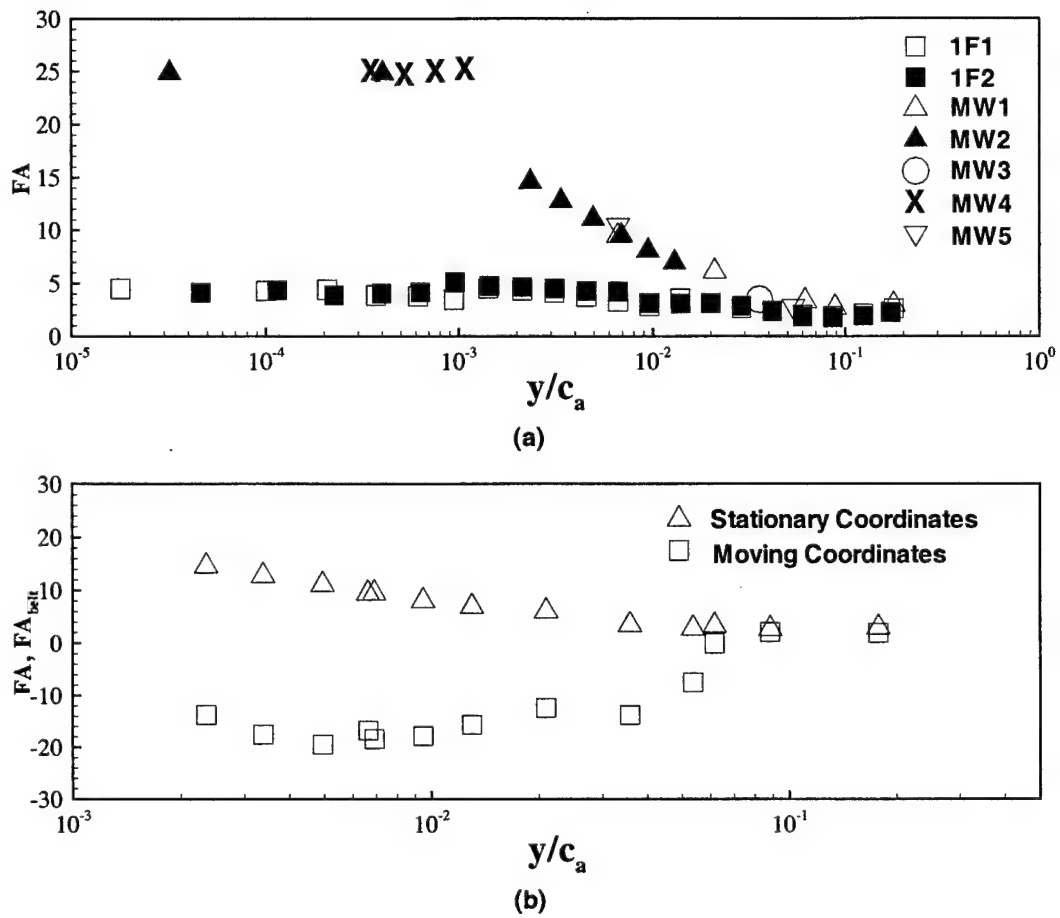


Figure 4.35: Moving Wall Flow Angle Plot with stationary wall

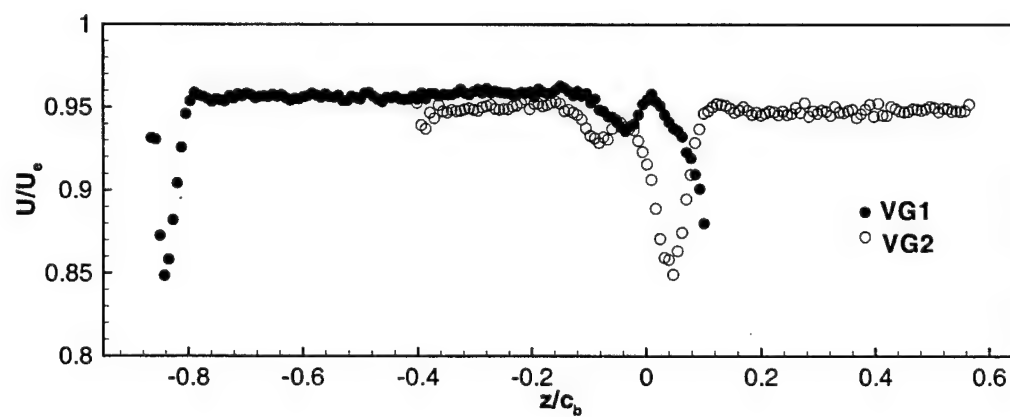


Figure 4.36: Vortex Generator Data Unshifted and Unmatched

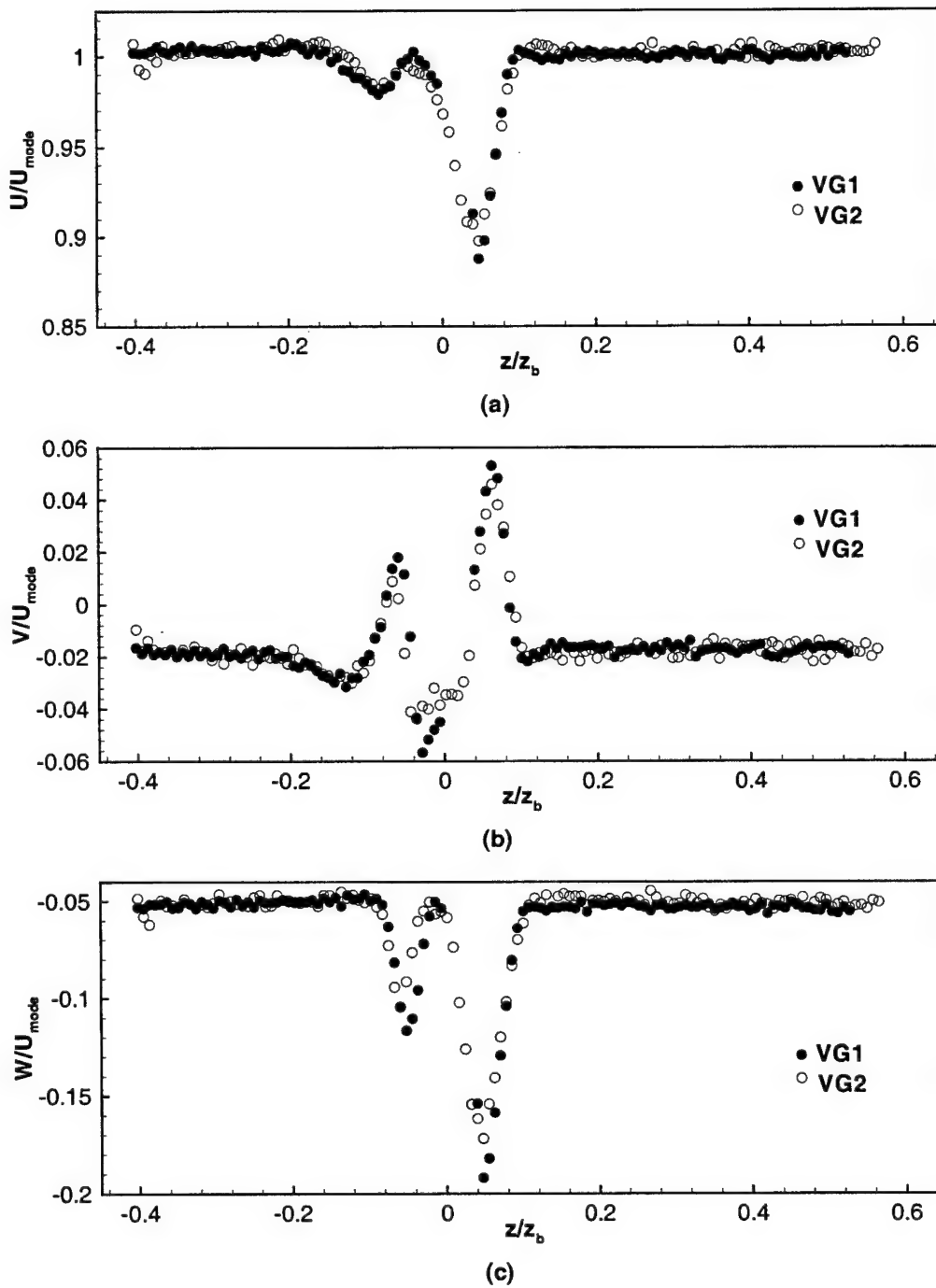
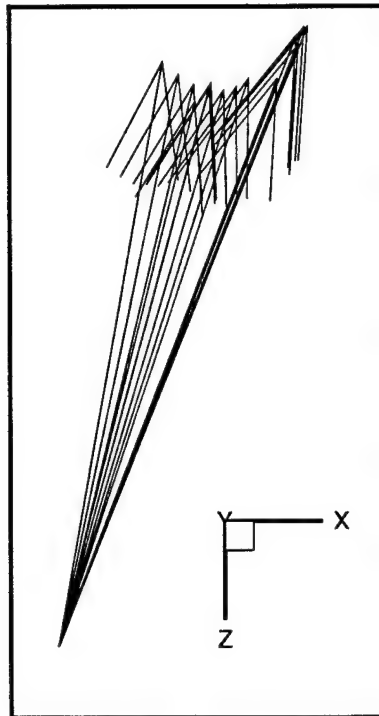
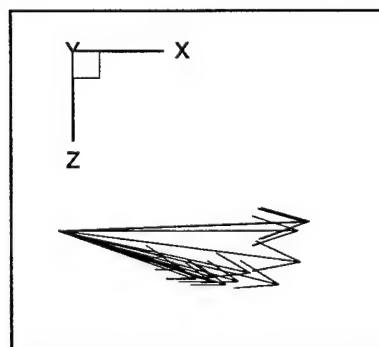


Figure 4.37: Vortex Generator Data shifted and matched



(a)



(b)

Figure 4.38: Moving Wall  $\overline{U}$   $\overline{W}$  vector plots, showing bed coordinate system [(a) stationary coordinate system (b) moving wall coordinate system]

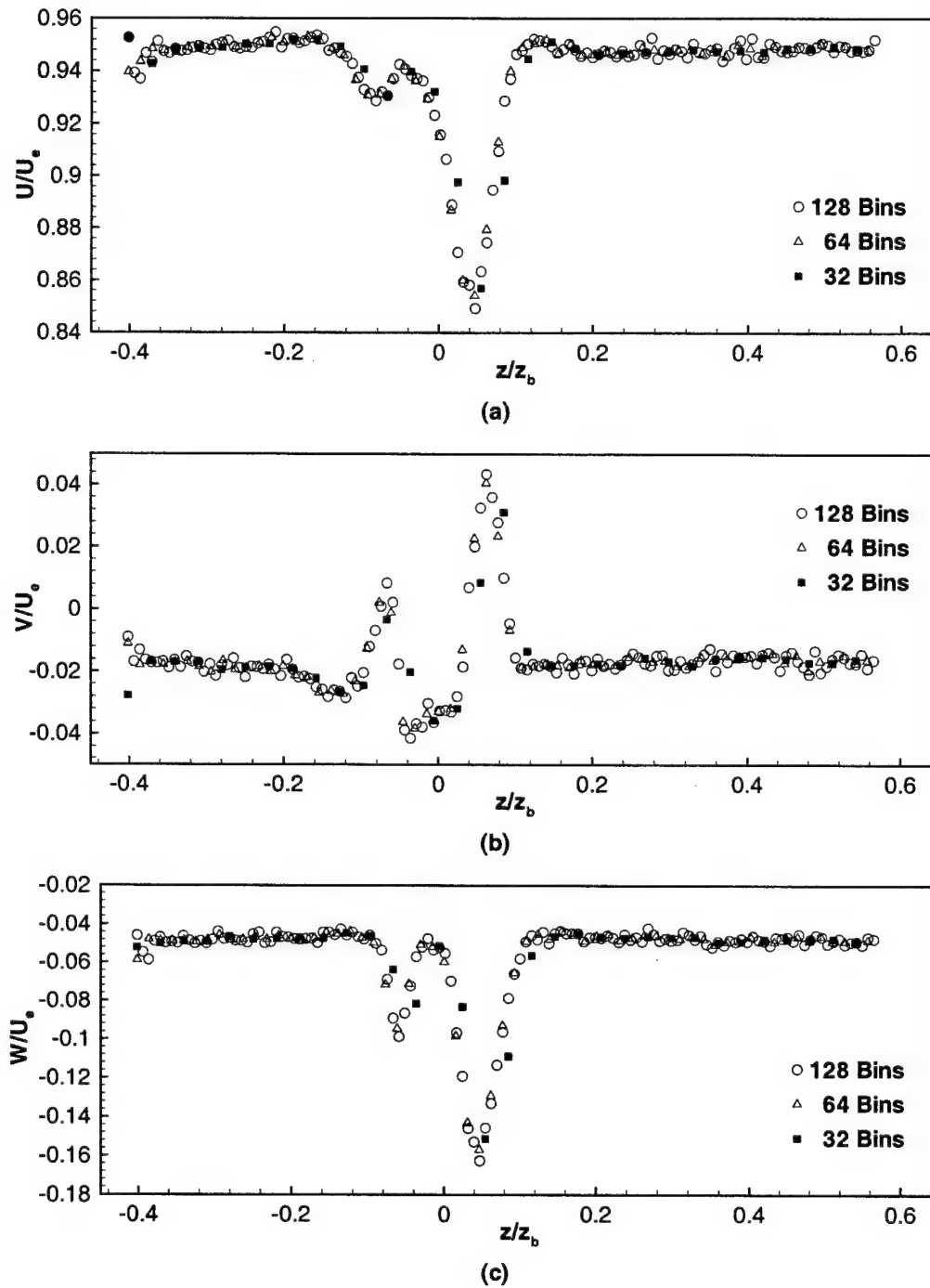
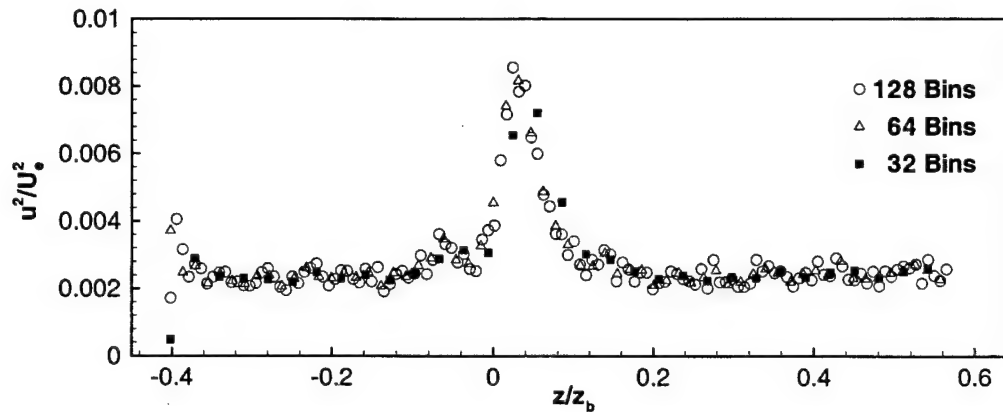
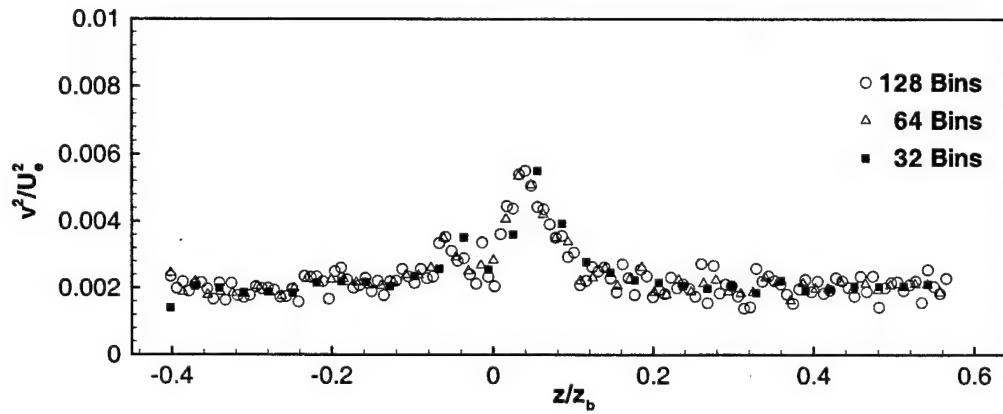


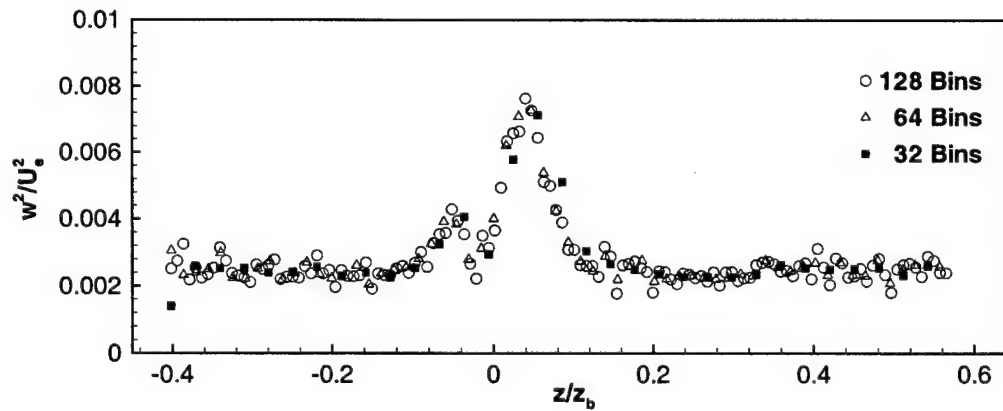
Figure 4.39: Vortex Generator bin size comparison, mean velocities, in upstream coordinate system



(a)



(b)



(c)

Figure 4.40: Vortex Generator bin size comparison, Reynolds normal stresses, in upstream coordinate system

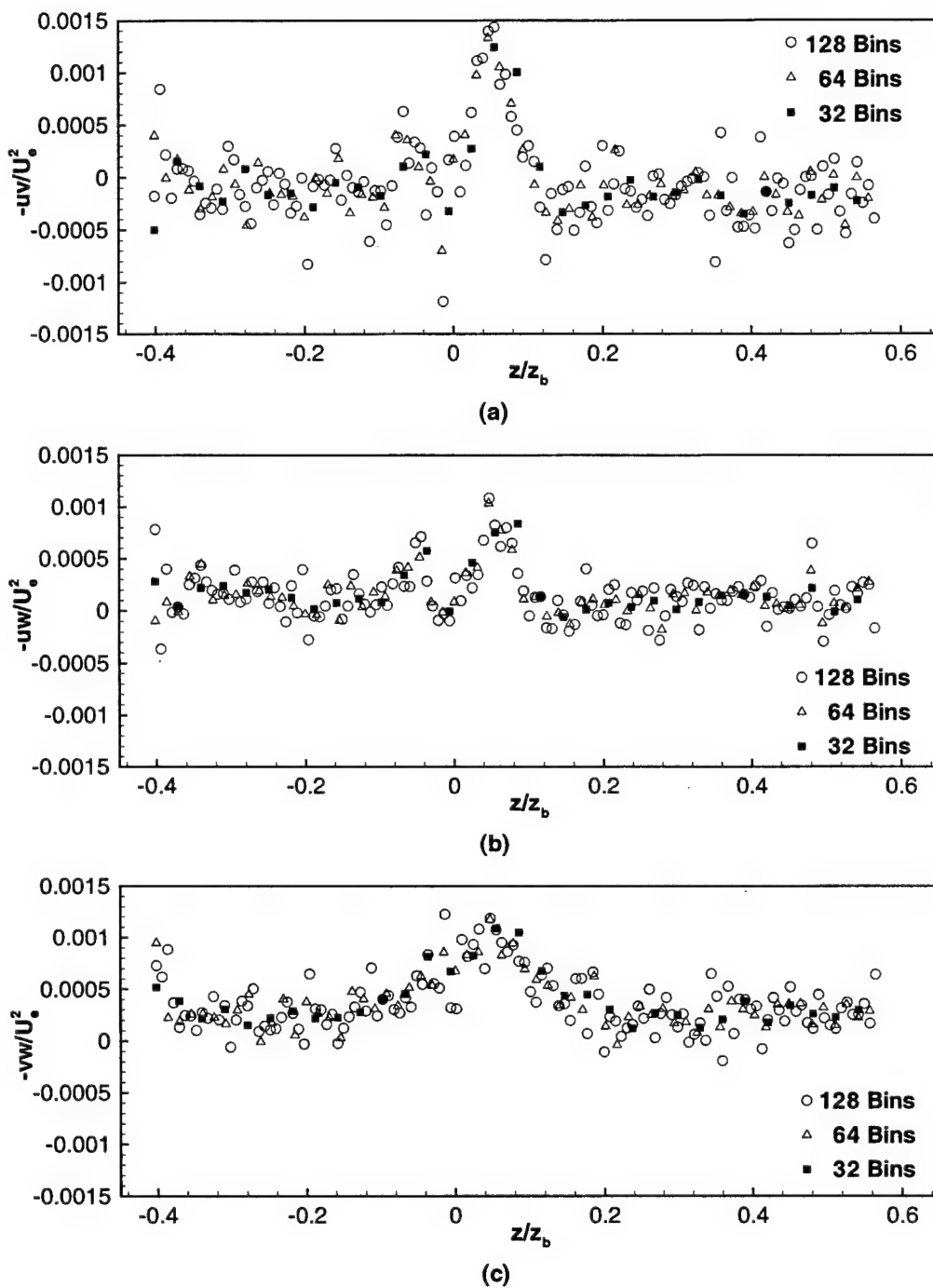


Figure 4.41: Vortex Generator bin size comparison, Reynolds shear stresses, in upstream coordinate system

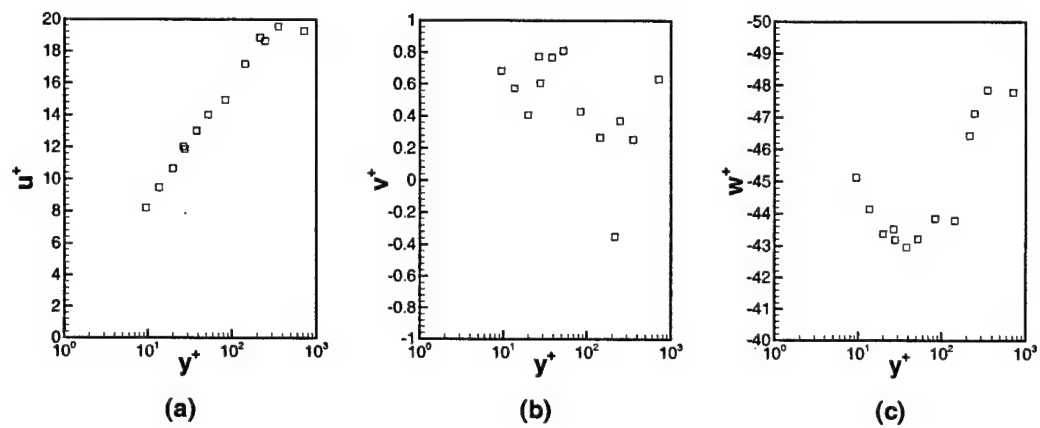


Figure 4.42: Moving wall flow mean velocities, in bed coordinate system (note:  $\overline{W}_{movingwall}/U_\tau = -47.85$ )



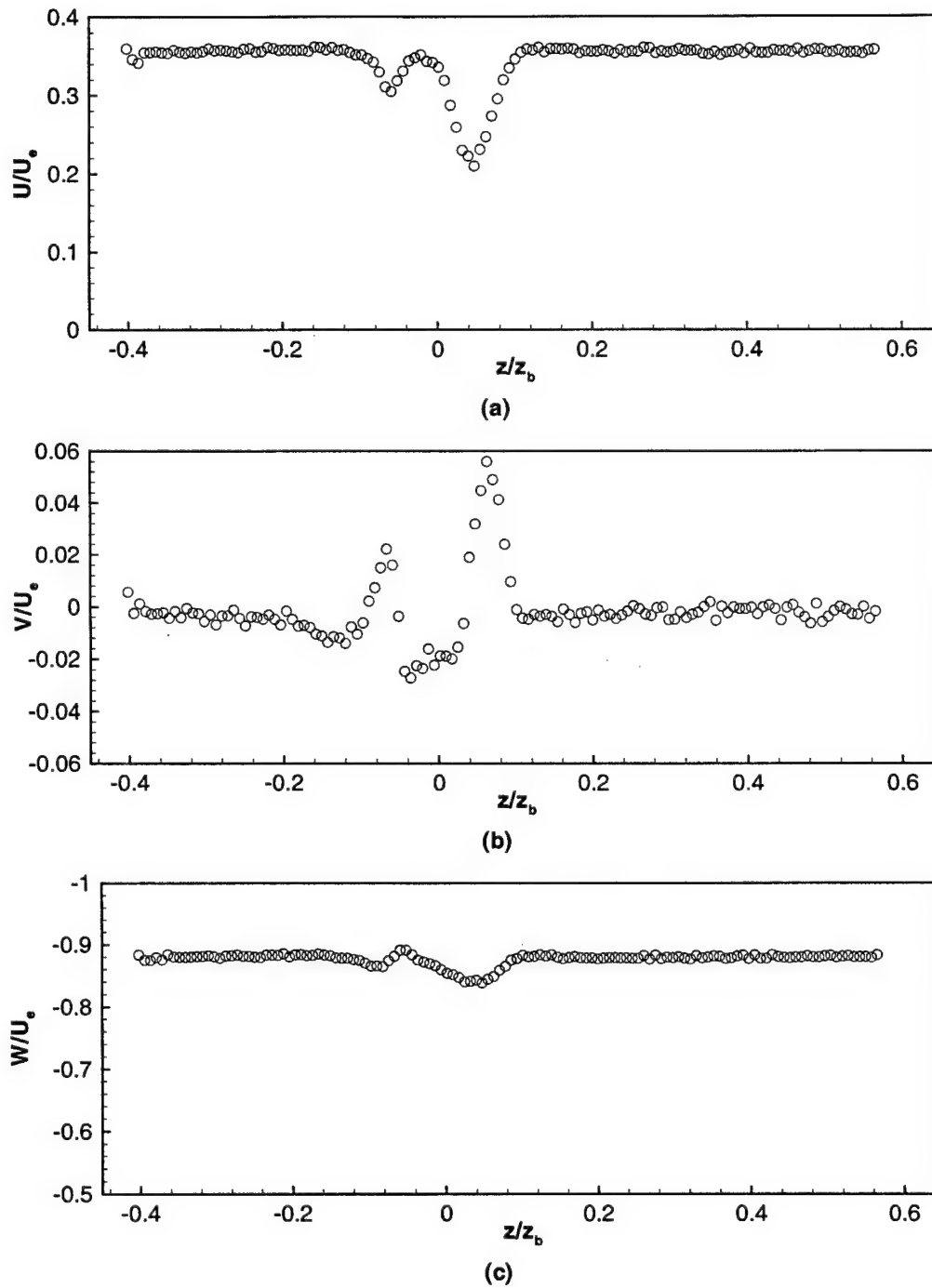


Figure 4.43: Vortex generator mean velocities, in bed coordinate system

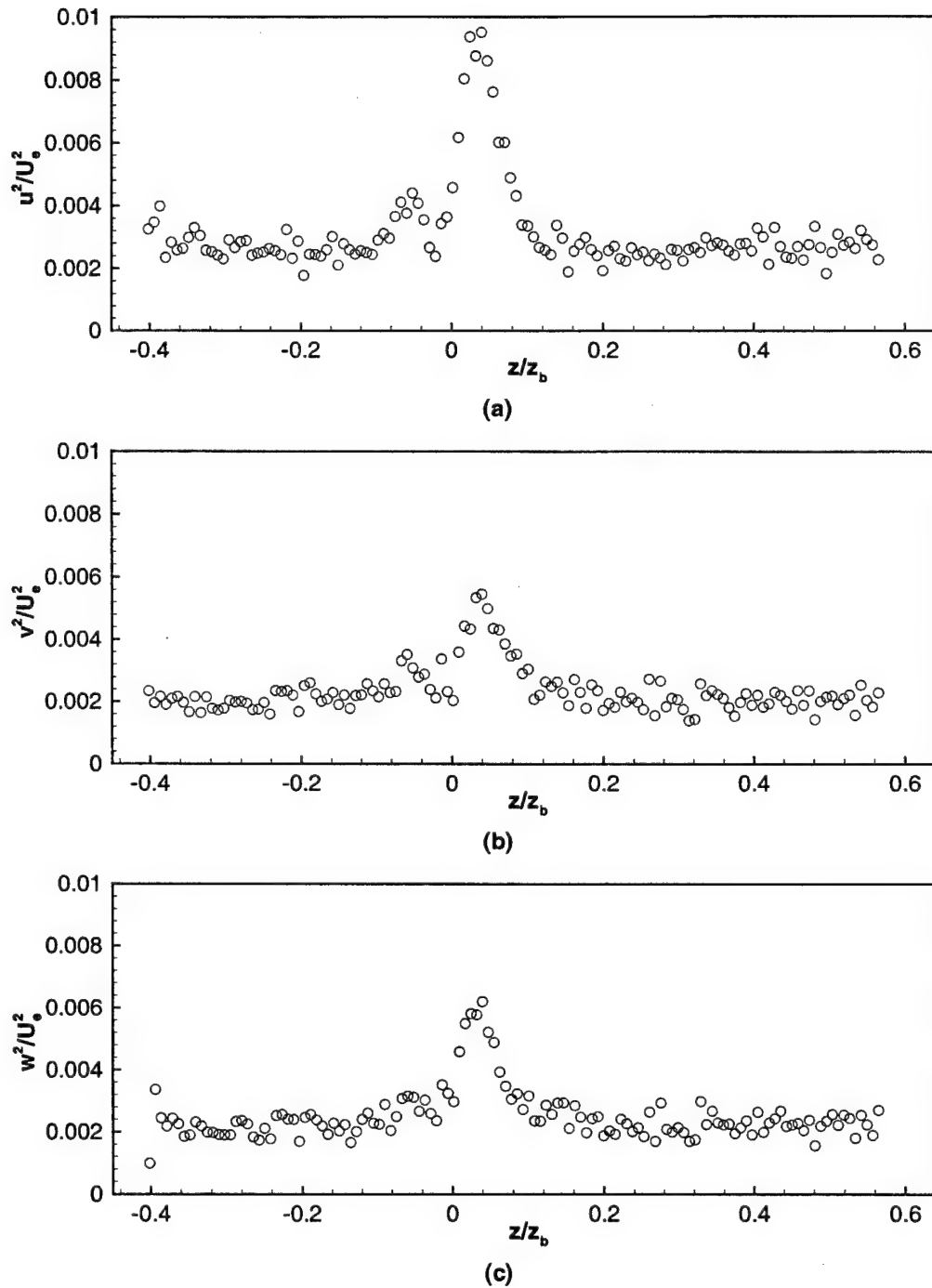


Figure 4.44: Vortex generator mean velocities, in bed coordinate system

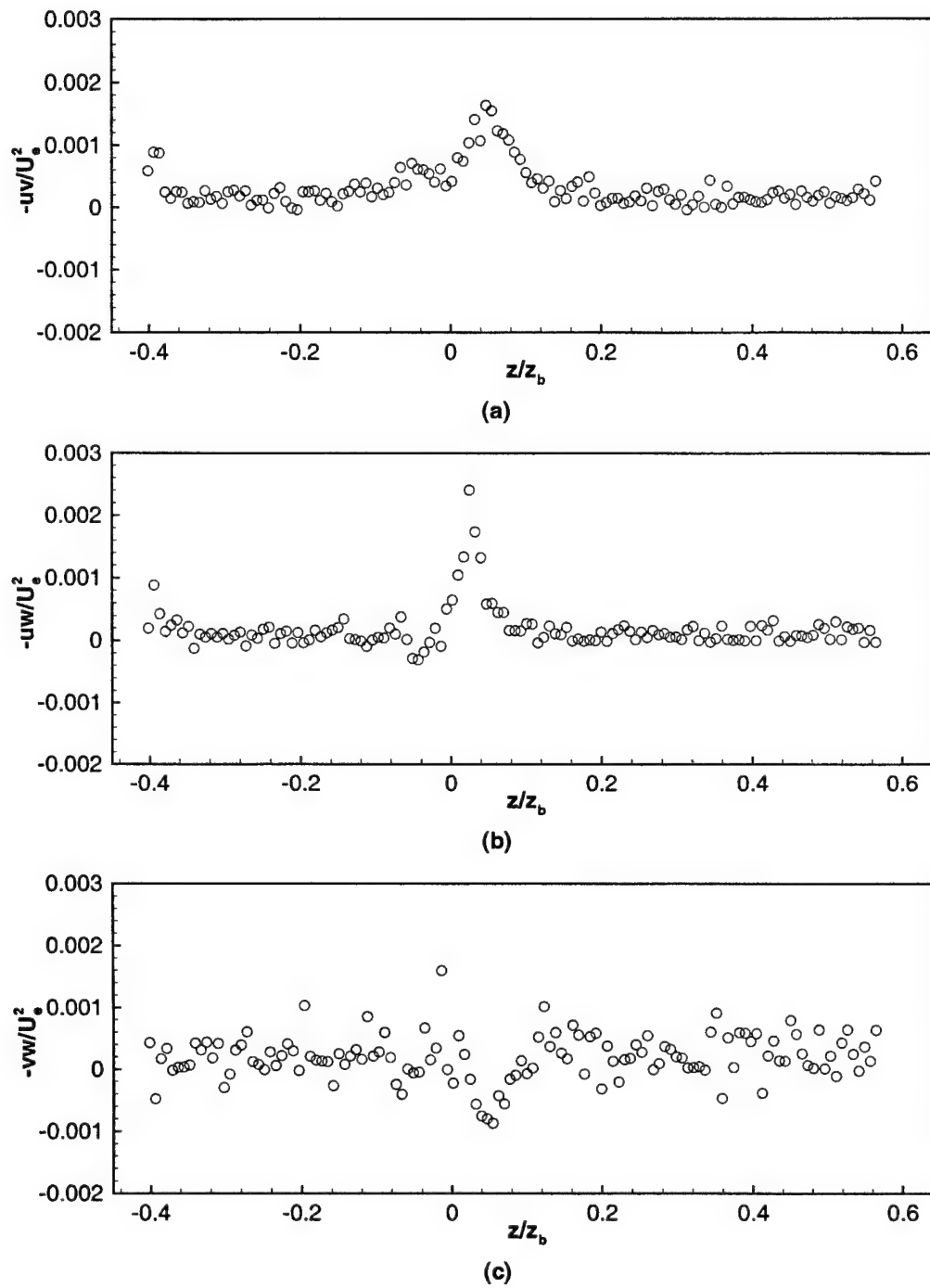


Figure 4.45: Vortex generator mean velocities, in bed coordinate system

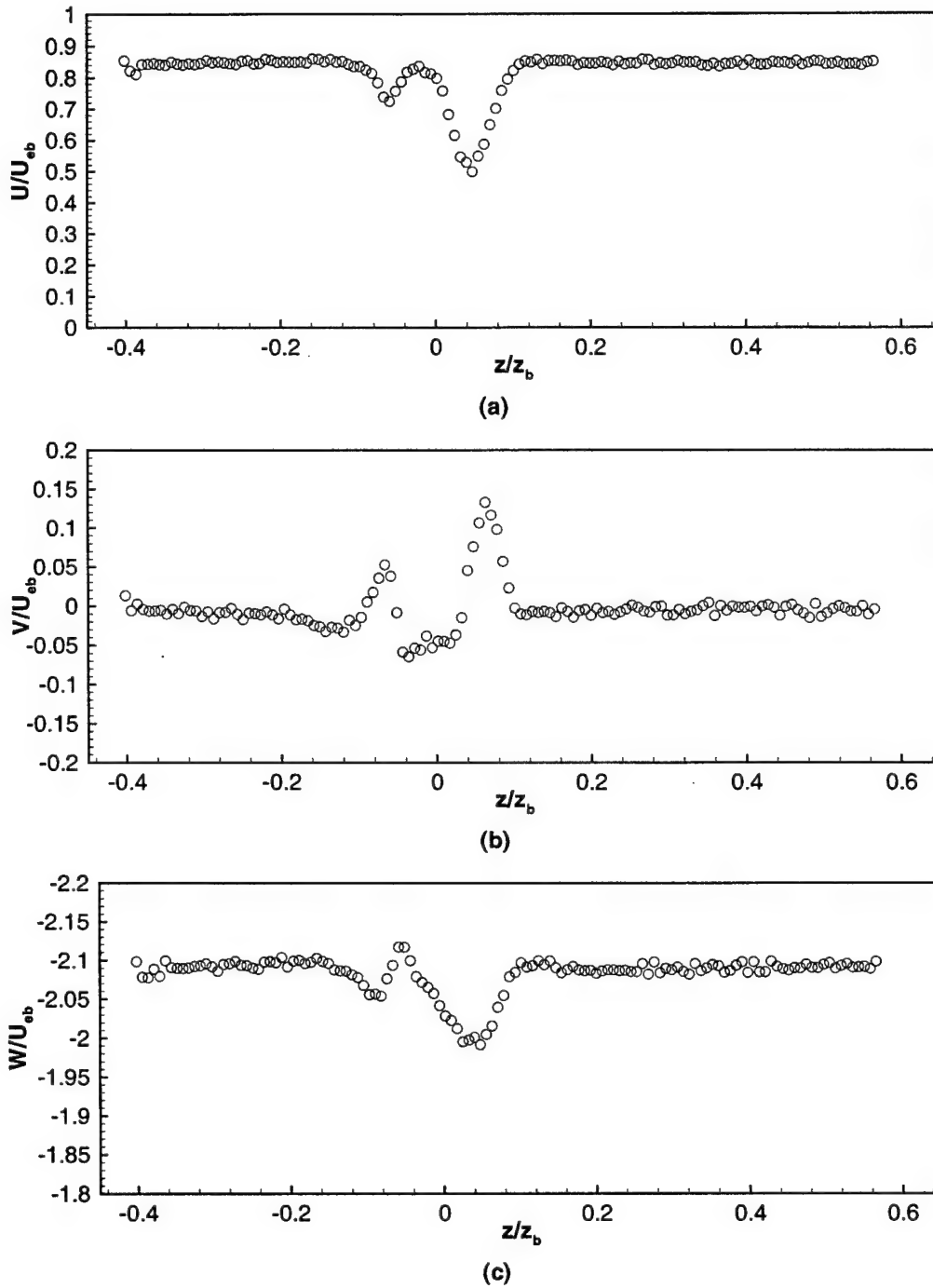


Figure 4.46: Vortex generator mean velocities normalized on  $U_{eb}$  (the free-stream velocity component normal to the wall movement), in bed coordinate system

# Chapter 5

## Conclusions

### 5.1 Auxiliary Tunnel

The velocity structure of a boundary layer with a streamwise vortex pair has been measured using a 3-orthogonal-velocity-component fiber-optic LDA system with a  $50\mu m$  measurement volume. There is no significant correlation between data rate fluctuations and velocity magnitude fluctuations. Results for a 2-D turbulent boundary layer agree closely with those from a DNS near the wall, which confirms that velocity bias and signal broadening effects are negligible. While large streamwise vorticity is generated away from the wall, significant opposite sign vorticity is generated by the viscous interaction of the vortex and the wall. It was found that an abrupt step change in the wall shear stress magnitude occurs just outside of the vortex center.

### 5.2 Cascade Tunnel Apparatus

The low-speed linear compressor cascade wind tunnel at Virginia Tech was modified to allow for LDA measurements upstream of the blades and in the tip gap of blade 5. Three basic areas were modified; 1) the tunnel itself, 2) the data acquisition system and 3) the post-processing programs.

Data rates of over 900 samples/sec show a good working LDA system for the stationary end-wall data. An adequate moving end-wall data rate of over 400 samples/sec was setup. Modifications to the LDV head beam traverse system would allow for more stable and easier alignment of the

beams.

Several problems arose in the course of this investigation which should be addressed in future studies. A new design should be developed to allow the BELT-HITE sensor to be used while gathering moving end-wall data. The triangular pulse processor is adequate for small sets of data. However the processor should be less sensitive to changing voltages out of the vortex generator pulse processor. One or all of the three following suggestions needs to followed to increase the data rate with a moving end-wall to an adequate level. First, a better belt material may be found to replace the Mylar belt. Second, the control system may be made more accurate for running the belt. Finally, the belt speed may be slowed down to decrease wear on the belt and increase control.

## 5.3 Cascade Tunnel Results

### 5.3.1 Stationary End-Wall

Eighteen profiles of stationary end-wall data are taken in and around the tip gap region. The stationary end-wall flow in the tunnel matches the conditions when hot-wire data were taken. The flow at position 1F, the upstream most point in front of the blade, is compared with two dimensional DNS results.

The Spalding equation is fit to the data to determine the  $U_\tau$  value for each profile taken in the flow. The flow is shown to be almost collateral for the free-stream points, and moderately collateral for the points under the blade. Due to lack of better method to determine  $U_\tau$ , the Spalding fit is used on all profiles.

Data taken at the wall while the belt is moving is the best way to set coordinate rotations for the data. A secondary method of comparing with older hot-wire data is used when the moving end-wall data is not available. All the coordinate rotations are less than  $2.5^\circ$ .

The major driving force of the flow under the blade, in the tip gap, is the pressure difference across the blade. This pressure force drives the flow from the pressure side to the suction side of the blades. The pressure force causes the  $U_\tau$  to increase both in the downstream direction along the blade as well as from the pressure to the suction side of the blade. This behavior is in contrast to the free-stream profiles which show a decrease in  $U_\tau$  in the downstream direction.

In the tip gap there are major viscous effects that slow down the velocity magnitudes. These viscous effects make the use of the Bernoulli equation not applicable.

The first several profiles in the tip gap basically show a collateral flow. Past these initial several profiles, the flow begins to show some three-dimensional effects. At quarter chord the three-dimensional effects in the flow are quite evident looking at the flow angles.

Vector plots in the x-z chord coordinate plane clearly show the flow forced through the tip gap. The leading edge of the blade shows little influence, but by the quarter chord the flow quite a bit turned relative to the free-stream flow. Further evidence of the pressure driven nature of the flow.

Three-dimensionality is shown through looking at the Reynolds shear stress magnitudes. Nearly all the  $\overline{uw}$  shear stress peak values are more than twice that of  $\overline{uv}$ . The  $\overline{uw}$  is close to an order of magnitude greater than the  $\overline{vw}$ ;  $\overline{uw}$  can be looked at a indicator of three dimensionality. High values and increasing values show that three-dimensional effects are most likely influencing the flow.

For any cross section beyond plane 3 it is found that the effective eddy viscosity is not isotropic. This is determined from the plots of the shear stress angle and the flow gradient angles. It is also seen in the  $N$ , eddy viscosity, ratio plot.

### 5.3.2 Moving End-Wall

One profile of moving end-wall data and one point of moving end-wall with vortex generator data were collected. The one profile of moving end-wall data is at position 1F in the flow. This one profile is a combination of five different sets of data on five different days. The one point of vortex generator data is at position 1F. The point is approximately 3.1 cm downstream of the vortex generators and at a height of 1 cm off the wall. The vortex generator height is 1 cm at the trailing edge.

A collateral region for the moving end-wall data is found by looking at the data in a moving end-wall coordinate system. The region contains eight points and the flow angle doesn't change more than 8 degrees. The Spalding fit is used on the eight points to determine the  $U_\tau$  value.

### 5.3.3 Moving End-Wall with Vortex Generators

There is not very much dependence on the mean velocity or Reynolds normal stresses on the bin size for the vortex generator data. The Reynolds shear stresses are fairly scattered and it is hard to tell dependence from the bin size. The 128 bins is chosen to represent the flow the

best.

The interaction of the shear layers with the moving end-wall rotates the near wall flow direction into the direction of the moving end-wall. This interaction seems to cause a 9% increase to the boundary layer thickness from the stationary end-wall profile. Figures show the belt viscous layer turning the flow to the belt movement direction near the wall. In the collateral region, of the moving end-wall coordinate system, the flow angle is found to be nearly the same as the angle of attack measured between the negative vortex generator and the tunnel centerline; this is merely a coincidence. However, this has the affect of decreasing the strength of the negative rotating vortex. Even though this effect will be less at the vortex generator, due to the shorter travel distance for the moving end-wall viscous layer, some turn would still be there. The velocity plots of the vortex generator data show that the positive rotating vortex deficit is almost three times the size of the negative rotating vortex deficit.

Many attributes of the flow match between the auxiliary tunnel's first cross section and the position of the data point with vortex generator data in the cascade tunnel. These similarities are shown in Figure 4.4. The boundary layer thickness at point 1F in the cascade tunnel with the moving end-wall roughly matches the boundary layer thickness at the first cross section of the auxiliary tunnel. The  $Re_\theta$  at point 1F in the cascade tunnel with the moving end-wall roughly matches the  $Re_\theta$  at the first cross section of the auxiliary tunnel. The peak velocity deficit in the auxiliary tunnel at the first cross section falls between the values of the two vortices in the cascade tunnel. The diameter of the vortex measured in the auxiliary tunnel at the first cross section fall between the two diameters measured for the cascade tunnel vortices. The circulation values calculated on the cascade tunnel vortices fall around the values calculated for auxiliary tunnel vortices at the first cross section.

It seems that there are similar vortices found in the cascade tunnel as there were in the auxiliary tunnel. Obviously much more data need to be taken to fully understand the flow, especially with the moving end-wall and vortex generators. However, some confirmations are made about the flow. The tip gap for a non-moving end-wall is generally driven by the pressure gradient. The moving end-wall viscous sublayer skews and increases the boundary layer. The skewed moving end-wall generates two asymmetrical vortices in the flow.

## 5.4 Final Thoughts

The LDA measurement technique is a useful tool with which to measure the three-dimensionality of complex flow in a non-intrusive manner. The small control volume of the probe allows near



wall measurements to be taken as well as for many points to be distributed in small spaces, such as tip gaps. Greater understanding of each of these three-dimensional flows has been gained and a data set has been compiled that may be used to calibrate future computational work.

# Appendix A

## Trips

### A.1 Introduction

To obtain the desired momentum thickness in the Auxiliary tunnel at the location of the vortex generators, a series of boundary layer trips were studied. The trips are located on the slight incline (1.75 inches long) at the leading edge of the tunnel test section (see Figure 2.7). Not only does the momentum thickness need to be large enough, but the flow needs to be relaxed and two dimensional at the vortex generators.

The LDA profiles are taken approximately 7.1 cm downstream of the leading edge of the test section. The trailing edge of the vortex generators is 11.3 cm downstream of the leading edge of the test section. If the flow is relaxed or closely relaxed at 7.1 cm, it certainly will be at 11.3 cm.

Eight trip configurations are studied. The first two configurations consist of posts. The next three are wire trips. The final three are bar trips. The convention used in referring to the profiles of data is first is the number of the configuration, second is "C" and third is the number of the profile taken, i.e. 1C2 is the first configuration second profile.

The flow conditions in the tunnel are the same as the ones described in Chapter 2. The flow speed is approximately 13 m/s and the tunnel test section is approximately 1.25 m in length, 24 cm in width and 10 cm in height. The LDA system used in the following experiments is the same as described in Chapter 2. The final trip configuration used in the auxiliary and cascade tunnels is configuration 8, the last configuration studied.

Table A.1: Trip test results in the Auxiliary tunnel

<i>Profile</i>	$Re_\theta$	<i>Profile</i>	$Re_\theta$
1C1	529	5C	679
1C2	408	6C	662
2C1	430	7C	932
2C2	372	8C1	703
2C3	361	8C2	716
3C	360	8C3	646
4C	405		

## A.2 Configurations

Table A.1 summarized all of the profiles taken and the resulting  $Re_\theta$ . Figure A.1 shows simple schematics of each of the trip configurations along with an average resulting  $Re_\theta$ . Figure A.2 through Figure A.12 shows the changes to the flow structure with changing the trips.

### Configuration 1

Four rows of cylindrical posts are mounted to the leading edge of the test section. The posts are applied to the tunnel floor using a strip mold of the posts. The molds are filled with Bondo. The first row of posts is 0.060 inches high, 0.078 inches in diameter. The last three rows are all 0.027 inches high and 0.045 inches in diameter.

The four rows are spread out over the leading edge of the test section. In the spanwise direction the first row, 0.060 inch posts, are spaced 0.216 inches apart. In the spanwise direction the last three rows of posts are 0.100 inches apart. The last three rows were not aligned with each other in any particular way, i.e. the rows of posts were neither in line with each other nor staggered against each other.

The first row is centered 0.25 inches from the leading edge of the test section. The second row is 0.65 inches from the leading edge of the test section. The third row is 0.90 inches from the leading edge of the test section. The fourth row is 1.15 inches from the leading edge of the test section.

Two profiles are taken at 2.8 inches downstream of the leading edge of the test section. The

first profile, 1C1, is located in the center,  $z = 0$ , of the tunnel; the second profile, 1C2, is located at  $z = -1.15$  inches (see Figure 2.1 for coordinate convention). The  $Re_\theta = 529$  for profile 1C1 and the  $Re_\theta = 408$  for profile 1C2.

### Configuration 2

The difference between configuration 1 and 2 is that the posts height of 0.027 inches are replaced by posts 0.030 inches in height. The 0.030 inch posts have a diameter of 0.078 inches not 0.045 inches, and the spanwise spacing is 0.216 inches not 0.100 inches. All four rows are staggered every other row by eye.

Four rows of cylindrical posts are mounted to the leading edge of the test section. The posts are applied to the tunnel floor using a strip mold of the posts. The molds are filled with Bondo. The first row of posts is 0.060 inches high, 0.078 inches in diameter and spread 0.216 inches apart in the spanwise direction. The last three rows are all 0.030 inches high, 0.078 inches in diameter and spread 0.216 inches apart in the spanwise direction. All the lines are staggered very well by eye in the spanwise direction.

The first row is centered 0.25 inches from the leading edge of the test section. The second row is 0.65 inches from the leading edge of the test section. The third row is 0.90 inches from the leading edge of the test section. The fourth row is 1.15 inches from the leading edge of the test section.

Three profiles are taken at approximately 2.76 inches downstream of the leading edge of the test section. All three profiles are located approximately in the center of the tunnel. The first profile, 2C1 Figure A.2, is located in the spanwise location of the center of the middle post in the last row. The second profile, 2C2 Figure A.3, is located in the spanwise location between two posts in the last row. The third profile, 2C3 Figure A.4, is located halfway between the first and second profiles. The  $Re_\theta = 430$  for profile 2C1;  $Re_\theta = 371$  for profile 2C2;  $Re_\theta = 361$  for profile 2C3.

### Configuration 3

Three wire trips are attached to the floor. The wires are mounted to the leading edge of the test section. The wires are applied to the tunnel floor using a super glue. Care is taken to make sure the wires are flat to the floor and aligned perpendicular to the walls. The three wires are 0.025 inches in diameter.

The first wire is centered 0.25 inches from the leading edge of the test section. The second wire is 0.45 inches from the leading edge of the test section. The third wire is 0.65 inches from the leading edge of the test section.

One profile is taken at the approximate center of the tunnel, 3C Figure A.5, 2.77 inches downstream of the leading edge of the test section. The  $Re_\theta = 360$  for this profile.

#### Configuration 4

One wire trip is attached to the floor. The wire is mounted to the leading edge of the test section. The wire is applied to the tunnel floor using a super glue. Care is taken to make sure the wire is flat to the floor and aligned perpendicular to the walls. The wire is 0.063 inches in diameter. The wire is centered 0.25 inches from the leading edge of the test section. One profile is taken at the approximate center of the tunnel, 4C Figure A.6, 2.77 inches downstream of the leading edge of the test section. The  $Re_\theta = 405$  for this profile.

#### Configuration 5

Three wire trips are attached to the floor. The wires are mounted to the leading edge of the test section. The wires are applied to the tunnel floor using a super glue. Care is taken to make sure the wires are flat to the floor and aligned perpendicular to the walls. The three wires are 0.063 inches in diameter.

The first wire is centered 0.25 inches from the leading edge of the test section. The second wire is 0.75 inches from the leading edge of the test section. The third wire is 1.25 inches from the leading edge of the test section.

One profile is taken at the approximate center of the tunnel, 5C Figure A.7, 2.77 inches downstream of the leading edge of the test section. The  $Re_\theta = 679$  for this profile.

#### Configuration 6

One bar trip is attached to the floor. The bar is mounted to the leading edge of the test section. The bar is applied to the tunnel floor using a super glue. Care is taken to make sure the bar is flat to the floor and aligned perpendicular to the walls. The bar is square and 0.095 inch each side. The bar is centered 0.25 inches from the leading edge of the test section. One profile is taken at the approximate center of the tunnel, 6C Figure A.8, 2.77 inches downstream of the

leading edge of the test section. The  $Re_\theta = 662$  for this profile.

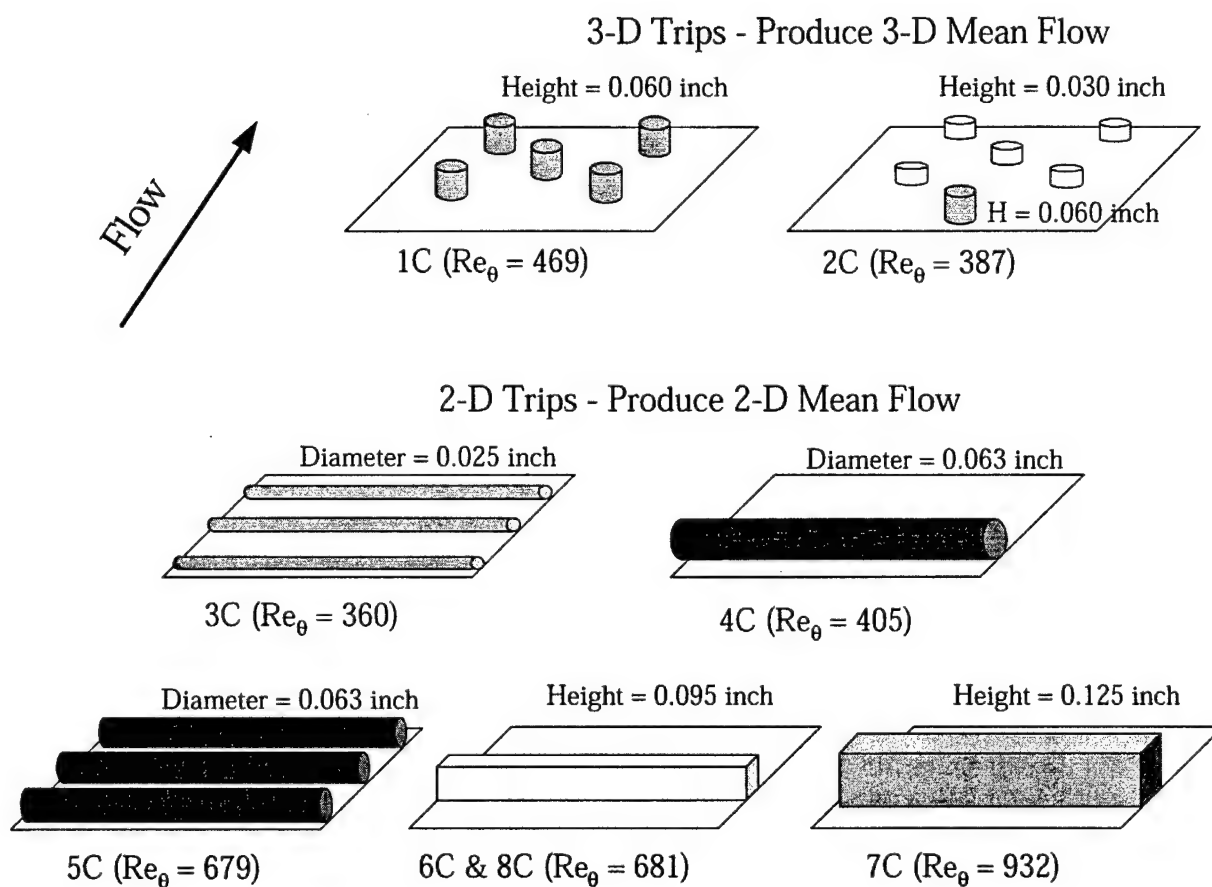
### Configuration 7

One bar trip is attached to the floor. The bar is mounted to the leading edge of the test section. The bar is applied to the tunnel floor using a super glue. Care is taken to make sure the bar is flat to the floor and aligned perpendicular to the walls. The bar is square and 0.125 inch each side. The leading edge of the bar is at 0.25 inches from the leading edge of the test section. One profile, 7C, is taken at the approximate center of the tunnel, Figure A.9, 2.77 inches downstream of the leading edge of the test section. The  $Re_\theta = 932$  for this profile.

### Configuration 8

One bar trip is attached to the floor. The bar is mounted to the leading edge of the test section. The bar is applied to the tunnel floor using a super glue. Care is taken to make sure the bar is flat to the floor and aligned perpendicular to the walls. The bar is square and 0.095 inch each side. The leading edge of the bar is 0.25 inches from the leading edge of the test section.

Three profiles are taken approximately 2.77 inches downstream of the leading edge of the test section. The first profile is taken at the approximate center of the tunnel,  $z = 0$ , 8C1 Figure A.10. The second profile, 8C2 Figure A.11, is at  $z = -1$  inches. The third profile, 8C3 Figure A.12, is at  $z = 1$  inches.  $Re_\theta = 703$  for profile 8C1;  $Re_\theta = 716$  for profile 8C2;  $Re_\theta = 646$  for profile 8C3.

Figure A.1: Simple schematics of trips on test surface along with average resulting  $Re_\theta$

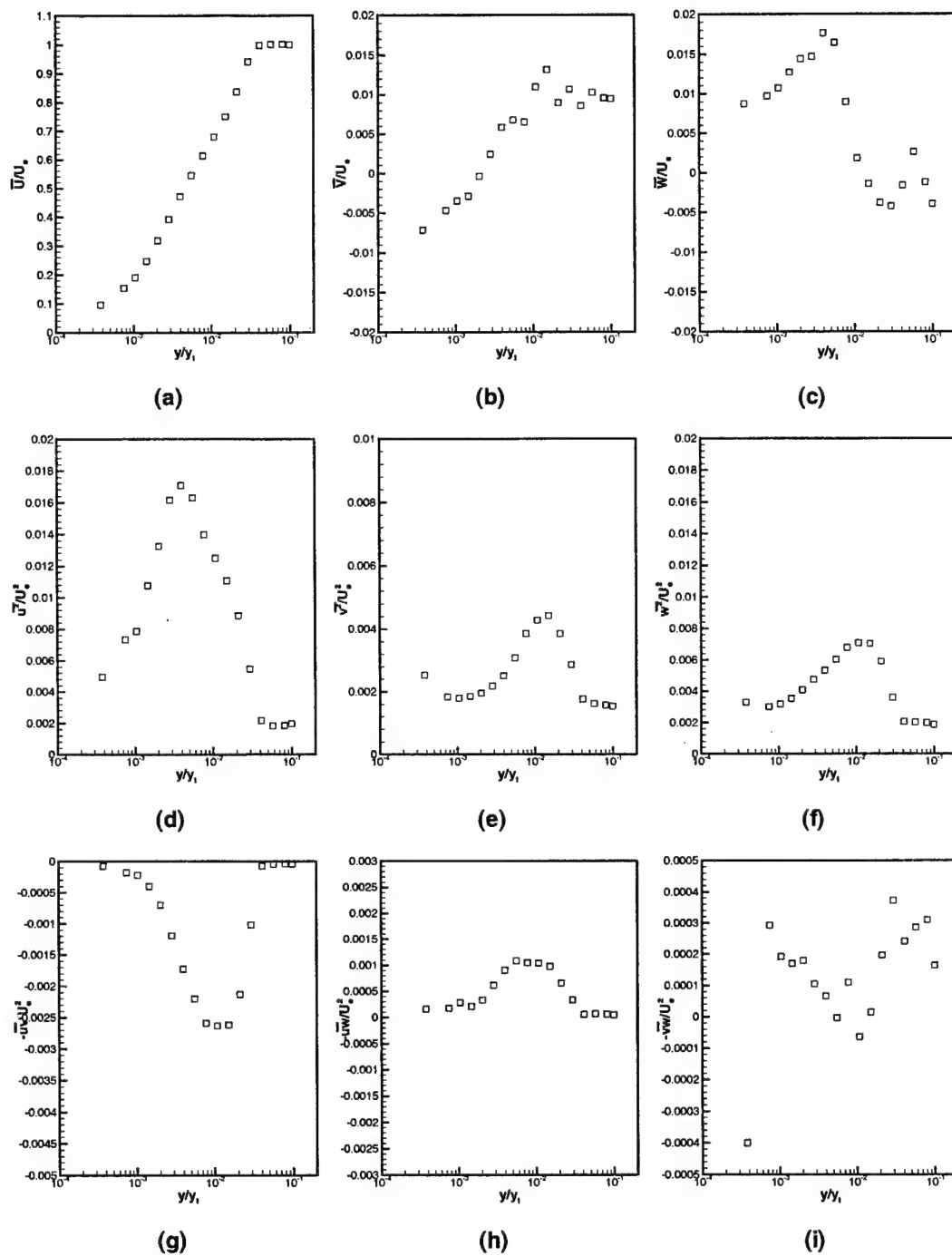


Figure A.2: Profile 2C1 Mean Velocities and Reynolds Stresses



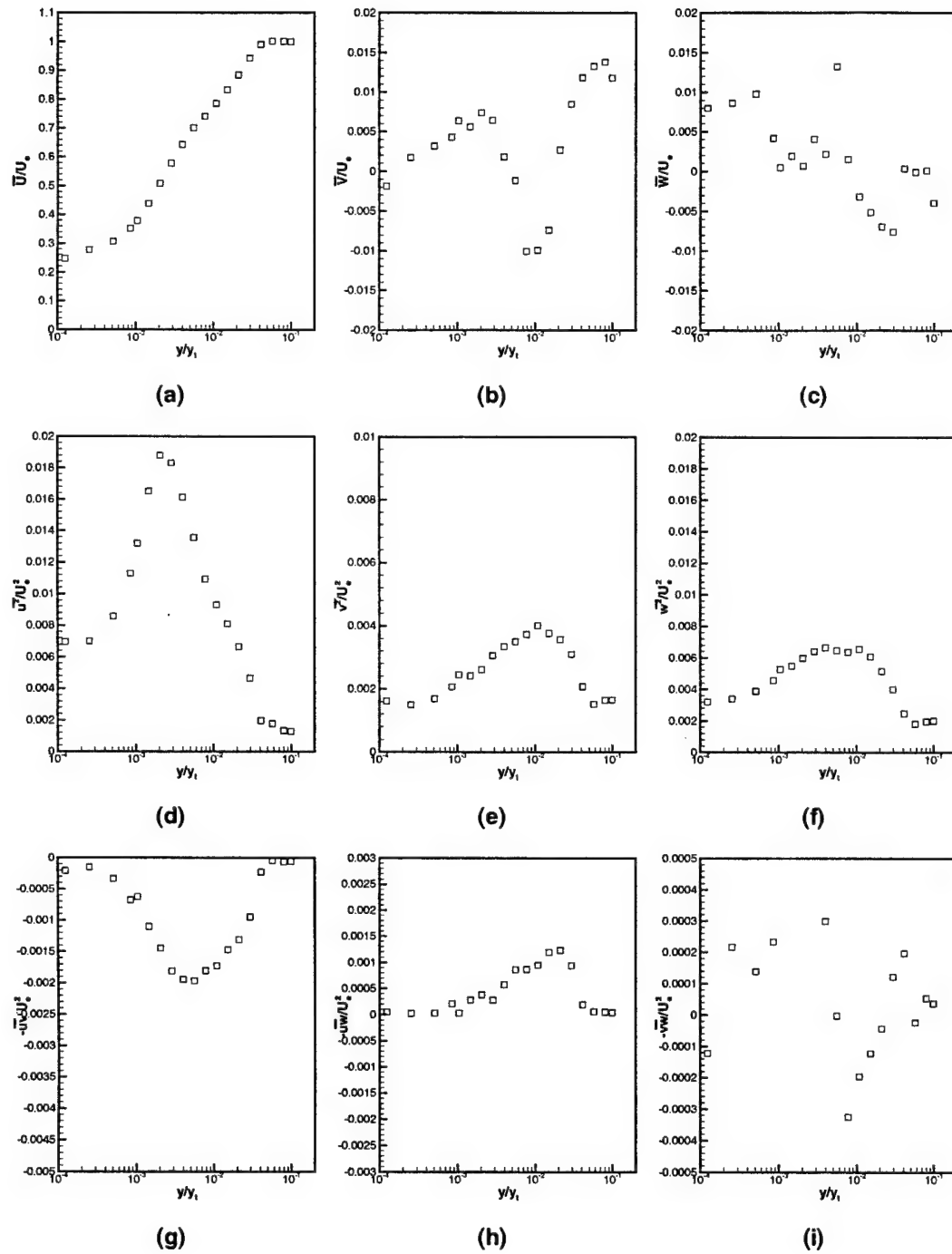


Figure A.3: Profile 2C2 Mean Velocities and Reynolds Stresses

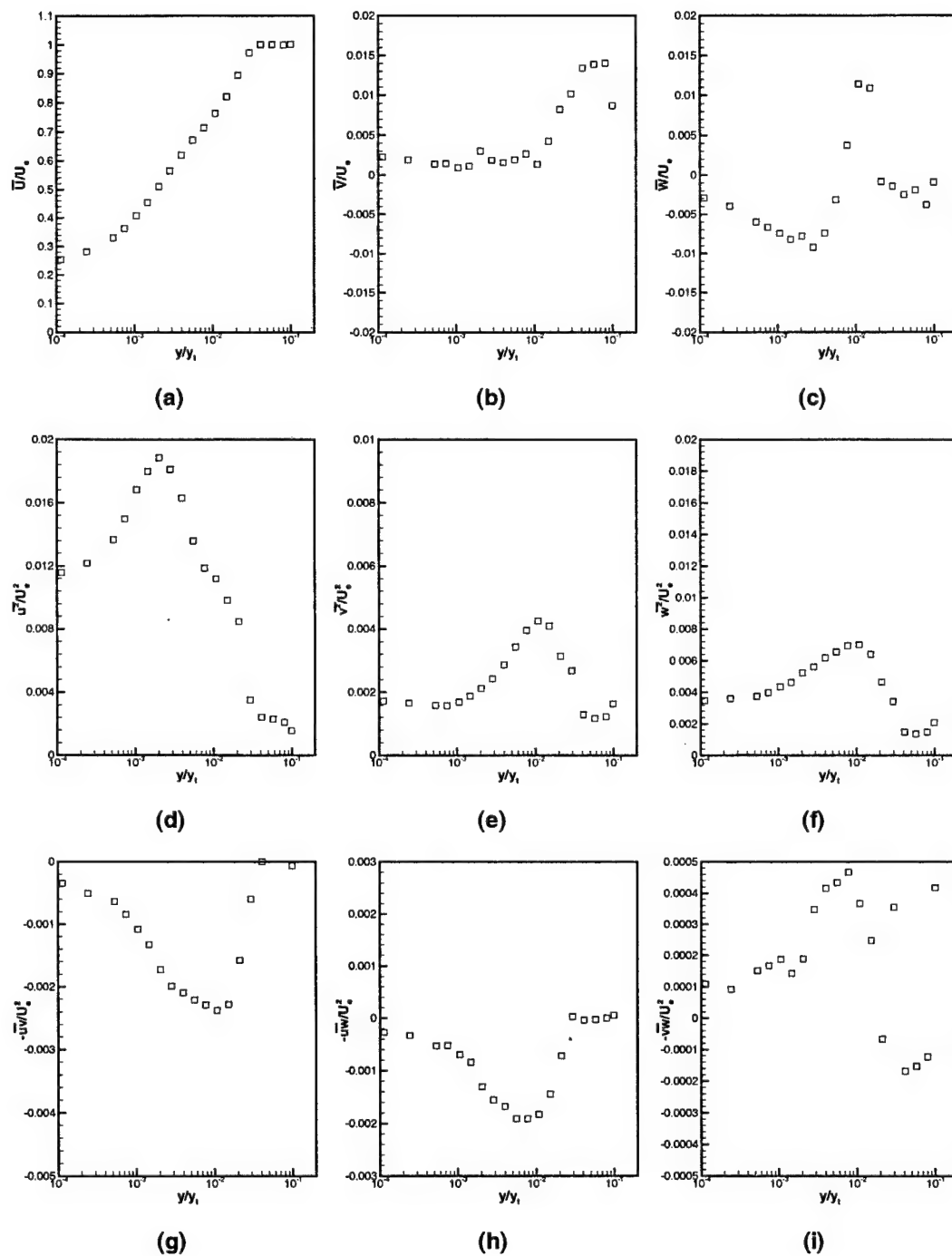


Figure A.4: Profile 2C3 Mean Velocities and Reynolds Stresses

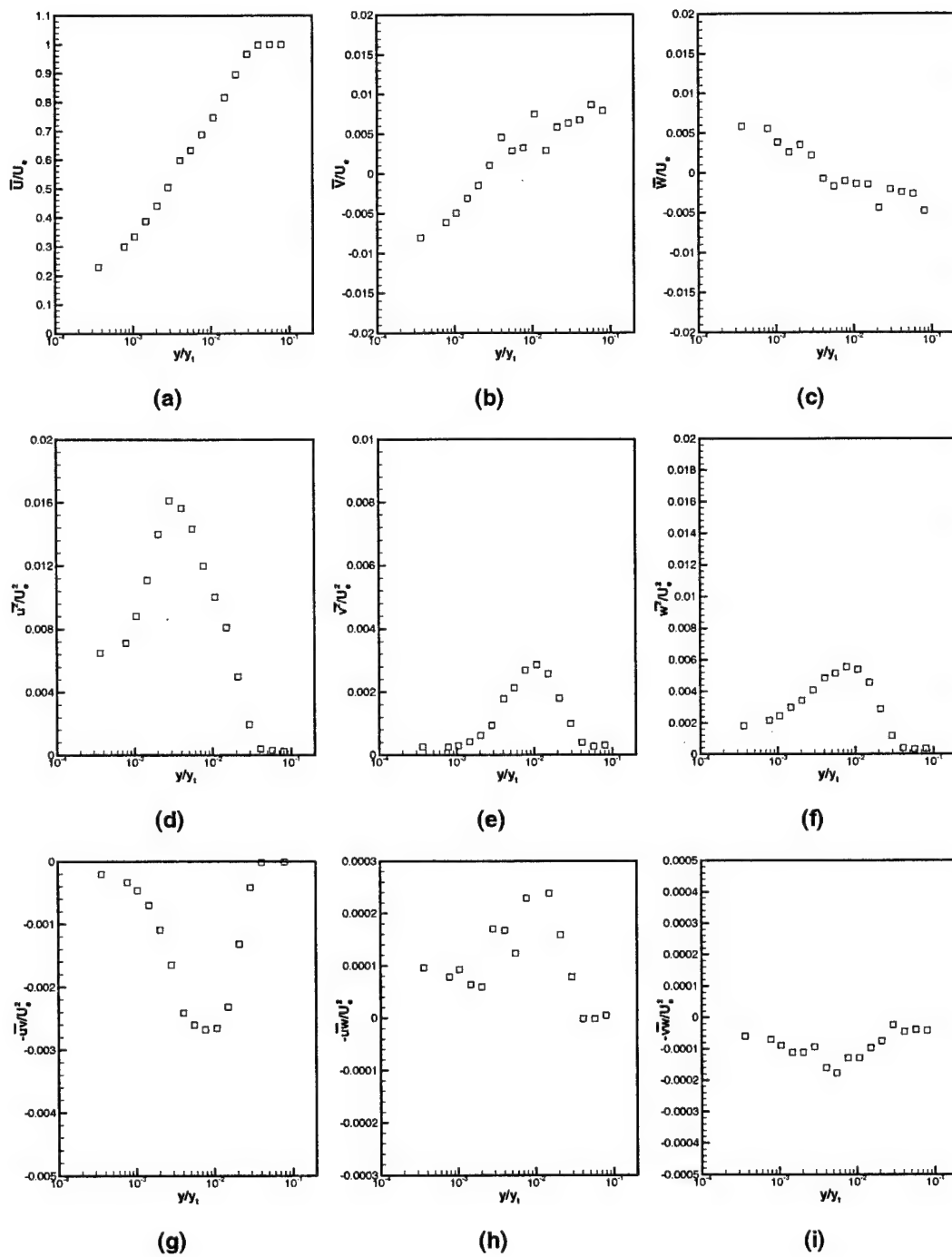


Figure A.5: Profile 3C Mean Velocities and Reynolds Stresses

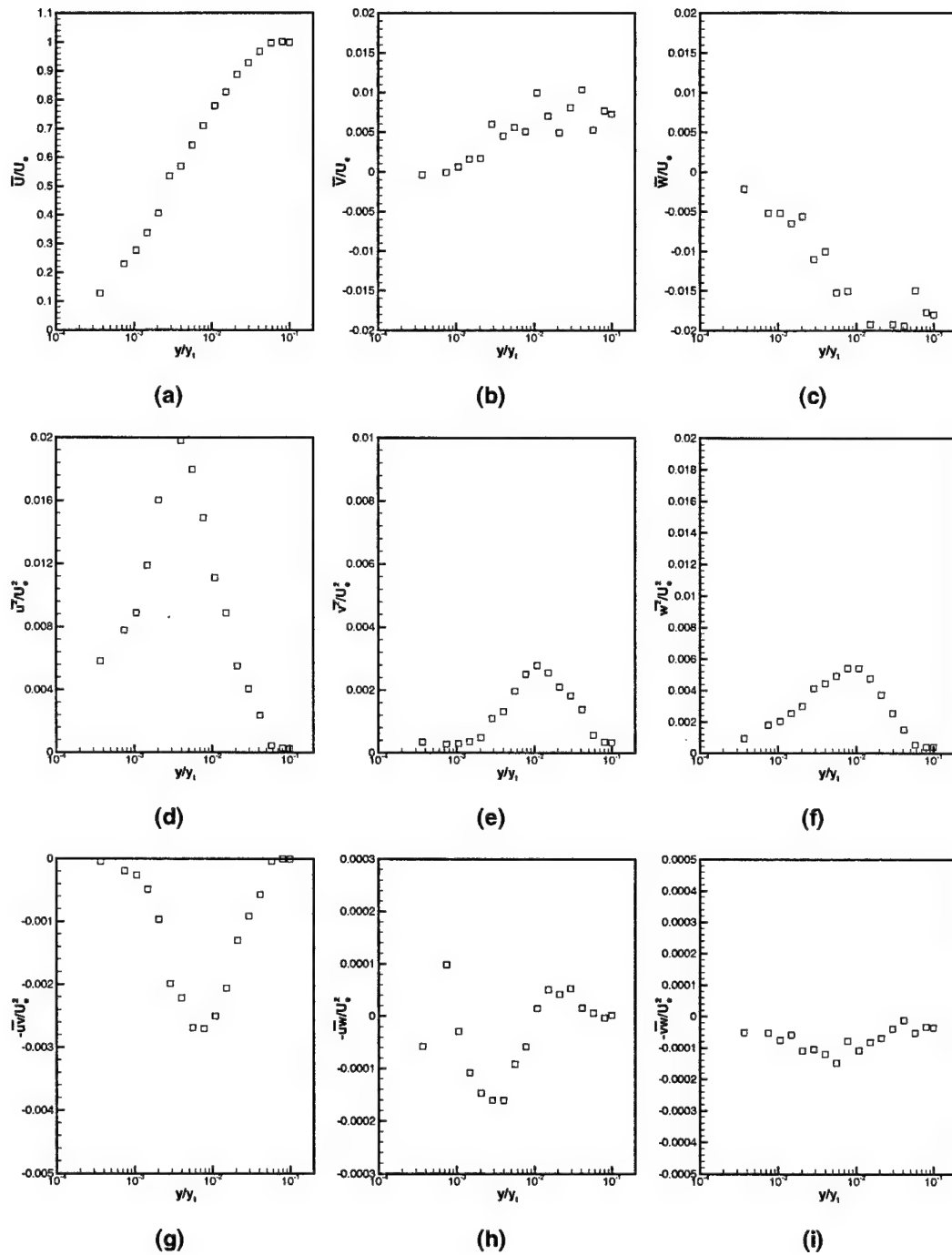


Figure A.6: Profile 4C Mean Velocities and Reynolds Stresses

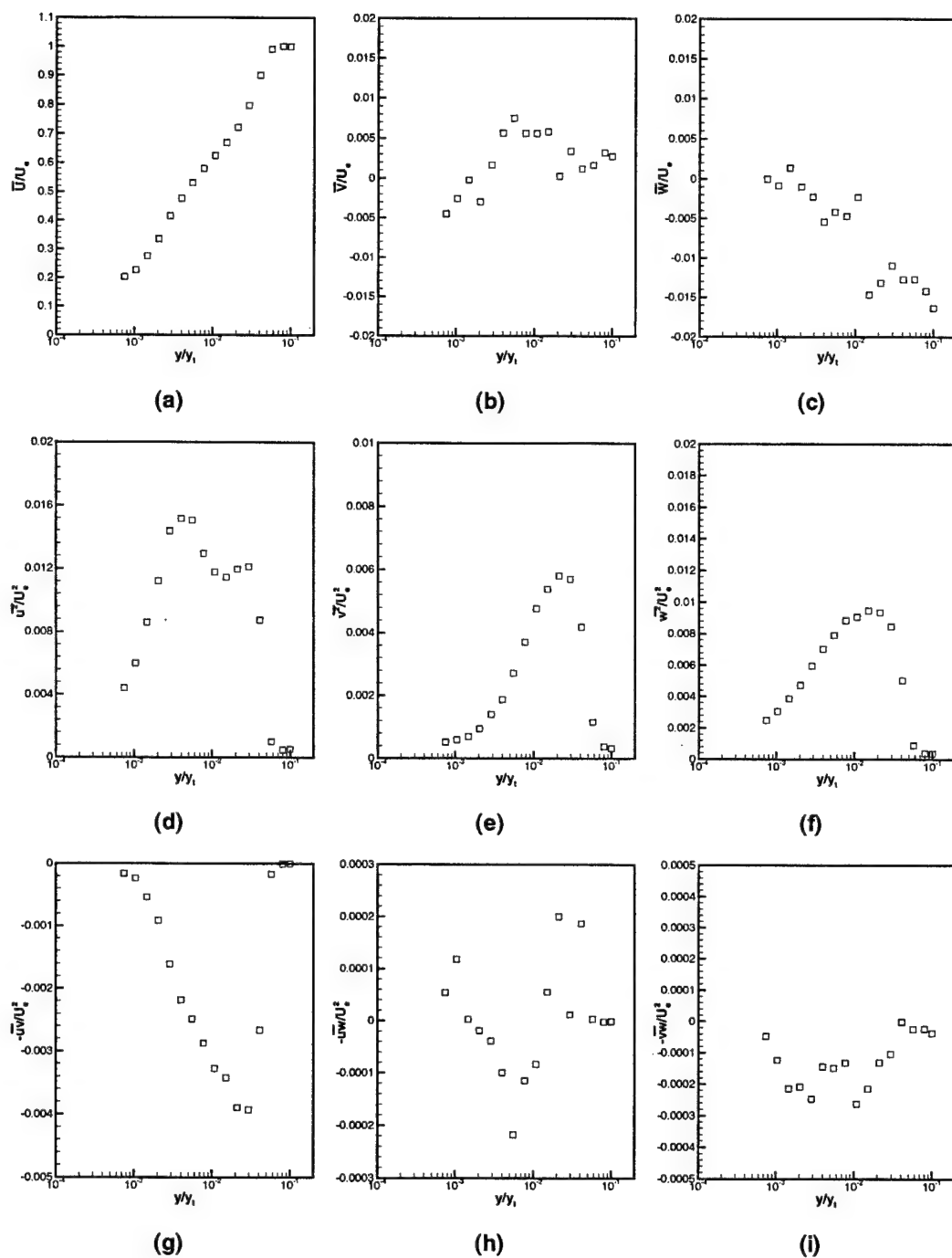


Figure A.7: Profile 5C Mean Velocities and Reynolds Stresses

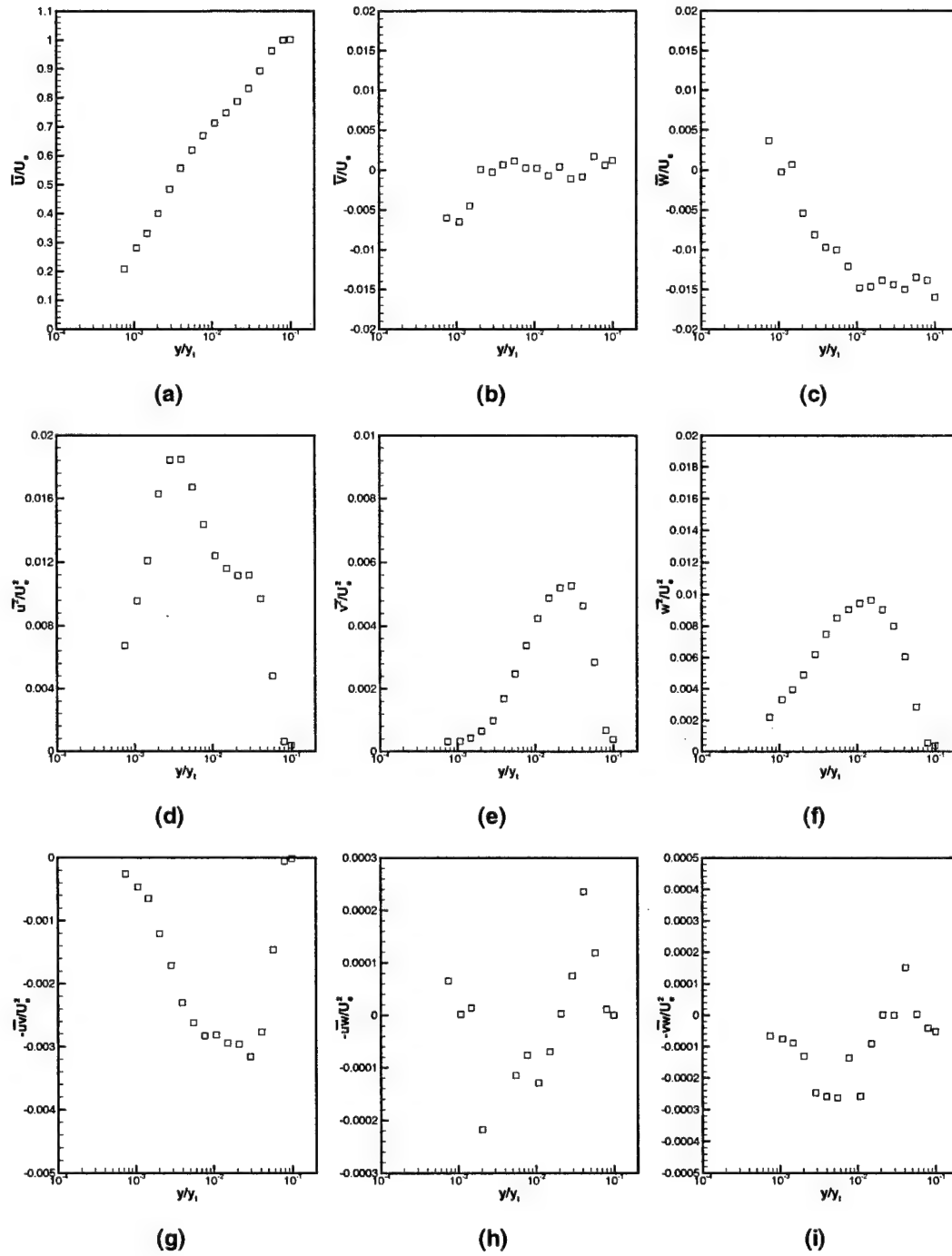


Figure A.8: Profile 6C Mean Velocities and Reynolds Stresses

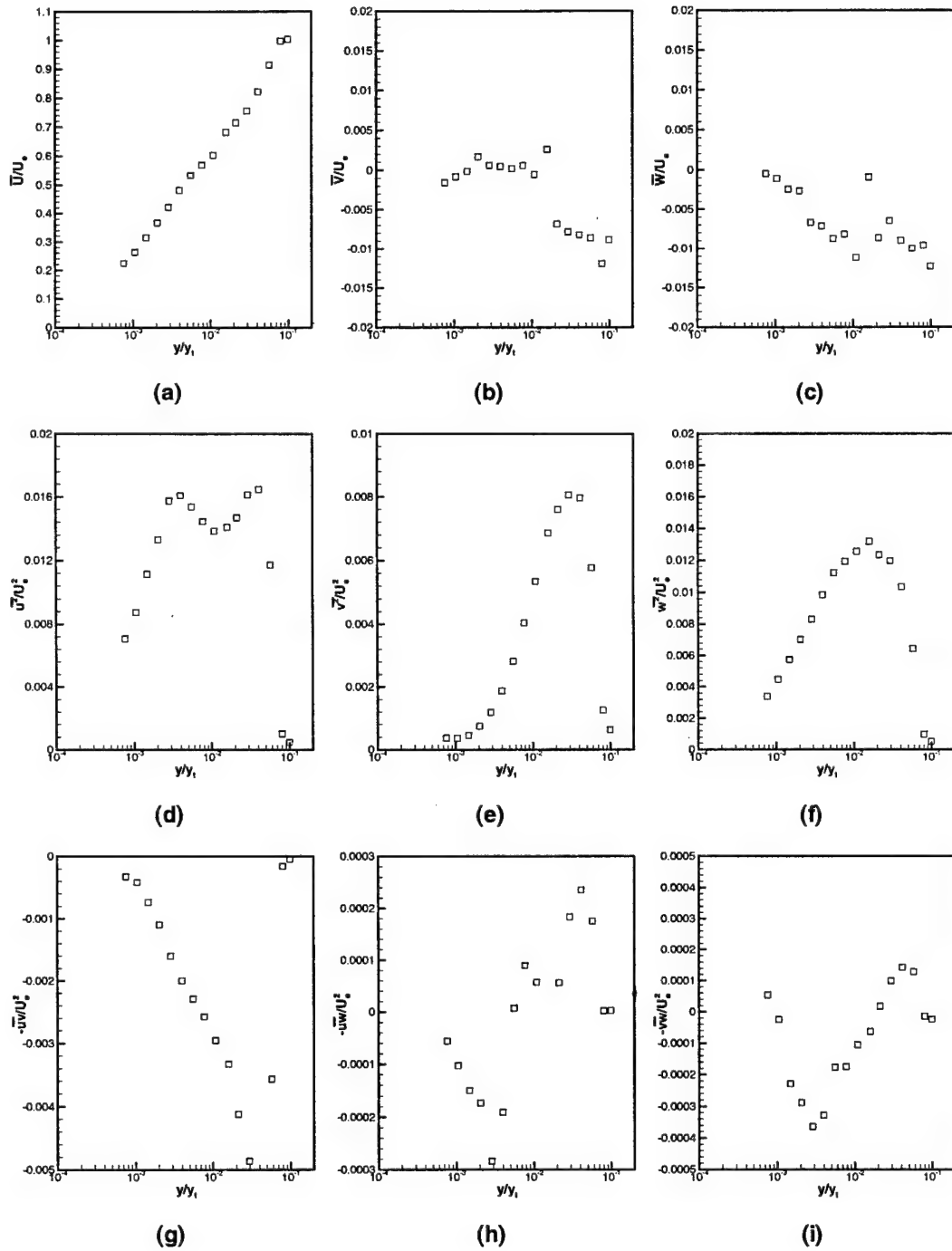


Figure A.9: Profile 7C Mean Velocities and Reynolds Stresses

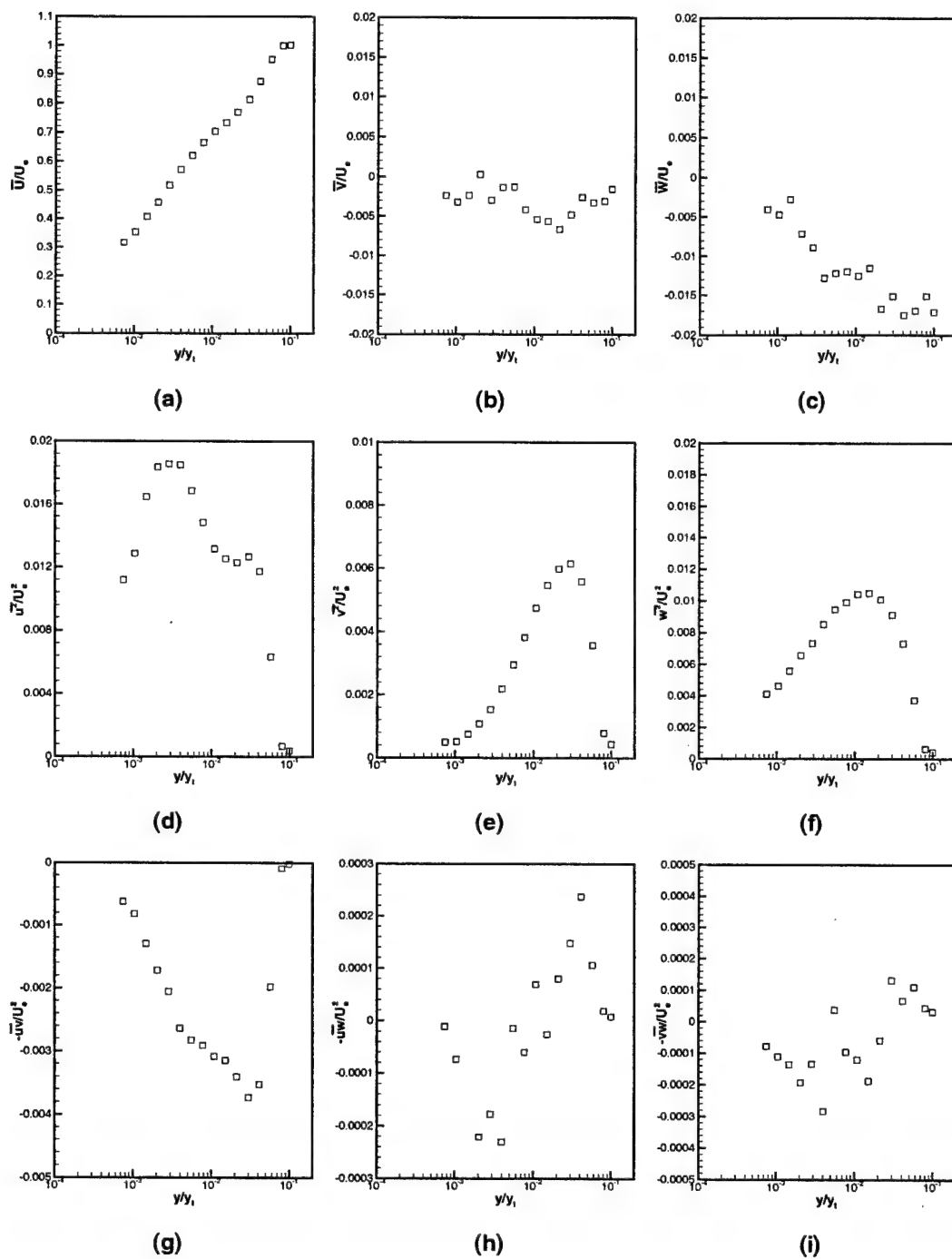


Figure A.10: Profile 8C1 Mean Velocities and Reynolds Stresses



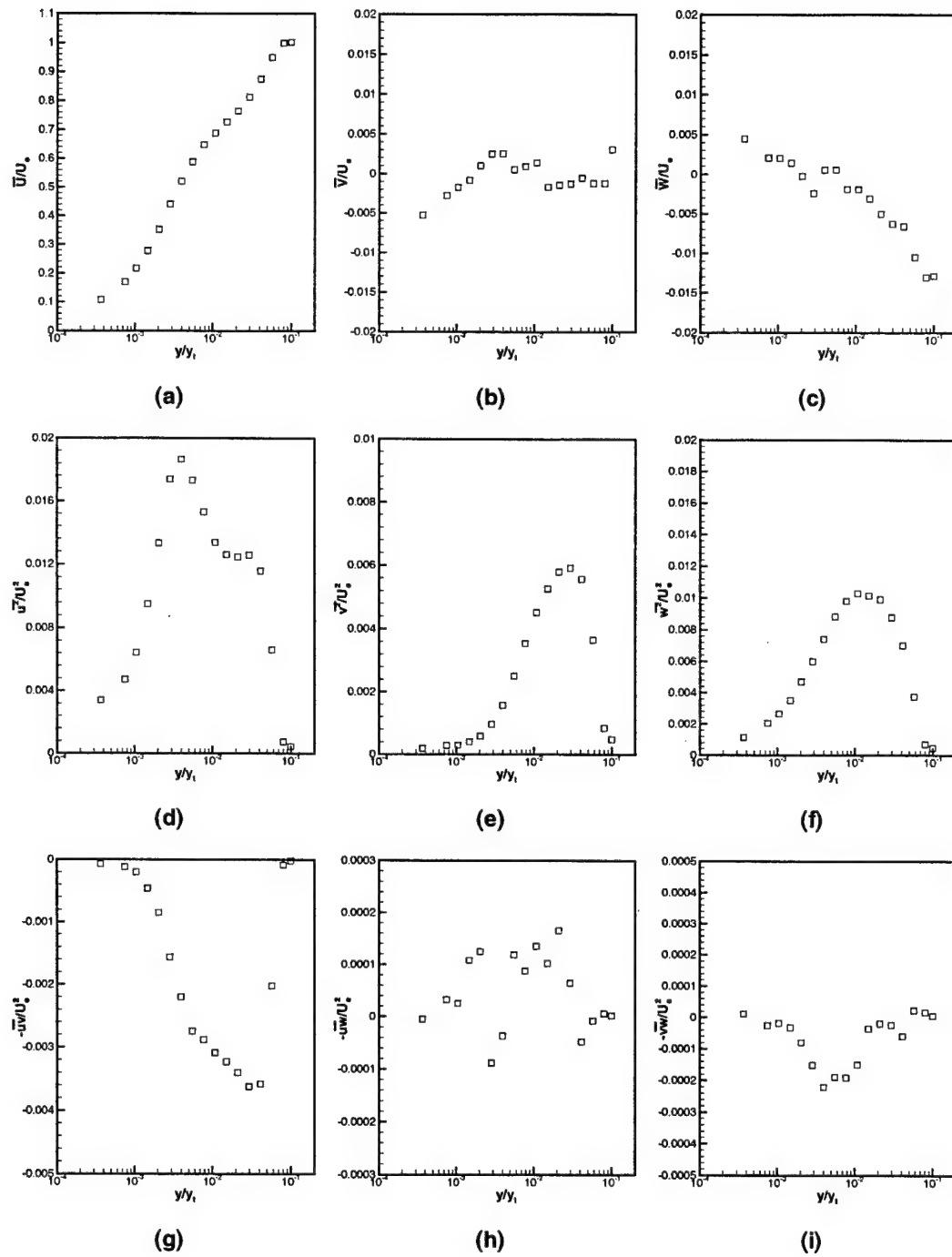


Figure A.11: Profile 8C2 Mean Velocities and Reynolds Stresses

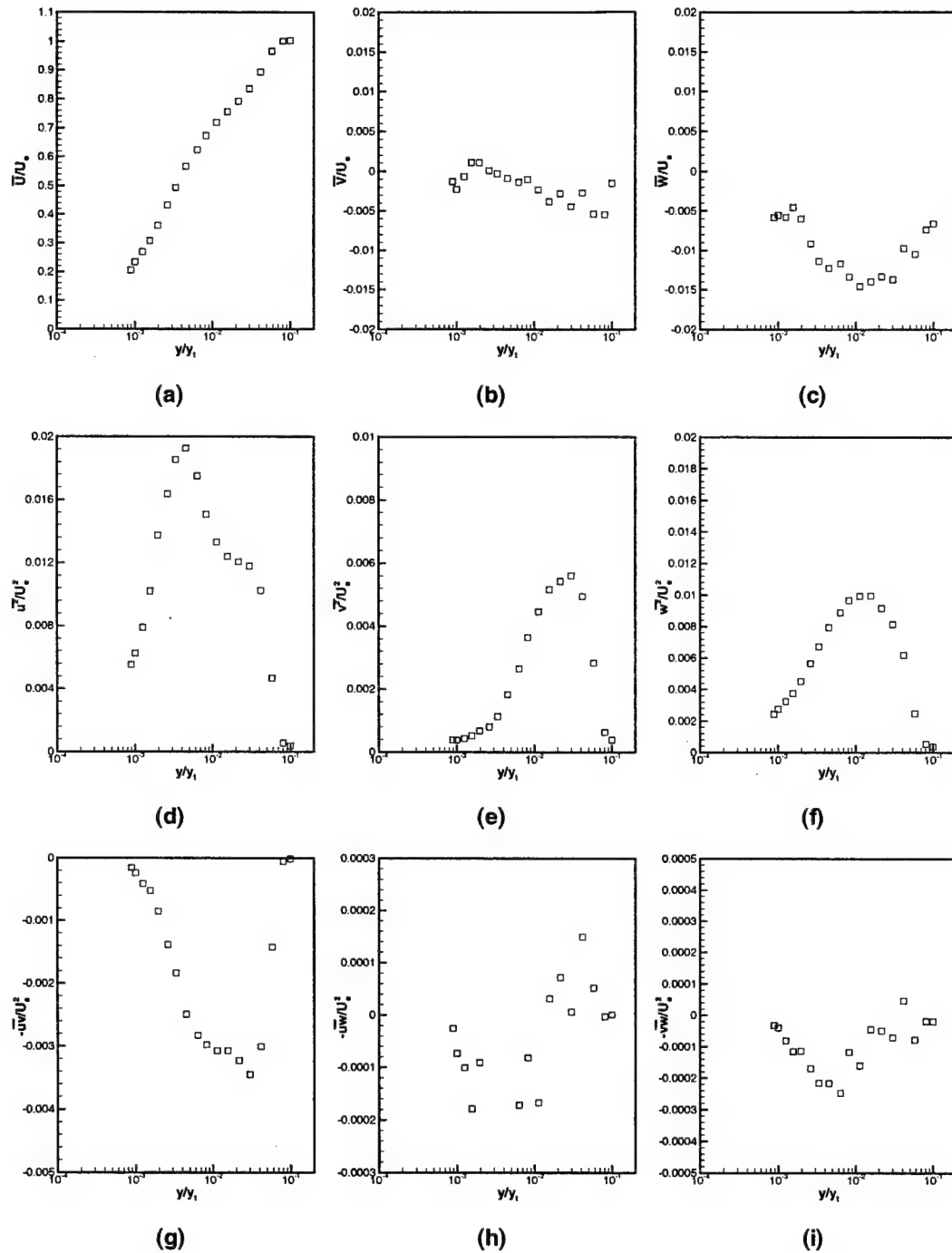


Figure A.12: Profile 8C3 Mean Velocities and Reynolds Stresses

# Appendix B

## Uncertainty Analysis

### B.1 Small Boundary Layer Tunnel Data

#### B.1.1 Velocities

The uncertainties are calculated using the same method as Olcmen and Simpson (1995). The same profile was taken on two different consecutive days. The profile is at 2.75 inches downstream of the test section leading edge and approximately at the center of the tunnel. No vortex generators were in the flow. The Uncertainty is calculated using Chauvenet's criterion to calculate the standard deviation. Chauvenet's criterion is basically only a selected constant ratio between an average value and the standard deviation. Equation B.1,

$$\frac{d_{max}}{\sigma} = 1.15 \quad (B.1)$$

where  $d_{max}$  is the average of the half of the differences between two data values. The value of 1.15 is chosen to give us 21 to 1 odds uncertainties calculated as  $\pm 2\sigma$ . The uncertainties are shown in Table B.1.

#### B.1.2 Y position

The uncertainty of the finding the wall is  $\pm 50\mu m$ . This value is determined by careful examination of the traverse system along with the y-shifts calculated from the fit of Equation 2.2.

Table B.1: Uncertainties in measured quantities with 21:1 odds

$U/U_\tau$	$\pm 0.182$	$\overline{u^2 v}/U_\tau^3$	$\pm 0.044$
$V/U_\tau$	$\pm 0.022$	$\overline{u^2 w}/U_\tau^3$	$\pm 0.008$
$W/U_\tau$	$\pm 0.042$	$\overline{v^2 w}/U_\tau^3$	$\pm 0.005$
$\overline{u^2}/U_\tau^2$	$\pm 0.726$	$\overline{uv^2}/U_\tau^3$	$\pm 0.002$
$\overline{v^2}/U_\tau^2$	$\pm 0.002$	$\overline{uw^2}/U_\tau^3$	$\pm 0.036$
$\overline{w^2}/U_\tau^2$	$\pm 0.023$	$\overline{vw^2}/U_\tau^3$	$\pm 0.017$
$-\overline{uv}/U_\tau^2$	$\pm 0.072$	$\overline{uvw}/U_\tau^3$	$\pm 0.019$
$-\overline{uw}/U_\tau^2$	$\pm 0.093$	$\overline{u^3}/U_\tau^3$	$\pm 0.756$
$-\overline{vw}/U_\tau^2$	$\pm 0.034$	$\overline{v^3}/U_\tau^3$	$\pm 0.007$
		$\overline{w^3}/U_\tau^3$	$\pm 0.014$

## B.2 Linear Cascade Tunnel Data

### B.2.1 Stationary Wall Velocities

The same method described above for finding the uncertainties in the velocities in the Auxiliary tunnel is used for the stationary wall data in the Cascade tunnel. The two profiles used for this examination are taken at profile 1F. The profiles were taken before the main set of data was acquired. The profiles were taken on two consecutive days at the same location. Table B.2 shows the uncertainties.

### B.2.2 Y position Uncertainty

The uncertainty of the finding the wall is  $\pm 50\mu m$ , which is the same as for the Auxiliary tunnel. The same traverse system and method is used in both tunnels for finding the wall; therefore, the uncertainties are the same. The y shifts calculated using the Spalding equation fit ended up too high and unreliable so the data were not adjusted using it.

Table B.2: Uncertainties for the stationary wall data measured quantities with 21:1 odds

$U/U_\tau$	$\pm 0.098$	$\overline{u^2 v}/U_\tau^3$	$\pm 0.056$
$V/U_\tau$	$\pm 0.245$	$\overline{u^2 w}/U_\tau^3$	$\pm 0.074$
$W/U_\tau$	$\pm 0.362$	$\overline{v^2 w}/U_\tau^3$	$\pm 0.239$
$\overline{u^2}/U_\tau^2$	$\pm 0.203$	$\overline{uv^2}/U_\tau^3$	$\pm 0.015$
$\overline{v^2}/U_\tau^2$	$\pm 0.307$	$\overline{uw^2}/U_\tau^3$	$\pm 0.105$
$\overline{w^2}/U_\tau^2$	$\pm 0.093$	$\overline{vw^2}/U_\tau^3$	$\pm 0.039$
$-\overline{uv}/U_\tau^2$	$\pm 0.001$	$\overline{uvw}/U_\tau^3$	$\pm 0.066$
$-\overline{uw}/U_\tau^2$	$\pm 0.105$	$\overline{u^3}/U_\tau^3$	$\pm 0.377$
$-\overline{vw}/U_\tau^2$	$\pm 0.032$	$\overline{v^3}/U_\tau^3$	$\pm 0.062$
		$\overline{w^3}/U_\tau^3$	$\pm 0.831$

### B.2.3 Flow Angle Uncertainty

To begin with  $FA = \tan^{-1}(\overline{W}/\overline{U})$ . Using a first order Taylor expansion of the equation the uncertainties for the flow angle can be calculated. Using Equation B.2 below.

$$\delta FA = \pm \sqrt{\left(\frac{dFA}{d\overline{U}}\right)^2 \delta \overline{U}^2 + \left(\frac{dFA}{d\overline{W}}\right)^2 \delta \overline{W}^2} \quad (\text{B.2})$$

Where  $\delta U$  and  $\delta W$  are the uncertainties of the velocities. For the stationary wall data  $\delta U = 0.0995$  m/s,  $\delta W = 0.3343$  m/s and we will use values of  $\overline{U} = 6.827$  m/s,  $\overline{W} = -16.2029$  m/s (the mean velocities are taken from the profiles used in the above uncertainty analysis). The equation for FA is:  $FA = \tan^{-1}(\frac{\overline{W}}{\overline{U}})$ . Taking the derivatives and plugging in the values,  $\delta FA = \pm 0.518^\circ$ . The uncertainty of the flow angles is approximately  $\pm 0.5^\circ$ .

### B.2.4 Moving Wall

By not having one continuous run of data increases the uncertainties of the measured quantities. Since there was not two complete sets of data to compare, the uncertainty analysis will follow that used for the flow angle calculation. The uncertainty is calculated for the  $\overline{U}$  velocity.

There are two sources for the uncertainty with the moving belt. The two sources come from the movement of the belt. The first source is uncertainty associated with vertical movement. The

second source is uncertainty associated with tangential movement. There is no axial uncertainty because the leading edge of the belt is kept constant by the stationary overlap flap.

The tangential movement of the belt comes from the uncertainty in the belt speed. From Ma et al. (2000) the stability of the belt speed while running was 0.24% r.m.s. ( $\delta V_{belt} = 0.0544$  m/s).

The belt moves up and down and this movement is recorded with the BELT-HITE sensor for each new belt. The standard deviation of the belt displacement is found to be  $\delta y = \pm 6.58$   $\mu\text{m}$ .

To simplify the analysis a version of the Law of the Wall, Overlap layer equation is fit to the data. The equation has the form shown in Equation B.3 (White, 1974).

$$U^+ = \frac{1}{\kappa} \ln(y^+) + B \quad (\text{B.3})$$

Where to fit it to the data with the moving wall the constants  $\kappa$  and  $B$  are given the values of 0.30 and 1 respectively. The fit of the curve is shown in Figure B.1. Taking this equation and putting it into a workable form normalized on the belt speed, Equation B.4

$$\bar{U}/V_{belt} = \frac{U_\tau}{V_{belt}} \left[ \frac{1}{\kappa} \ln\left(\frac{y * U_\tau}{\nu}\right) + B \right] \quad (\text{B.4})$$

Using the analysis for the flow angle above, the equation to find the uncertainties is shown in Equation B.5.

$$\delta\left(\frac{\bar{U}}{V_{belt}}\right) = \pm \sqrt{\left(\frac{d\bar{U}/V_{belt}}{dV_{belt}}\right)^2 \delta V_{belt}^2 + \left(\frac{d\bar{U}/V_{belt}}{dy}\right)^2 \delta y^2} \quad (\text{B.5})$$

Where  $\delta V_{belt}$  and  $\delta y$  are discussed above as the uncertainties in the belt movement. We will use values of  $\bar{U} = 6.81$  m/s,  $y = 0.0029$  m (values are taken at a mid point on Figure B.1). The equation for  $\bar{U}/V_{belt}$  is shown in Equation B.4. The other values for the equation are;  $U_\tau = 0.46$  m/s,  $\nu = 1.5663 \times 10^{-5}$   $\text{m}^2/\text{s}$  and  $V_{belt} = 21.47$  m/s. Taking the derivatives and plugging in the values,  $\delta(\bar{U}/V_{belt}) = \pm 0.000818$ .

### B.2.5 Moving Wall With Vortex Generators

Four variables contribute to the uncertainty in calculating the vortex generators position as a function of time. This is the uncertainty of the  $z$  position of the vortex generators,  $\delta z/z_b$ . Two of the variables deal with the movement of the belt in the transverse direction, two of the variables deal with the movement of the belt in the axial direction.

The two variables in the transverse direction are the spacing of the vortex generators,  $Z_{vg}$ , and the belt velocity,  $V_{belt}$ . The spacing between the vortex generators was set as well as possible however there is still some deviation. The vortex generators were spaced 23.6 cm apart with a standard deviation of 0.266 mm in the spacing,  $\delta Z_{vg}$ . The belt velocity uncertainty is discussed above and it was found to be  $\delta V_{belt} = \pm 0.0515$  m/s.

The two variables in the axial direction are the axial movement of the belt and the variation in the free-stream velocity. The axial positioning of the vortex generators is neglected because it is so small compared with the axial movement of the belt. The axial positioning uncertainty comes from the control problems with the belt. However because the data is limited to only being acquired when the beams shoot through the optically clear window, 9 mm wide, there is a control. All five beam must shoot through this window to get a valid signal. Therefore the closer together the beams are at the window the more uncertain the position of the belt. The range of spacing of the beams at the belt is approximately 0.1 mm apart beams just off the wall to 7.5 mm apart beams at the last y position (the closer to the wall the more uncertain this axial position). Therefore the range of the uncertainty is from  $\pm 0.75$  mm to  $\pm 4.45$  mm. This effect causes the decreases the data rate the further from the wall the measurement volume is. Since the point of data was taken at  $y = 1$  cm, the spacing of the beams is approximately 2.5 mm, the uncertainty axial movement is therefore  $\pm 3.25$  mm,  $\delta X_{vg}$ . The uncertainty in the axial velocity in the freestream (for this profile), approximating with the moving wall uncertainty analysis, is  $\pm 0.0176$  m/s,  $\delta U_{ap}$ .

A simple relationship is derived for this analysis. The magnitude of the distances travelled divided by the magnitude of the velocities gives the time it took the vortex to travel that far. Equation B.6 shows this equation.

$$\tau_{vg} = \frac{\sqrt{X_{vg}^2 + Z_{vg}^2}}{\sqrt{U_{ap}^2 + V_{belt}^2}} \quad (B.6)$$

$Z_{vg} = 23.6$  cm,  $V_{belt} = 21.47$  m/s,  $X_{vg} = 3.1$  cm and  $U_{ap} = 10.53$  m/s.  $U_{ap}$  is in the bed coordinate system. The value is the measured free-stream velocity with the moving wall profile data. To calculate the uncertainty of the time,  $\delta \tau$ , Equation B.7 is derived from propagation of error analysis.

$$\delta \tau_{vg} = \pm \sqrt{\left(\frac{d\tau_{vg}}{dZ_{vg}}\right)^2 \delta Z_{vg}^2 + \left(\frac{d\tau_{vg}}{dV_{belt}}\right)^2 \delta V_{belt}^2 + \left(\frac{d\tau_{vg}}{dX_{vg}}\right)^2 \delta X_{vg}^2 + \left(\frac{d\tau_{vg}}{dU_{ap}}\right)^2 \delta U_{ap}^2} \quad (B.7)$$

The solving Equation B.7 using the values listed above,  $\delta\tau_{vg} = \pm 2.8565 * 10^{-5}$ . Converting this into  $\delta z$ , or the uncertainty of the position of the vortex generator,  $\pm 0.61$  mm.

## References

- Ma, R., Saha, N., Devenport, W.J., and Wang, Y., 2000 "*Unsteady Behavior of a Tip Leakage Vortex Produced by Simulated Stator/Rotor Interaction*," AIAA paper 2000-2217, Fluids 2000, Denver, CO, June 19-22.
- Olcmen, S.M., and Simpson, R.L. 1995 "*A five-velocity -component laser-Doppler velocimeter for measurements of a three-dimensional turbulent boundary layer*," Measurement Science and Technology, Vol. 6, pp. 702-716.
- White, F.M. "*Viscous Fluid Flow*," Mcgraw-Hill pp. 475.



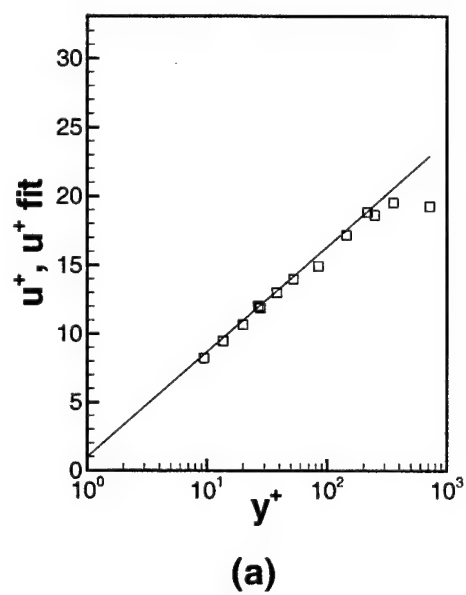


Figure B.1: Law of the wall fit to moving wall data ( $\kappa=0.30$  and  $B=1$ )

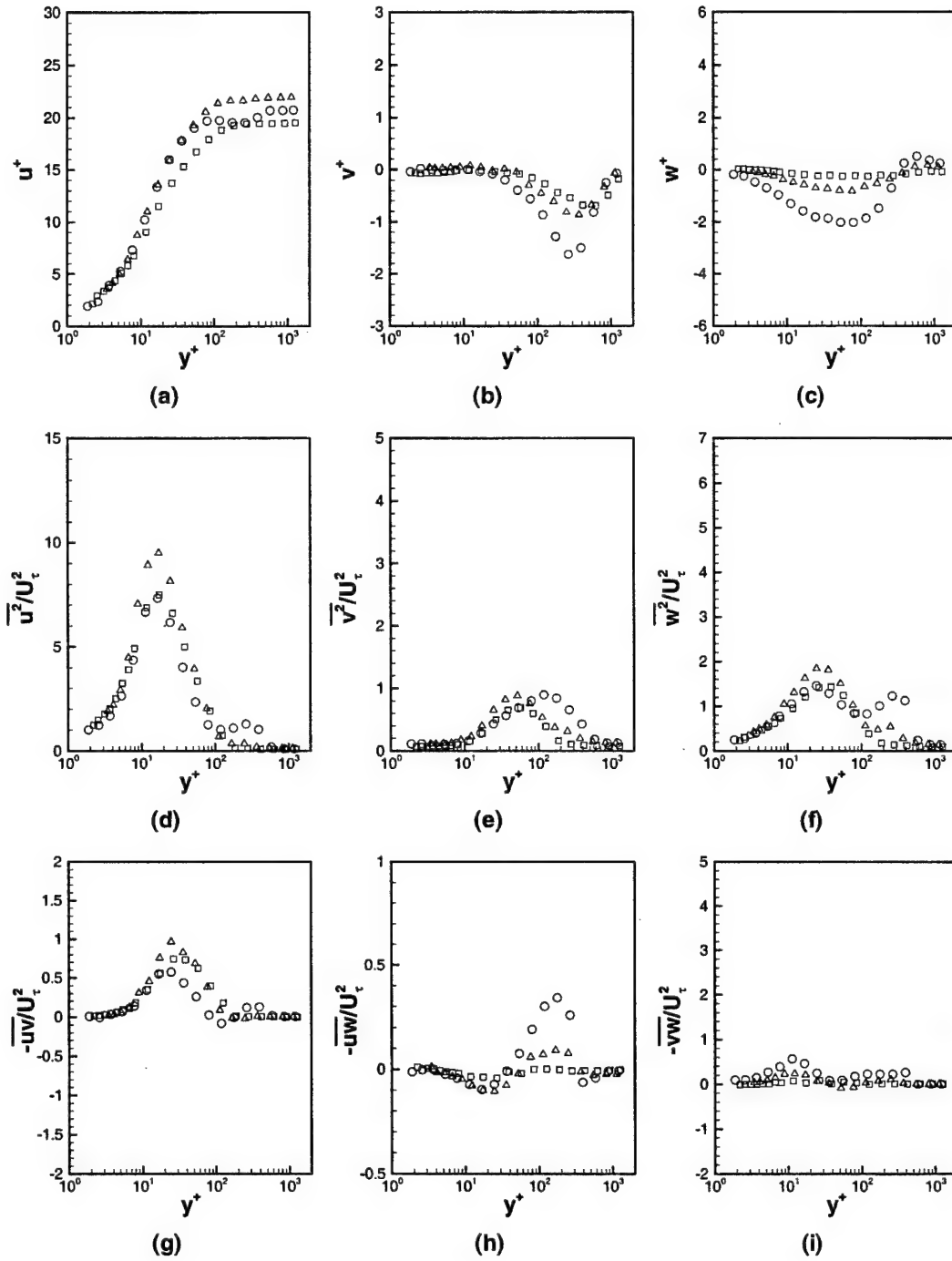
# Appendix C

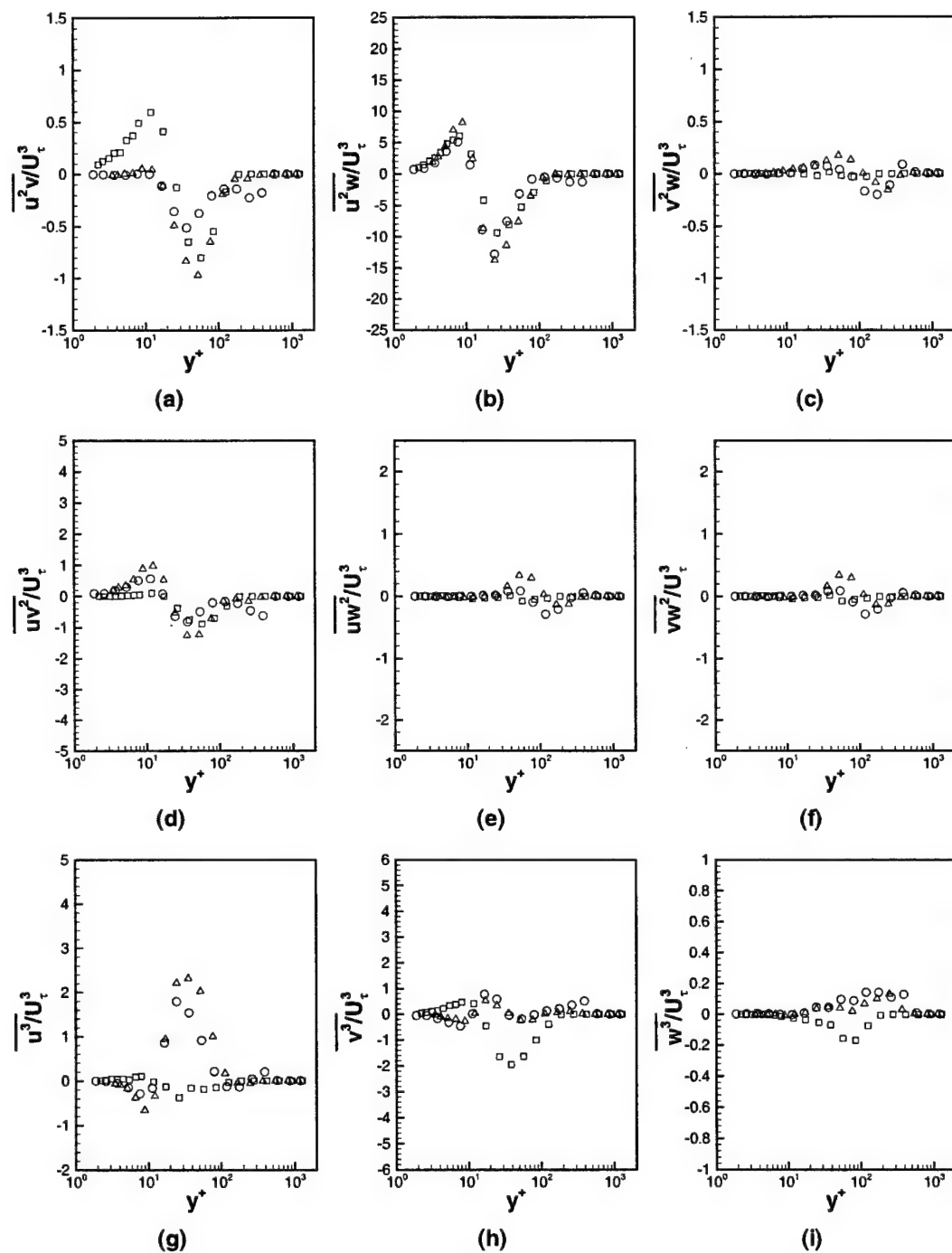
## Auxiliary Tunnel Data

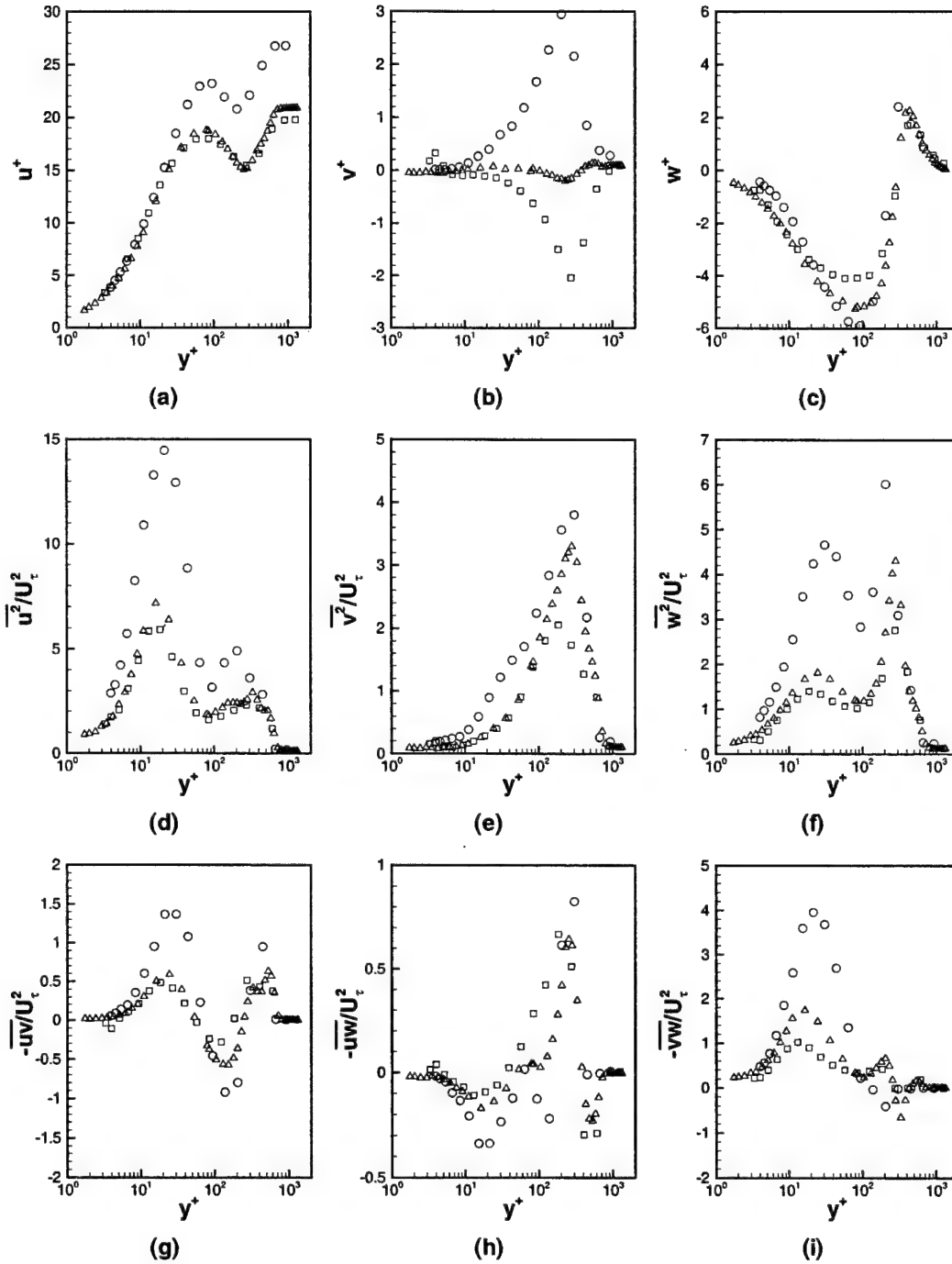
This appendix documents the mean velocities, Reynolds stresses and triple products for all of the main profiles of the test matrix in the Auxiliary tunnel. Table C.1 lists all of the profiles and the x and z locations for each. The same naming convention is used for the plots which are found in Figures C.1 to C.16. 0 denotes the center of the tunnel and 11 is farthest out in the negative z direction. The two cross sections are denoted by "F" the first cross section approximately 10.5 cm downstream of the vortex generator and "S" the second cross section approximately 44.4 cm downstream of the vortex generators.

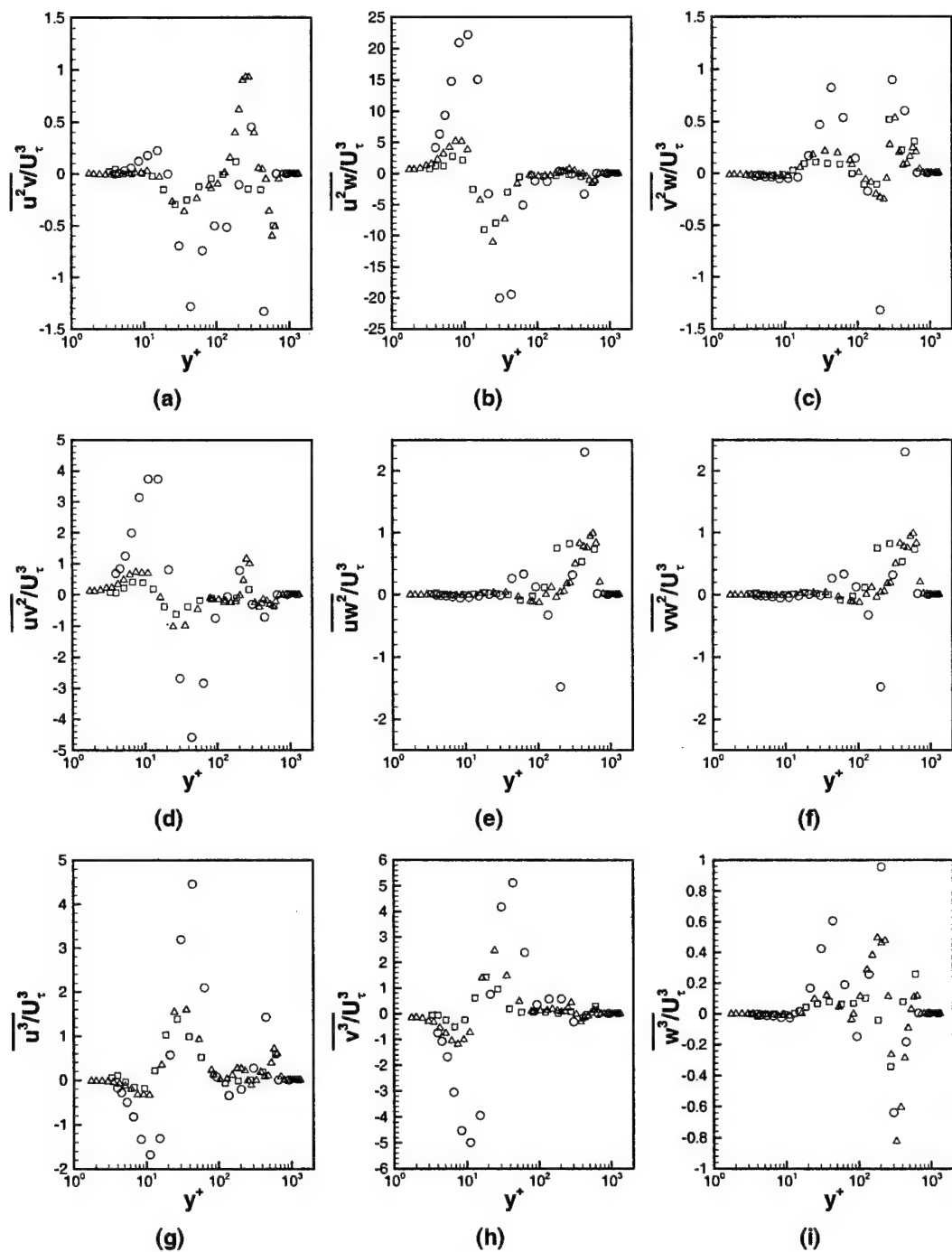
Table C.1: Auxiliary Tunnel Test Matrix

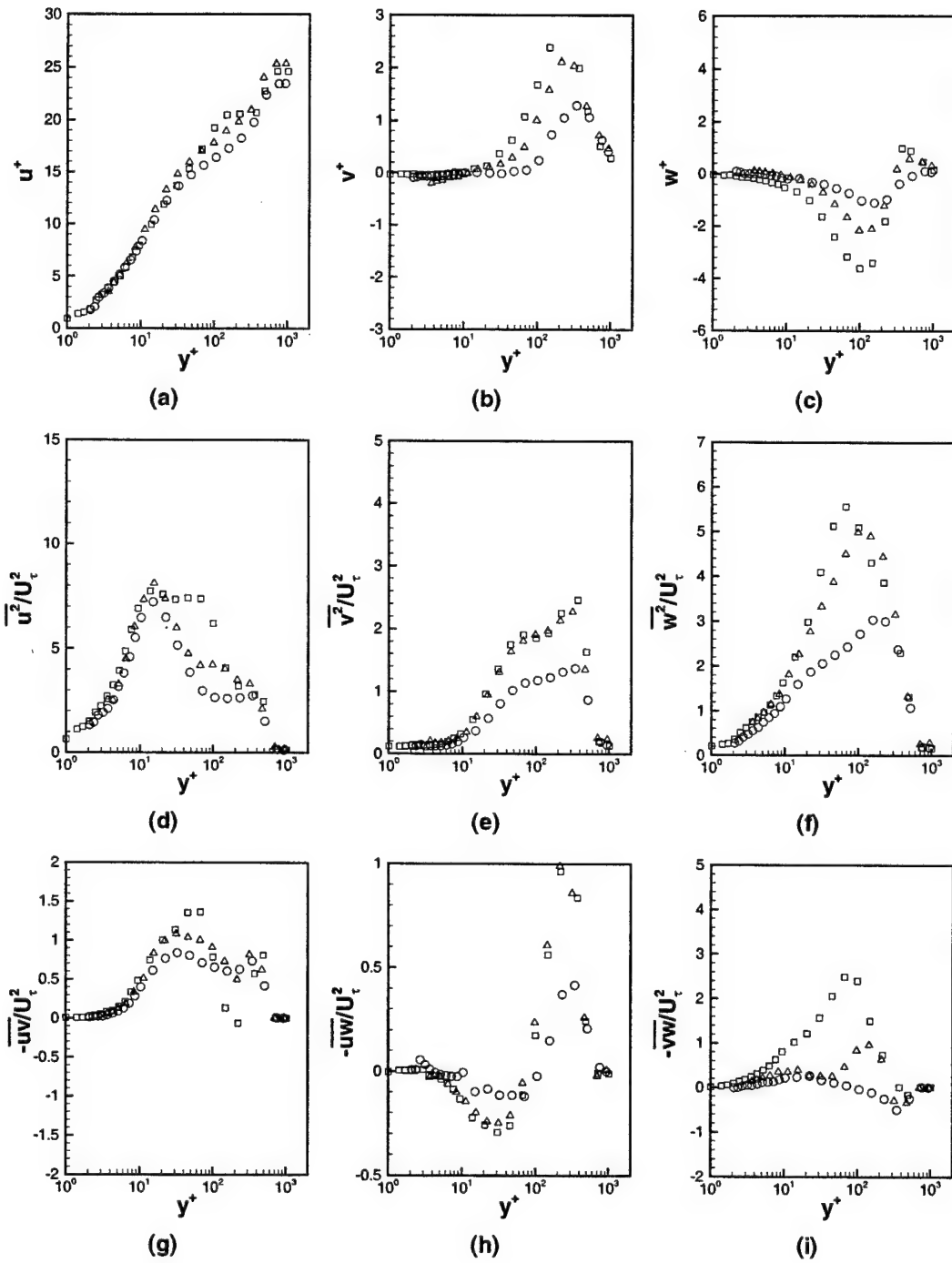
Vortex Generator Flow					
<i>Profile</i>	<i>X (cm)</i>	<i>Z (cm)</i>	<i>Profile</i>	<i>X (cm)</i>	<i>Z (cm)</i>
0F	10.59	-0.10	6F	10.59	-2.29
1F	10.59	-0.51	7F	10.60	-2.55
2F	10.59	-1.01	8F	10.60	-2.80
3F	10.59	-1.52	9F	10.60	-3.05
4F	10.59	-1.78	10F	10.60	-3.30
5F	10.59	-2.03	11F	10.61	-3.99
0S	44.37	0.1	6S	44.41	-4.03
1S	44.38	-1.01	7S	44.42	-4.54
2S	44.39	-1.99	8S	44.42	-5.04
3S	44.39	-2.50	9S	44.38	-1.51
4S	44.40	-3.01	10S	44.39	-2.25
5S	44.41	-3.53	11S	44.40	-2.80

Figure C.1: Profiles 0F  $\square$ , 1F  $\triangle$  and 2F  $\circ$  Mean Velocities and Reynolds Stresses

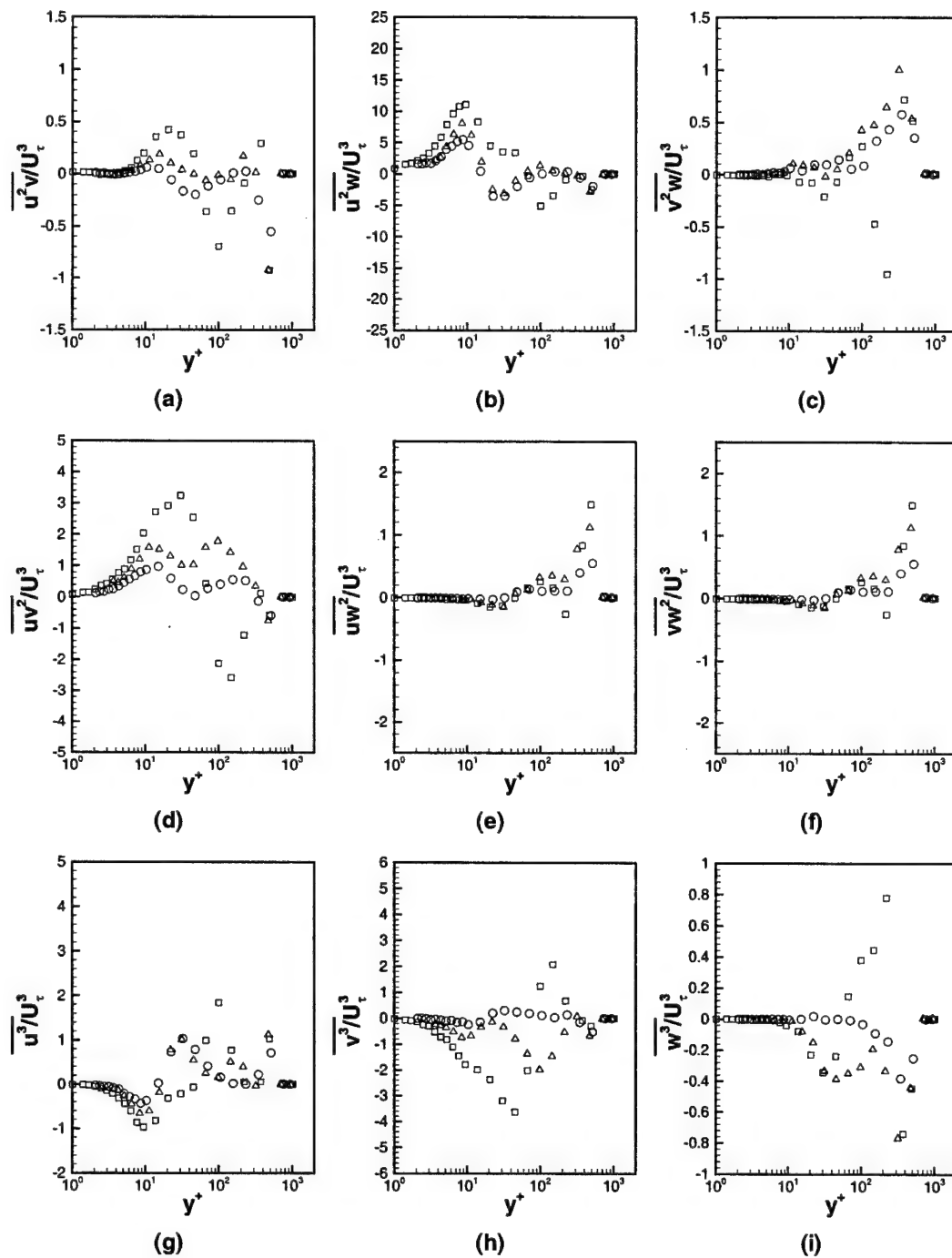
Figure C.2: Profiles 0F  $\square$ , 1F  $\triangle$  and 2F  $\circ$  Triple Products

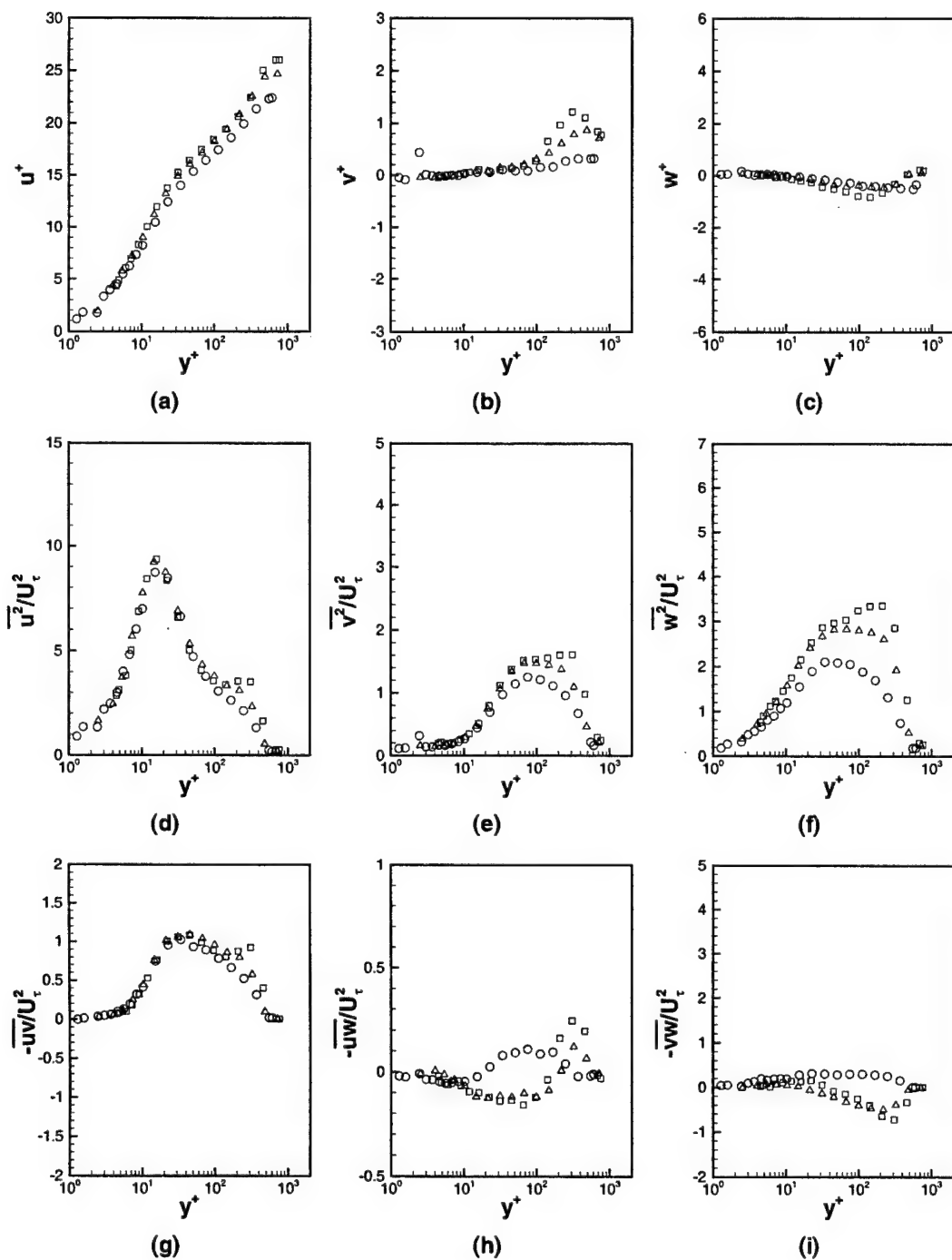
Figure C.3: Profiles 3F  $\square$ , 4F  $\triangle$  and 5F  $\circ$  Mean Velocities and Reynolds Stresses

Figure C.4: Profiles 3F  $\square$ , 4F  $\triangle$  and 5F  $\circ$  Triple Products

Figure C.5: Profiles 6F  $\square$ , 7F  $\triangle$  and 8F  $\circ$  Mean Velocities and Reynolds Stresses



Figure C.6: Profiles 6F  $\square$ , 7F  $\triangle$  and 8F  $\circ$  Triple Products

Figure C.7: Profiles 9F  $\square$ , 10F  $\triangle$  and 11F  $\circ$  Mean Velocities and Reynolds Stresses

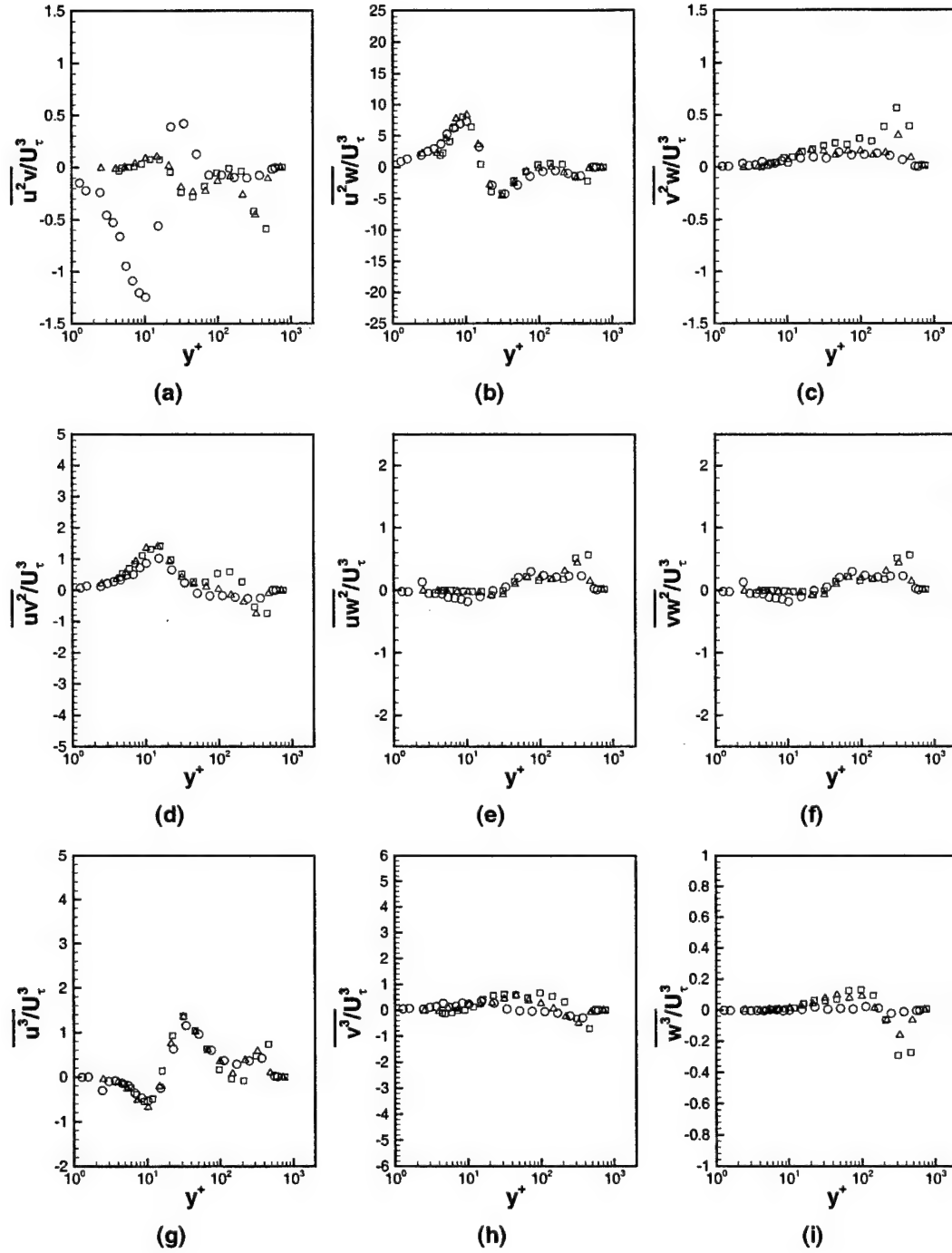
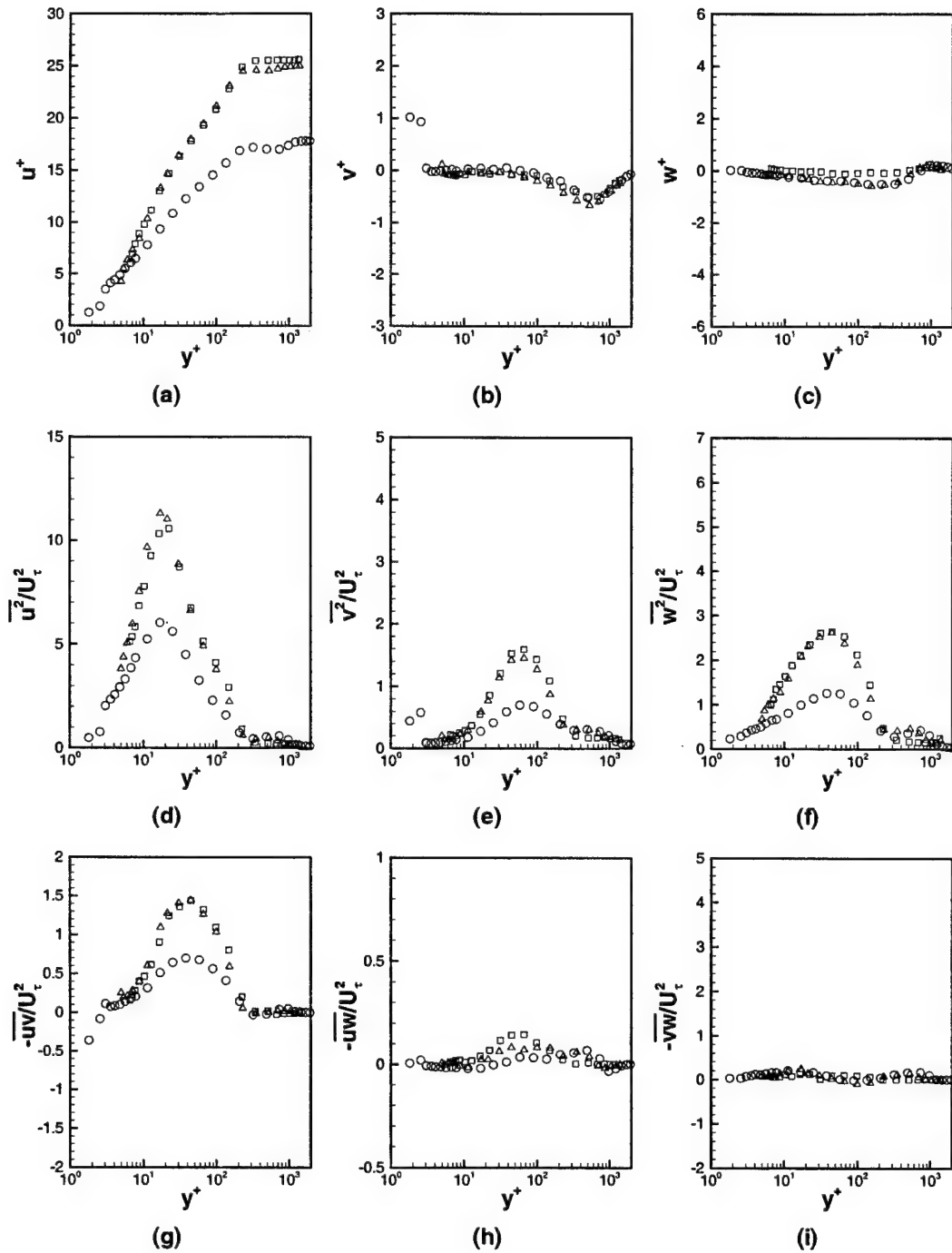
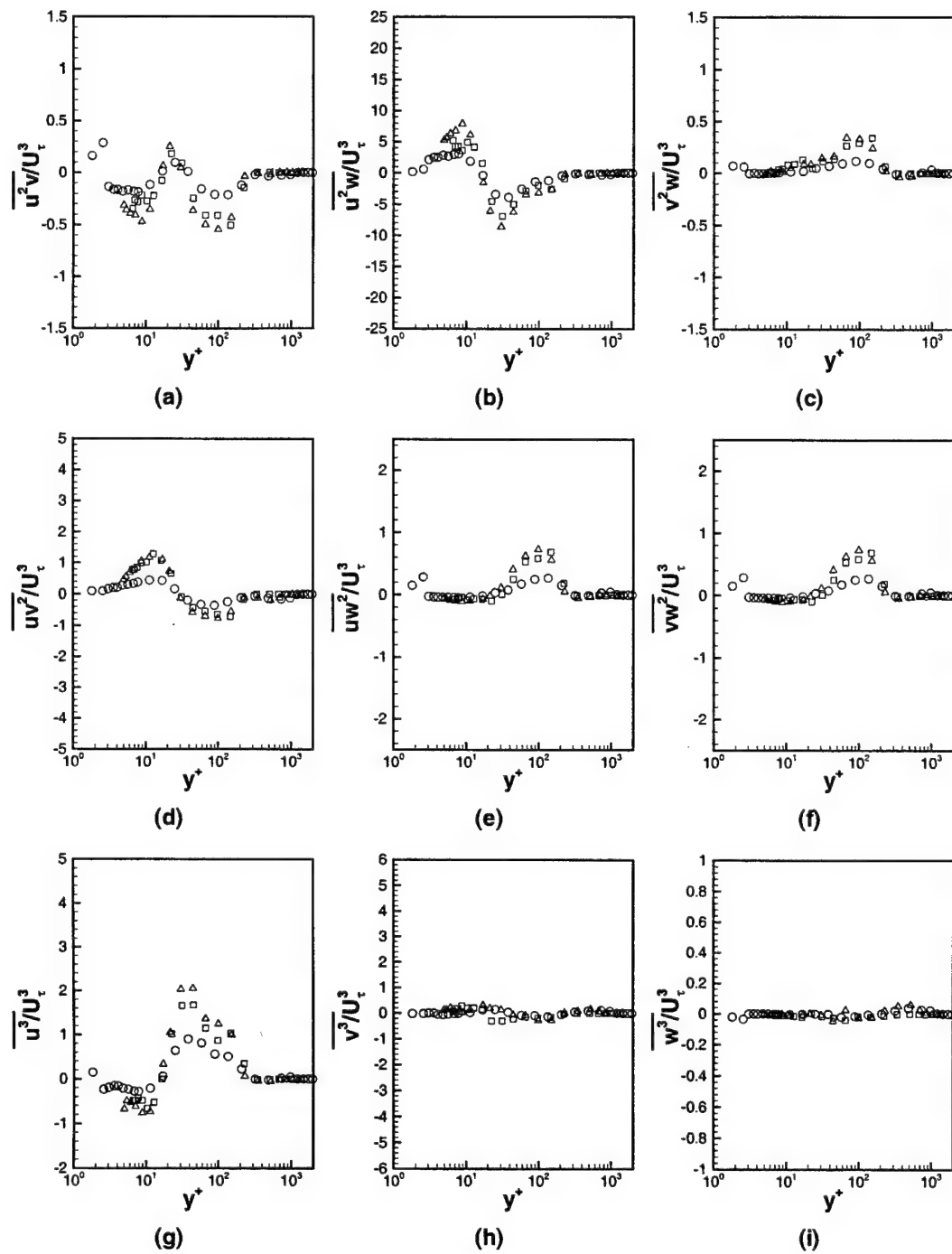
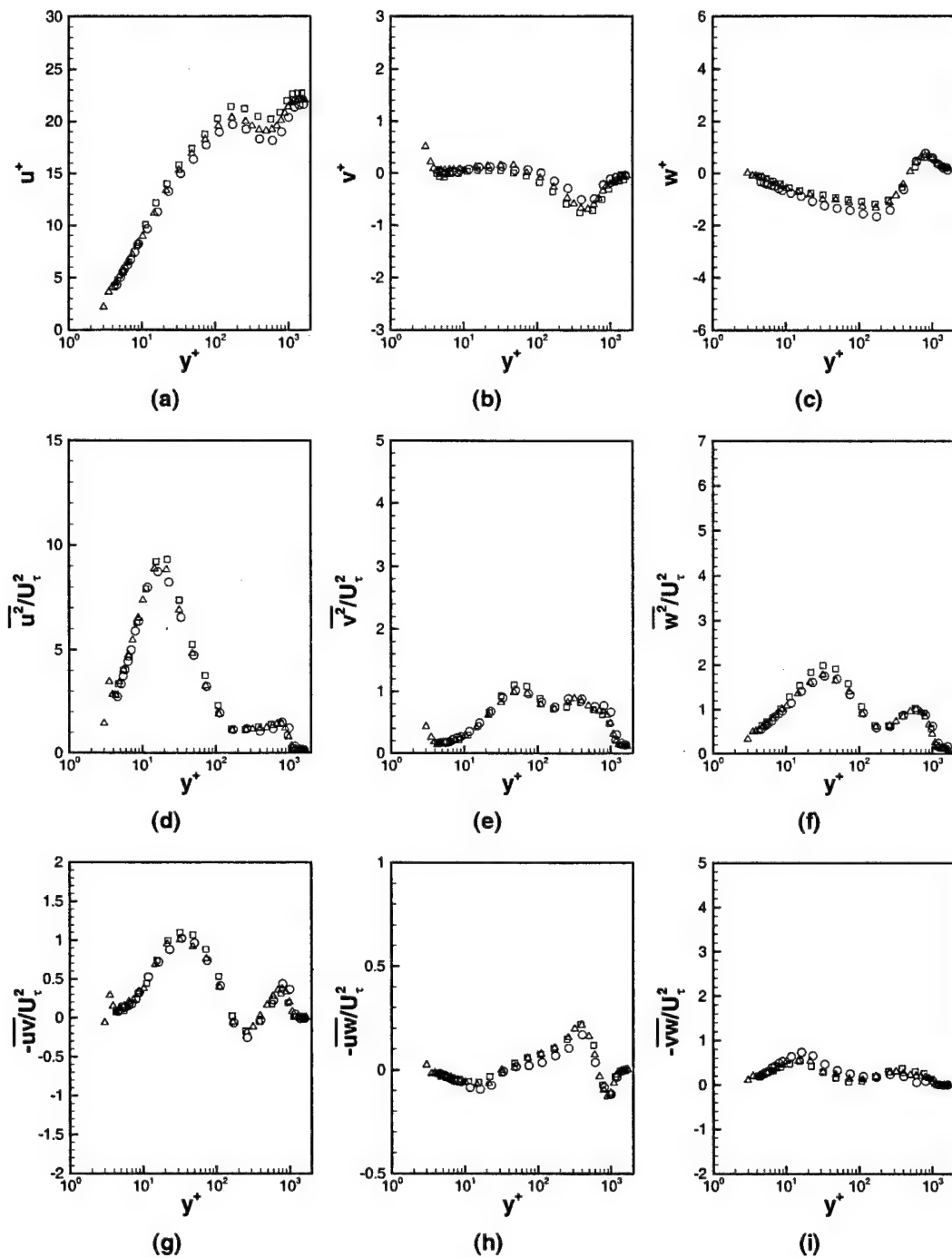
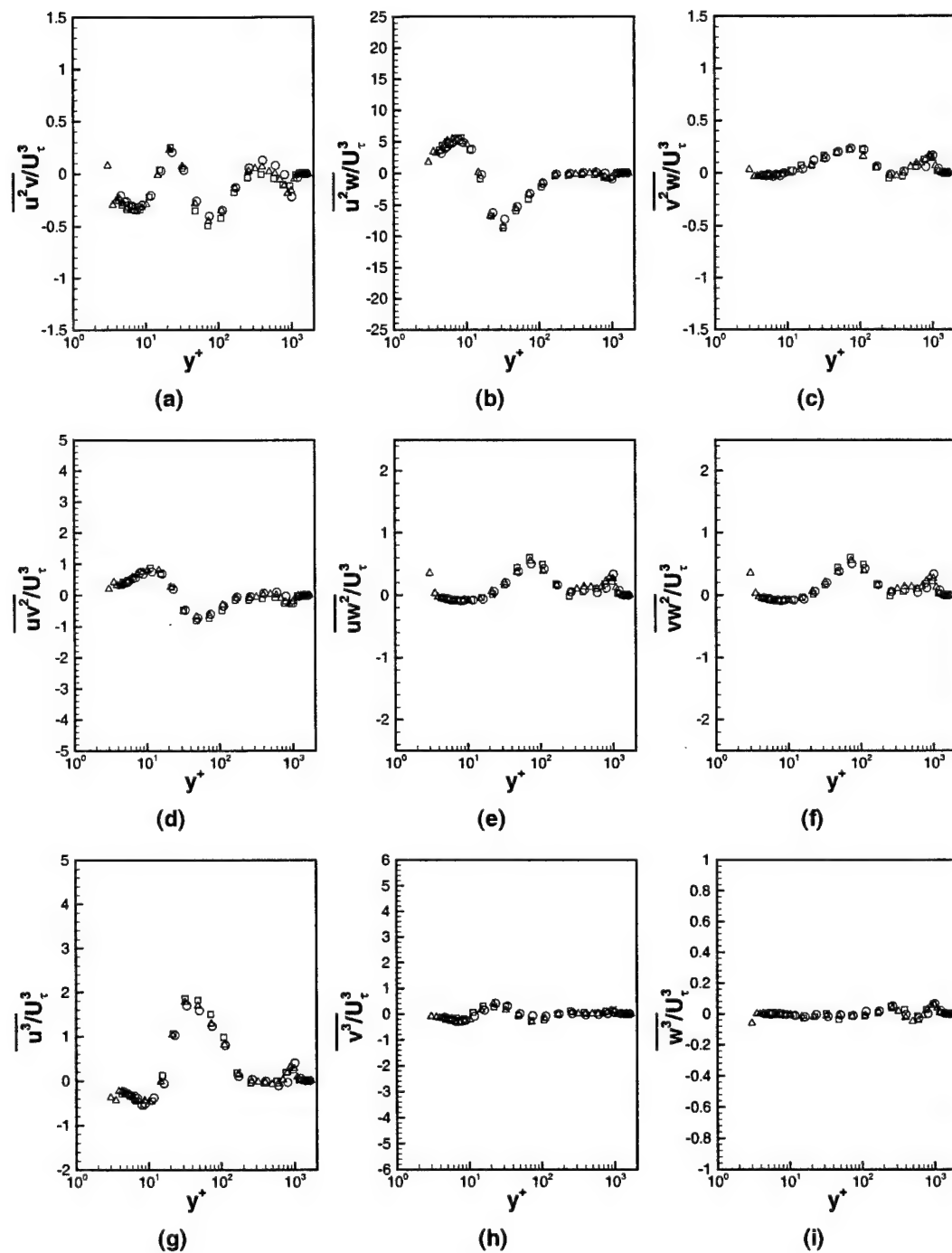


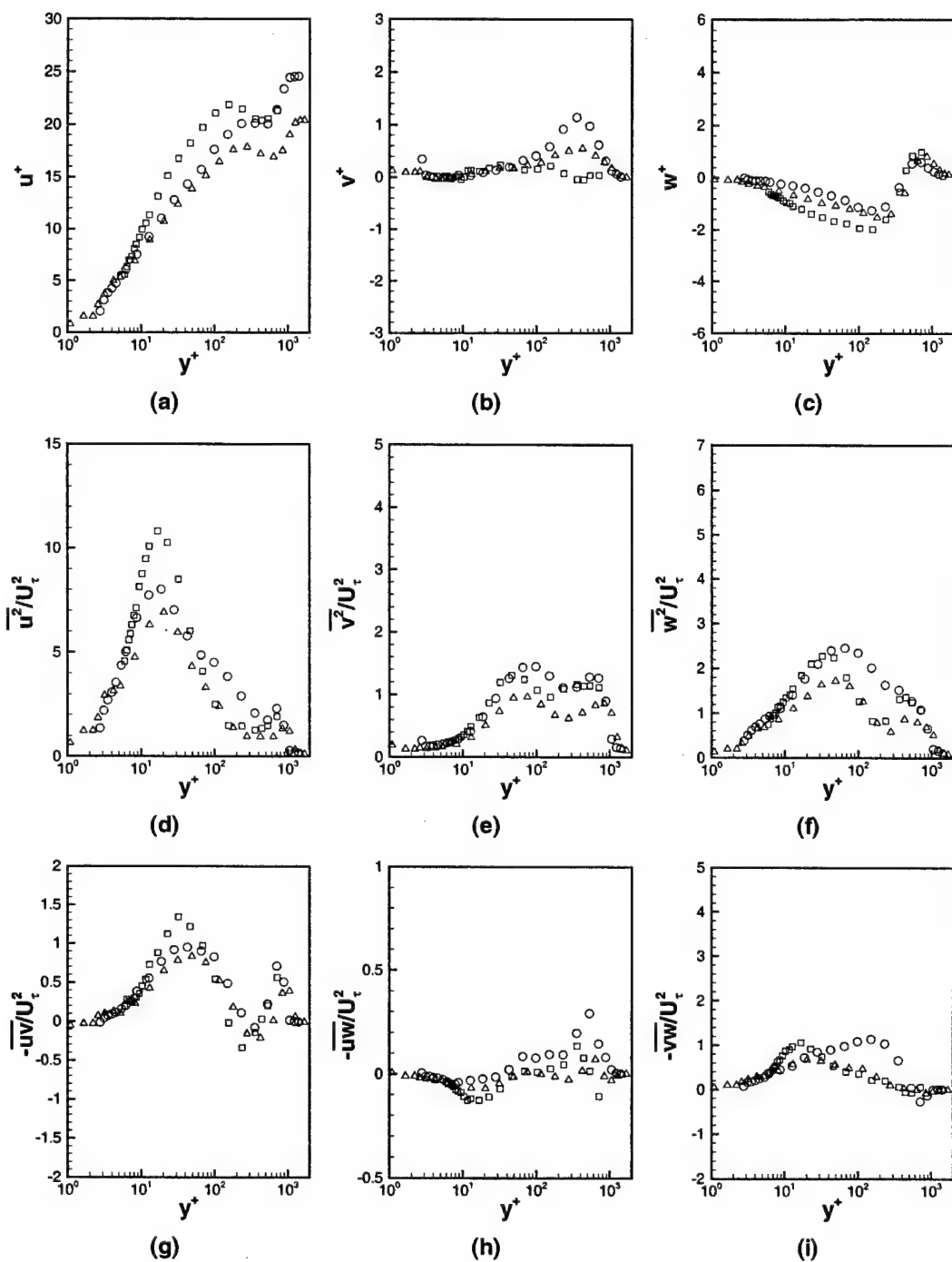
Figure C.8: Profiles 9F □, 10F △ and 11F ○ Triple Products

Figure C.9: Profiles 0S  $\square$ , 1S  $\triangle$  and 2S  $\circ$  Mean Velocities and Reynolds Stresses

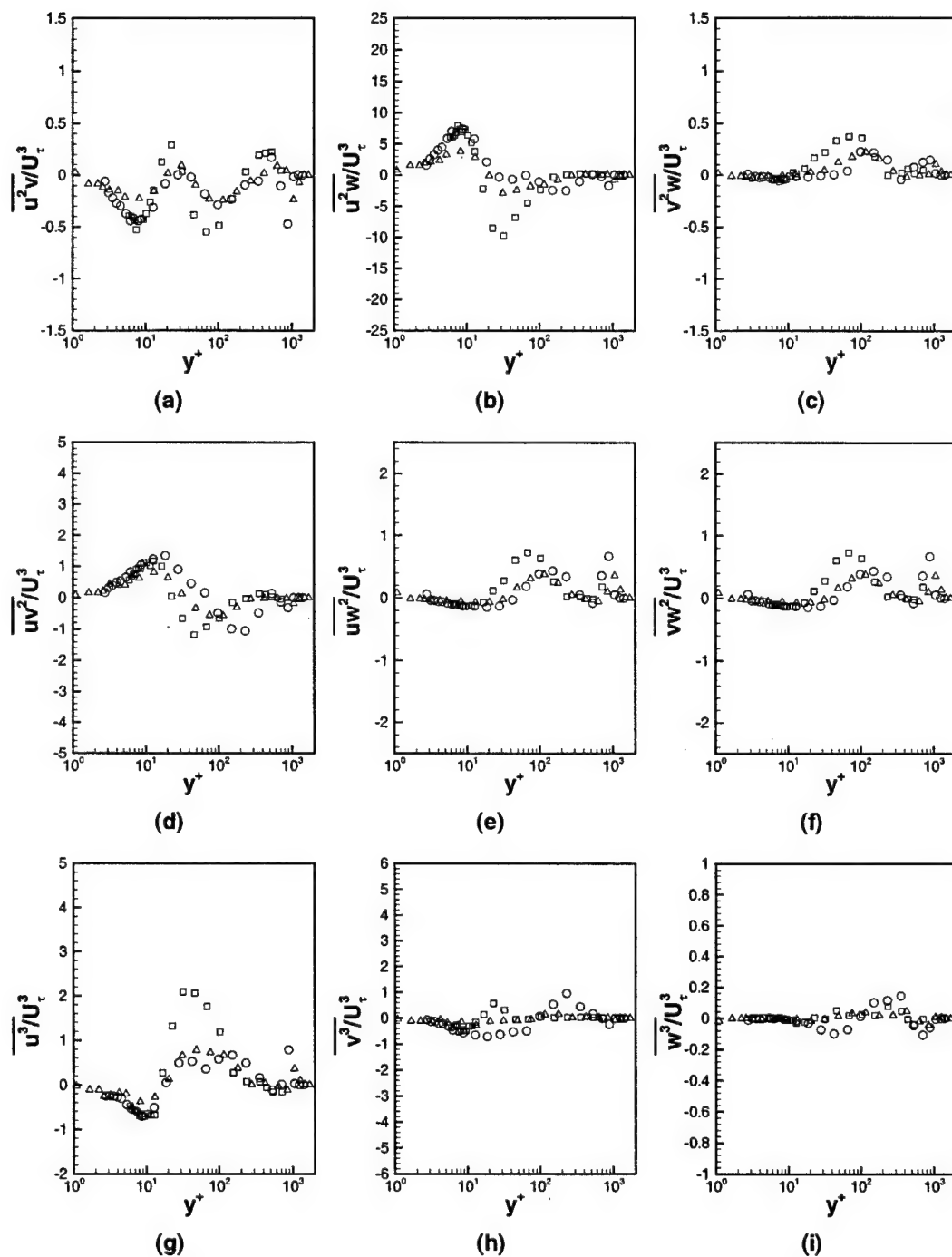
Figure C.10: Profiles OS  $\square$ , 1S  $\triangle$  and 2S  $\circ$  Triple Products

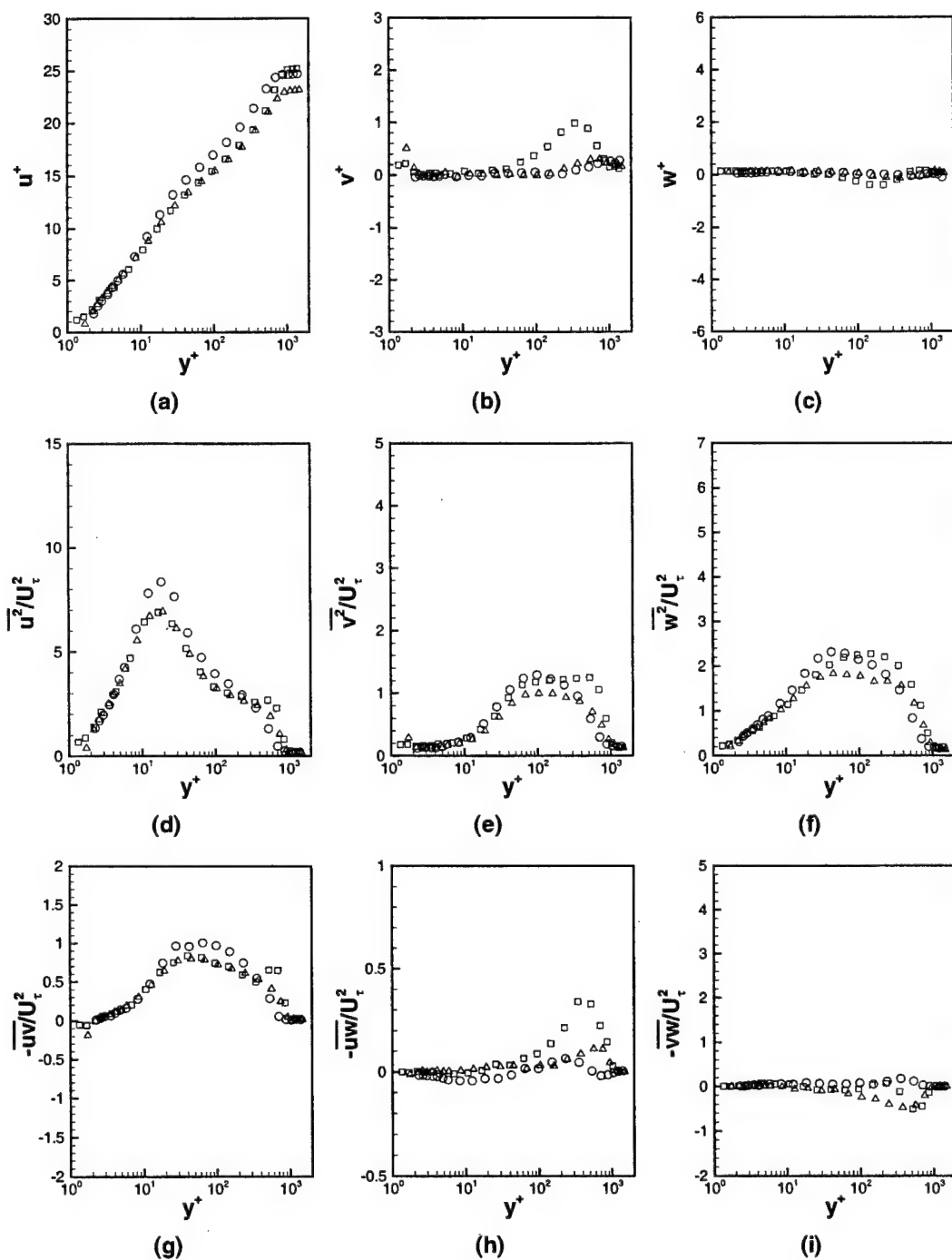
Figure C.11: Profiles 3S  $\square$ , 4S  $\triangle$  and 5S  $\circ$  Mean Velocities and Reynolds Stresses

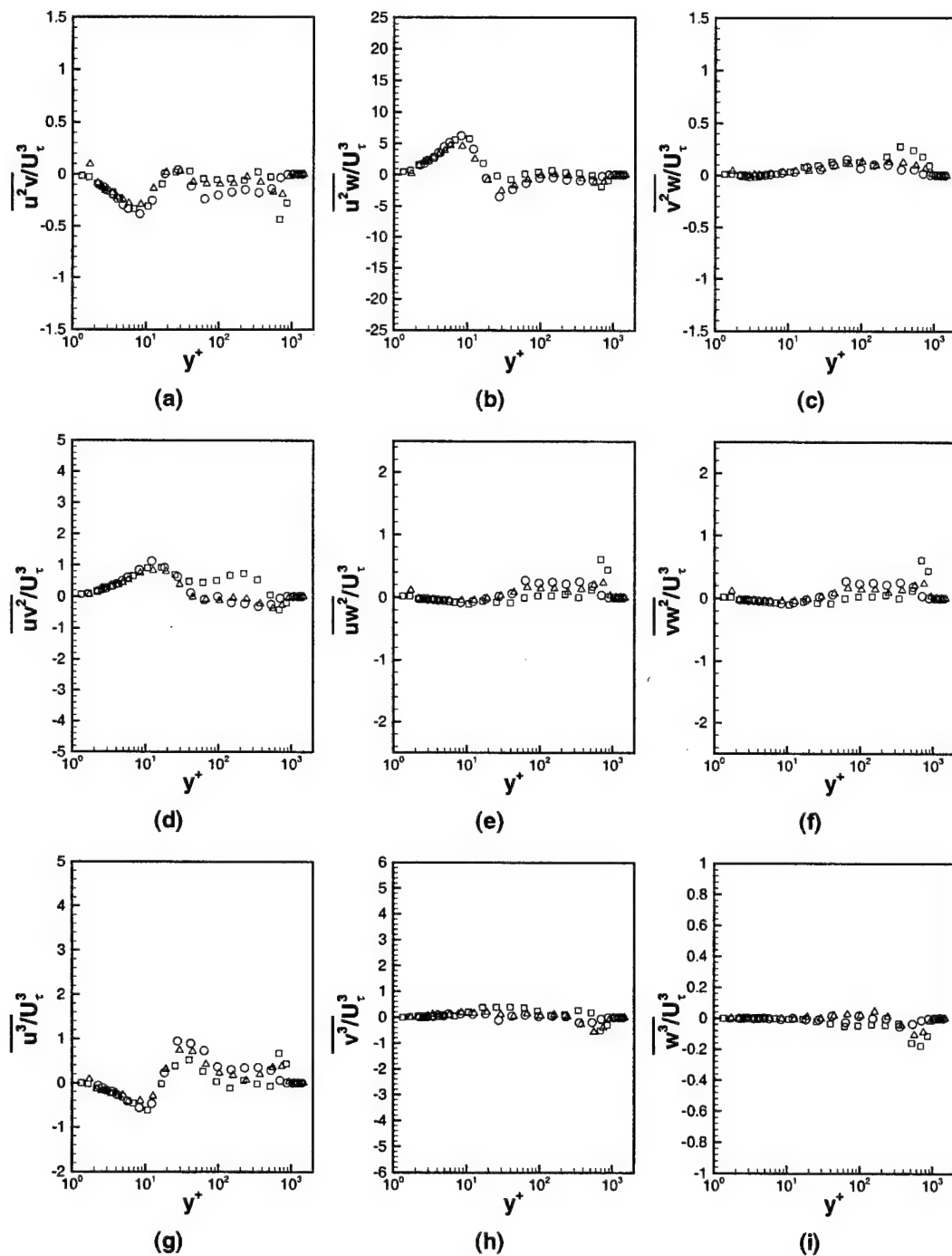
Figure C.12: Profiles 3S  $\square$ , 4S  $\triangle$  and 5S  $\circ$  Triple Products

Figure C.13: Profiles 6S  $\square$ , 7S  $\triangle$  and 8S  $\circ$  Mean Velocities and Reynolds Stresses



Figure C.14: Profiles 6S  $\square$ , 7S  $\triangle$  and 8S  $\circ$  Triple Products

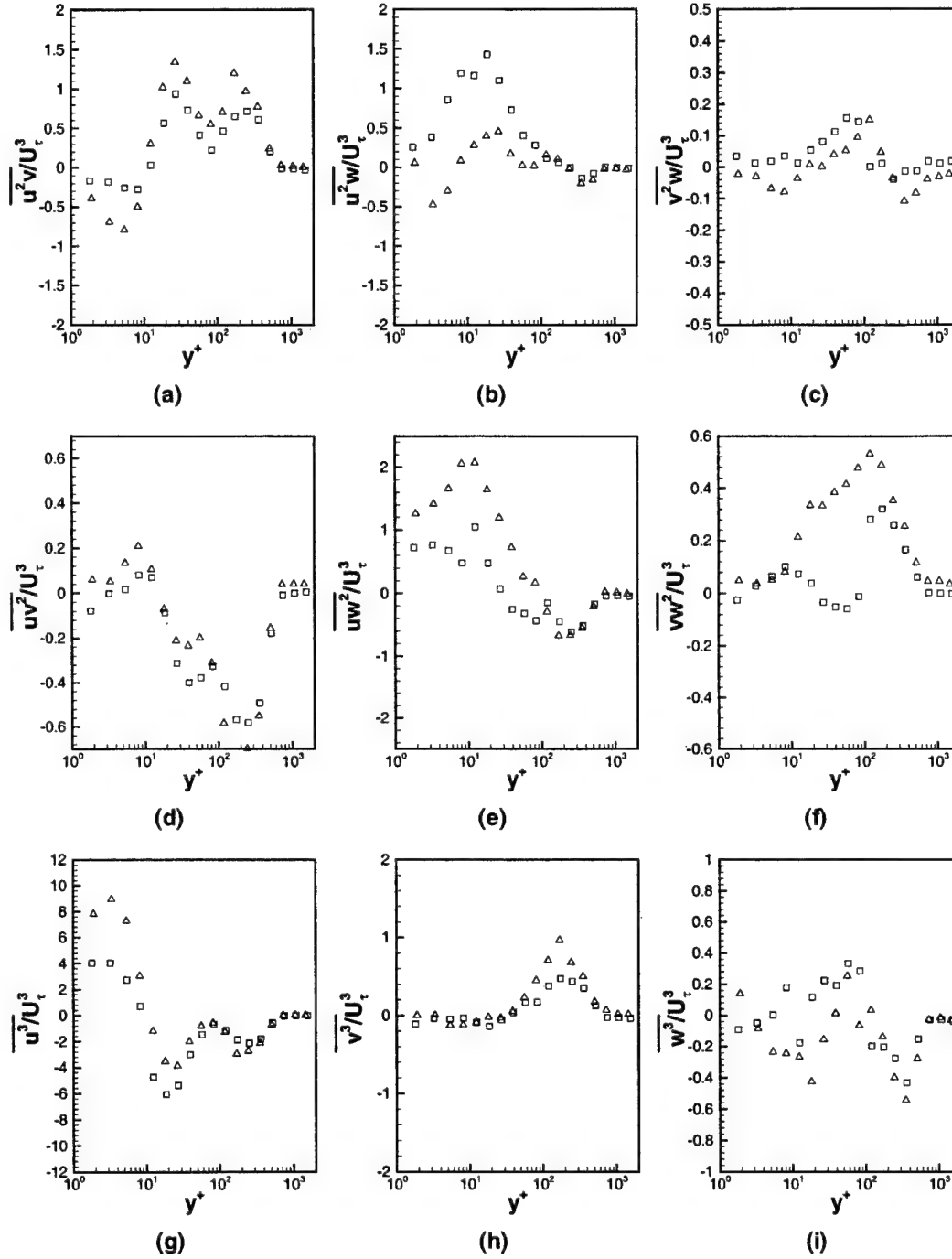
Figure C.15: Profiles 9S  $\square$ , 10S  $\triangle$  and 11S  $\circ$  Mean Velocities and Reynolds Stresses

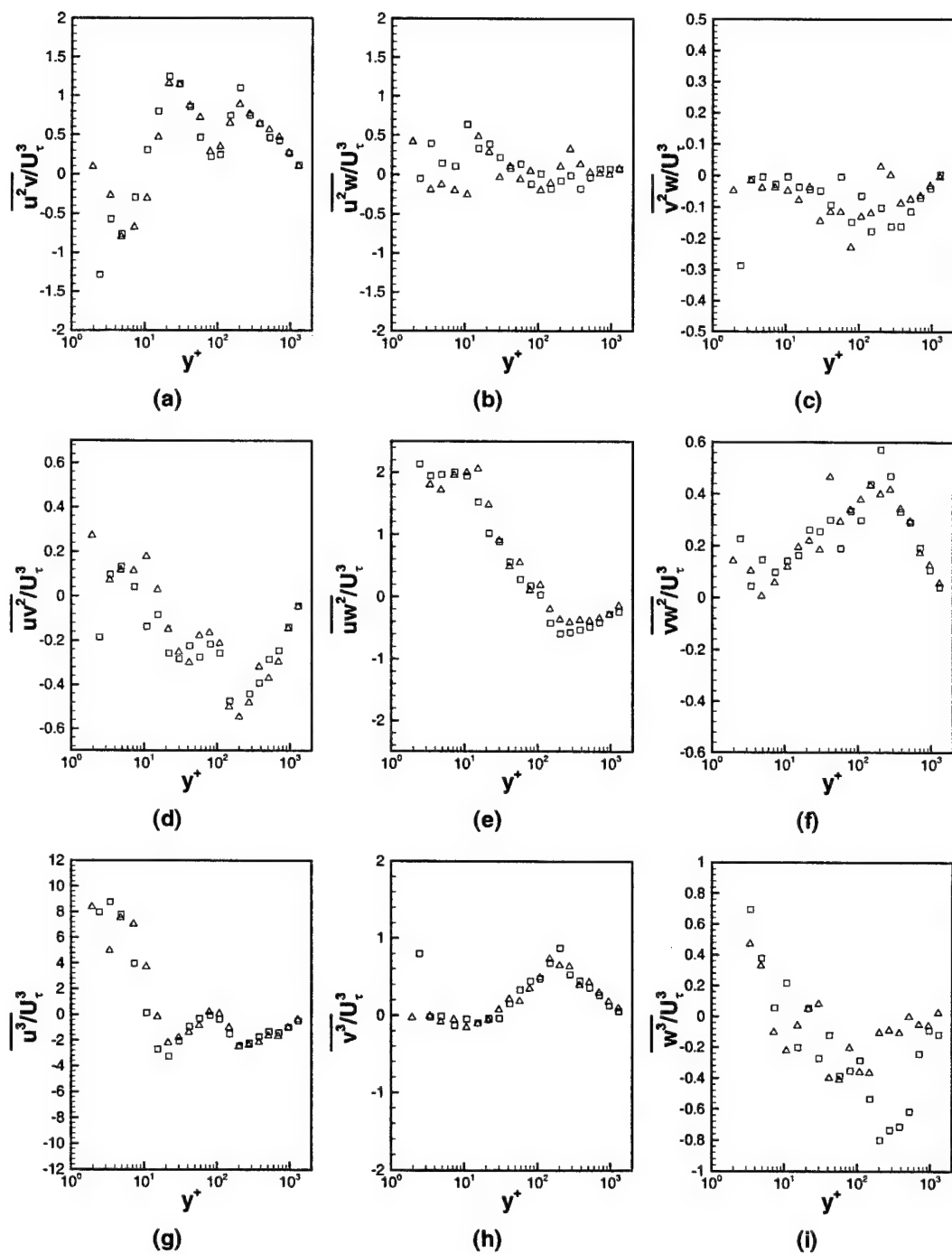
Figure C.16: Profiles 9S  $\square$ , 10S  $\triangle$  and 11S  $\circ$  Triple Products

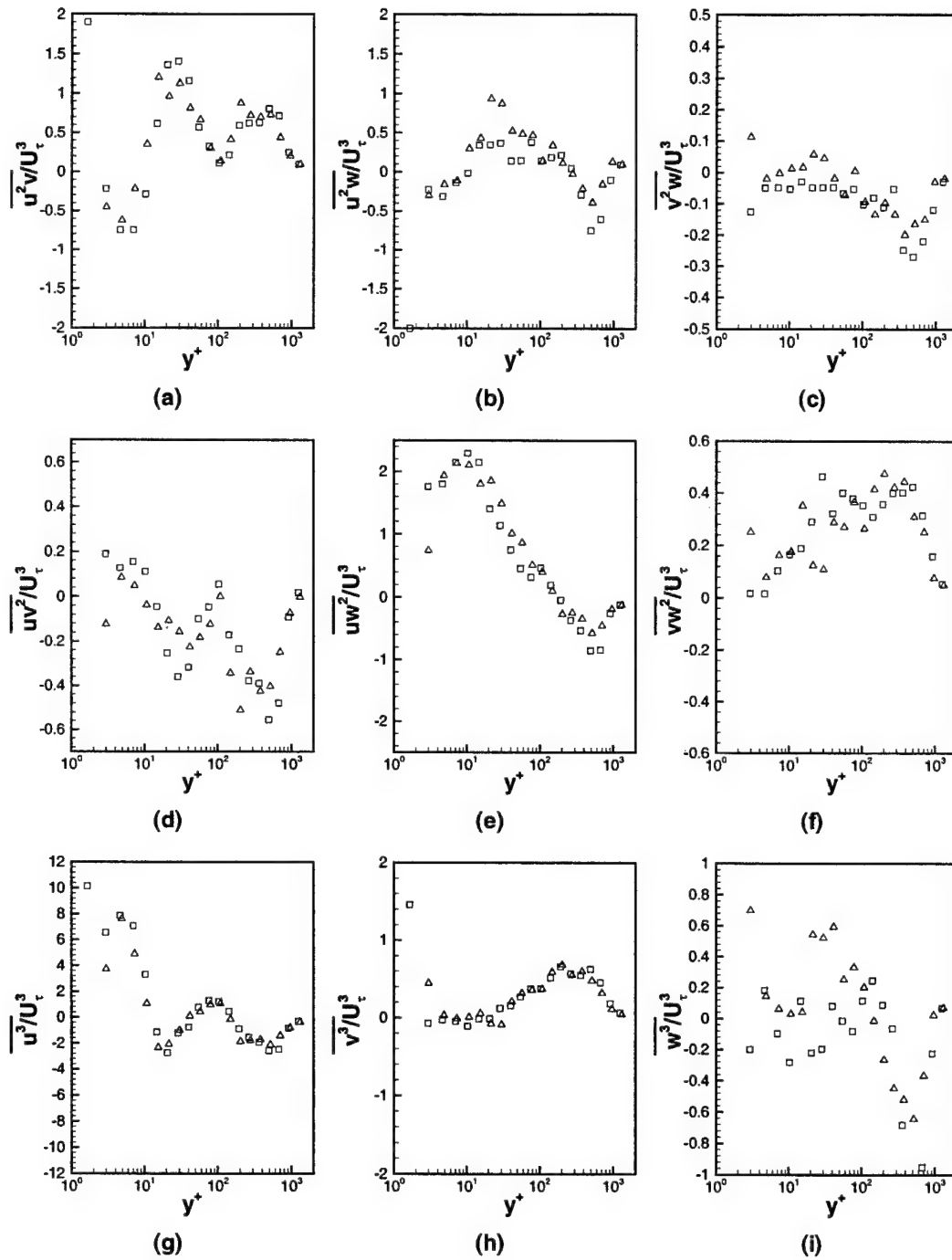
# Appendix D

## Cascade Tunnel Triple Product Data

This appendix documents the triple product data for all of the stationary profiles of the test matrix. Table 4.1 lists all of the profiles and the x and z locations for each. The same naming convention is used for the plots which are found in Figures D.1 to D.8. The data split up into three groups: the first is the free-stream profiles (Figures D.1 to D.3), the second are the front of the blade profile (Figure D.4), and the third is the tip gap profiles (Figures D.5 to D.8). The first and second groups are presented in the free-stream coordinate system. The third group is presented in the chord coordinate system. All the groups are normalized on  $U_\tau$ .

Figure D.1: Profiles 1F1  $\square$  and 1F2  $\triangle$  triple products in free-stream coordinates

Figure D.2: Profiles 3F  $\square$  and 4F  $\triangle$  triple products in free-stream coordinates

Figure D.3: Profiles 5F  $\square$  and 6F  $\triangle$  triple products in free-stream coordinates

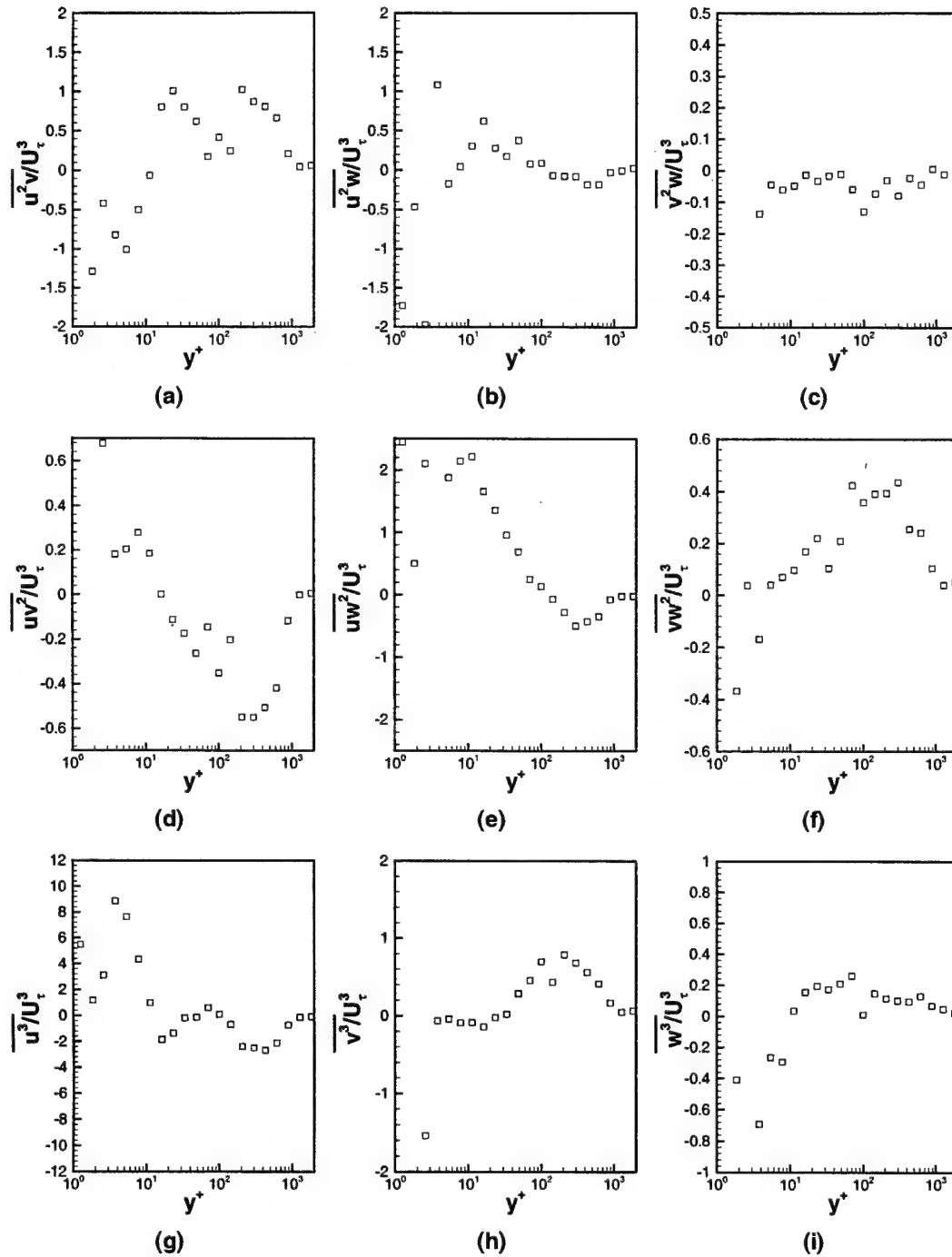
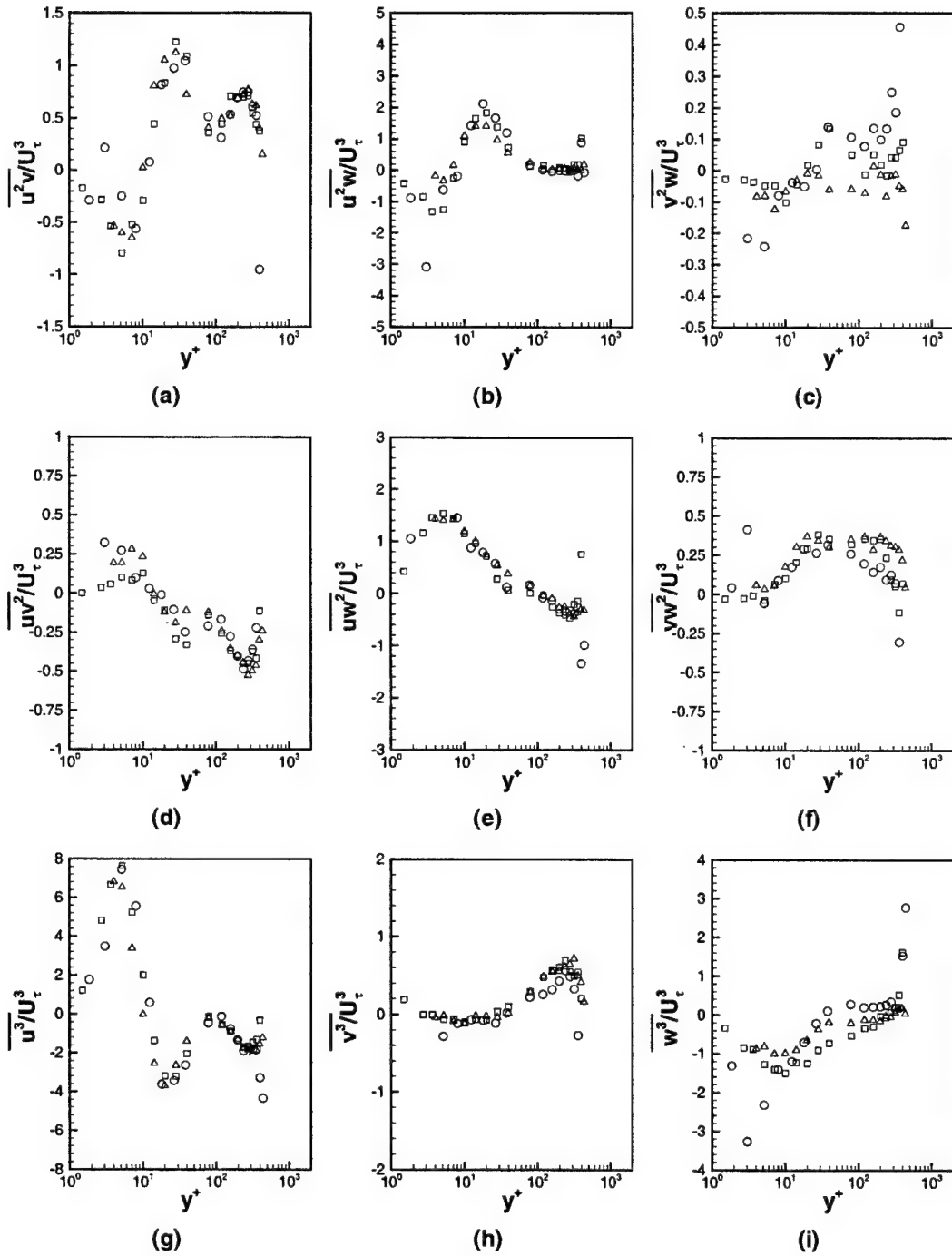
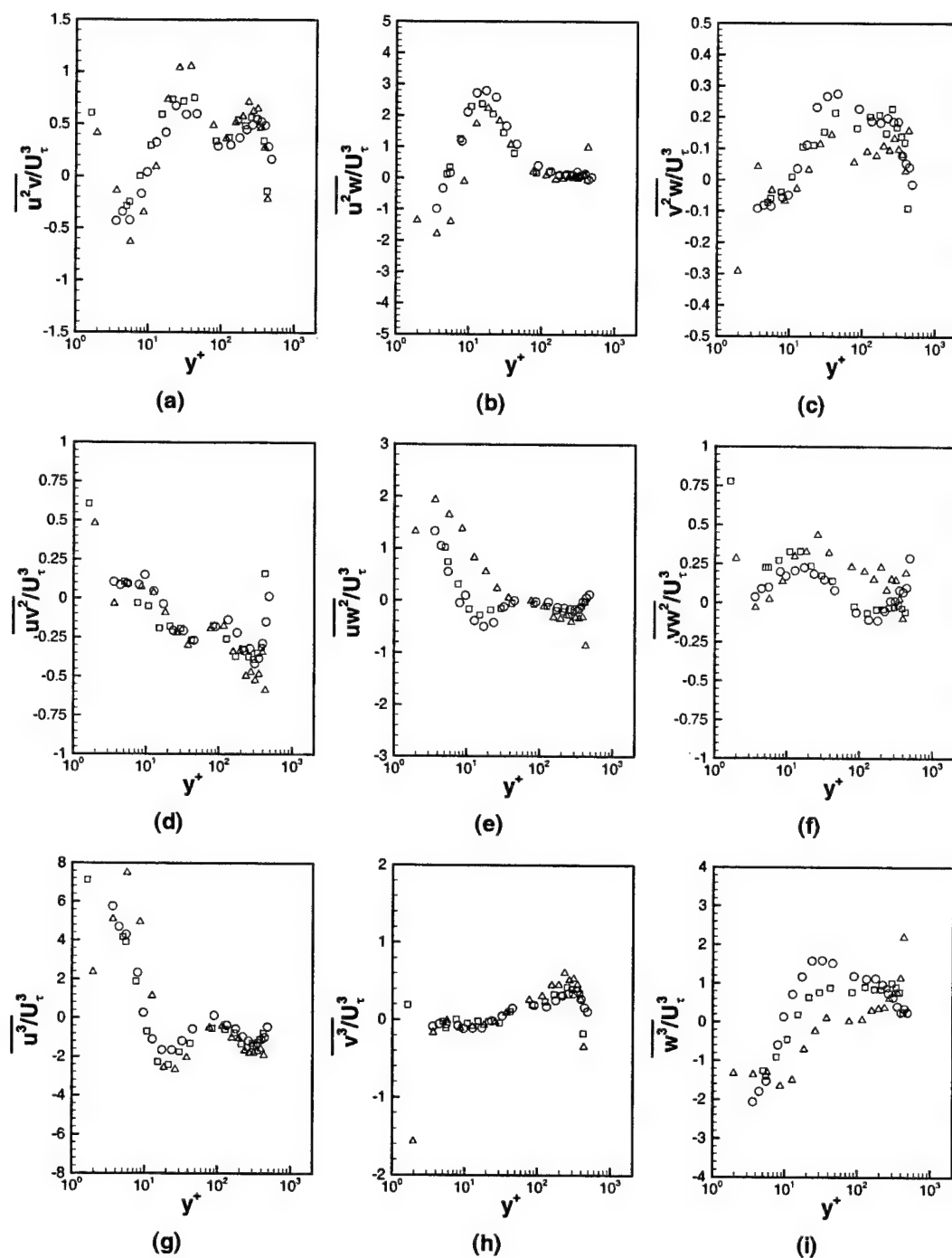
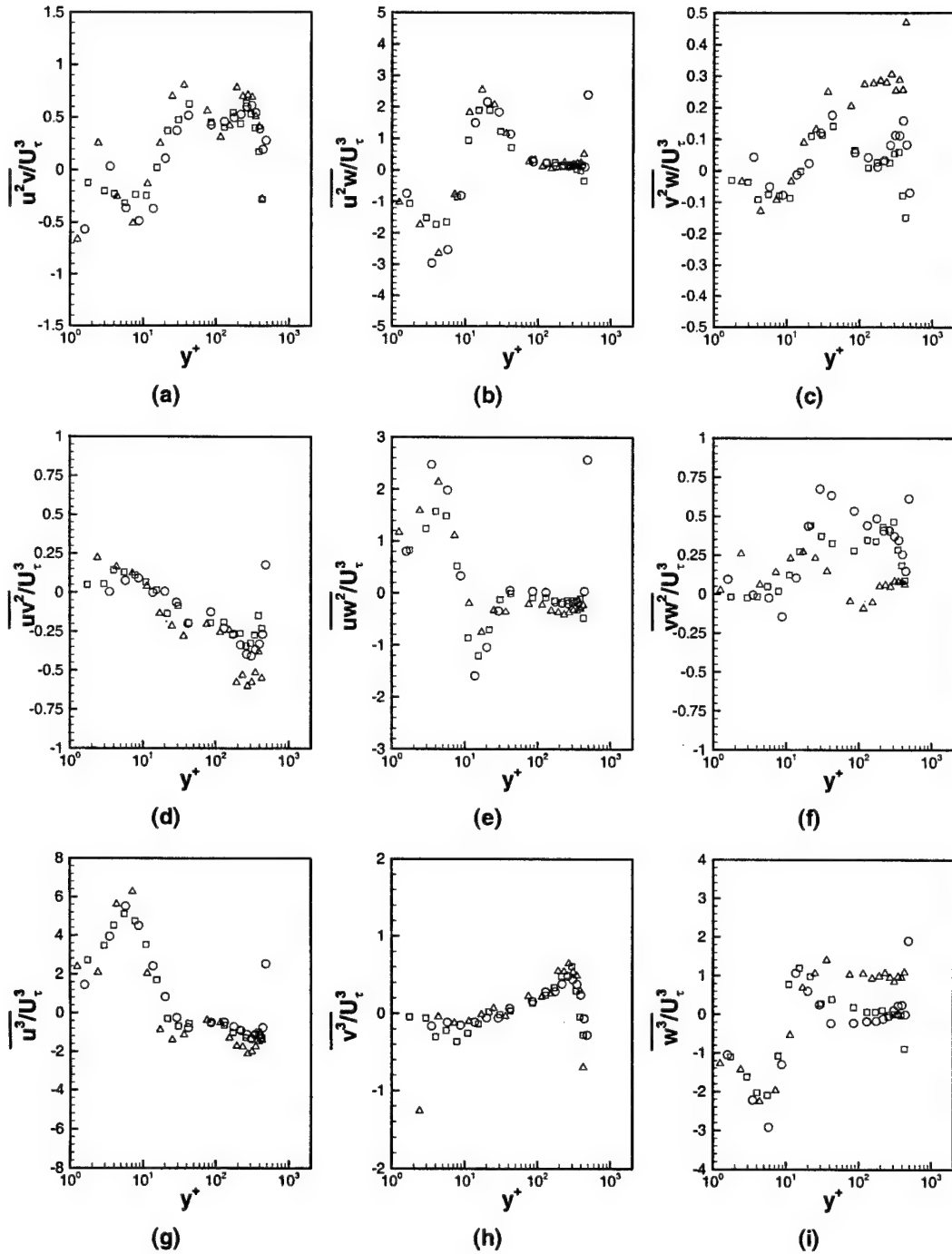


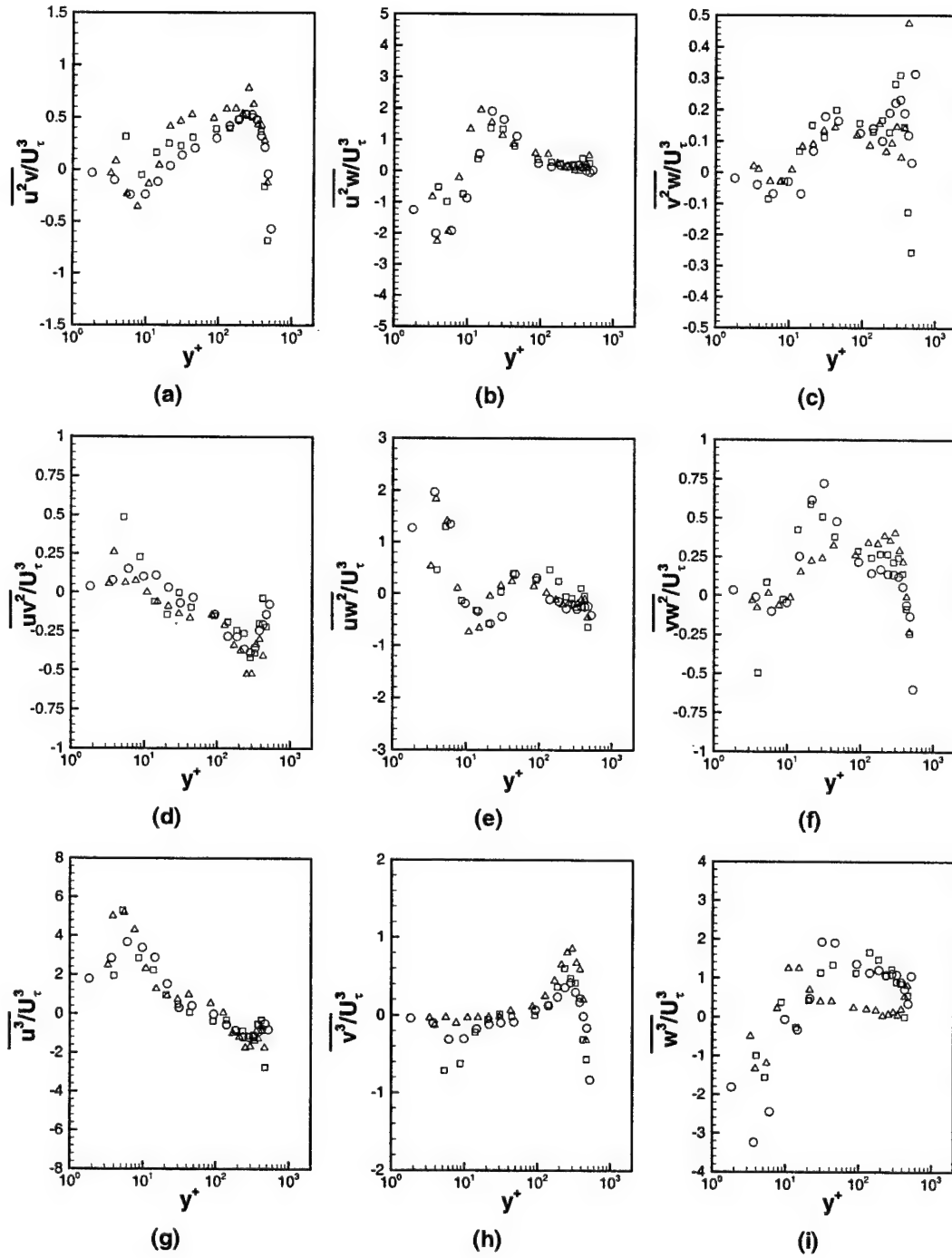
Figure D.4: Profile 1B triple products in free-stream coordinates



Figure D.5: Profiles 3S  $\circ$ , 3C  $\square$  and 3P  $\triangle$  triple products in chord coordinates

Figure D.6: Profiles 4S  $\circ$ , 4C  $\square$  and 4P  $\triangle$  triple products in chord coordinates

Figure D.7: Profiles 5S  $\circ$ , 5C  $\square$  and 5P  $\triangle$  triple products in chord coordinates

Figure D.8: Profiles 6S  $\circ$ , 6C  $\square$  and 6P  $\triangle$  triple products in chord coordinates

# Appendix E

## Turbulence Grid Flow

This appendix details the results from a single profile taken with a turbulence generating grid placed in the flow upstream of the test section, approximately 175 cm upstream of the tip of blade 4). The measurement profile was taken at 3C (see Figure 4.2).

The turbulence generating grid consists of 10 vertical and 4 horizontal steel rods. The rods have a diameter of 0.625 inches. The rods are welded together into a square mesh with the horizontal rods downstream of the vertical rods. The cell size of the mesh is 2.95 inches. The open air ratio of the grid is 62%. The grid is perpendicular to the flow. For more information see Muthanna (2001).

Figures E.1 and E.2 shows the comparisons of the calculated velocities for the case with and without grid in the tunnel. The profiles were taken at point 6C as shown in Figure 4.14. In general the velocity magnitude decreases when the turbulence grid is placed in the flow. However there is a slight rise near the wall. The average difference, at the same height between with and without grid is 1.435 m/s.

Hancock and Bradshaw (1983) developed a relationship to estimate the change in the shear stresses due to changes in freestream turbulence. The relationship is shown in Equation E.1.

$$\Delta C_f / C_{f_o} = f[(\sqrt{u^2} / U_e) * 100 / (L_u^e / \delta_h + 2)] \quad (E.1)$$

f signifies a function of the argument.  $\Delta C_f$  is change skin friction from no-grid to grid.  $C_{f_o}$  is no grid,  $L_u^e$  integral length scale,  $\delta_h$  is height length scale. The values from the flow are shown in Table E.1

Table E.1: Values used in Hancock Relationship for With and Without Turbulence Grid

$\Delta C_f$	$7.078 \times 10^{-4}$
$C_{f_o}$	0.197858
$\overline{u^2}$	$3 (m/s)^2$
$U_e$	25 m/s
$L_u^e$	2.21 cm
$\delta_h$	0.8382

The  $L_u^e$  value is from de la Riva (2001),  $\delta_h = 0.8382$  cm is the gap height. In Hancock and Bradshaw (1983)  $\delta_h$  is the boundary layer thickness. However turbulence completely fills the tip gap and the tip gap length scale is used.

The left side of Equation E.1 calculates to 0.198. The right side of Equation E.1 calculates to 1.49. Hancock and Bradshaw (1983) estimates the right hand side of the relationship to be 1.51. The  $U_\tau$  decreases when putting in the turbulence grid from 1.06 m/s to 0.95 m/s putting.

## References

- de la Riva, D.H., 2001 "Turbulence Interaction in a Highly Sataggered Cascade-Propulsor Configuration" M.S. Thesis, Virginia Tech, Blacksburg VA.
- Muthanna, C., 2001 "Effects of Free Stream Turbulence on the Viscous Flow Field of a Compressor Cascade," AIAA paper 2001-3209, 37th AIAA/ASME/SAE/ASEE Joint Propulsion Conference and Exhibit, Salt Lake City, UT, July 8-11.
- Hancock, P. E. and Bradshaw, P., 1983 "The Effect of Free-Stream Turbulence on Turbulent Boundary Layers," Transactions of the Journal of Fluids Engineering, Vol. 105, Sept. pp. 284-289.

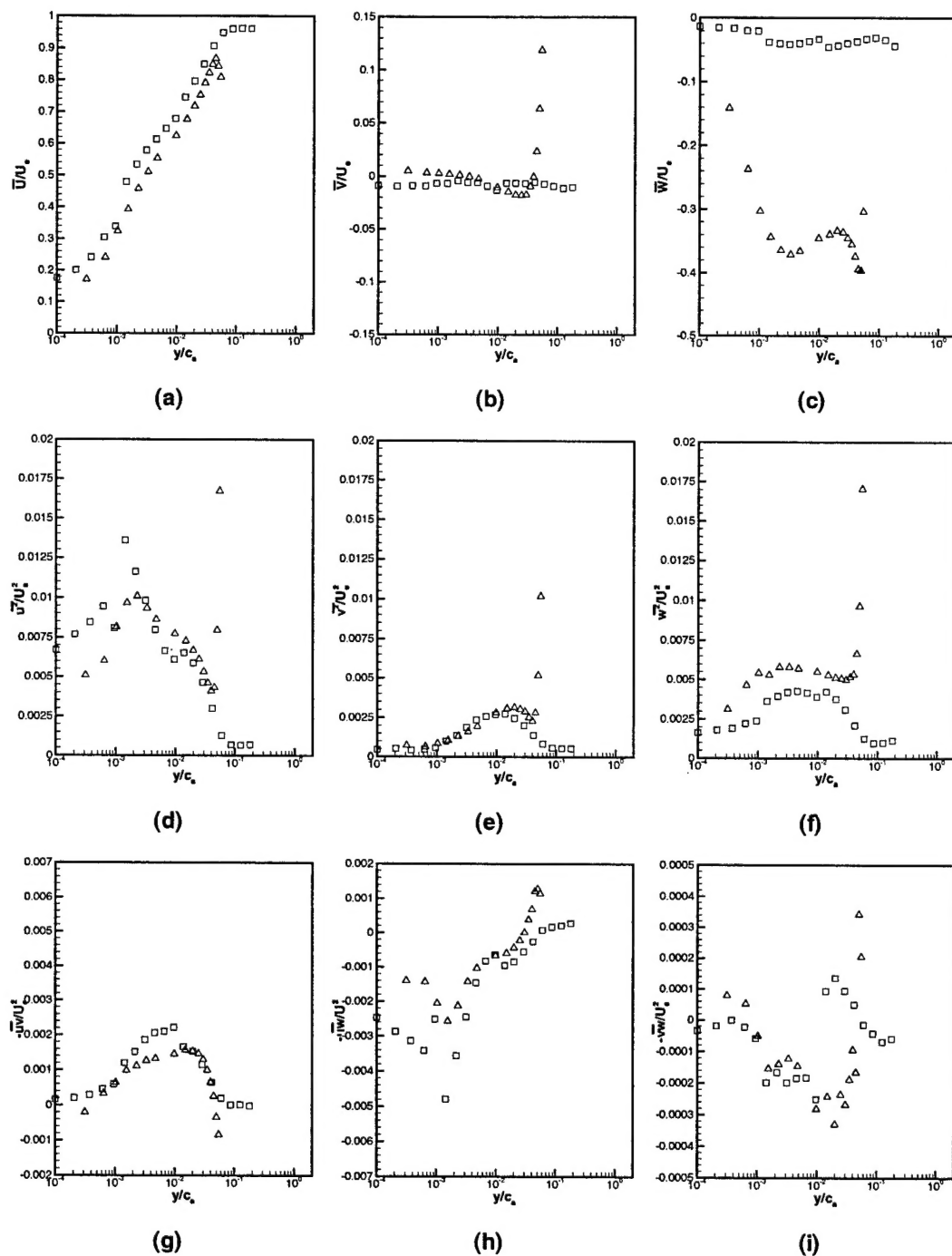


Figure E.1: With and Without Turbulence Grid Point 6C Mean and Reynolds Velocities ( $\square$  With Grid,  $\triangle$  Without Grid)

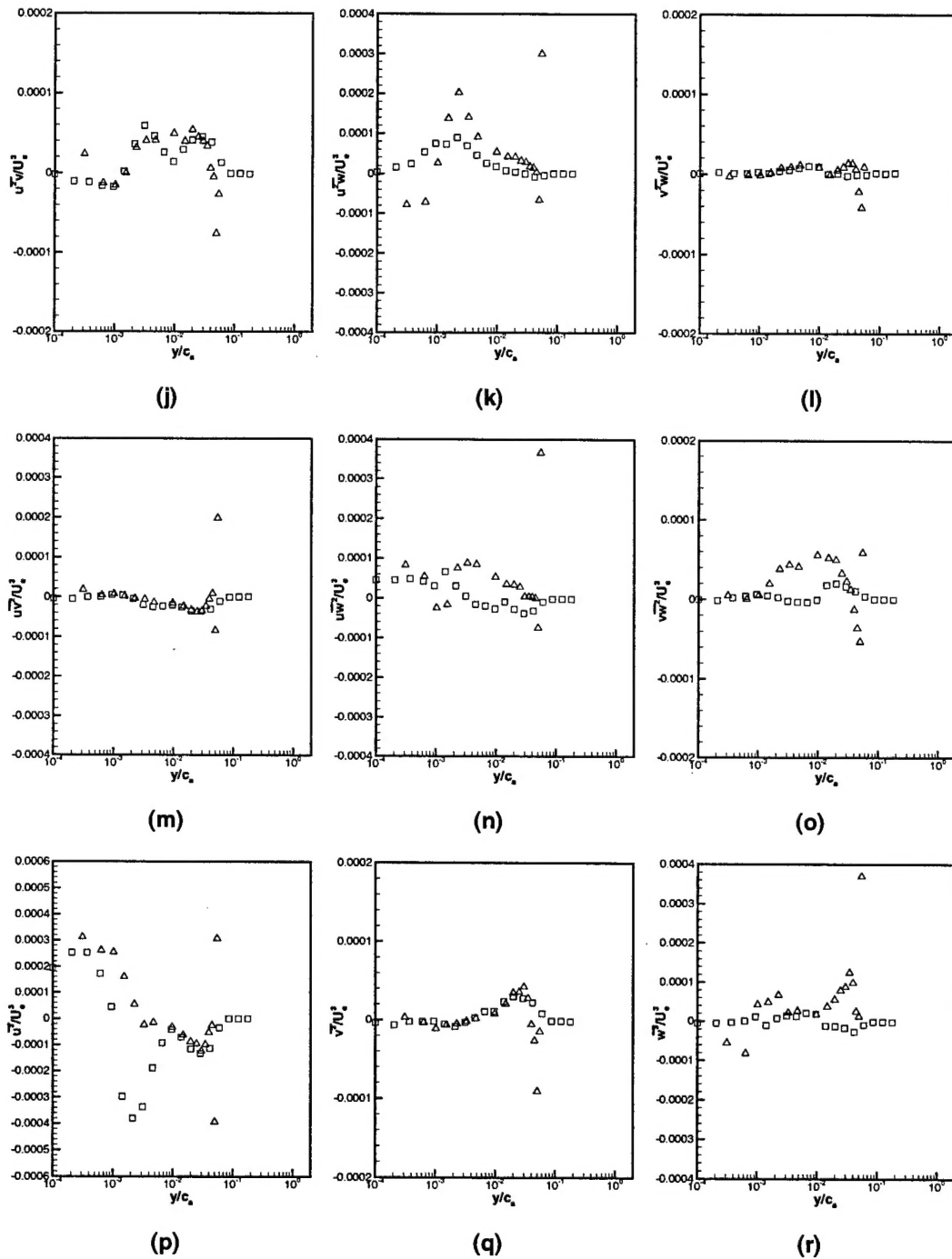


Figure E.2: With and Without Turbulence Grid Point 6C Triple Product Velocities ( $\square$  With Grid,  $\triangle$  Without Grid)



# Vita

David D. Kuhl was born in Lexington, Kentucky May 1975. After living in Kentucky and then Harrisburg, Pennsylvania for a short period of time he moved to Ames, Iowa. He attended public schools in Ames and graduated from Ames Senior High School in 1994. The University of Iowa, in Iowa City Iowa, is where he received his Bachelor of Mechanical Engineering degree with Honors in December of 1998. From January 1995 to December 1998 David worked at the Iowa Institute for Hydraulic Research (IIHR) as an undergraduate research assistant, helping with with fluid dynamics experimentation. He worked at IIHR while in school except for the summer and fall of 1997 when David did a co-op at General Electric Power Systems in Schenectady, NY investigating materials for Gas Turbines. In January of 1999 he moved to Blacksburg, VA to begin graduate school at Virginia Polytechnic Institute and State University. August of 2001 David graduates from the Aerospace and Ocean Engineering Department with a Master of Science degree.